ORIGIN AND EVOLUTION OF ATMOSPHERES AND OCEANS*

A. G. W. CAMERON, P. J. BRANCAZIO, AND N. W. PANAGAKOS

In recent years it has become evident that the atmosphere and oceans have been produced by the outgassing of volatile materials from the earth's interior, principally from volcanoes. In 1950 W. W. Rubey presented geological evidence indicating that sea water has progressively accumulated in this way. At about the same time, Harrison Brown pointed out that the very low abundances of the noble gases in the earth's atmosphere constituted compelling evidence that at least the atmospheric oxygen and nitrogen were almost entirely of secondary origin, having been outgassed, possibly in different chemical form.

The main purpose of the 1963 conference was to consider new evidence for mechanisms which might add to or subtract from the contents of the atmosphere and oceans, and to consider mechanisms which could contribute to the origin of atmospheres of other planets. H. H. Hess opened the discussion with a consideration of the problems of convection currents in planetary mantles. The important factor is the time between nucleosynthesis and the formation of the solid planet. The protoplanet will contain radioactive materials which generate heat, and the rate at which it is generated will decrease as the activity of the radioisotopes decreases. A planet may or may not have convection, depending on whether enough radioactive materials remain in the mantle to cause vigorous heating at the base.

K. K. Turekian of Yale University discussed some models for the degassing of argon from the earth. He showed that at least eighty percent of the argon now in the atmosphere must have come from the mantle. He proposed that the most useful degassing model appeared to be one with continuous degassing of the earth as a whole. Turekian pointed out, however, that one should be careful in applying the results thus obtained to the escape of the other rare gases from the earth.

L. V. Berkner of the Southwest Center for Advanced Studies, Dallas, Texas, discussed the origin of oxygen in the earth's atmosphere. According to Berkner, the existence of an appreciable atmosphere of oxygen implies the presence of life. He pointed out that the production of oxygen in the primitive atmosphere from the photochemical dissociation of water would in turn lead to a layer of ozone in the atmosphere. The ozone layer is a buffer against the destruction of terrestrial life as we know it by the ultraviolet rays of the sun. If the amount of oxygen in the atmosphere were very small, the ozone layer would occur at ground level, and the sun's ultraviolet radiation would penetrate to the surface. In such a harmful environment, life would be unable to emerge from the seas onto land.

Tracing the history of the earth's atmosphere, Berkner pointed out that a sufficiently long period of time had to elapse for marine life to produce sufficient oxygen to change the composition of the atmosphere and produce high-lying ozone layers. When this took place, life was able to emerge—first in plant form, then in animal form in perhaps a few million years.

The helium problem was examined by G. J. F. MacDonald of the University of California at Los Angeles. He pointed out that if it is assumed that the escape of gases from the earth's atmosphere is due only to temperate effects, then the rate of influx of helium by outgassing is larger than the rate of escape. The helium in the earth's atmosphere should be building up at a rapid rate, but this is not the case. MacDonald noted that analyses of satellite drag data by I. Harris and W. Priester showed that an additional heat source derived from the solar wind is necessary to account for the time variations in the temperature of the

*Published in *Physics Today*, :19–22, February 1964.

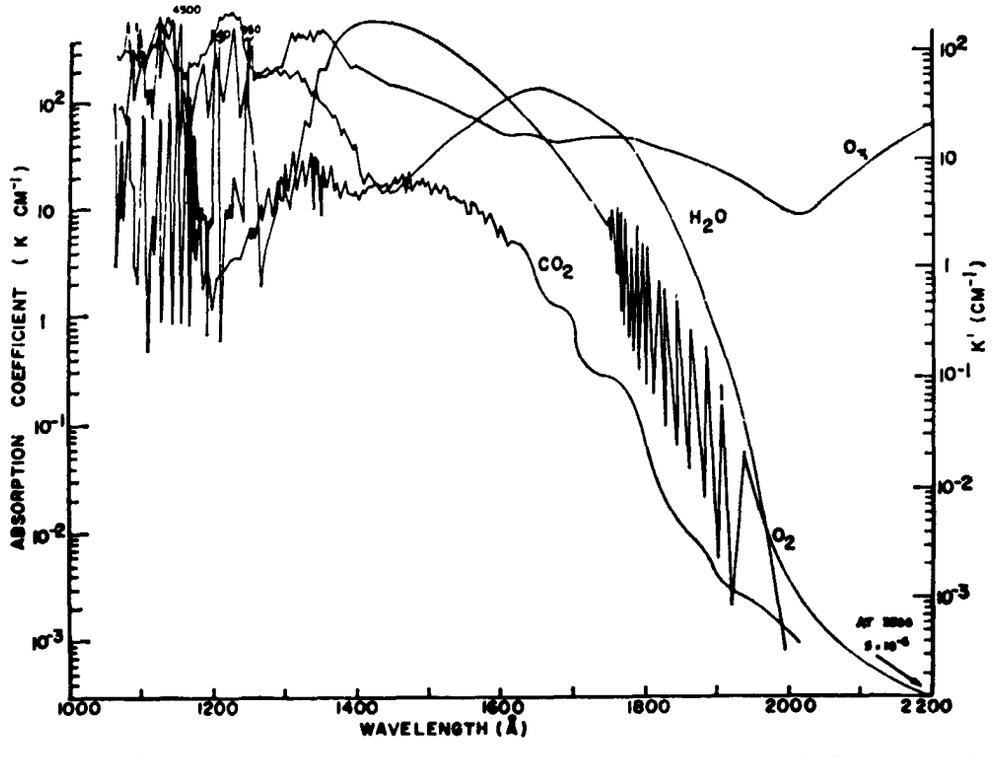

SKETCH 1.—Ultraviolet absorption by various atmospheric constituents, as presented by L. V. Berkner of the Southwest Center for Advanced Studies. The absorption beyond 2000 angstroms is almost entirely due to ozone.

upper atmosphere. He also noted that if the earth's magnetic field was at one time significantly stronger, as indicated by measurements of ancient baked clay, the interaction between the field and solar plasma could increase the heating of the upper atmosphere. This could account for a greater rate of escape of helium, averaged over a long time scale.

R. O. Pepin discussed some of the recent work done by J. R. Reynolds and his group at the University of California, Berkeley, in the field of "xenology"—the study of the isotopic abundances of the xenon isotopes. These studies are providing considerable information about the early history of the solar system; for example, the anomalously high abundance of ^{129}Xe resulting from the decay of primordial ^{129}I allows us to obtain the formation ages of meteorites. He pointed out that the relative abundances of the xenon isotopes differ for different types of meteorites and, in particular, the isotopic abundances of the xenon isotopes in the earth's atmosphere differ from the abundances found in meteorites. The problem is to account for all these anomalies.

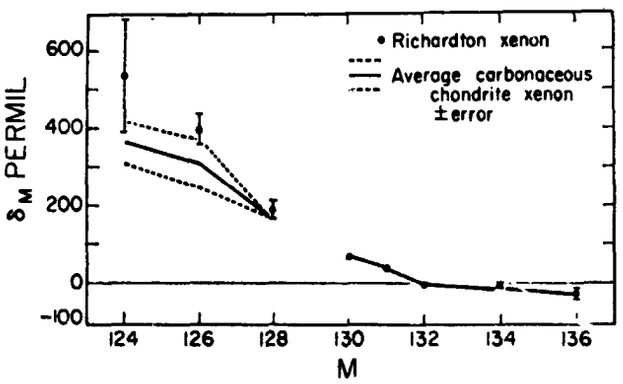

SKETCH 2.—Comparison between the general anomalies in xenon from the Richardton stone meteorite (an ordinary chrondrite) and in xenon from carbonaceous chondrites.

In this respect, Pepin cited the work of W. B. Clarke, who conducted heating experiments on irradiated uranium oxide samples. Clarke found that the xenon evolved at low temperatures was isotopically different from that evolved at high temperatures. The inference is that the isotopic anomalies may be due to temperature fractionation effects on a fissionogenic component of the xenon gas.

Among the studies done by the Berkeley group was an analysis of some deep-seated terrestrial rocks. They found that the xenon evolved from these rocks contained a fission component resulting from uranium spontaneous fission. This suggests the feasibility of a U-Xe dating method, to be used in conjunction with other established dating techniques.

Peter Signer of the University of Minnesota showed that the abundances of primordial gases in meteorites are generally similar to those in the atmosphere or in the sun only when there is a great amount of this gas in the meteorites. If the amount of gas is small, then a very large degree of fractionation can occur among the elements.

In order to understand the composition of the earth's atmosphere, one must be able to explain the differences between the isotopic abundances of xenon isotopes in meteorites and in the earth. A. G. W. Cameron of the Goddard Institute for Space Studies interpreted the differences in abundances of the light "shielded" xenon isotopes as resulting from neutron capture in the sun during the deuterium-burning stage of early solar history. However, this interpretation requires that the bulk of the xenon in the earth's atmosphere should have once been in the sun, and that it has since been captured by the earth from the solar wind.

The composition of Mercury's atmosphere raised considerable discussion among participants at the conference. Mercury is the smallest planet, and, because of its small size, has been generally believed to have no atmosphere, or a very tenuous one at best. George Field of Princeton University discussed measurements of the differential polarization of scattered light from Mercury made by Audouin Dollfus of the Observatoire de Paris, Meudon, France, who had interpreted them as showing the presence of a small atmosphere.

Field suggested that the atmosphere of Mercury may be composed of a considerable amount of radiogenic argon which escaped from the interior of the planet. The observed atmosphere would require that Mercury had outgassed to about the same extent as the earth. However, if the atmospheric constitution is to be nearly pure argon, the temperature of the upper atmosphere should not exceed 1400 degrees. Above this temperature, evaporative escape would take place. A problem arises in that theoretical estimates place the temperature of an upper atmosphere of pure argon at well above 1400 degrees, since argon is a very inefficient radiator of electromagnetic energy. It was agreed that much more study is needed for an understanding of the manner in which an argon atmosphere—if it exists—could be maintained on Mercury.

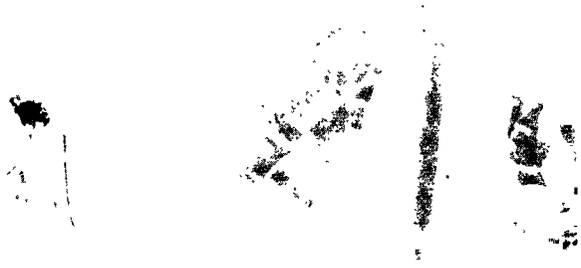

SKETCH 3.—Seated in the cabin of his balloon observatory, Audouin Dollfus of the Observatoire de Paris prepares for a flight in which he attempted to detect extraterrestrial water.

Important new data concerning the presence of water vapor on Mars and Venus was presented by Audouin Dollfus. Reporting on observations made with a specially designed telescope which he carried aloft in a balloon, and on observations made from an elevated mountain observatory, Dollfus said he measured 0.01 gm/cm² of water vapor for Venus above the cloud-top level.

For Mars, Dollfus found 0.02 gm/cm² of water vapor, enough to cover that planet to a depth of a fifth of a millimeter. This is five times as much as had been generally estimated. The disagreement between Dollfus' observations and those of several other scientists who give lower values for the water-vapor content of the Martian atmosphere raised sharp debate at the conference. Participants concluded that various experiments may have been subject to unforeseen sources of error, and that it is extremely important to make new measurements.

H. D. Holland of Princeton University suggested that pools of molten sulphur, rather than oceans of water, will be found on the surface of Venus. When that planet was formed, much less water was accreted than when the earth was formed, he suggested. The main substance ejected from Venusian volcanoes probably is sulphur dioxide, which would react with carbon

monoxide to form liquid sulphur on the surface.

Thomas Gold of Cornell University suggested that some of the depressions on the moon's surface may be regions of collapse caused by underground rivers which result from an "outgassing" process taking place in the moon.

He reasoned that if there is water in the interior of the moon, radioactivity should produce enough heat to vaporize it. The water vapor would then seek to rise from the interior to the surface, but it would be trapped by a permafrost or ice layer which must exist below the surface at a depth of 150 feet. However, large meteorites striking the lunar surface could form craters extending below the ice layer; the water in the area of the explosion would then flow underground towards the crater. The extensive area that is drained might then collapse, forming the rills that are a common feature in moon photographs. Gold pointed out that these rills or depressions, converging on craters in flat ground from many angles, could hardly be caused by stresses from the craters themselves. Unlike the stress pattern, the rills do not converge in a straight line, but zigzag—sometimes for hundreds of miles.

Gold also suggested that Venus may possibly be covered by water which has escaped from the interior of the planet. The consensus among scientists has been that if there is water on Venus, it is in the planet's atmosphere and does not exist in appreciable amounts. However, Gold cautioned against ruling out the possibility of water on the surface. His contention was that it is too difficult to explain what happened to the water that must have been present on Venus at some time in its past if this were not the case.

Venus resembles the earth closely in many of its properties. Hence, Gold reasoned that water should have been outgassed from Venusian volcanoes to the same extent that this outgassing had occurred on earth. If Venus' surface temperature is somewhat less than that measured by instruments on Mariner II (perhaps a little less than 600° K), then water would be in equilibrium with steam. Hence, Venus should possess a very massive lower atmosphere composed primarily of steam.

Discussing the atmosphere of Venus, [illegible] Sagan of Harvard University reviewed many of [illegible]eat uncertainties in the measured parameters [illegible]e planet. He also discussed some of the chemical equilibria that could influence the composition of gas in the Venusian atmosphere.

Sagan noted that the planet must be extremely hot at the surface, a temperature of perhaps 650° K on the dark side and about 750° K on the bright side. The pressure at the base of the Venusian atmosphere appears to be at least 30 atmospheres, which would indicate that there may be an appreciable amount of water vapor. Nevertheless, because of the high temperatures, the amount of water in the Venusian atmosphere would be enormously less than that in the earth's oceans. Hence, Sagan disagreed with Gold's suggestion that an approximation of the Venusian atmosphere could be obtained by heating the surface of the earth.

Despite the relatively large amount of observational data on Mars, there is still a considerable degree of uncertainty about the abundances of the planet's atmospheric constituents, according to Richard M. Goody of Harvard University. The amount of carbon dioxide could be reliably determined if the atmospheric pressure at ground level were known, but this is uncertain by at least a factor of two. The amount of oxygen is probably very small. One clue to the abundance of oxygen in the Martian atmosphere might be obtained by detecting that element's allotrope, ozone. This raises a problem, however. If there is oxygen on Mars, ozone should be present even at the ground level. Berkner pointed out that ozone formed near the ground may react with anything that can be oxidized, unless the entire surface of Mars is sufficiently covered by an oxide layer that further oxidation is impossible. It is possible that the continual weathering by wind on Mars would expose fresh rock surfaces and that the subsequent loss of ozone would eventually result in a very small amount of oxygen in the atmosphere.

P. J. E. Peebles of Princeton University presented new calculations showing that Jupiter and Saturn have approximately the same composition, predominantly hydrogen and helium, and that the ratio of hydrogen to helium is similar to that of the sun. Using a variety of reasonable values for different mixtures of hydrogen and helium—and with a core of heavier elements near the center of the planet—Peebles found that a helium-hydrogen ratio by number of 0.075 to 0.08 for Jupiter, and

perhaps twice this amount for Saturn, was required in order to reproduce the mechanical properties of these planets. The amount of heavier elements has not been well determined, but it is only a few percent by mass.

Rupert Wildt of Yale University Observatory summarized the results obtained by H. Spinrad of the Jet Propulsion Laboratory, who showed that at times there are clouds of ammonia in the upper atmosphere of Jupiter which have velocities as high as four kilometers per second relative to the underlying atmosphere. This has become known as the "Spinrad effect." Spinrad has also determined some preliminary values for the composition of the Jovian atmosphere. His work indicates that the ratio of carbon to hydrogen on Jupiter is greater than that in the sun, and that it is higher still in the atmosphere of Saturn.

THE RED LINE OF ATOMIC OXYGEN IN THE DAY AIRGLOW*

A. DALGARNO† AND JAMES C. G. WALKER

It is argued from the observations of the red line that the rate coefficient for deactivation of the excited oxygen atoms in collisions with molecular oxygen cannot be much less than 10^{-10} cm^3 sec^{-1} and that the solar flux in the region of 1450Å cannot be as large as the reported measured values. It is further argued that photodissociation of molecular oxygen and recombination of molecular ions are inadequate to explain the observations and that an additional mechanism is operative at high altitudes. The mechanisms of fluorescent excitation and of non-thermal excitation by photoelectrons are briefly examined and it is concluded that although the latter may be a significant source of excited atoms, neither mechanism explains the observed variability. It is suggested that the variability in red line intensities is associated with the presence of hot thermal electrons and sample calculations are presented of the altitude profiles that may result from this source.

1. INTRODUCTION

From a theoretical survey, Bates and Dalgarno (1954) concluded that the red line of atomic oxygen at 6300 Å is one of the strongest features of the dayglow spectrum, and a more quantitative study of the red line by Brandt (1958) yielded an intensity of 50 kilorayleighs (kR), about half arising from photodissociation of molecular oxygen in the Schumann-Runge continuum

$$O_2+h\nu\rightarrow O(^3P)+O(^1D) \qquad (1)$$

and about half arising from dissociative recombination of the molecular ions O_2^+

$$O_2^++e\rightarrow O(^1D)+O'. \qquad (2)$$

The ground-based measurements of the red line in the dayglow by Noxon and Goody (1962) and by Jarrett and Hoey (1963) yielded intensities comparable with those predicted by Brandt, but other ground-based measurements by Noxon (1963) and rocket-based measurements by Zipf and Fastie (1963) and by Wallace and Nidey (1964) have shown that the intensity of the red line is often much less than the predicted value. This variation in intensity is significant for it suggests that the mechanisms leading to the emission of the red line have not been correctly identified and described.

2. MODEL ATMOSPHERES

To describe the structure of the neutral component of the upper atmosphere, we have employed the analytic representation of Bates (1959) which is specified by the temperature, temperature gradient and composition at a reference altitude, z_0, and by the exospheric temperature, $T(\infty)$. For the atmospheric parameters, we adopted the values

$$z_0=120 \text{ km}, \left.\frac{dT}{dz}\right|_{z_0}=20\text{K/km}, \quad T(z_0)=350\text{K}$$

and for the number densities of atomic oxygen, molecular oxygen, and molecular nitrogen at 120 km the alternative sets (i) $n(O)=5\times10^{10}$ cm^{-3}, $n(O_2)=1\times10^{11}$ cm^{-3}, $n(N_2)=5\times10^{11}$ cm^{-3}, which we shall describe as the high O_2 atmosphere, and (ii) $n(O)=5\times10^{11}$ cm^{-3}, $n(O_2)=2\times10^{10}$ cm^{-3}, $n(N_2)=5\times10^{11}$ cm^{-3}, which we shall describe as the low O_2 atmosphere. The models appear to span the possible atmospheres (Nicolet, 1961; Harris and Priester, 1962; Pokhunkov, 1963; Jursa, Nakamura and Tanaka, 1963; Schaefer, 1963; Hall, Schweizer, and Hinteregger, 1963; Nier, Hoffman, Johnson, and Holmes, 1964).

The mass density distribution corresponding to the low O_2 atmosphere with $T(\infty)=750$K and to

*Published in *Journal of the Atmospheric Sciences*, 21(6):463–474, September 1964.

†Queens University, Belfast, Northern Ireland.

high O_2 atmospheres with $T(\infty)=750$K and 1000K are compared in Fig. 1 with the density distributions derived from satellite drag data (King-Hele, 1963; Jacchia and Slowey, 1964; Bryant, 1964). The red line observations that we shall discuss were carried out in 1962 and 1963 and except when otherwise noted our results refer to the low O_2 atmosphere with $T(\infty)=750$K, an atmosphere in harmony with the drag data and an atmosphere more easily reconciled with observations of the red line than are the high O_2 atmospheres. The number density, temperature, and mass density distributions corresponding to the low O_2 atmosphere with $T(\infty)=750$K are presented in Table 1.

At altitudes below 120 km we used an atmosphere similar to the model of Jastrow and Kyle (1961).

3. PHOTODISSOCIATION IN THE SCHUMANN-RUNGE CONTINUUM

At wavelengths between 1300 Å and 1750 Å, ultraviolet radiation is strongly absorbed in the Schumann-Runge continuum of molecular oxygen

$$O_2(X^3\Sigma_g^-)+h\nu\rightarrow O_2(B^3\Sigma_u^-)\rightarrow O(^3P)+O(^1D), \quad (3)$$

the process providing a substantial source of $O(^1D)$

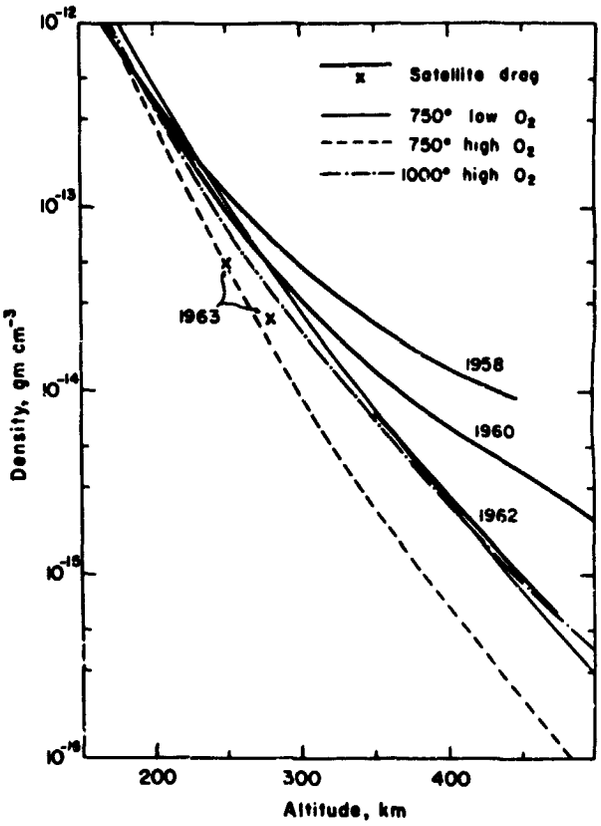

FIGURE 1.—Comparison of the model atmospheres with mid-year daytime maximum satellite drag densities (King-Hele, 1963; Jacchia and Slowey, 1964; Bryant, 1964).

TABLE 1.—*750° low O_2 model atmosphere.*

Altitude km	Temperature °K	Density gm cm^{-3}	Concentration, cm^{-3}				Emission probability, p, for $\beta=10^{-10}$ cm^3 sec^{-1}
			O	O_2	N_2	e	
120	350	2.96(−11)*	2.00(11)	2.00(10)	5.00(11)	1.25(5)	3.43(−3)
130	507	1.04(−11)	9.05(10)	5.94 (9)	1.65(11)	1.43(5)	1.14(−2)
140	602	5.26(−12)	5.51(10)	2.61 (9)	7.87(10)	1.70(5)	2.55(−2)
150	660	3.11(−12)	3.78(10)	1.35 (9)	4.37(10)	2.05(5)	4.79(−2)
160	695	1.98(−12)	2.76(10)	7.55 (8)	2.61(10)	2.53(5)	8.15(−2)
170	717	1.33(−12)	2.08(10)	4.41 (8)	1.62(10)	3.13(5)	1.30(−1)
180	730	18(−13)	1.59(10)	2.64 (8)	1.04(10)	3.80(5)	1.94(−1)
190	737	6.48(−13)	1.24(10)	1.61 (8)	6.70 (9)	4.38(5)	2.74(−1)
200	742	4.65(−13)	9.66 (9)	9.90 (7)	4.37 (9)	5.30(5)	3.63(−1)
225	748	2.14(−13)	5.30 (9)	3.01 (7)	1.54 (9)	7.65(5)	5.71(−1)
250	749	1.04(−13)	2.95 (9)	9.30 (6)	5.52 (8)	1.01(6)	6.87(−1)
275	750	5.32(−14)	1.65 (9)	2.91 (6)	2.00 (8)	1.25(6)	7.32(−1)
300	750	2.81(−14)	9.27 (8)	9.21 (5)	7.30 (7)	1.37(6)	7.50(−1)
350	750	8.36(−15)	2.97 (8)	9.46 (4)	9.95 (6)	1.09(6)	7.55(−1)
400	750	2.64(−15)	9.68 (7)	1.00 (4)	1.40 (6)	7.00(5)	7.58(−1)
450	750	8.61(−16)	3.21 (7)	1.10 (3)	2.02 (5)	4.50(5)	7.58(−1)
500	750	2.88(−16)	1.08 (7)	1.25 (2)	3.01 (4)	3.00(5)	7.58(−1)

atoms in the upper atmosphere (Bates, 1948). The rate of production of $O(^1D)$ atoms at an altitude, z, and for a solar zenith angle, θ, is given by

$$Q_1(z,\theta) = n(O_2|z)\int_{1350}^{1750} F_\infty(\lambda)\sigma(\lambda)\exp[-\mu(\lambda)]d\lambda \quad (4)$$

where $F_\infty(\lambda)$ is the incident flux, $\sigma(\lambda)$ is the absorption cross section and μ is the attenuation factor,

$$\mu(\lambda) = \sigma(\lambda)\int_{(R+z)\cos\theta}^{\infty} n(Q_2|\{y^2+(R+z)^2\sin^2\theta\}^{\frac{1}{2}})dy, \quad (5)$$

R being the radius of the earth. For the calculation of Q_1 we have used the measurements of $\sigma(\lambda)$ by Metzger and Cook (1964) and we have supposed the solar ultraviolet flux to be that of a black body at a temperature, T_s. The limited data (Purcell, Packer and Tousey, 1960; Detwiler, Garrett, Purcell, and Tousey, 1961; Tousey, 1963) are consistent with a value of 4750K for T_s. The results shown in Figs. 2 to 5 are actually appropriate to a solar temperature of 4500K, but they may all be scaled to a temperature of 4750K by multiplying by a factor of 2.9, the loss of accuracy being negligible.

Values of the production rates of $O(^1D)$ atoms are shown in Fig. 2 for several values of θ. Since the intensity of the red line at 6300 Å in the night airglow is much less than that of the green line at 5577 Å (cf. Chamberlain, 1961a) and since the red line is emitted at a much greater altitude than is the green line (Packer, 1961; Tarasova, 1963), it is clear that severe deactivation of the $O(^1D)$ atoms must occur at the lower altitudes (Bates and

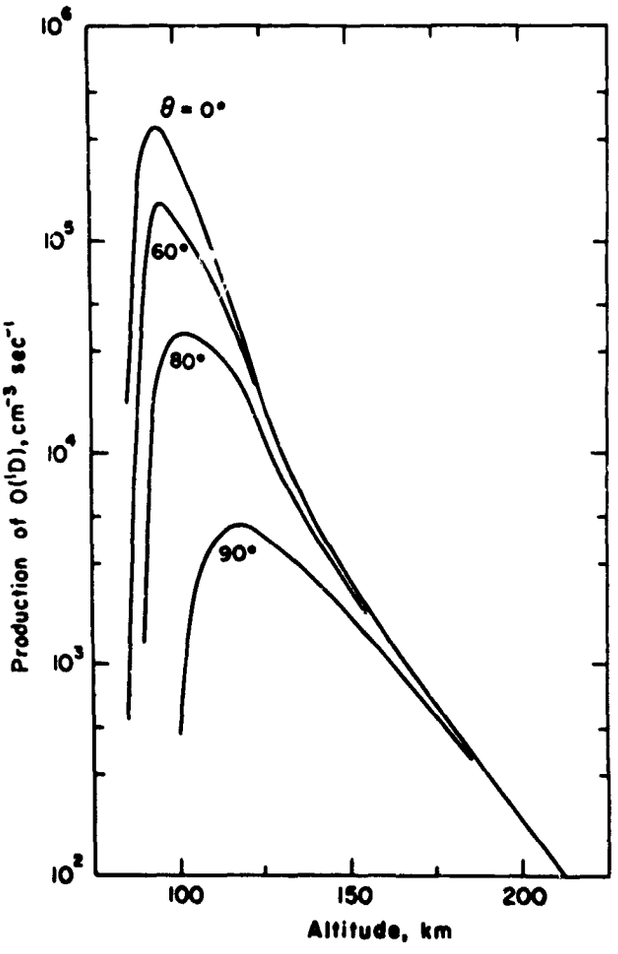

FIGURE 2.—Dependence on altitude of the rate of production of $O(^1D)$ atoms by photodissociation of O_2 for the 750° low O_2 model atmosphere with $T_s = 4500$K. Results are shown for several values of solar zenith angle, θ.

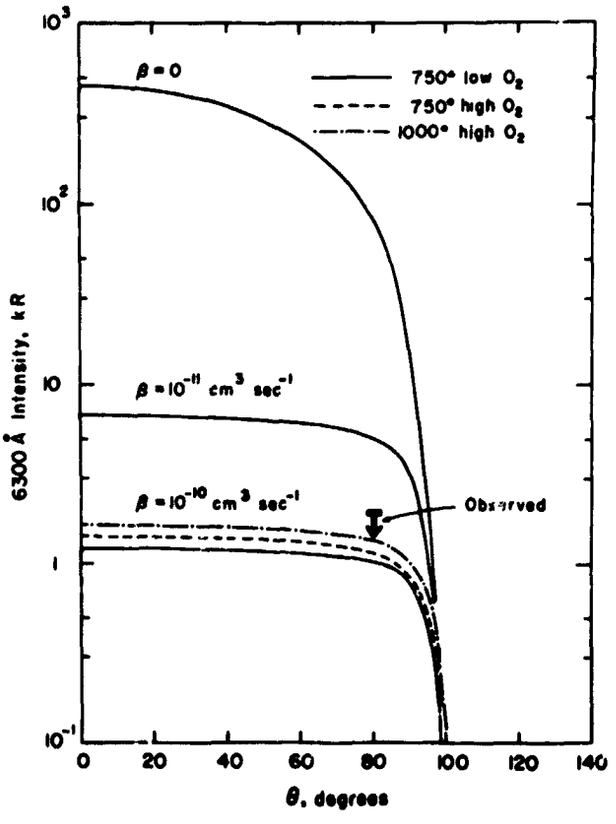

FIGURE 3.—Dependence on solar zenith angle of the intensity which results from the photodissociation of O_2 with $T_s = 4500$K. Results are shown for several atmospheric models and several values of the deactivation coefficient, β. The upper limit imposed by Noxon's (1963) observation is indicated.

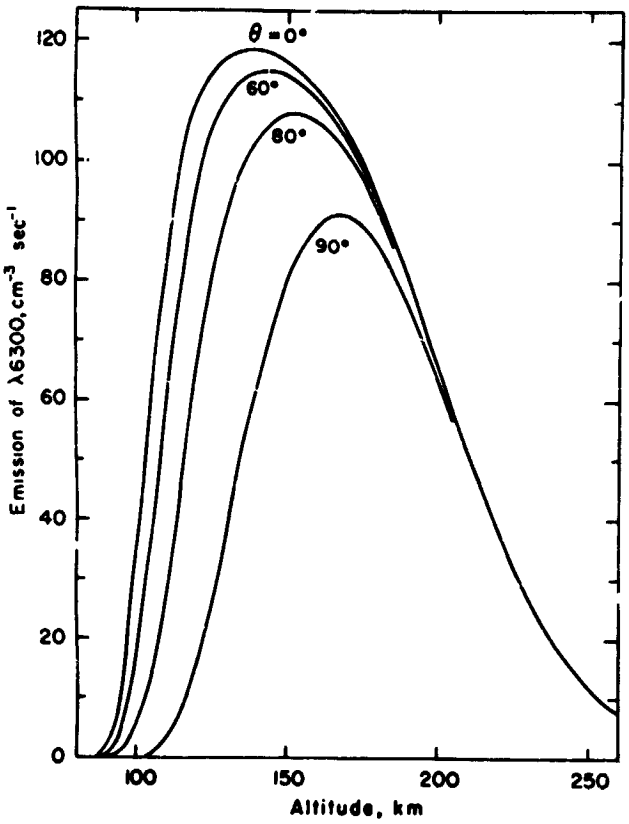

FIGURE 4.—Dependence on altitude of the emission of λ6300 which results from the photodissociation of O_2. The results are for the 750° low O_2 model atmosphere with $T_e = 4500$K and $\beta = 10^{-10}$ cm,³ sec⁻¹.

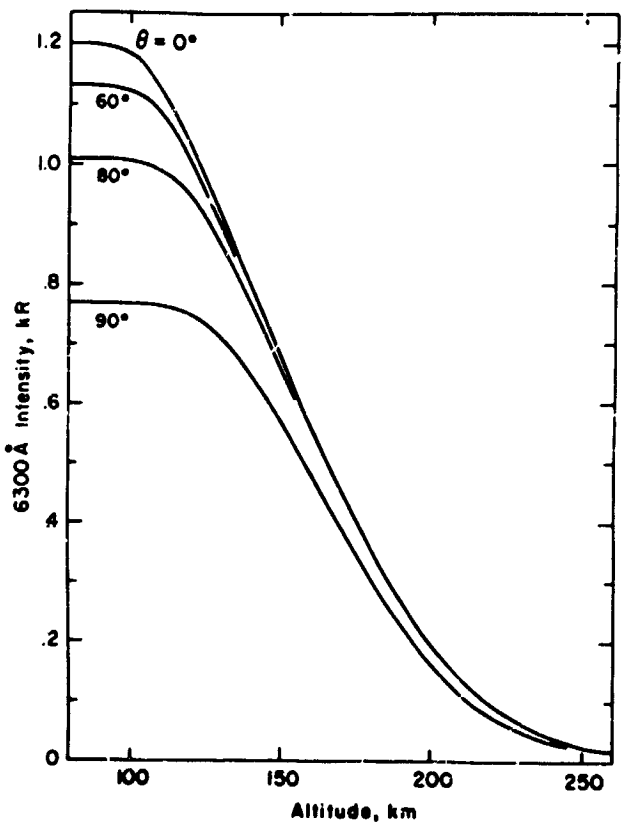

FIGURE 5.—Dependence on altitude of the zenith intensity which results from the photodissociation of O_2. The results are for the 750° low O_2 model atmosphere with $T_e = 4500$K and $\beta = 10^{-10}$ cm³ sec⁻¹.

Dalgarno, 1953; Seaton, 1954). Deactivation by electron impact is negligible (cf. Bates, 1960), and Bates and Dalgarno (1953) and Seaton (1958) have argued that the deactivation probably occurs in collisions with molecular oxygen. With this assumption, Wallace and Chamberlain (1959) have derived from an analysis of auroral observations of the O_2 atmospheric band system a rate coefficient, β, such that

$$4\times10^{-12}\ \text{cm}^3\ \text{sec}^{-1} < \beta < 10^{-10}\ \text{cm}^3\ \text{sec}^{-1}.$$

Despite the fact that the mechanism does not conserve spin, it has been suggested that deactivation of $O(^1D)$ by molecular nitrogen is comparable in efficiency (DeMore and Raper, 1964) and, although the arguments are not convincing, the possibility cannot be excluded. Because the N_2 density profile closely parallels the O_2 density profile, the inclusion of N_2 deactivation would involve no important modification of our subsequent arguments and we shall largely ignore it.

During the day, deactivation by electron impact is still negligible but there occurs the possibility that $O(^1D)$ atoms may be removed by resonance absorption of solar radiation.

There appears to be only one allowed transition, the wavelength of which coincides with a strong solar line, and that is the transition to the $O(2p^3 3s\,^1D)$ state at 1152 Å, the solar flux of λ1152 being about 10^9 photons cm^{-2} sec^{-1} (Hinteregger, 1961; Hinteregger and Watanabe, 1962). Despite the substantial flux and the wavelength coincidence, the mechanism can be discounted because the only allowed transition from the upper state returns the atom to the original ^1D state.

The probability that an $O(^1D)$ atom at altitude, z, will emit a 6300 Å photon is given by

$$p(z) = \left\{1+\frac{A_{6364}}{A_{6300}}+\frac{\beta n(O_2|z)}{A_{6300}}\right\}^{-1} = \{1.32+1.45\times10^2\beta n(O_2|z)\}^{-1}, \quad (6)$$

where A_λ is the radiative transition probability for

the line of wavelength λ (cf. Chamberlain, 1961b). Values of $p(z)$ are given in Table 1 for $\beta = 10^{-10}$ cm^3 sec^{-1}.

The intensities of red line emission for a solar temperature of 4500K and various values of the deactivation coefficient, β, are shown in Fig. 3 as a function of solar zenith angle. The intensity for an overhead sun varies from 433 kR in the absence of deactivation to 1.2 kR if β has a value of 10^{-10} cm^3 sec^{-1}, which is close to the maximum possible for a thermal collision. Fig. 3 includes also the intensities corresponding to two other model atmospheres to show the lack of sensitivity to the details of the number density distribution.

To determine β we note that Noxon (1963) has reported that the intensity of the dayglow red line at noon at Fort Churchill was less than 2 kR on 15 December, 1962, a result in harmony with an observation of Wallace and Nidey (1964). [illegible] Noxon was observing with the sun at a zenith angle of about 80°, it follows from Fig. 3 that, for the low O_2 atmosphere with $T(\infty) = 750$K, $\beta \geq 1.7 \times 10^{-10}$ cm^3 sec^{-1} if $T_e = 4750$K and that $\beta \geq 3.7 \times 10^{-11}$ cm^3 sec^{-1} if $T_e = 4500$K. If deactivation in collisions with N_2 were significant, the implied upper limit on T_e would be increased.

Bates and Dalgarno (1954) pointed out that photodissociation in the Hartley continuum of ozone is an intense source of O(^{1}D) atoms below 100 km, and Cadle (1964) has predicted an intensity of 2 kR for the resulting red line emission, his calculations following Brandt (1958) in using a value of 10^{-12} cm^3 sec^{-1} for β. With either of the two limits derived from Noxon's observations, the actual red line emission below 100 km must be negligible.

Adopting a value of 10^{-10} cm^3 sec^{-1} for β, we show in Figs. 4 and 5, respectively, the emission rate and zenith intensity as functions of altitude for a number of solar zenith angles.

4. IONIC RECOMBINATION

There is usually a good correlation between the nocturnal intensity of the red line and the critical frequency of the F region (Barbier, 1957; Barbier and Glaume, 1962; Barbier, Roach, and Steiger, 1962; Carman and Kilfoyle, 1963; Barbier, 1964), supporting the belief that the main excitation mechanism is dissociative recombination. Originally the molecular ion involved was identified as O_2^+ but it is apparently now believed that NO^+ is the major participant (cf. Wallace and Nidey, 1964). The proposed reaction

$$NO^+(X^1\Sigma^+) + e \rightarrow N(^4S) + O(^1D) \qquad (7)$$

fails to conserve spin. We therefore concentrate on O_2^+ recombination as a source of O(^{1}D) atoms. The ionospheric and airglow data presented by Barbier (1964) indicate that the rate of electron removal in the nocturnal ionosphere exceeds the rate of emission of 6300 Å photons by a factor of about 8, consistent with our suggestion that (7) is not an important mechanism for O(^{1}D) excitation.

The nocturnal intensity of the red line is between 50R and 100R (cf. Chamberlain, 1961a) and considerable daytime enhancement is to be expected. The calculations by Brandt (1958) were based upon a simple sequence of ion-removal reactions and his results were sensitive to the adopted reaction rates. It is now clear that the actual reaction paths in the ionosphere are much more complicated (Nicolet and Swider, 1963; Dalgarno, 1964a). Serious uncertainties remain, the consequences of which can be largely avoided by assuming that local equilibrium prevails between ion production and removal rates, an assumption which is valid below 300 km throughout most of the day but fails at greater altitudes because of the increasing importance of diffusion.

The ion production rates, $q(O^+)$, $q(N_2^+)$, and $q(O_2^+)$ cm^{-3} sec^{-1} have been calculated for a wide range of model atmospheres and solar zenith angles by Dalgarno and McElroy (1964a) and some of their results are reproduced in Fig. 6.

In order to estimate what fractions of the ions, O^+, N_2^+, and O_2^+, lead to (O^{1}D) atoms, it is necessary first to determine what fractions of the ions O^+ and N_2^+ are converted to O_2^+ ions or possibly to NO^+ ions. The fractions depend upon the electron density distribution and we have adopted the distribution measured by Brace, Spencer, and Carignan (1963) in a quiet ionosphere and included in Table 1. The intensity of the red line is insensitive to the details of the adopted electron density profile.

The reactions which remove N_2^+ ions have been discussed by Nicolet and Swider (1963). They are

$$N_2^+ + e \rightarrow N' + N'' \qquad (8)$$

$$N_2^+ + O_2 \rightarrow N_2 + O_2^+ \qquad (9)$$

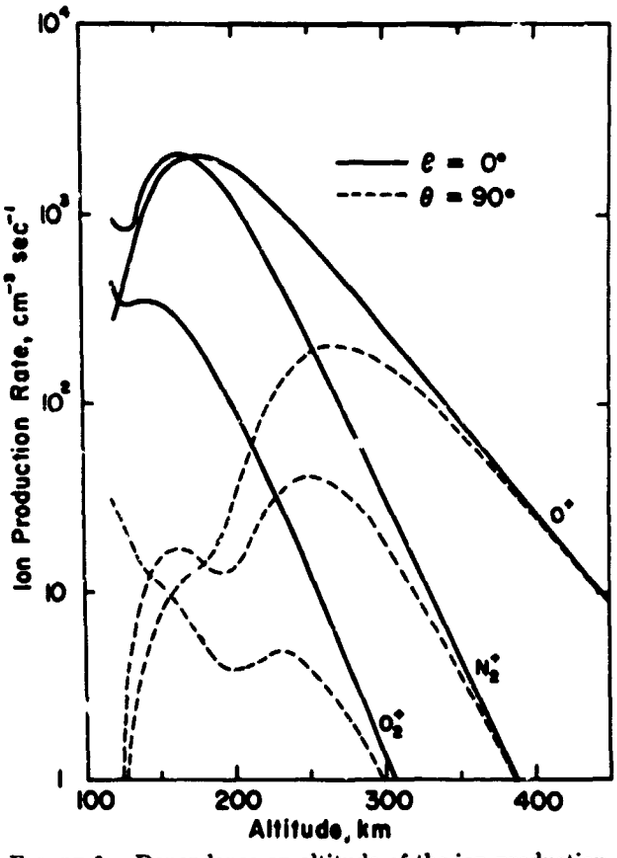

FIGURE 6.—Dependence on altitude of the ion production rates for the 750° low O_2 model atmosphere.

$$N_2^+ + O \rightarrow N_2 + O^+ \quad (10)$$

$$N_2^+ + O \rightarrow NO^+ + N. \quad (11)$$

The rate coefficient of (8) has been measured as 2×10^{-7} cm^3 sec^{-1} (cf. Biondi, 1964) and of (9) as 2×10^{-10} cm^3 sec^{-1} (Fite, Rutherford, Snow, and van Lint, 1962). Rate coefficients of 2×10^{-11} cm^3 sec^{-1} for (10) and (11) have been derived by Norton, Van Zandt, and Denison (1963) and by Whitten and Poppoff (1964) from ionospheric data. The analyses of ionospheric data impose arbitrary temperature variations on the rates of the possible processes and the derived coefficients have little quantitative significance. However, the measured concentrations of N_2^+ apparently require that one or both of (10) and (11) be rapid so we assume that each of them has a rate coefficient of 1×10^{-11} cm^3 sec^{-1}. Since, in the atmosphere, (10) is usually followed by

$$O^+ + N_2 \rightarrow NO^+ + N \quad (12)$$

the distinction between (10) and (11) is unimportant for our purposes.

The O^+ ions are removed by the ion-atom interchange reactions, (12) and

$$O^+ + O_2 \rightarrow O_2^+ + O \quad (13)$$

(Bates, 1955). For our calculations we have adopted a rate coefficient of 1×10^{-11} cm^3 sec^{-1} for both (12) and (13) (Sayers and Smith, 1964) but the red line intensity depends only upon the ratio of the rates of the two reactions.

The ion, O_2^+, disappears by dissociative recombination

$$O_2^+ + e \rightarrow O' + O'' \quad (14)$$

throughout the altitude region in which (14) might provide a significant source of emission of the red line. Thus, if f is the probability that (14) produces an $O(^1D)$ atom, the rate of production is given by

$$Q_2 = f\left\{ q(O_2^+) + q(N_2^+)\left[\alpha_9 n(O_2) + \frac{\alpha_{10} n(O)}{1+\frac{\alpha_{10} n(N_2)}{\alpha_{13} n(O_2)}}\right] \times [\alpha_8 n(e) + \alpha_9 n(O_2) + (\alpha_{10}+\alpha_{11}) n(O)]^{-1} + q(O^+)\left[1+\frac{\alpha_{12} n(N_2)}{\alpha_{13} n(O_2)}\right]^{-1}\right\} \quad (15)$$

The reaction is energetically capable of producing two $O(^1D)$ atoms so that f may be as large as 2. In Fig. 7 $Q_2(z)$ is shown as a function of altitude for several solar zenith angles with f taken equal to 2. The results provide an upper limit to the possible excitation rates consistent with the adopted ultraviolet flux and reaction rates.

Because $n(N_2)$ is much greater than $n(O_2)$ in the altitude region where $q(O^+)$ and $q(O_2^+)$ are comparable, the last term of (15) is important only at high altitudes where the production rates are small. Thus the intensity of the red line is insensitive to the magnitudes of α_{12} and α_{13}. In contrast is the sensitivity to the relative values of α_8 and α_9. Reaction (9) is an important source of O_2^+ ions at the lower altitudes where the production rates are large, whereas the sequence of (10) followed by (13) is important only at high altitudes where the production of $O(^1D)$ is small. Accordingly, we illustrate in Fig. 7 only the sensitivity to the ratio α_8/α_9, the dashed curves of Fig. 7 arising when the value of 2×10^{-10} cm^3 sec^{-1} for α_9 is replaced by zero so that most of the N_2^+ ions disappear by dissociative recombination.

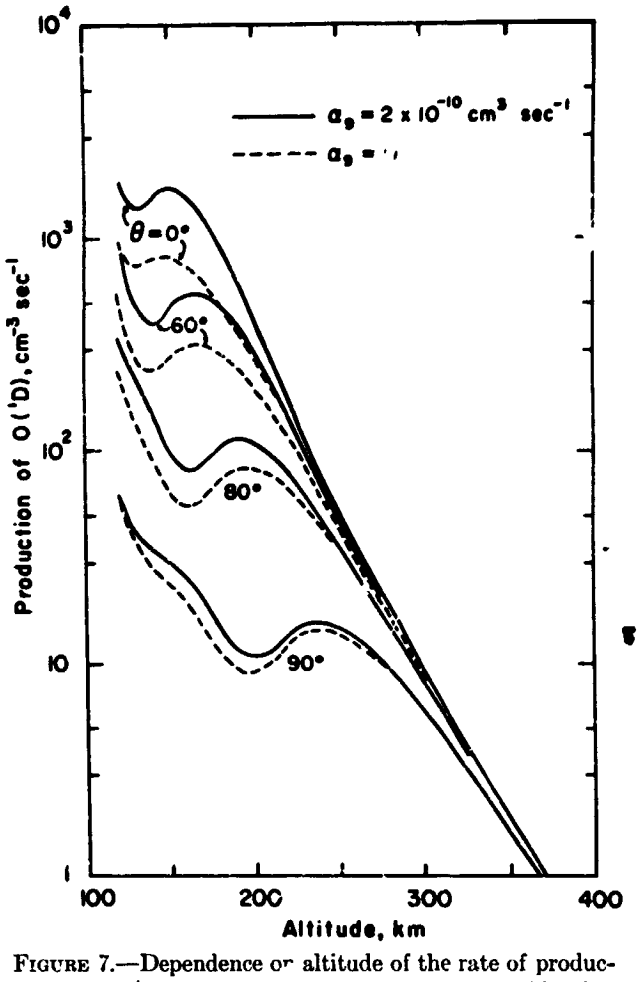

FIGURE 7.—Dependence on altitude of the rate of production of O(¹D) atoms by the dissociative recombination of O_2^+ for the 750° low O_2 model atmosphere.

The possible additional source of O(¹D) atoms provided by the dissociative recombination of NO^+ (7) is shown in Fig. 8 on the assumption that every NO^+ recombination yields an O(¹D) atom. The actual yield is presumably much less than unity.

The rate of emission of 6300 Å photons produced by dissociative recombination of O_2^+ with $\alpha_3/\alpha_9 = 10^3$, $\alpha_8/\alpha_{10} = \alpha_8/\alpha_{11} = 2 \times 10^4$, $\alpha_{11}/\alpha_{12} = 1$, $\beta = 10^{-10}$ cm^3 sec^{-1}, and $f = 2$ is shown in Fig. 9. The corresponding zenith intensities are shown in Fig. 10.

Fig. 11 shows the sensitivity of the predicted intensities to the atmospheric model.

5. PHOTODISSOCIATION AND IONIC RECOMBINATION

A comparison of Figs. 3 and 11, and 5 and 10 shows that the contributions of photodissociation and of ionic recombination to the zenith intensity of the red line may be comparable, depending upon the values of T_s and f, but there are significant differences in the variations with solar zenith angle and with altitude. The zenith intensity has been measured as a function of altitude by Zipf and Fastie (1963) at Wallops Island on 7 May 1964 with the sun at a zenith angle of 60°. We have attempted to reproduce the observational data of Zipf and Fastie by combining the contributions of photodissociation, shown in Fig. 5, and of ionic recombination, shown in Fig. 10, and regarding the solar temperature, T_s, and the excitation probability, f, as disposable parameters subject to $f \leqslant 2$.

Fig. 12 shows the best fits we have been able to obtain by this procedure for three model atmospheres. The results for the 1000° high O_2 atmosphere with $T_s = 4660$K and $f = 2$ agree closely with the observations, the total zenith intensity being 4.8 kR of which 3.1 kR is due to photodissociation and 1.7 kR to ionic recombination. The corresponding intensities appropriate to a zenith angle of 80° are, respectively, 2.7 kR and 1.0 kR,

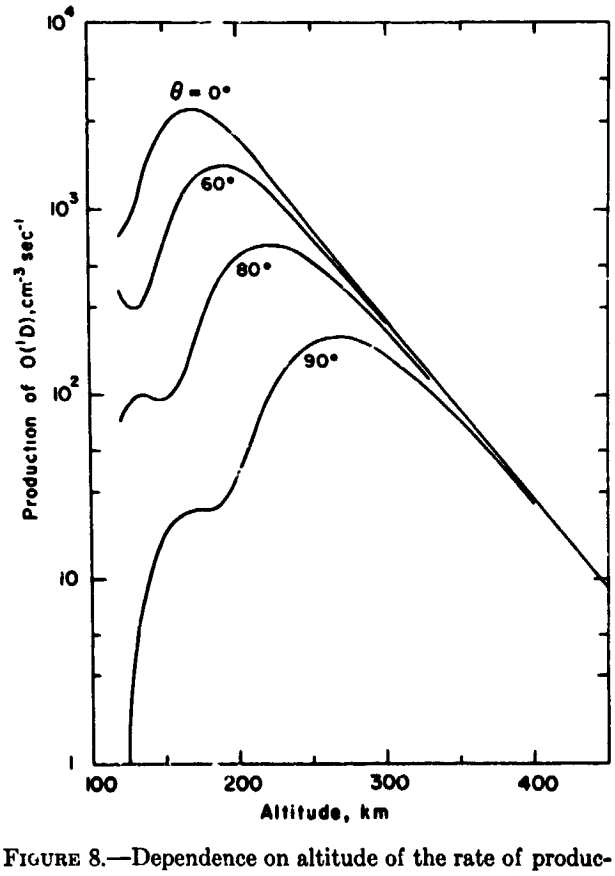

FIGURE 8.—Dependence on altitude of the rate of production of O(¹D) atoms by the dissociative recombination of NO^+ for the 750° low O_2 model atmosphere.

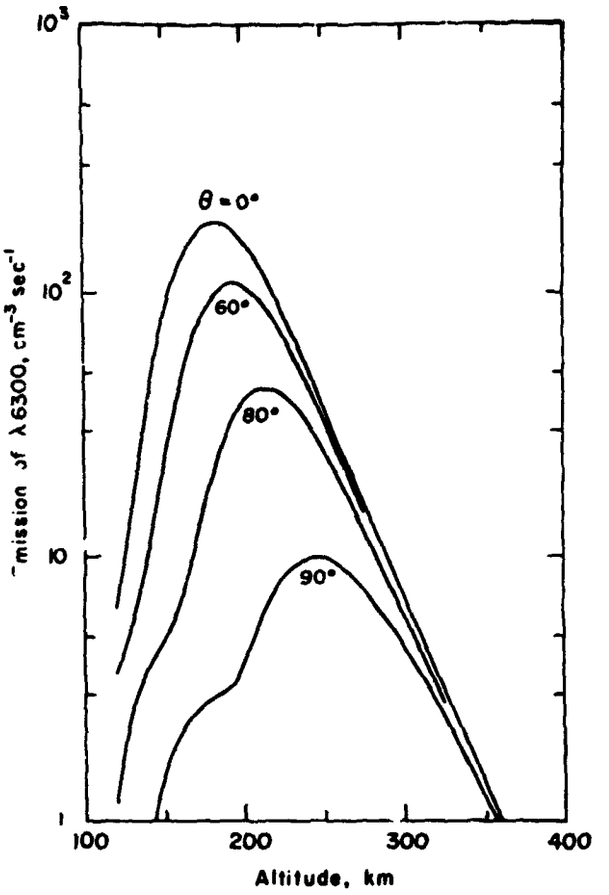

FIGURE 9.—Dependence on altitude of the emission of λ6300 which results from the dissociative recombination of O_2^+ for the 750° low O_2 model atmosphere.

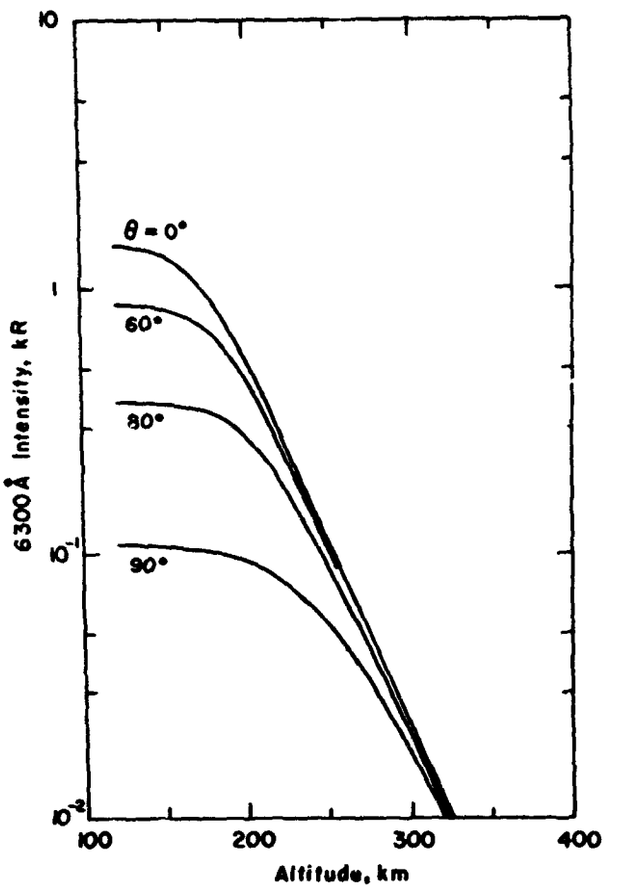

FIGURE 10.—Dependence on altitude of the zenith intensity which results from the dissociative recombination of O_2^+ for the 750° low O_2 model atmosphere.

the sum of which exceeds the upper limit of 2 kR observed by Noxon (1963) at Fort Churchill at noon on 15 December 1962. In order to be consistent with an upper limit of 2 kR at 80°, it is necessary with the 1000° high O_2 model atmosphere to adopt a solar temperature not greater than 4580K, even with $f=0$. The results for the other models shown in Fig. 12 lead to even greater conflict with Noxon's upper limit.

Temporal variations in the solar ultraviolet flux in the neighborhood of 1216 Å are small (Lindsay, 1963), and there is no evidence to suggest that large variations occur in the flux at the longer wavelengths of the Schumann-Runge continuum. Ignoring the possibility of temporal change in T_s, we have determined the values of T_s which give the largest intensities at 60° consistent with the upper limit of 2 kR at 80°. The intensities as a function of altitude for the three model atmospheres are shown in Fig. 13. All of these models lead to intensities which are markedly lower than the Zipf and Fastie results. The situation cannot be improved by using lower values of f and higher values of T_s because, with a deactivation coefficient, β, of 10^{-10} cm^3 sec^{-1}, the photodissociation contribution is nearly independent of θ as θ varies from 60° to 80°, as shown in Fig. 3.

There are also discrepancies in the detailed dependence of emission on altitude, Zipf and Fastie (1963) finding that the emission rate is 2.6×10^2 cm^{-3} sec^{-1} from 120 km to 190 km, increasing abruptly to 5.0×10^2 cm^{-3} sec^{-1} from 190 km to 220 km. The dependence of emission on altitude would be modified if the deactivation coefficient, β, were to change rapidly with increasing temperature. As Bates (1960) has pointed out, O(^{1}D) atoms produced by dissociative recombination initially possess considerable kinetic energy so that the effective temperature controlling β may be higher than the ambient temperature. The effect

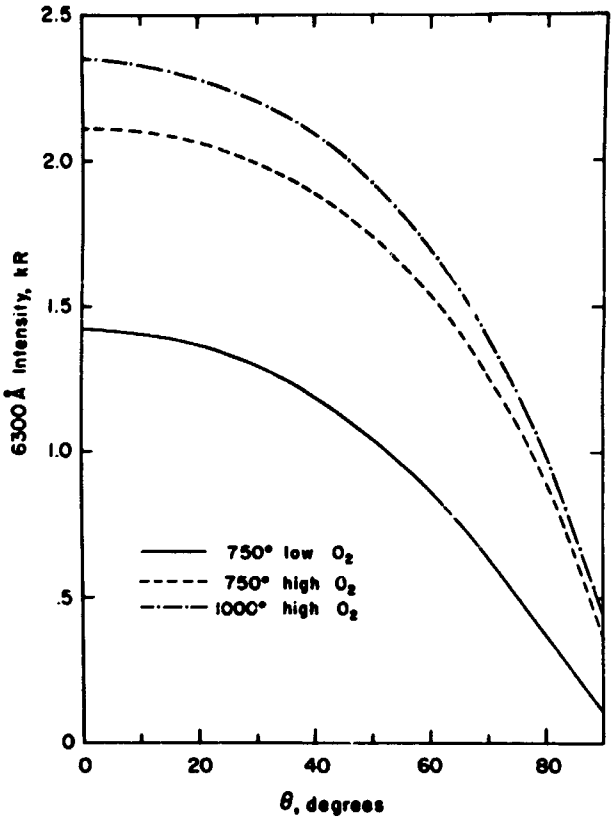

FIGURE 11.—Dependence on solar zenith angle of the intensity which results from the dissociative recombination of O_2^+ for several model atmospheres with $\beta = 10^{-10}$ cm^3 sec^{-1} and $f = 2$.

is probably small since molecular oxygen is a minor constituent at the altitudes of interest and thermalizing collisions with the major constituents, O and N_2, occur more frequently than deactivating collisions with O_2. A rapid change of β with increasing altitude will not, in any case, remove the discrepancy between the predicted intensities of Fig. 13 and the observed intensities. The discrepancy can more plausibly be attributed to an additional excitation mechanism.

6. FLUORESCENT EXCITATION

Bates (1948) and Chamberlain (1958) have shown that resonance scattering of sunlight

$$O(^3P) + \lambda 6300 \rightarrow O(^1D) \qquad (16)$$

does not contribute significantly to the twilight-glow in the red line and it follows from their calculations, but including deactivation, that the yield in the dayglow does not exceed 20R.

Fluorescence through the sequences

$$O(^3P) + \lambda 1304 \rightarrow O(^3S) \qquad (17)$$

$$O(^3S) \rightarrow O(^1D) + \lambda 1641, \qquad (18)$$

or

$$O(^3S) \rightarrow O(^1S) + \lambda 2325 \qquad (19)$$

followed by

$$O(^1S) \rightarrow O(^1D) + \lambda 5577, \qquad (20)$$

may be a more abundant source of dayglow red line emission and incidentally of dayglow green line emission also, for the atmosphere is optically very thick in the triplet centered at λ1304.

The intensity of λ1304 has been measured by Donahue and Fastie (1964) and by Fastie, Crosswhite and Heath (1964). If we assume a Doppler width corresponding to a temperature in the region of 2000K for the line and a value of 4.0×10^{-6} (Garstang, 1961) for the ratio of the transition probabilities for the emission of λ1641 and λ1304 radiation, the measured intensities of λ1304 lead to an estimate of the order of 100R for the red

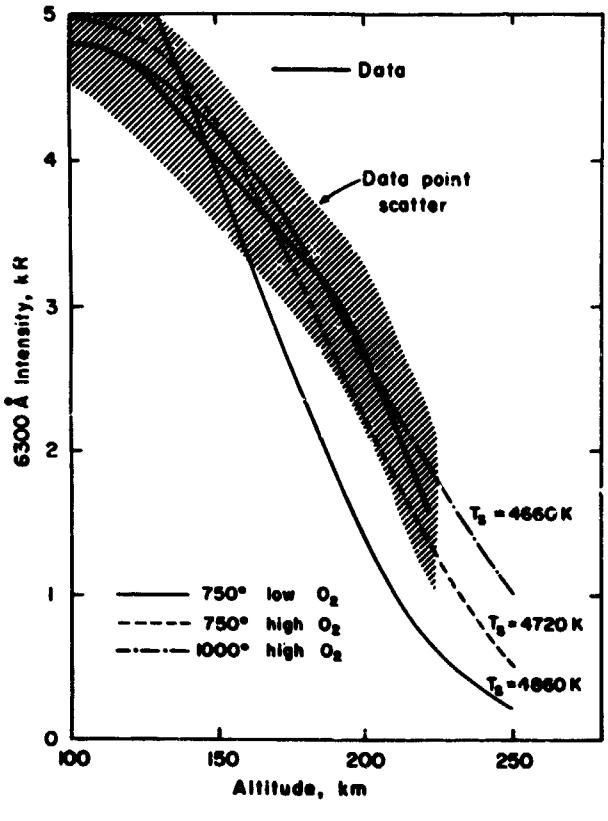

FIGURE 12.—Comparison of the data of Zipf and Fastie (1963) with the theoretical intensities at $\theta = 60°$ which result from photodissociation and ionic recombination. All three models use $f = 2$ and $\beta = 10^{-10}$ cm^3 sec^{-1}.

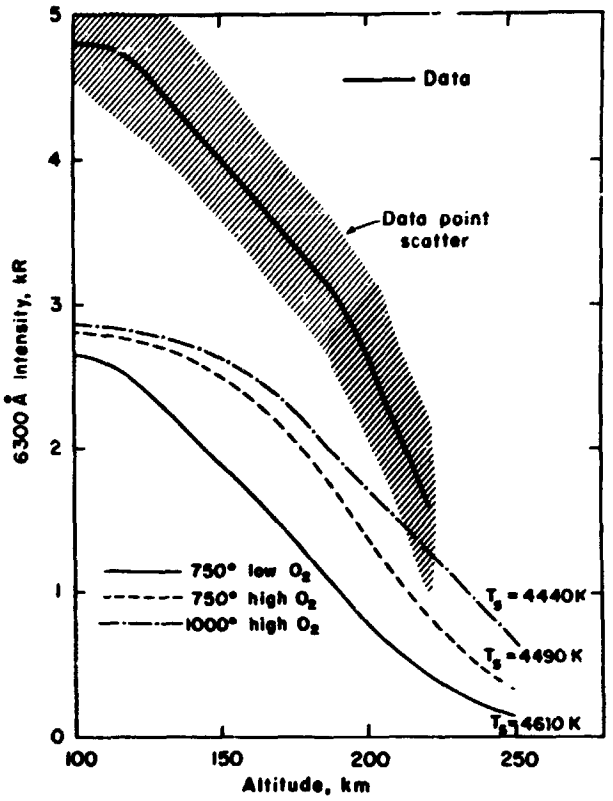

FIGURE 13.—Comparison of the data of Zipf and Fastie (1963) with theoretical intensities at $\theta = 60°$ due to photodissociation and ionic recombination for models which lead to an intensity of 2kR at $\theta = 80°$. The calculations assume $f = 2$ and $\beta = 10^{-10}$ cm^3 sec^{-1}.

line, an estimate which is consistent with the fact that λ1641 radiation has not been detected in the airglow. The contribution of (19) and (20) is much smaller because the ratio of the transition probabilities for the emission of λ2325 and λ1304 is 1.6×10^{-8} (Garstang, 1961).

None of the mechanisms discussed so far explains the great variability of the red line intensity, discovered by Noxon (1964). The electron temperature is markedly higher than the neutral particle temperature in the F region and may well be very variable (Spencer, Brace and Carignan, 1962; Brace, Spencer and Carignan, 1963; Nagy, Brace, Carignan and Kanal, 1963) and the energy source responsible may also be a source of excitation of the red line.

7. ELECTRON IMPACT EXCITATION

7.1 Thermal Excitation

It has been pointed out (Dalgarno, 1964b) that a rise in the temperature of the ambient electron gas will be accompanied by an enhancement of the red line. Spencer, Brace and Carignan (1962) and Brace, Spencer and Carignan (1963) have presented the results of measurements of electron densities and electron temperatures from several rocket flights. If we assume that there is no depletion of the high energy tail of the velocity distribution, the associated red line emission rates may be easily computed using rate coefficients derived from Seaton (1956). The emission rates and intensities as functions of altitude are shown in Figs. 14 and 15 for a deactivation coefficient $\beta = 10^{-10}$ cm^3 sec^{-1}.

In calculating the zenith intensities, it is necessary to estimate the emission at altitudes above those for which electron temperature and density data are available. We have assumed that the electron gas is isothermal and in diffusive equilibrium at these altitudes. The contribution of the high altitudes to the overhead intensity is

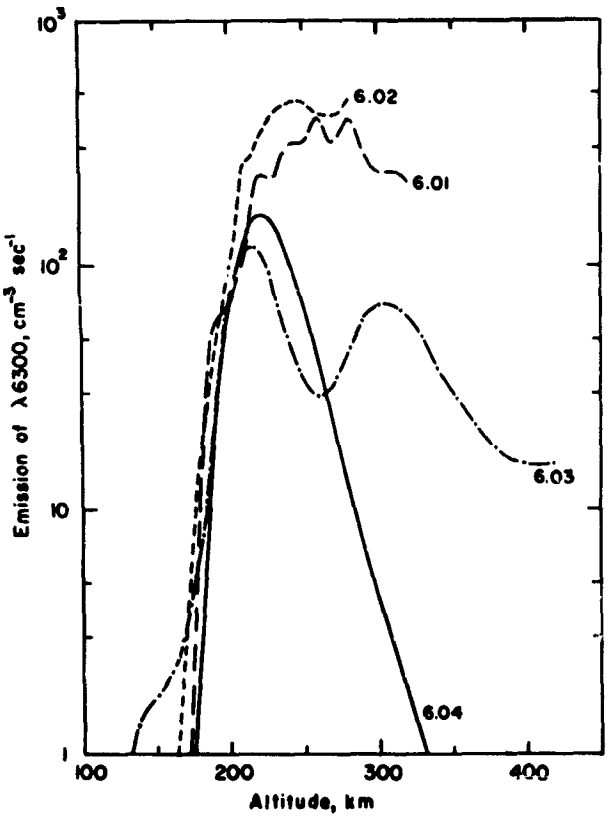

FIGURE 14.—Dependence on altitude of the emission of λ6300 which results from excitation by thermal electrons for four measured profiles of electron temperature and density (Spencer, Brace, and Carignan, 1962; Brace, Spencer, and Carignan, 1963. The results are for the 750° low O_2 model atmosphere with $\beta = 10^{-10}$ cm^3 sec^{-1}.

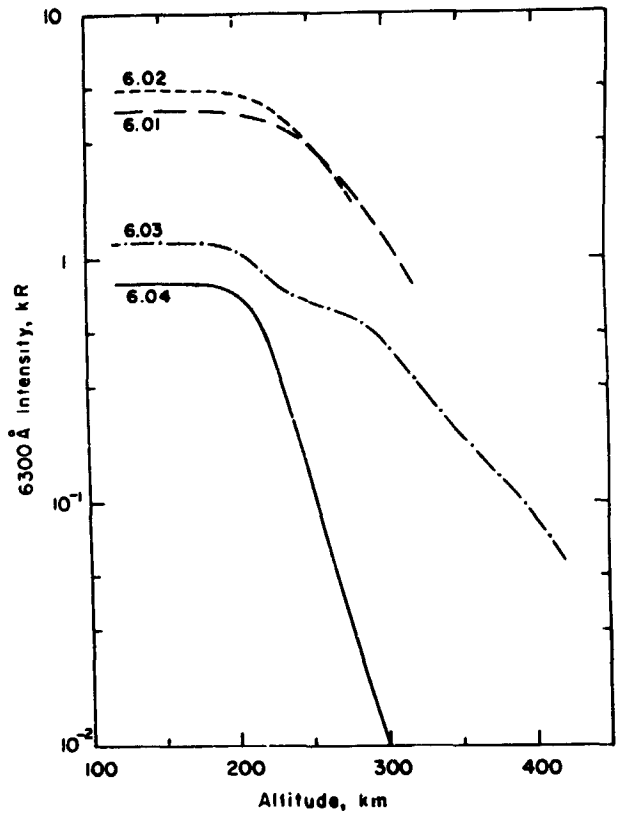

FIGURE 15.—Dependence on altitude of the zenith intensity which results from excitation by thermal electrons for four measured profiles of electron temperature and density (Spencer, Brace, and Carignan, 1962; Brace, Spencer, and Carignan, 1963). The results are for the 750° low O_2 model atmosphere with $\beta = 10^{-10}$ cm^3 sec^{-1}.

about 30 percent for flight 6.02, 20 percent for flight 6.01, 5 percent for flight 6.03, and 0.1 percent for flight 6.04.

Flight 6.01 was fired from Fort Churchill on 16 March 1960, during spread *F* conditions and flight 6.04 was fired from Wallops Island on 3 March 1961, during quiet ionospheric conditions. The red line intensities predicted for thermal excitation are 4.1 kR and 0.79 kR, respectively. The altitude profiles are markedly different, the emission rate for flight 6.04 peaking at 220 km and decreasing rapidly and that for flight 6.01 varying little from 220 km up to at least 320 km.

Flight 6.04 provides an interesting contrast to flight 6.02 which was fired from Fort Churchill on 15 June 1960, also during quiet ionospheric conditions. Flight 6.02 is actually very similar to the spread *F* flight 6.01 with a predicted intensity of 4.9 kR and an emission rate varying little from 225 km up to at least 280 km.

Flight 6.03 was fired from Wallops Island on 3 August 1960, following a period of magnetic disturbance. Below 250 km the results are similar to those for the quiet ionosphere Wallops Island flight 6.04. However, the 6.03 emission rate is enhanced at greater altitudes, with a second maximum at 310 km and a relatively slow decrease above this altitude. The predicted intensity for flight 6.03 is 1.2 kR.

The daytime electron temperature is very sensitive to small disturbances and it appears that the intensity and the altitude dependence of the red line may be still more sensitive. Thus an increase of 10 percent in the electron temperatures measured on flight 6.04 would raise the predicted red line intensity from 0.79 kR to 2.1 kR. The combined profile due to such arbitrary thermal excitation, to Schumann-Runge photodissociation with $T_s = 4610$K and to ionic recombination with $f = 2$

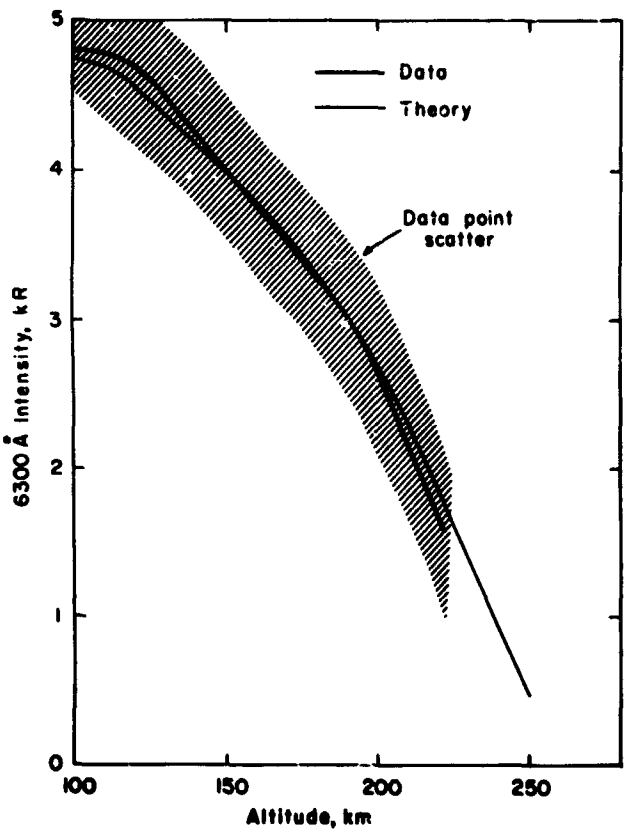

FIGURE 16.—Comparison of the data of Zipf and Fastie (1963) with the theoretical intensity which results from the combination of photodissociation with $T_s = 4610$K, ionic recombination with $f = 2$, and electron excitation given by the profile calculated for flight 6.04 enhanced by a factor of 2.7. The theoretical results are for the 750° low O_2 model atmopshere with $\beta = 10^{-10}$ cm^3 sec^{-1}.

is in harmony with that observed by Zipf and Fastie (1963), as Fig. 16 demonstrates. This model reconciles the observation of Zipf and Fastie with Noxon's (1963) upper limit on the intensity at Fort Churchill if we assume that electron impact excitation was negligible at the time of Noxon's measurement.

The very high intensities of the order of 40 kR observed by Noxon and Goody (1962) and by Jarrett and Hoey (1963) can be ascribed to thermal excitation by electrons with a temperature in the region of 4000K. Such high temperatures have been detected, but only occasionally, on Explorer XVII (Brace and Spencer, 1964) and it is significant that very intense red line emission is also a rare phenomenon (Noxon, 1964).

The Explorer XVII data show an early morning maximum in the electron temperature (Brace and Spencer, 1964), related presumably to the dawn effect (Dalgarno and McElroy, 1964b), and an early morning enhancement of the red line may be a regular feature of its diurnal variation.

Satellite observations (Willmore, Henderson, Boyd, and Bowen, 1964; Brace and Spencer, 1964) show that the electron temperature remains higher than the neutral particle temperature during the night. The temperatures are usually too low to give rise to significant thermal excitation and the intensity associated with the nocturnal rocket flight 6.05 of Brace, Spencer and Carignan (1963) was a fraction of a rayleigh. However, the energy source associated with the heating of the electrons may contribute directly to excitation of the red line and it is interesting to note that Barbier (1964) has suggested that about 20R of red line emission is not directly correlated with the normal ionospheric parameters.

A similar effect may occur during the day.

7.2 Non-Thermal Excitation

A major source of heat during daylight exists in the fast photoelectrons produced by photoionization by solar ultraviolet radiation. The photoelectrons lose energy through a complicated sequence of collision processes, one of which is electron impact excitation of atomic oxygen to the $O(^1D)$ state (Hanson and Johnson, 1961; Hanson, 1963; Dalgarno, McElroy and Moffett, 1963; Dalgarno, 1964b). The resulting altitude profile will be similar to that derived for thermal excitation and the intensity may be of the order of a kilorayleigh in which case the importance of thermal excitation in the interpretation (Fig. 16) of the observed profile (Zipf and Fastie, 1963) must be correspondingly diminished.

8. CONCLUSIONS

Noxon's observation that the intensity of the red line at a zenith angle of 80° is less than 2 kR places severe restrictions upon the contributions from photodissociation of molecular oxygen and from recombination of molecular ions. It appears necessary that the deactivation coefficient for collisions of $O(^1D)$ atoms with O_2 be as large as 10^{-10} cm^3 sec^{-1}, and that the solar flux in the region of 1450 Å be less than the reported values. Then the contributions of photodissociation and of ionic recombination vary from at most 3.4 kR for an overhead sun to at most 1.3 kR for a zenith angle of 90°.

It is difficult to reconcile the limit placed by Noxon with the altitude profile measured by Zipf and Fastie without postulating an additional excitation mechanism effective at high altitude. The additional mechanism may be impact excitation by photoelectrons or it may be thermal excitation by hot electrons. The latter source can tentatively be identified as that responsible for the observed variability of the dayglow intensities. The dayglow red line may therefore provide a means of monitoring the electron temperature and thereby of gaining information about temporal variations in upper atmosphere energy sources. A search for correlations between simultaneous measurements of the red line and the electron temperature would be instructive.

ACKNOWLEDGMENTS

Our study of the emission of the red line in the dayglow was stimulated by Dr. J. F. Noxon's observations and we have enjoyed many discussions with him on the subject. Mrs. O. P. Ko provided valuable assistance in programming and running the computer.

A part of this research was performed while Walker was at Columbia University and was supported by the National Aeronautics and Space Administration under Grant Number NsG–445.

REFERENCES

EARBIER, D., 1957: La lumière du ciel nocturne en été a Tamanrasset. *Compt. Rend.*, **245**, 1559–1561.

———, 1964: Nouvelles observations de la raie rouge du ciel nocturne en Afrique. *Ann. Geophys.*, **20**, 22–33.

———, and J. GLAUME, 1962: La couche ionosphérique nocturne *F* dans la zone intertropicale et ses relations avec l'emission de la raie 6300 Å du ciel nocturne. *Planetary Space Sci.*, **9**, 133–148.

BARBIER, D., F. E. ROACH and W. R. STEIGER, 1962: The summer intensity variation of [01] 6300 Å in the tropics. *J. Res. NBS*, **66D** (1), 145–152.

BATES, D. R., 1948: Theoretical considerations regarding the night sky emission. *Emission Spectra of Night Sky and Aurorae*, London, Physical Society, 21–33.

———, 1955: Charge transfer and ion-atom interchange collisions. *Proc. Phys. Soc. London*, **A68**, 344–345.

———, 1959: Some problems concerning the terrestrial atmosphere above about the 100 km level. *Proc. Roy. Soc. London*, **A253**, 451–462.

———, 1960: The airglow. *Physics of the Upper Atmosphere*, New York, Academic Press, 219–267.

——— , and A. DALGARNO, 1953: The altitudes of the luminous layers in the earth's atmosphere. *J. Atmos. Terr. Phys.*, **4**, 112–123.

——— and ———, 1954: Theoretical considerations regarding the dayglow. *J. Atmos. Terr. Phys.*, **5**, 329–344.

BIONDI, M. A., 1964: Electron-ion and ion-ion recombination. *Ann. Geophys.*, **20**, 34–46.

BRACE, L. H., and N. W. SPENCER, 1964: First electrostatic probe from Explorer XVII. *J. Geophys. Res.* **69**, in press.

———, ———, and G. R. CARIGNAN, 1963: Ionosphere electron temperature measurements and their implications. *J. Geophys. Res.*, **68**, 5397–5412.

BRANDT, J. C., 1958: Oxygen red lines in the airglow. III. The dayglow. *Astrophys. J.*, **128**, 718–723.

BRYANT, R., 1964: Densities obtained from drag on the Explorer 17 satellite. *J. Geophys. Res.*, **69**, 1423–1425.

CADLE, R., 1964: Daytime atmospheric O(^{1}D). *Discussions Faraday Soc.*, **37**, in press.

CARMAN, E. H., and B. P. KILFOYLE, 1963: Relationship between [01] 6300 A zenith airglow and ionospheric parameters f_0F_2 and $h'F$ at Townsville. *J. Geophys. Res.*, **68**, 5605–5607.

CHAMBERLAIN, J. W., 1958: Oxygen red lines in the airglow. I. Twilight and night excitation processes. *Astrophys. J.*, **127**, 54–66.

———, 1961a: The energies in the spectra of the airglow and aurora. *Ann. Geophys.*, **17**, 90–99.

———, 1961b: *Physics of the Aurora and Airglow.* New York, Academic Press, 704, pp.

DALGARNO, A., 1964a: Thermal reactions involving charged particles. *Discussions Faraday Soc.*, in press.

———, 1964b: Corpuscular radiation in the upper atmosphere. *Ann. Geophys.*, **20**, 65–74.

———, and M. B. MCELROY, 1964a: Electron and ion production rates in the upper atmosphere. To be published.

——— and ———, 1964b: Electron temperatures at dawn. To be published.

———, ———, and R. J. MOFFETT, 1963: Electron temperatures in the ionosphere. *Planetary Space Sci.*, **11**, 463–484.

DEMORE, W., and O. F. RAPER, 1964: Deactivation of O(^{1}D) in the atmosphere. *Astrophys. J.*, **139**, 1381–1383.

DETWILER, C. R., D. L. GARRETT, J. D. PURCELL and R. TOUSEY, 1961: The intensity distribution in the ultraviolet solar spectrum. *Ann. Geophys.*, **17**, 9–18.

DONAHUE, T. M., and W. G. FASTIE, 1964: Observation and interpretation of resonance scattering of Lyman α and OI (1300) in the upper atmosphere. *Space Research*, **4**, Amsterdam, North-Holland Publishing Company, 304–324.

FASTIE, W. G., H. M. CROSSWHITE and D. F. HEATH, 1964: Rocket spectrophotometer airglow measurements in the far ultraviolet. *J. Geophys. Res.*, **69**, in press.

FITE, W. L., J. A. RUTHERFORD, W. R. SNOW and V. A. J. VAN LINT, 1962: Ion-neutral collisions in afterglow. *Discussions Faraday Soc.*, **33**, 264–272.

GARSTANG, R. H., 1961: Mutual magnetic interactions and oscillator strengths in the first spectrum of oxygen. *Proc. Cambridge Phil. Soc.*, **57**, 115–120.

HALL, L. A., W. SCHWEIZER and H. E. HINTEREGGER, 1963: Diurnal variation of the atmosphere around 190 kilometers derived from solar extreme ultraviolet absorption measurements. *J. Geophys. Res.*, **68**, 6413–6417.

HANSON, W. B., 1963: Electron temperatures in the upper atmosphere. *Space Research*, **3**, Amsterdam, North-Holland Publishing Company, 282–302.

———, and F. S. JOHNSON, 1961: Electron temperatures in the ionosphere. *Mèmoires Soc. R. Sci. Liège, Ser. 5*, **4**, 390–424.

HARRIS, I., and W. PRIESTER, 1962: Time-dependent structure of the upper atmosphere. *J. Atmos. Sci.*, **19**, 286–301.

HINTEREGGER, H. E., 1961: Preliminary data on solar extreme ultraviolet radiation in the upper atmosphere. *J. Geophys. Res.*, **66**, 2367–2380.

———, and K. WATANABE, 1962: Photoionization rates in the *E* and *F* regions, 2. *J. Geophys. Res.*, **67**, 3373–3392.

JACCHIA, L. G., and J. SLOWEY, 1964: Atmospheric heating in the auroral zones: A preliminary analysis of the atmospheric drag of the Injun 3 satellite. *J. Geophys. Res.*, **69**, 905–910.

JARRETT, A. H., and M. J. HOEY, 1963: A ground-level photographic observation of the day airglow emission of atomic oxygen at 6300 Å. *Planetary Space Sci.*, **11**, 1251–1252.

JASTROW, R., and L. KYLE, 1961: The earth atmosphere. *Handbook of Astronautical Engineering*, New York, McGraw-Hill, Chap. 2, 2–13.

JURSA, A. S., M. NAKAMURA and Y. TANAKA, 1963: Molecular oxygen distribution in the upper atmosphere. *J. Geophys. Res.*, **68**, 6145–6155.

KING-HELE, D. G., 1963: Decrease in upper atmosphere density since the sunspot maximum of 1957–58. *Nature*, **198**, 832–834.

LINDSAY, J. C., 1963: Scientific results of the first orbiting solar observatory. *Trans. Amer. Geophys. Union*, **44**, 722–725.

METZGER, P. H., and G. R. COOK, 1964: A reinvestigation of the absorption cross sections of molecular oxygen in the 1050–1800 A region. *J. Quantitative Spectroscopy Radiative Transfer*, **4**, 107–116.

NAGY, A. F., L. H. BRACE, G. R. CARIGNAN and M. KANAL, 1963: Direct measurements bearing on the extent of thermal nonequilibrium in the ionosphere. *J. Geophys. Res.*, **68**, 6401–6412.

NICOLET, M., 1961: Density of the heterosphere related to temperature. *Res. in Space Sci.*, Smithsonian Inst. Astrophys Observ., Spec. Rpt. 75, 30 pp.

———, and W. SWIDER, 1963: Ionospheric conditions. *Planetary Space Sci.*, **11**, 1459–1482.

NIER, A. O., J. H. HOFFMAN, C. Y. JOHNSON and J. C. HOLMES, 1964: Neutral composition of the atmosphere in the 100- to 200-kilometer range. *J. Geophys. Res.*, **69**, 979–989.

NORTON, R. B., T. E. VAN ZANDT and J. S. DENISON, 1963: A model of the atmosphere and ionosphere in the *E* and *F1* regions. *Proc. Int. Conf. on the Ionosphere*, London, Institute of Physics and Physical Society, 26–34.

NOXON, J. F., 1963: Observation of daytime aurora. *J. Atmos. Terr. Phys.*, **25**, 637–645.

———, 1964: A study of the 6300 Å oxygen line in the day airglow. *J. Geophys. Res.*, **69**, 3245–3255.

———, and R. M. GOODY, 1962: Observation of day airglow emission. *J. Atmos. Sci.*, **19**, 342–343.

PACKER, D. M., 1961: Altitudes of the night airglow radiations. *Ann. Geophys.*, **17**, 67–74.

POKHUNKOV, A. A., 1963: Gravitational separation, composition and structural parameters of the night atmosphere at altitudes between 100 and 210 km. *Planetary Space Sci.*, **11**, 441–449.

PURCELL, J. D., D. M. PACKER and R. TOUSEY, 1960: The ultraviolet spectrum of the sun. *Space Research*, **1**, Amsterdam, North-Holland Publishing Company, 581–589.

SAYERS, J., and D. SMITH, 1964: Ion and charge exchange reactions involving atmospheric gases. *Discussions Faraday Soc.*, **37**, in press.

SCHAEFER, E. J., 1963: The dissociation of oxygen measured by a rocket-borne mass spectrometer. *J. Geophys. Res.*, **68**, 1175–1176.

SEATON, M. J., 1954: Excitation processes in the aurora and airglow, 2. Excitation of forbidden atomic lines in high altitude aurorae. *J. Atmos. Terr. Phys.*, **4**, 295–313.

———, 1956: The calculation of cross-sections for excitation of forbidden atomic lines by electron impact. *The Airglow and the Aurorae*, London, Pergamon Press, 289–301.

———, 1958: Oxygen red lines in the airglow. II. Collisonal deactivation effects. *Astrophys. J.*, **127**, 67–74.

SPENCER, N. W. L. H. BRACE and G. R. CARIGNAN, 1962: Electron temperature evidence for nonthermal equilibrium in the ionosphere. *J. Geophys. Res.*, **67**, 157–175.

TARASOVA, T. M., 1963: Night-sky emission-line intensity distribution with respect to height. *Space Research*, **3**, Amsterdam, North-Holland Publishing Company, 162–172.

TOUSEY, R., 1963: The extreme ultraviolet spectrum of the sun. *Space Science Rev.*, **2**, 3–69.

WALLACE, L., and J. W. CHAMBERLAIN, 1959: Excitation of O_2 atmospheric bands in the aurora. *Planetary Space Sci.*, **2**, 60–70.

WALLACE, L., and R. A. NIDEY, 1964: Measurement of the daytime airglow in the visual region. *J. Geophys. Res.*, **69**, 471–479.

WHITTEN, R. C., and I. G. POPPOFF, 1964: Ion kinetics in the lower ionosphere. *J. Atmos. Sci.*, **21**, 117–133.

WILLMORE, A. P., C. L. HENDERSON, R. L. F. BOYD and P. J. BOWEN, 1964: Electron temperature in the upper *F*-region. *Proc. Roy. Soc. London, A*, in press.

ZIPF, E. C., and W. G. FASTIE, 1963: An observation of day airglow emission at 6300 Å. *J. Geophys. Res.*, **68**, 6208–6209.

N65 - 32163

A LATITUDE SURVEY OF THE NIGHT AIRGLOW*

T. N. DAVIS† AND L. L. SMITH‡

A four-color turret photometer has been used for shipboard observations of the night airglow and the aurora. Zenith observations have been obtained during 1962 close to the 70°W meridian from the northern auroral zone to the Antarctic pack ice. Most of the observations were taken during the Southern Winter.

Maximums in the [OI] 5577A intensity were found near 30–40°N and 40°S, with the Southern Hemisphere level being generally lower than that in the Northern Hemisphere. The [OI] 6300A latitudinal variation was similar to that of [OI] 5577A except that maximums in the latitudinal distribution were found near 15° geomagnetic north and south latitudes. In contrast with the [OI] emissions, the sodium group (NaD doublet and OH bands near 5893A) generally increased to the south with maximums near 20–30°N and 40–50°S geographic latitude. The total 5340A background increased from north to south. When the integrated starlight and zodiacal light components were subtracted from the total background, the resultant terrestrial component showed a pronounced minimum at low latitudes and apparent symmetry about the geomagnetic equator.

I. INTRODUCTION

Photometric observations of the aurora and the night airglow made aboard the U.S.N.S. *Eltanin* during the period March/November, 1962. The *Eltanin* departed from New York in late March and moved northward into the Laborador Sea where photometric observations of aurora were made on four nights. After returning to New York, the *Eltanin* departed on May 24 on a trip southward and arrived in Valparaiso, Chile on June 27. Clear skies existed throughout most of this cruise and useful airglow observations were obtained on 17 nights. In the period July/November 1962, the *Eltanin* made several cruises southward from Valparaiso and useful observations (during clear, moonless dark hours) were obtained on 36 nights. See Figure 1 for the positions of the *Eltanin* when the observations were made.

Observations were made in four narrow wavelength bands centered near 5577, 6300, 5893 and 5340A with a turret photometer built by the Fritz Peak Observatory following a design by Purdy, Megill and Roach (1961). This instrument has a 5° diameter circular field of view and was mounted on a free swinging gimbal to assure observation of the zenith. The gimbal mount was effective in reducing the effect of the ship's motion to the extent that the photometer axis pointed to within 5° of the zenith throughout most of the observations. Observations at a given wavelength were obtained at 5 minute intervals.

The two-color method (Roach and Meinel, 1955) was applied to the 5577, 6300 and 5893A observations in an attempt to remove the contributions due to airglow continuum, zodiacal light, and integrated starlight; the method involves subtraction of these contributions as determined by observation through the 5340A filter. Details of the data reduction and calibration procedures together with tabulations of the results are given in a limited circulation report (Davis and Smith, 1964).

A complication to the determination of the intensities of the [OI] 5577, [OI] 6300 and NaD 5893A emissions arises due to contamination from nearby OH band emissions. Figur 2 shows the filter transmission characteristics and wavelengths

*Published in the *Journal of Geophysical Research*, 70(5):1127–1138, March 1, 1965.

†Goddard Space Flight Center and University of Alaska, College, Alaska

‡Fritz Peak Observatory, National Bureau of Standards, Boulder, Colorado.

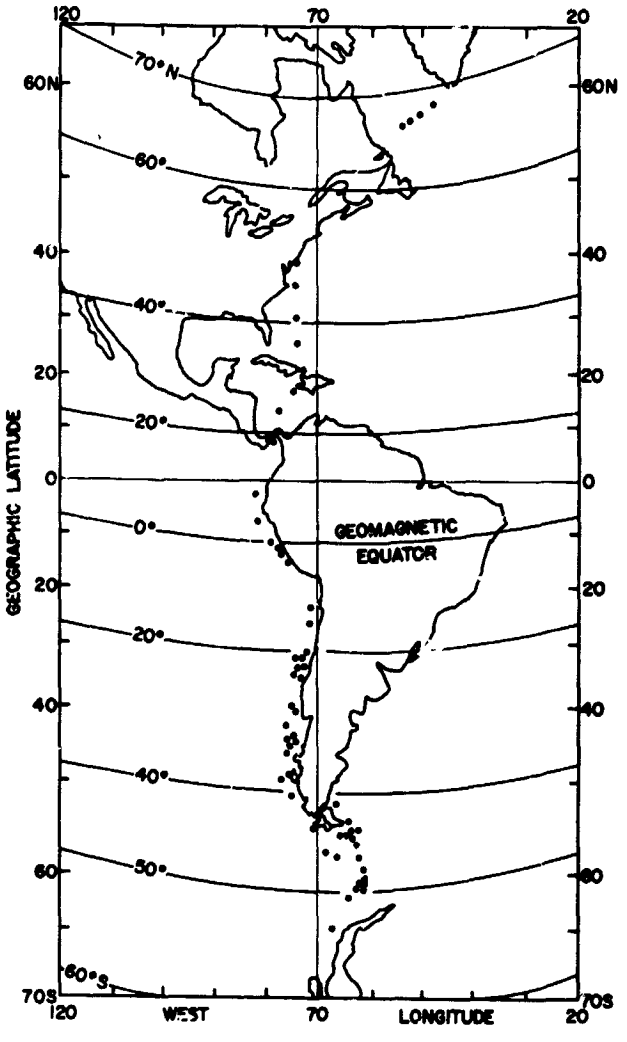

FIGURE 1.—Location of the *Eltanin* on nights when useful nighttime observations were made.

of the [OI] and NaD (doublet) emissions. A correction to the [OI] 5577A intensity is required due to the presence of the OH [7/1] band emissions with the band head at 5562A. Using estimates of the mean zenith intensities of the OH 5562A and [OI] 5577A line emissions given by Roach (1956), 15R and 250R, respectively, or measurements by Krassovsky, Shefov, and Yarin (1962) together with the known transmission characteristics of the 5577A filter, it is estimated that on the average approximately 90 percent of the intensity remaining after correction for continuum sources is due to the [OI] 5577A emission. Although the 6300A filter is quite narrow, contamination from the OH (9/3) band with band head near 6256A is significant. Based on data given by Chamberlain (1961, pp. 555/557) the OH contribution through the 6300A filter is estimated to be in the neighborhood of 10 to 20 Rayleighs. At low levels of [OI] 6300A emission encountered during some of the measurements described below, the OH contamination is especially severe. Serious contamination also occurs through the 5893A filter as a result of the OH (8/2) band near 5386A. The NaD and OH emissions can covary (see Chamberlain, 1961 p. 517) and it is estimated that approximately 70 percent of the line and band emission measured through the 5893A filter is due to the NaD doublet at 5890/5896A. Since the observations reported here are obtained over a wide range of latitude, it must be recognized that there is much uncertainty about the OH contributions. Hence, no attempt has been made to correct the results presented below for OH contamination.

II. RESULTS

Several types of variation occur in the night airglow; these types include latitudinal variation, seasonal variation, diurnal variation, nightly variation and possibly also effects produced by high-altitude explosions. Considering the nature of the data taken so far aboard the *Eltanin* it is impossible to completely separate the different types of variation. An additional complication arises from inhomogenieties of the data, since on some nights complete observations are obtained, while on others, as little as only an hour of observation may be available.

II. A. Variation of [OI] 5577A

A. 1 *Night-to-night and Diurnal Variations*

The observations show two categories of diurnal variation in 5577A. One type, illustrated in Figure 3A, is one in which little variation in the 5577A intensity occurs during the middle of the night. In the second category are those nights in which an enhancement occurs during some part of the night; see Figures 3B and 3C. Evidently the time at which the enhancement occurs is random, since averaging over a number of nights (Figure 4A) yields a nearly constant level of 5577A emission throughout the night. The data do not indicate any latitude dependence of the character of the diurnal variation, although the quantity of data is not sufficient to rule out such a dependence.

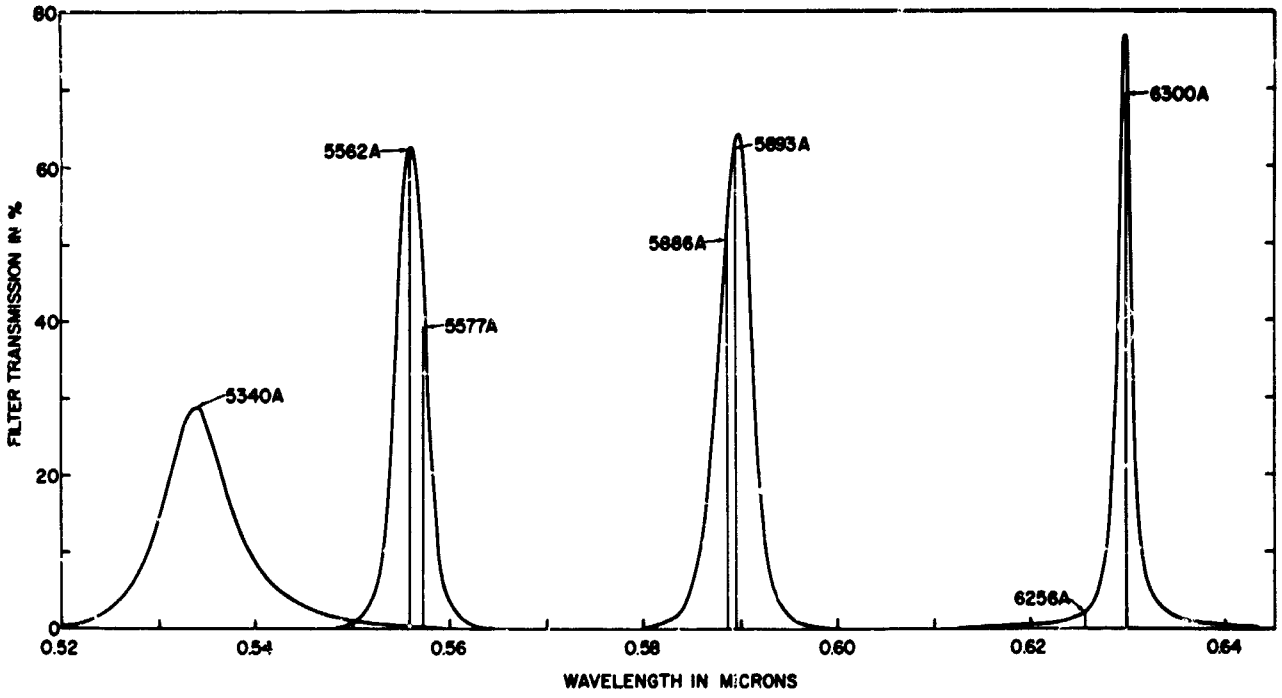

FIGURE 2.—Transmission characteristics of the interference filters and locations of line emissions near the filter peaks.

A. 2 *Latitude and Seasonal Variations*

Figure 5A shows a plot of the nightly average and nightly range of hourly averages of 5577A intensity versus date. The variations here are of several types: latitude, nightly, and seasonal. The same data are plotted in Figure 5B against latitude and those taken during a limited period, May 24/September 1, 1962, are plotted similarly in Figure 5C. An attempt to eliminate part of the nightly variation is shown in Figure 5D, which is compiled by taking the averages of all data in 10 latitude-degree groups. Figures 5C and 5D provide the best indication of both the seasonal and latitude variation in 5577A intensity. The northern hemisphere data are obtained over a short period of time (May 24/June 2) and therefore include only diurnal, nightly and latitudinal variations. These types of variation cannot be separated completely, however Figures 5C and 5D indicate the possibility of a latitudinal maximum near 30/40° geographical latitude and decreasing intensity as the eqator is approached. Moving southward from the equator, there is some increase in the average intensities (Figures 5C and 5D) with a weak maximum occurring near geographic latitude 40°. There appears to be a definite decrease in the 5577A airglow level to the south as far as 65° geographic latitude where the observations end. The data are consistent with a seasonal variation in which there is a maximum summer and minimum in winter.

II. B. Variation of [OI] 6300A

B. 1 *Night-to-night and Diurnal Variations*

Unlike the [OI] 5577A, the [OI] 6300A emission shows a definite variation through the night. The well-known post-twilight decay and the lesser predawn increase are evident in the data taken at all latitudes; see Figure 4B. A nightly variation occurs in [OI] 6300A; for the most part it appears as an over-all change in the level of the emission through the night.

The only exception occurred when the *Ellanin* was near the equator. On the two nights shown in Figure 6, and possibly on a third, an enhancement in [OI] 6300A developed in the hours near midnight. These monochromatic enhancements may be related to the intertropical red arcs described by Barbier, Weill, and Glaume (1961); however, the enhancement is relatively small and apparently restricted in time to the hours near

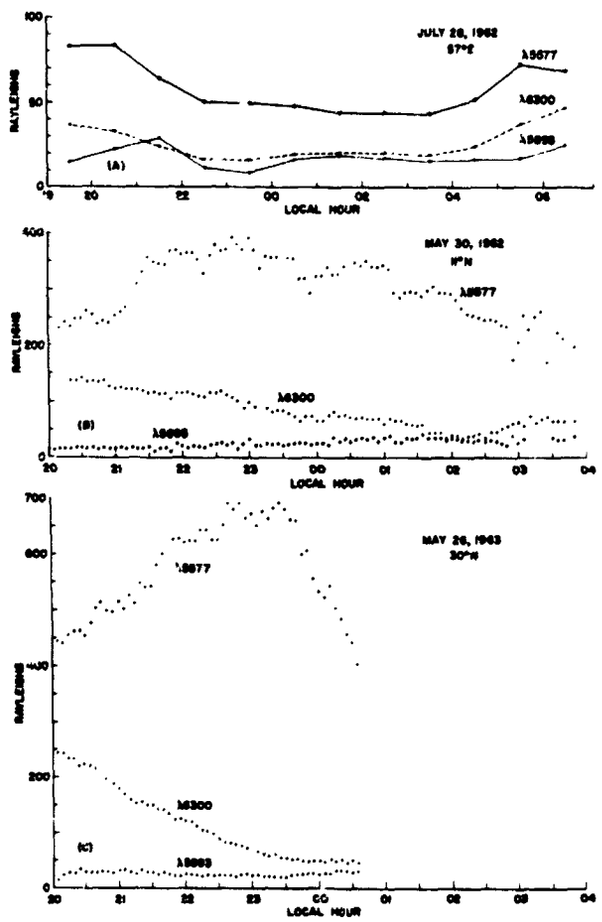

FIGURE 3.—A) Example of a night of relative quiet in the airglow variations (plot of hourly averages); B) and C) are examples of active variations in 5577A.

local midnight. Although the midnight enhancements observed on June 2 and 6, 1962 may not be related to the intertropical red arcs, the zones where the intertropical red arcs appear coincide with the positions of the two maxima on the curve of Figure 7C. There is much similarity between the observed latitudinal distribution of 6300A in the region within 30°N and 30°S magnetic latitude and the F region electron content per vertical column by Duncan (1960). In this calculation, he assumed an initially uniform electron distribution to be modified by electrodynamic lift and subsequent settling down the geomagnetic field lines. Since it has been found that the intensity of the 6300A emission is approximately proportional to the maximum electron density in the F2 region (Huruhata et al., 1959), it appears possible that the processes described by Duncan may contribute to the observed 6300A distribution in the tropic regions.

B. 2 *Seasonal and Latitudinal Variation*

The diagrams showing all data versus latitude (Figure 7A), Southern Hemisphere Winter versus latitude (Figure 7B) and 10-latitude-degree averages (Figure 7C) show generally higher intensities in the Northern Hemisphere and thus may indicate a seasonal variation of [OI] 6300A similar to that of [OI] 5577A; namely, a maximum in summer and minimum in winter. Maximums in the latitudinal distribution of intensity appear near the equator at approximately 15°N and 15°S geomagnetic latitude.

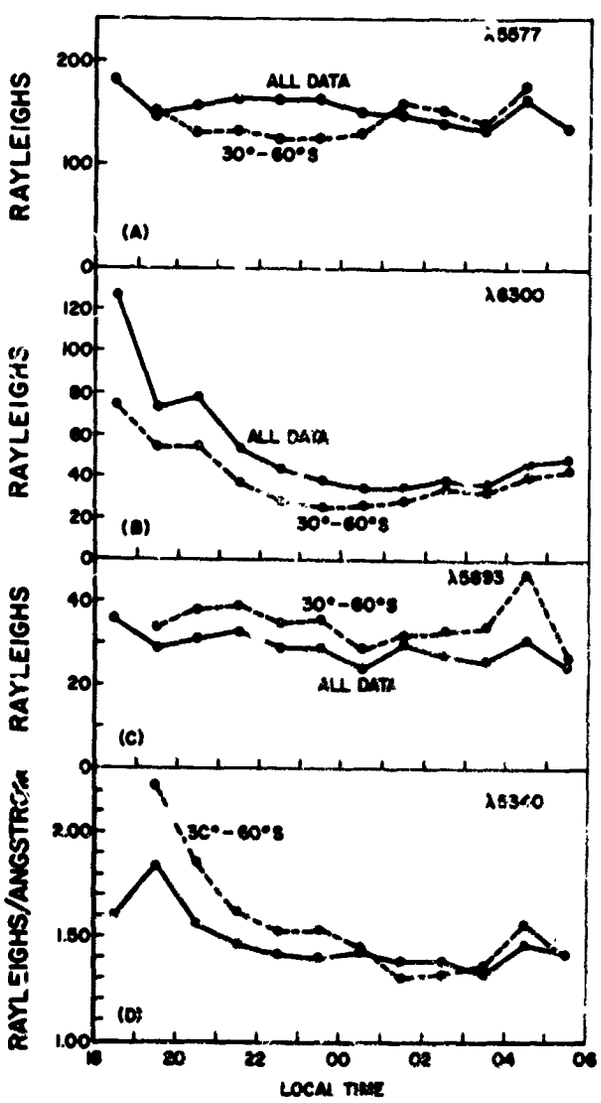

FIGURE 4.—Average diurnal variation of the airglow emissions.

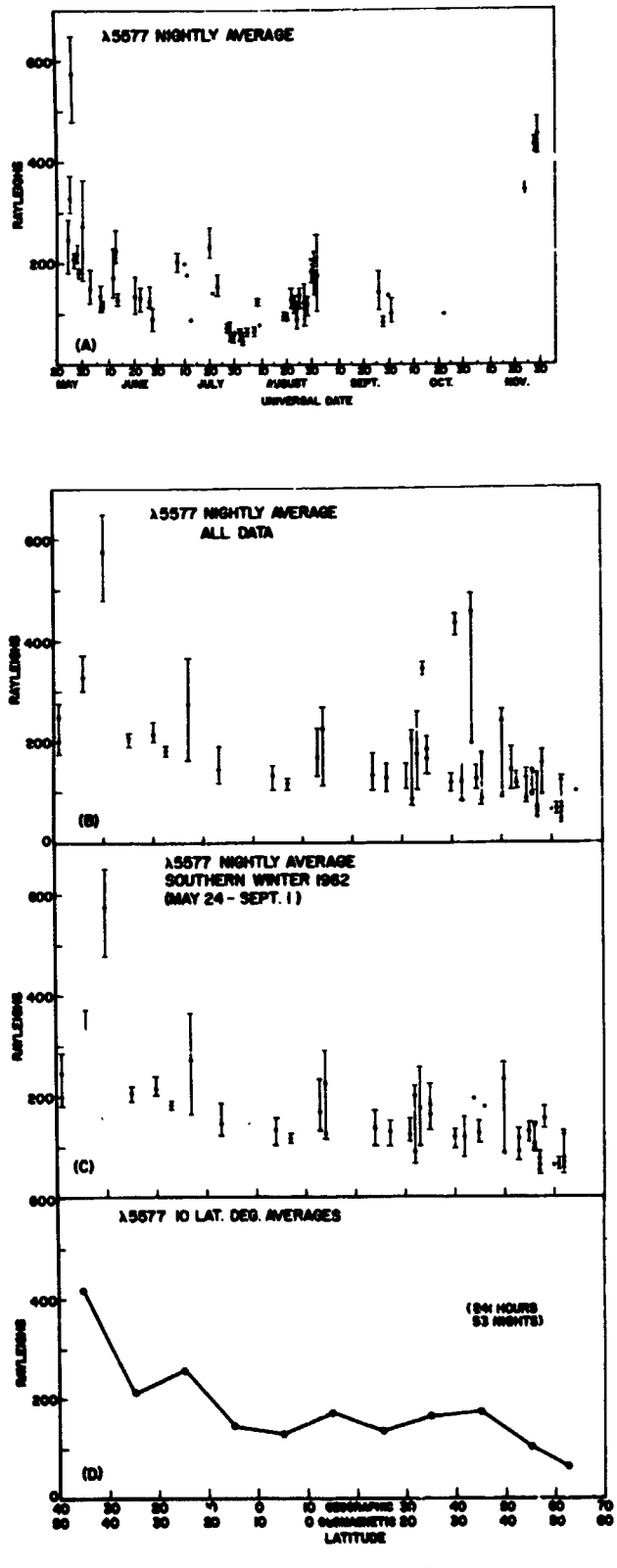

FIGURE 5.—Nightly average and range of hourly average of 5577A: A) versus date, B) all data versus latitude, and C) for data taken May 24 to September 1, 1962. D) ten-degree latitude averages versus latitude, all data.

Another representation of the [OI] 6300A data is shown in Figure 8, where the observations are plotted against latitude and local time and then used to compile isophotes of zenith intensity. This diagram is suggested by a similar one by Barbier (1961) and should be compared with it.

The intensity ratio 6300A/5577A obtained from individual airglow observations is highly variable; ratios averaged over a night's observations range between 0.09 and 0.67. The average ratio of the observations in the region 30/60°S is 0.25.

II. C. Variation of the NaD group

As mentioned previously, the 5893A filter passes both the NaD doublet centered near 5893A and OH emissions including the OH (8/2) emission at 5886A. These emissions will be referred to here as the sodium group. The sodium group intensity remains relatively constant on a given night, and the average diurnal variation curves, Figure 4C, indicate little or no regular variation through the night.

Plots of the sodium group variations versus latitude (Figure 9), show a trend toward higher intensities going from north to south. Superimposed on this trend are irregularities. A maximum appears near 20/30°N, and there is a minimum centered near 0/10°N. Another minimum may exist near 10/20°S, and relatively high intensities are observed over the latitude range 30/57°S. The intensities observed between 58 and 65°S are relatively low. Overall, the variation with latitude of the sodium group intensity is somewhat less than that of the [OI] 5577A and 6300A emissions. The observed sodium group intensities are consistent with a seasonal variation in which there is a maximum in winter and minimum in summer.

II. D. Variation of the Background near 5340A

Except for some evening twilight contamination or post-twilight enhancement, the background near 5340A averaged over all data remained relatively constant through the night; see Figure 4D. The total background near 5340A, shows a general increase from north to south. This total background includes components from integrated starlight, zodiacal light and airglow continuum. Using integrated starlight intensities given by

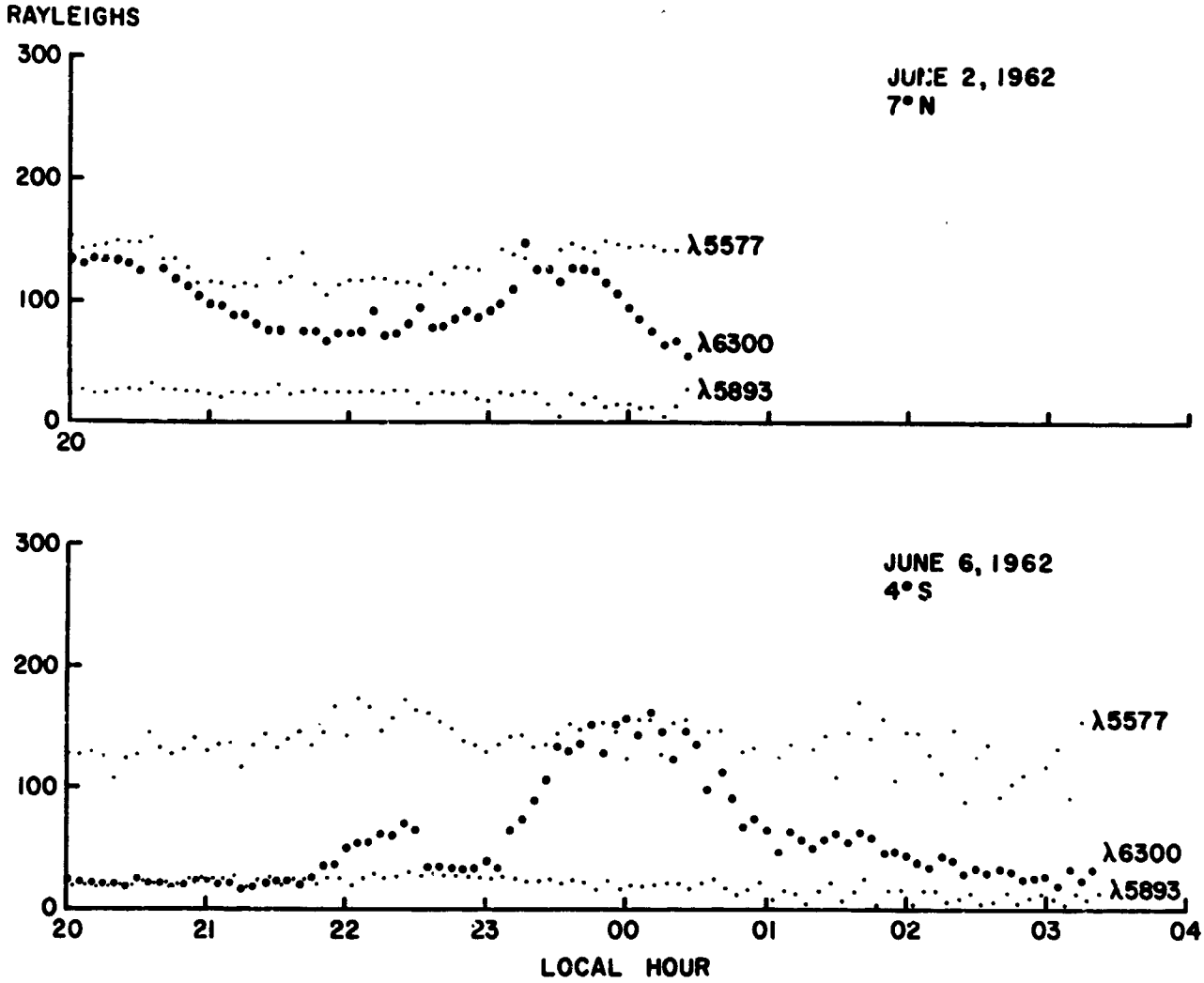

FIGURE 6.—Nights on which enhancements in 6300A occurred.

Roach and Megill (1961) and zodiacal light intensities from Roach and Smith (manuscript in preparation) the contribution of these components to the total background is determined and displayed in Figure 10. The background component due to airglow continuum is obtained by subtraction and is also shown in Figure 10. The airglow continuum determined by this method shows a pronounced minimum at low latitudes and appears to be fairly symmetrical about the goemagnetic equator. For comparison, one-year average values of the airglow continuum obtained by Roach and Smith for two airglow observatories, Fritz Peak, Colorado and Haleakala, Hawaii, are indicated on Figure 10 by the numbers 1 and 2, respectively.

II. E. Auroral Zone Observations

Limited observations of auroras were made during March and April 1962 at the northern auroral zone, however high seas and partial cloudiness during the period of these observations detract from their value. Bright auroral forms were observed in the zenith during part of the observations; 5577A intensities ranged up to 92kR, those of 6300A ranged up to 1.8kR. Although the results may not be meaningful, intensities of the sodium group were not much greater than that observed in the airglow (see Figure 7).

One interesting aspect of the auroral observations is the behavior of the average [OI] 6300/5577 ratio. Individual values of the ratio varied be-

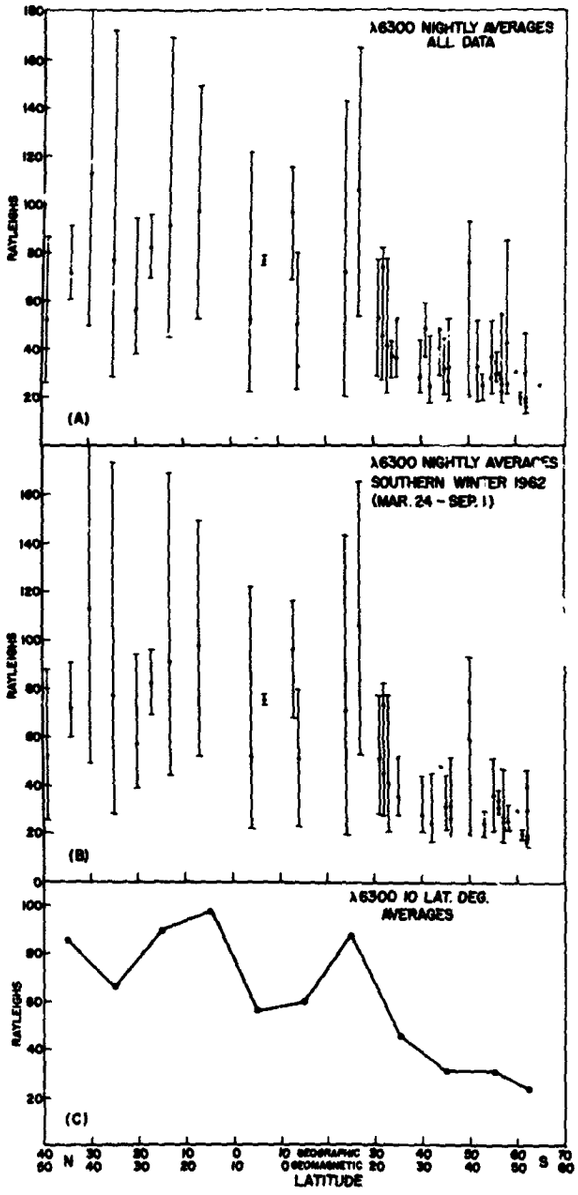

FIGURE 7.—Nightly average and range of hourly averages of 6300A: A) for all data and B) for data taken May 24 to September 1, 1962. C) ten-degree latitude averages versus latitude for all data.

tween 0.007 and 0.5, with the ratio decreasing with increasing 5577A and 6300A intensity: see Figure 11. The higher values of the ratio tend to occur in the hours before midnight, and the lower values after midnight. The tendency for the 6300A/5577A ratio to decrease with increasing 5577A intensity may be due to electron deactivation of the oxygen ^1D level in the brighter

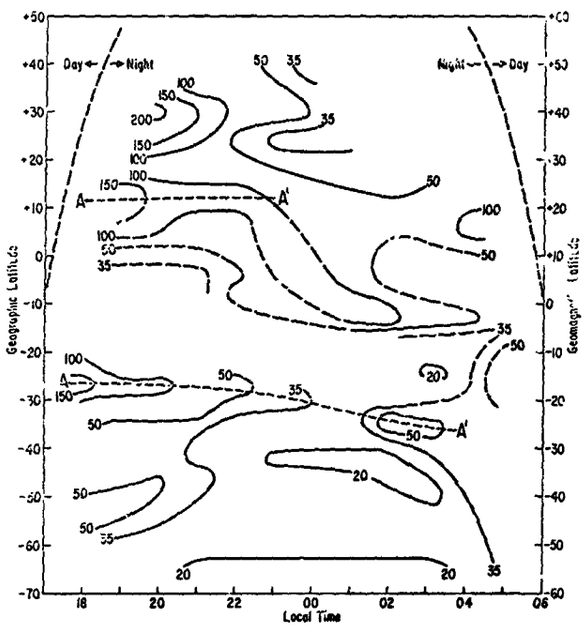

FIGURE 8.—Isophote map giving zenith intensity of 6300A in rayleighs as derived from the *Eltanin* observations during Southern Winter 1962. The dashed lines A–A' indicate possible arc-like zones of enhanced radiation. (Compare with Barbier, 1961)

auroras (Chamberlain 1961, p. 315). Also, molecular deactivation of the ^1D level by collisions with O_2 may be responsible for the results shown in Figure 12 if the brightening of 5577A is associated with increasing auroral exitation at low altitude in the post-midnight hours.

III SUMMARY AND DISCUSSION OF RESULTS

While it is not possible to separate completely the types of variations which influence the results obtained here, these results are compatible with the diurnal, seasonal, and latitudinal variations shown in Table I in summary form. As indicated in the right-hand column of Table I, the observations may be interpreted as suggesting either a rather general seasonal variation or a pronounced hemispherical effect. One aspect of the observations which is evident in the various diagrams but which is not indicated in Table I is the sizable nightly variation observed in each of the airglow components. A comparison of these nightly variations with the global magnetic activity index Kp did not reveal any connection. However, it is interesting that the results of this study do suggest

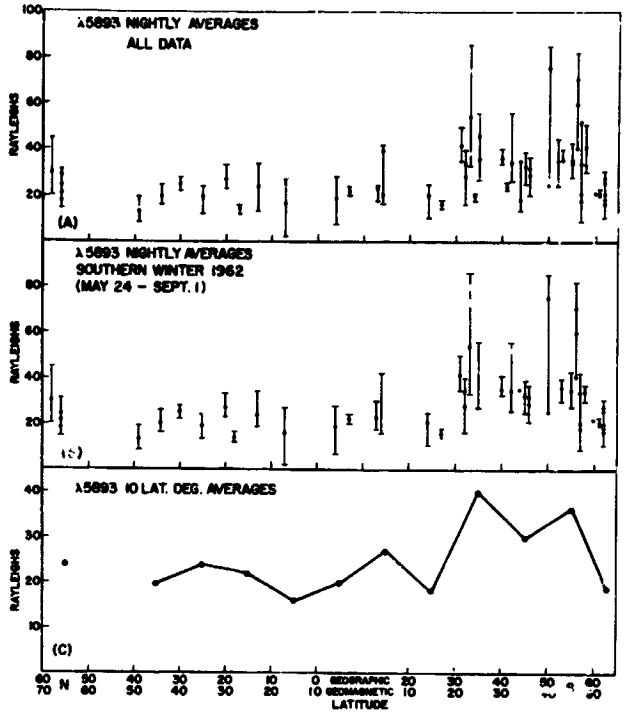

FIGURE 9.—Nightly average and range of hourly averages of the sodium group (NaD 5893A and OH): A) for all data and B) for observations taken May 24 to September 1, 1962. C) ten-degree latitude averages versus latitude, all data.

that the latitudinal distribution of intensity of some airglow emissions may be influenced by the configuration of the geomagnetic field.

The diurnal and nightly variation of 5577A observed on the *Eltanin* in 1962 is somewhat less that that observed in previous years on the *Soya* (Nakamura, 1957 and 1959). Assuming that the calibrations are correct for each set of data, the *Eltanin* observations show lower absolute 5577A intensities as well. Two differences exist in the conditions under which these sets of data were obtained: the observation aboard the *Soya* were made during southern summer and during a period of high solar activity whereas the *Eltanin* observations were made near a minimum in the solar cycle and during southern winter.

Several factors affect the accuracy of the results reported here. One is the uncertainty in the absolute calibration of the comparison source. Another is the problem of OH contamination, which is discussed above. Since the observed 5577A intensities in the southern hemisphere are low, somewhat more than 10 percent of the 5577A intensities reported here may be due to OH. If it is assumed that the NaD and OH emissions

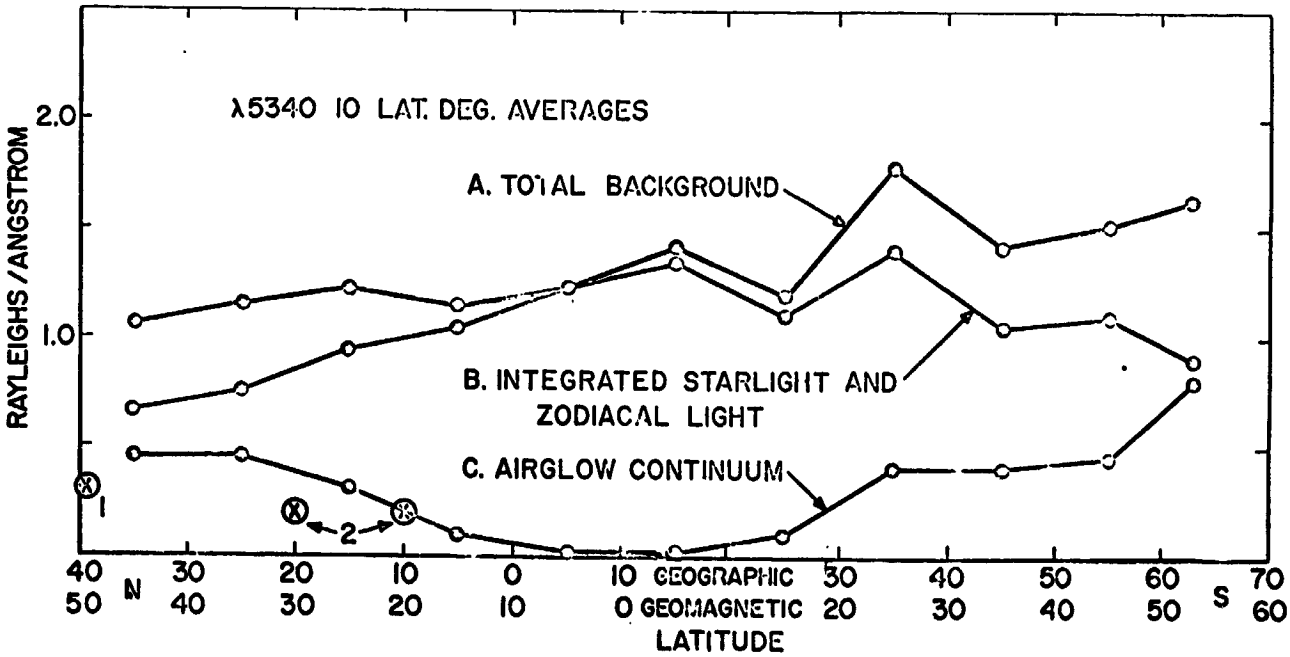

FIGURE 10.—Ten-degree latitude averages of the 5340A background: A) total background, B) the component due to integrated starlight and zodiacal light as computed by Roach and Smith (private communication), and C) the airglow continuum component determined by subtracting curve B from curve A. The point labeled (a) represents the one-year average airglow continuum obtained by Roach and Smith for the Fritz Peak Observation (geographic latitude 40°, geomagnetic latitude 50°) and the points labeled (2) are the same for the Haleakala Observatory (geographic latitude 20°, geomagnetic latitude 10°).

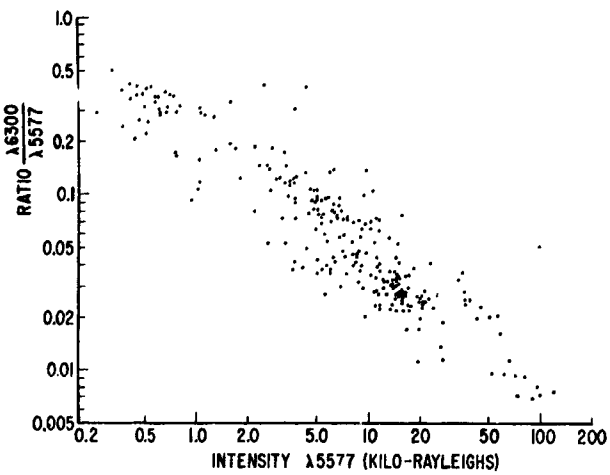

FIGURE 11.—The zenith intensity ratio 6300A/5577A plotted against the zenith intensity of 5577A in the auroral zone aurora.

co-vary, then, at all times, approximately 70 percent of the sodium group intensity observed through the 5893A filter is due to NaD 5893A. It has been found during these observations that these observations that the 2-color method is not a completely satisfactory means of eliminating the astronomical and airglow continuum components from the observations. In using that method it has been assumed that a single proportionality constant relating the contaminants to the 5340A intensity is applicable at all observed light intensities. Observations made during periods of relative stability in the level of the various airglow emissions and in which the astronomical component varied (for example, passage of the Milky Way over the photometer) indicate that the proportionality constant for each wavelength was too low to correct for the astronomical component. On the other hand, if one adopts proportionality constants of sufficient size to give a complete correction when the astronomical components are large, an obvious over-correction occurs at other

TABLE I.—*Summary of* Eltanin *Airglow Observations*

Emission	Diurnal Variation	Latitudinal Variation	Seasonal Variation (or Hemispherical Difference)
[OI] λ5577	No regular diurnal variation irregular activity (sometimes monochromatic) on some nights.	Apparent maximum near 30–40°N, decreasing to minimum near equator, then gradual increase to maximum near 40°S. Decreasing intensity southward as far as 65°S.	Compatible with maximum in summer and minimum in winter. (Or if no such general seasonal variation, the intensities are greater in the northern hemisphere than in the southern hemisphere).
[OI] λ6300	Common post-twilight and predawn variations persist at all latitudes. Monochromatic enhancement observed at local midnight near equator.	Apparent maxima near 15° geomagnetic north and south.	
NaD+ OH near λ5893	No diurnal variation evident.	Apparent maximum near 20–30°N. Shallow minimum near 0–10°N. Irregular increase southward to maximum near 40–50°S and decreasing from 55°S to 65° south.	Compatible with minimum in summer and maximum in winter. (or, as above, higher relative intensity in the southern hemisphere).
Background near λ5340	Possible post-twilight enhancement, otherwise no regular diurnal variation.	Relatively steady increase of total background from 40°N to 65°S. Astronomical components maximize in equatorial region; airglow continuum lowest in equatorial region with apparent symmetry about geomagnetic equator.	

times (the line emission intensities become negative). Consequently, the 2-color method, as used here, must be considered as a very crude means of correction for the atmospheric continuum and astronomical backgrounds. Despite the various uncertainties which influence the absolute values of the emissions reported here, the trends summarized in Table I appear to be real in that they appear in the data prior to and after the application of any corrections.

ACKNOWLEDGMENTS

We are grateful to Dr. Franklin E. Roach for his aid and advice throughout this study. Dr. Manfred H. Rees also has contributed many helpful discussions and several specific suggestions which we have followed. Most of the data presented here were collected through the conscientious shipboard efforts of Mr. F. T. Berkey. Part of the work was accomplished while one of us (T.N.D.) was a Guest Worker at the Fritz Peak Observatory of the National Bureau of Standards. This work was supported by the Office of Antarctic Programs of the National Science Foundation grant number 18704.

REFERENCES

Barbier, D., Les variations d'intensité de la raie 6300A de la luminescence nocturne, *Ann. Geophys.*, 17, 3–15, 1961.

Barbier, D., G. Weill, and J. Glaume, L'emission de la raie rouge du ciel nocturne en Afrique, *Ann Geophys.*, 17, 305–318, 1961.

Chamberlain, J. W., *Physics of the Aurora and Airglow*, Academic Press, New York and London, pp. 315, 517, 555–557, 1961.

Davis, T. N., and L. L. Smith, Latitudinal and seasonal variations in the night airglow, Report No. UAG-R156, Geophysical Institute, College, Alaska, p. 19, 1964.

Duncan, R. A., The equatorial F-region of the ionospher, *J. Atmos, Terr. Phys., 18*, 89–100, 1960.

Huruhata, M. T. Nakamura, H. Tanabe, and T. Tohmatsu, Oxygen red line in the night airglow and ionospheric F2 region, *Rept. Ionos. and Space Res. in Japan*, 13, 283–289, 1959.

Krassovksy, V. I., N. N. Shefov, and V. I. Yarin, Atlas of the airglow spectrum 3000–12400Å, *Planet. Space Sci., 9*, 883–915, 1962.

Nakamura, Jungi, Latitude effect of night airglow, *J. Geophys. Res., 62*, 487–488, 1957.

Nakamura, Junji, Latitude effect of night airglow, *Rept. Ionosphere Res. in Japan, 12*, 419–427, 1959.

Purdy, C. M., L. R. Megill, and F. E. Roach, A new airglow photometer, *J. of Research of the National Bureau of Standards, 650*, 213–216, 1961.

Roach, F. E., Manual for photometric observations of the airglow during the International Geophysical Year, NBS Rept. 5006, National Bureau of Standards, Boulder, Colorado, 1956.

Roach, F. E., and L. R. Megill, Integrated starlight over the sky, *Astrophys. J., 133*, 228, 1961.

Roach, F. E., and A. B. Meinel, The height of the nightglow by the Van Rhijn method, *Astrophysical Journal*, 122, 530–553, 1955.

A65-13158

THE UPPER ATMOSPHERE OF JUPITER*

S. H. GROSS† AND S. I. RASOOL‡

The properties of the upper atmosphere of Jupiter have been theoretically investigated. The vertical temperature profile in the atmosphere above the clouds and the structure of the ionosphere have been computed for two different model atmospheres: Model I corresponds to a H/He mixing ratio of 20 : 1 by volume (Urey, 1959), and Model II has a H/He ratio as low as 0.03 : 1 (Öpik, 1962). Assuming that the atmosphere of Jupiter above the clouds is in radiative equilibrium, the temperature distribution in the upper atmosphere of Jupiter has been computed. With a cloudtop temperature of 153° K and the total optical thickness of the atmosphere in the far infrared of 0.66, the radiation emitted by the planet is 3.1×10^4 ergs cm^{-3} sec^{-1}. This value of radiation flux is about four times higher than the solar flux received by Jupiter. The equilibrium distribution of electron densities in the ionosphere of Jupiter has also been calculated. The maximum electron densities of $\sim 10^6$ electrons/cc are found to occur at the altitudes of 220 km and 110 km above the cloudtop for the two model atmospheres.

INTRODUCTION

Revived interest in planetary astronomy has provided us with a considerable amount of new data on the temperature, pressure, and composition of the upper atmosphere of Jupiter. These data may now be used to derive coherent and satisfactory models of the structure of the Jovian atmosphere.

In this paper we first derive the two extreme model atmospheres for Jupiter which are consistent with the available data on the relative abundances of gases on the planet. We then derive the thermal structure of the upper atmosphere of Jupiter for these two extreme cases, and study the formation of an ionosphere due to the photoionization effect of the solar ultraviolet radiation.

MODELS OF THE JOVIAN ATMOSPHERE

Based on the recent observational evidence, the following assumptions have been made regarding the composition, temperature, and pressure in the Jovian atmosphere.

Composition and Pressure

The atmosphere of Jupiter, above the clouds, contains 150 m-atm of CH_4 and 7 m-atm of NH_3 (Kuiper, 1952). Recently Spinrad and Trafton (1963) estimated the pressure at the cloudtops to be ~ 3 atm. This pressure value indicates that the amounts of CH_4 and NH_3 quoted above would account for less than 1 percent of the total atmosphere of Jupiter, indicating that more than 99 percent of the atmosphere may be composed of hydrogen and helium with, perhaps, some traces of neon (Gallet, 1962).

The exact abundances of hydrogen and helium in the atmosphere of Jupiter are, at the present time, a subject of considerable controversy (Kuiper, 1952; Urey, 1959; Öpik, 1962; Spinrad and Trafton, 1963; Foltz and Rank, 1963). The controversy lies in the quantitative interpretation of the quadrupole lines of molecular hydrogen observed in the high dispersion spectra of Jupiter (Kiess, Corliss, and Kiess, 1960; and Spinrad and Trafton, 1963). The estimates of the amount of H_2 present in the atmosphere of Jupiter above the clouds vary from 5.5 km atm (Zabriskie, 1960) to ~ 200 km atm (Foltz and Rank, 1963).

For the calculations of the structure of the upper atmosphere of Jupiter, therefore, two extreme models for the composition have been considered. In the first, the hydrogen/helium ratio by volume is 20:1 (Urey, 1959), while in the second, it is as low as 0.03:1 (Öpik, 1962). The mean molecular weight of the atmosphere of Jupiter above the clouds in these two models

*Published in *Icarus*, 3(4):311–322, November 1964.
†Airborne Instruments Laboratory, Long Island, New York.
‡Goddard Space Flight Center, and New York University, New York.

would be 2.2 and 3.95. respectively. The pressure at the cloudtop, for both cases, has been assumed to be 3 atm.

Temperature

Murray and Wildey (1963) have recently reported a temperature of 128° K measured in the 8–12 μ atmospheric "window," confirming the older measurements (Menzel *et al.*, 1926) which gave a value of 130° K.

Estimates of the temperature at the Jovian cloudtop have also been made by measuring the radiation emitted by the planet in the microwave regions. Thornton and Welch (1963), from their measurements made at $\lambda = 8.35$ mm, estimate a cloudtop temperature of $144 \pm 23°$ K. Radio-brightness temperatures at cm wavelength regions are contaminated with nonthermal radiation from the planet and therefore cannot be used for a reliable estimate of the cloudtop temperatures.

Because of the presence of 700 cm-atm of NH_3 in the atmosphere of Jupiter (Kuiper, 1952), the levels in the atmosphere to which the infrared and the microwave measurements refer are not reliably known. NH_3 has a strong absorption band in the 8–12 μ interval and therefore the temperatures observed in the infrared may correspond to a level high up in the atmosphere. At $\lambda = 8.35$ mm the absorption due to NH_3 is much less, and therefore the level to which the temperature measured at this wavelength would refer may be deep in the atmosphere and near the cloud level.

Several authors (Öpik, 1962; Kuiper, 1952; Gallet, private communication) have given estimates of the cloudtop temperature on the assumption that the clouds are composed of NH_3 crystals and therefore they are in phase equilibrium with the amount of NH_3 vapor above. On this basis, Öpik has suggested a temperature of 156° K at the cloudtop.

VERTICAL DISTRIBUTION OF TEMPERATURE

In order to calculate the vertical distribution of temperature above the clouds, it is assumed that the atmosphere is in radiative equilibrium. With the Eddington's approximation and assuming a frequency-independent absorption (gray atmosphere), the equation of radiative transfer gives the following expression for the distribution of temperature with altitude:

$$T_z^4 = T_e^4\left(\tfrac{1}{2} + \tfrac{3}{4}\tau_z\right). \qquad (1)$$

Here T_z is the temperature at any level z, T_e is the effective blackbody temperature of the planet, and τ_z is the average infrared optical thickness of the atmosphere above the level z.

In the case of Jupiter, it is assumed that $z = 0$ at the cloudtop where $\tau_z = \tau_0 =$ the total optical thickness of the atmosphere above the clouds.

The absorption in the infrared is due to NH_3 and CH_4. In Fig. 1 is shown the absorption spectrum of NH_3 for the wavelengths between 7 and 60 μ, based on the band intensities for the vibration–rotation bands of ν_2 and ν_4 and the line intensities of the rotation lines recently tabulated by Gille (1964). The absorption has been computed for a mean pressure of 1.5 atm and a mean temperature of 150° K for the total amount of NH_3 of 7 m-atm (Kuiper, 1952). The only absorption band of CH_4 which is significant in this spectral interval is the 7.7-μ vibration–rotation band, and for the measured amount of 150 m-atm, the atmosphere of Jupiter is completely opaque in this spectral interval.

The absorption for the total amounts of NH_3 and CH_4 in the atmosphere has been folded into the 150° K blackbody energy curve and the net energy emitted is shown as the dashed line curve in Fig. 1. The mean transmittance of the Jovian atmosphere over the entire spectral region is 52 percent, giving the total optical thickness of the atmosphere $\tau_0 = 0.66$.

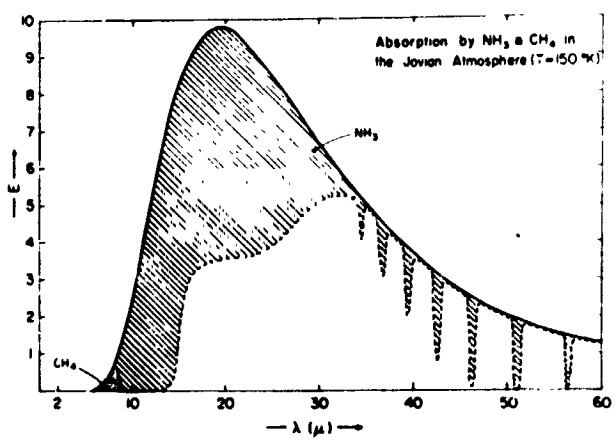

FIGURE 1.—Transmission of infrared radiation through the Jovian atmosphere, composed of 150 m-atm of CH_4 and 7m-atm of NH_3 at 150°K.

Above the cloud level, the opacity (τ_z) will, at any level z, be given by

$$\tau_z = \tau_0 e^{-z/H}, \quad (2)$$

where H is the atmospheric scale height in km, and z is the height in km above the clouds.

We now assume that the 128° K temperature measured by Murray and Wildey (1963) refers to a level high up in the atmosphere where the optical thickness of NH_3 in the 8–12 μ spectral interval has decreased to a value of unity. At this level the total optical thickness of the atmosphere above will be <0.1. We therefore solve Eq. (1) for T_e putting $T_z = 128°$ K and $\tau_z = 0$. The effective temperature of the planet thus calculated is 153° K. Equations (1) and (2) are now combined to obtain the temperature profile of the atmosphere above the clouds.

For the total optical thickness of 0.66, the cloudtop temperature is also found to be 153° K. For the vertical distribution of the temperature, calculations have been made for the two model atmospheres and the results are shown on the left-hand side of Fig. 2.

From this figure it may be noted that the 128° K temperature measured by Murray and Wildey corresponds to the level of 35 or 70 km, depending on which model is being considered. This is consistent with the fact that Murray and Wildey observed a very slight limb darkening, which denotes the existence of a very small temperature gradient at these levels.

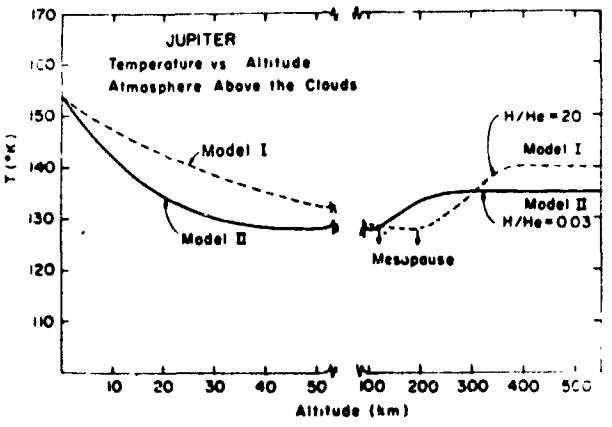

FIGURE 2.—The vertical distribution of temperature in the atmosphere of Jupiter above the clouds for the two model atmospheres.

Also to be noted is the probability that the effective temperature of the planet Jupiter may be about 153° K and not 102° K. The latter should be the effective temperature if the planet were in radiative equilibrium with the incoming solar radiation. The total flux radiated from Jupiter, for an effective temperature of 153° K, is 3.1×10^4 ergs cm^{-2} sec^{-1}. The incoming radiation flux from the Sun for a Jovian albedo of 0.47 is, however, only 0.8×10^4 ergs cm^{-2} sec^{-1}. The difference of 2.3×10^4 ergs cm^{-2} sec^{-1} is probably the radiation being emitted from the interior of the planet.

A rough estimate of the gravitational potential energy released by Jupiter ($3M^2G/5R$, where M and R are the mass and radius of the planet) indicates that if this energy were uniformly distributed over a period of 10^{10} years, the present flux from the interior of the planet could be as high as 3.2×10^5 ergs cm^{-2} sec^{-1}. The rate of the release of energy due to the gravitational contraction of the planet has certainly not remained uniform over this length of time, and the luminosity of the planet is probably much less now than in the earlier period of the planetary history. Our calculations indicate that if the present rate of radiation from the interior of the planet were only 1/12 of its average value, the relatively higher temperatures observed in the atmosphere of Jupiter could be explained by the release of energy due to the gravitational contraction.

In the higher atmosphere of Jupiter, the temperature profile is modified by the deposition of the solar untraviolet energy. We shall therefore assume that the isothermal region extends only up to a level defined as the "mesopause." Above this level the absorption of solar ultraviolet radiation by hydrogen and helium is very significant and part of the energy deposited at that level will heat the atmosphere above the isothermal value of 128° K. This increase in temperature in the "exosphere" gives rise to a positive temperature gradient and permits the energy deposited in the upper atmosphere to be conducted downwards. The "mesopause" is defined as the altitude at which all the energy conducted downwards from the higher atmosphere is radiated away. In the case of Jupiter CH_4 and NH_3 are the radiating molecules.

Following the method described by Bates (1951) and Chamberlain (1962), we find that the mesopause is at a level where the total number density is $\sim 3\times10^{14}$ cm^{-3}. These calculations are made on the assumption that "vibrational relaxation" exists at this altitude, i.e., collisions are rare during the radiative lifetime of the molecules.

The levels at which the number density equals 3×10^{11} cm^{-3} correspond to 104 and 187 km above the clouds for the two model atmospheres as shown in Fig. 2.

Below the level of the mesopause, the atmosphere is thoroughly mixed and the mean molecular weight does not vary with the altitude. Above the level of the mesopause, the atmosphere is assumed to be in diffusive separation and the vertical distribution of each constituent is calculated for its own molecular weight. This assumption is based on the analogy with the Earth, and is supported by the suggestion of Spinrad and Trafton (1963) that strong circulation currents leading to thorough mixing may exist in the atmosphere above the clouds.

The rise in temperature in the atmosphere above the mesopause level is calculated by asuming that 50 percent of the ultraviolet radiation absorbed in the upper atmosphere ($\lambda<912$Å) goes into heating. The method used for these calculations is that described by Nicolet (1959), and for the two model atmospheres, exospheric temperatures of 140° and 135° K, respectively, are obtained (Fig. 2).

This considerably smaller increase in temperature on Jupiter, as compared with the exospheric temperature of the Earth, which is of the order of 1500° K, results because (1) the intensity of solar radiation at Jupiter is 27 times less than at the distance of the Earth; (2) the conductivity for the gaseous mixture on Jupiter is higher than for the O_2–N_2 mixture for the Earth; and (3) the density scale heights in the upper atmosphere are $\sim$5 times less than in the upper atmosphere of the Earth.

IONOSPHERE

Using the temperature distribution in the upper atmosphere of Jupiter shown in Fig. 2, we can now proceed to investigate the properties of an ionospheric layer which may be formed by the photoionization of the atmospheric constituents by the solar ultraviolet radiation.

In an atmosphere mainly composed of hydrogen and helium, the equilibrium electron density in the ionosphere will be determined by a number of ionizing, recombination, and charge exchange processes. The most important of these reactions are shown in Table 1 and have been considered in the present study.

From Table 1 it is readily seen that though only the ions of He and H_2 will be formed by direction photoionization of these gases, H_3^+, H^+, and HeH^+ can also be expected to be produced by charge transfer mechanisms. The reaction (6) to form H_3^+ is very rapid, so that, in equilibrium, little H_2^+ can be expected. HeH^+ is also formed fairly rapidly [reactions (5) and (8)], further decreasing the concentration of H_2^+ and also of He^+ ions. Hydrogen atoms are generated by these reactions at a fairly fast rate and H^+ ions can be produced by direct photoionization. Because of the slow recombination rate of H^+ [reaction (13)], it becomes an important constituent of the ionosphere. We therefore first calculate the distribution of H atoms in the upper atmosphere of Jupiter and then proceed to the computation of equilibrium electron densities in the ionosphere of Jupiter.

Distribution of Hydrogen

Hydrogen atoms generated at higher altitudes are assumed to diffuse downward and recombine by three-body recombination processes [reaction (14)] at lower altitudes, the third body being either H_2 or He depending on the atmospheric model being considered. Since the recombination time is long compared with the time to diffuse through the atmosphere, H atoms may be considered in diffusive equilibrium, distributed exponentially at high altitudes but with the density decreasing rapidly at lower levels where recombination is significant. In equilibrium, the total hydrogen atoms generated each second must equal the total lost due to recombination.

From reactions (5), (6), (8), 10, and (12) of Table 1, it is seen that every ionized H_2 molecule will form two H atoms, and also every ionized He atom will result in two H atoms. The total rate of formation of atomic hydrogen, J(H), can be obtained by integrating the ionization rates of H_2 and He over a vertical column.

TABLE 1.—*Hydrogen and Helium Reactions*

Process	Reaction	Cross section or rate symbol and value	Reference	Remarks
Photoionization	(1) $H_2+h\nu\rightarrow H_2^++e$	$\sigma(H_2)$	*a,b*	$\lambda\leq 804$ Å
	(2) $H+h\nu\rightarrow H^++e$	$\sigma(H)$	*c*	$\lambda\leq 912$ Å
	(3) $He+h\nu\rightarrow He^++e$	$\sigma(He)$	*d*	$\lambda\leq 504$ Å
Charge transfer and ion–molecule reactions	(4) $He^++H_2\rightarrow He+H_2^+$	$\alpha_4=10^{-13}$	*f*	Estimated
	(5) $He^++H_2\rightarrow HeH^++H$	$\alpha_5=10^{-12}$	*e*	Upper limit
	(6) $H_2^++H_2\rightarrow H_3^++H$	$\alpha_6=5\times10^{-10}$	*e*	
	(7) $H_2^++H\rightarrow H^++H_2$	$\alpha_7=10^{-10}$	*f,o*	Not measured, unimportant relative to (6)
	(8) $H_2^++He\rightarrow HeH^++H$	$\alpha_8=10^{-10}$	*e*	
Recombination	(9) $H_2^++e\rightarrow H'+H''$	$\alpha_9=10^{-8}$	*c,f–n*	Upper limit
	(10) $HeH^++e\rightarrow He+H$	$\alpha_{10}=10^{-8}$	*f*	Estimated
	(11) $He^++e\rightarrow He$	$\alpha_{11}=10^{-12}$	*c*	Theoretical, He_2^+ negligible at low pressures
	(12) $H_3^++e\rightarrow H_2+H$	$\alpha_{12}=10^{-8}$	*f*	Estimated
	(13) $H^++e\rightarrow H$	$\alpha_{13}=10^{-12}$	*c*	Theoretical
	(14) $H+H+X\rightarrow H_2+X$	$\alpha_{14}=10^{-32}$	*f,h,p*	X may be H_2 or He
	(15) $H+e\rightarrow H^-+h_\nu$	$\alpha_{15}=10^{-16}$	*q*	Rate to small too be significant

[a] Po Lee and G. L. Weissler, *Astrophys. J.* **115**, 570 (1952).
[b] N. Wainfan, W. C. Walker, and G. L. Weissler, *Phys. Rev.* **99**, 542 (1955).
[c] D. R. Bates, "Atomic and Molecular Processes." Academic Press, New York, 1962.
[d] Po Lee and G. L. Weissler, *Phys. Rev.* **99**, 540 (1955).
[e] C. F. Giese and W. B. Maier II, *J. Chem. Phys.* **39**, 739 (1963).
[f] A. Dalgarno, private communication, 1963.
[g] E. Bauer and T. Wu, *Can. J. Phys.* **34**, 1436 (1956).
[h] F. R. Zabriskie, Dissertation, Princeton University, Princeton, New Jersey, 1960.
[i] M. A. Biondi and S. C. Brown, *Phys. Rev.* **76**, 1697 (1949).
[j] J. M. Richardson and R. B. Nolt, *Phys. Rev.* **81**, 1531 (1951).
[k] L. J. Varnerin, *Phys. Rev.* **84**, 563 (1951).
[l] K. B. Perrson and S. C. Brown, *Phys. Rev.* **100**, 729 (1955).
[m] N. A. Popov and E. A. Afaneseva, *Soviet Phys.–Tech. Phys.* (*English Transl.*) **4**, 764 (1960).
[n] L. B. Loeb, "Handbuch der Physik," Vol. 21, p. 471. Springer-Verlag, Berlin, 1955–60.
[o] C. F. Giese, private communication.
[p] E. Rabinowitch, *Trans. Faraday Soc.* **33**, 283 (1937).
[q] A. Dalgarno and A. E. Kingston, *The Observatory* **83**, 39 (1963).

Assuming that the solar flux of wavelengths <804Å is completely absorbed above the mesopause in the ionization of H_2 and He, then $J(H)=2\times$ the total number of photons incident on a square centimeter column. At the distance of Jupiter, the solar flux of $\lambda<804$Å can be obtained by reducing by a factor of 27 the observed values of the solar flux at the distance of the Earth recently published by Hinterreger (1961). This gives $J(H)=2\times10^9$ atoms cm^{-2} sec^{-1}.

Having obtained the total rate of production of atomic hydrogen, we can now determine the vertical distribution of this gas following the method described by Zabriskie (1960). This method consists of solving the diffusion equation given by Chapman and Cowling (1939) with the following boundary conditions: (1) At higher altitudes the diffusion current equals the rate of formation of H. This is a reasonable assumption since recombination will occur mainly at lower altitudes. (2) At some lower altitude both the diffusion current and the density of atomic hydrogen must go to zero. This is probably also reasonable since recombination will simultaneously reduce both of these quantities.

Using these boundary conditions, Zabriskie derives a simple expression to compute the vertical distribution of atomic hydrogen. His

formulation has been applied to the two model atmospheres that have been studied, and the resulting distributions are shown in Fig. 3.

It is noted in Fig. 3 that the maximum density of atomic hydrogen is of the order of 5×10^9 cm^{-3} and occurs at a level 10–20 km above the mesopause. It is also noted that the density of atomic hydrogen increases rapidly above the mesopause and then decreases exponentially with a scale height of approximately 44 km for the two cases.

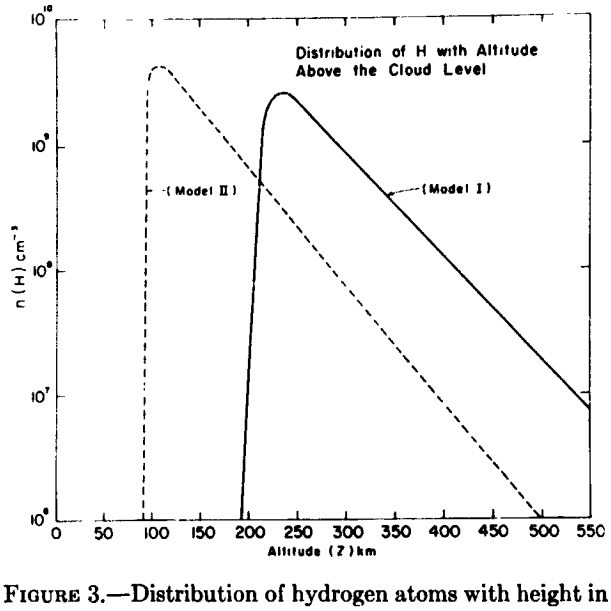

FIGURE 3.—Distribution of hydrogen atoms with height in the upper atmosphere of Jupiter.

Although the two model atmospheres are two extreme cases in which the H/He ratio varies by a factor of 600, it is interesting to note that the equilibrium number density of atomic hydrogen for the two cases is approximately the same. The amount of atomic hydrogen however, even at the level of its peak density, is some 10^4 times less than the total number of particles.

Since it has been assumed that diffusive separation applies above the mesopause, the densities of molecular hydrogen and of helium at these altitudes are readily found from the temperature distribution and they will decrease more rapidly than the density of atomic hydrogen. Consequently, at an altitude of roughly 400 km above the mesopause for Model I, and at 240 km above the mesopause for Model II, atomic hydrogen is the dominant constituent.

Ionization

Having obtained the distributions of He, H_2, and H with altitude, it is now possible to compute the equilibrium ion density distribution as a function of height.

The ionization equations for the reactions listed in Table 1 are as follows:

$$\dot{n}_e = Q_e(H_2)+Q_e(He)+Q_e(H)-\alpha_9 n\ i(H_2^+) - \alpha_{10}n_e n(HeH^+)-\alpha_{11}n_e n(He^+) - \alpha_{12}n_e n(H_3^+)-\alpha_{13}n_e n(H^+) \quad (3)$$

$$\dot{n}(He^+) = Q_e(He)-\alpha_{11}n_e n(He^+) - \alpha_4 n(He^+)n(H_2) - \alpha_5 n(He^+)n(H_2) \quad (4)$$

$$\dot{n}(H_2^+) = Q_e(H_2)-\alpha_9 n_e n(H_2^+)-\alpha_8 n(He)n(H_2^+) - \alpha_6 n(H_2)n(H_2^+)-\alpha_7 n(H)n(H_2^+) + \alpha_4 n(H_2)n(He^+) \quad (5)$$

$$\dot{n}(HeH^+) = \alpha_5 n(H_2)n(He^+)+\alpha_8 n(He)n(H_2^+) - \alpha_{10}n_e n(HeH^+) \quad (6)$$

$$\dot{n}(H_3^+) = \alpha_6 n(H_2)n(H_2^+)-\alpha_{12}n_e n(H_3^+) \quad (7)$$

$$\dot{n}(H^+) = Q_e(H)+\alpha_7 n(H_2^+)n(H)-\alpha_{13}n_e n(H^+) \quad (8)$$

and the total ion density

$$n_e = n(He^+)+n(H_2^+)+n(HeH^+) + n(H_3^+)+n(H^+). \quad (9)$$

In these equations $n(X)$ is the density of constituent X at any altitude z, α_n's are the corresponding values of reaction rates given in Table 1, $Q_e(X)$ is the photoionization rate, and n_e is the electron density in cm^{-3}.

The rate of formation of H^- from reaction (15) is so slow that it has been neglected in the above equations. He_2^+ is also neglected since it is too unstable to contribute significantly. In addition, it is found that there is little He^+ to produce He_2^+ by the three-body reaction.

Since $n(He^+)$ and $n(H_2^+)$ will be small in comparison with $n(H_3^+)$ or $n(HeH^+)$ and n_e with respect to $n(H_2)$ or $n(He)$, we can neglect certain terms in these equations. In Eq. (4) one can neglect the term involving α_{11} and in Eq. (5), the term with α_9. Also reaction (4) is unimportant compared to reaction (6). This is because $n(He^+)$ will not be sufficiently larger than $n(H_2^+)$ to make up for the difference in rate coefficients.

From these equations we find that the contribution of $n(He^+)$ and $n(H_2^+)$ to the total electron

density is relatively small and therefore we can safely neglect these terms in Eq. (9). The total equilibrium electron density is therefore

$$n_e = n(H^+) + n(H_3^+) + n(HeH^+). \quad (10)$$

On solving the resulting set of simultaneous equations and inserting the values of the reaction rates from Table 1, we find

$$n_e = \left\{ 10_8 \left[Q_e(He) + \frac{\{5n(H_2)+n(He)\}Q_e(H_2)}{5n(H_2)+n(H)+n(He)} \right] + 10^{12} \left[Q_e(H) + \frac{n(H)Q_e(H_2)}{5n(H_2)+n(H)} \right] \right\}^{1/2}. \quad (11)$$

In order to evaluate the concentration of electron density as a function of altitude, we first determine the rates of production of H^+, H_2^+, and He^+.

The rate of production of ions is

$$Q_e(X) = \tfrac{1}{4} \int_{\lambda 1}^{\lambda 2} n_z(X)\sigma_\lambda(X)\mathfrak{F}_z(\lambda)d\lambda, \quad (12)$$

where $n_z(X)$ is the number density of the ionizing constituent X at the level z, $\sigma_\lambda(X)$ is the ionization cross section for the constituent at the wavelength λ, and $\mathfrak{F}_z(\lambda)$ is the solar radiation flux at wavelength λ reaching the level z, after having been attenuated by all the ionizing constituents above. The factor 1/4 is due to the fast rotation of Jupiter, so the evaluation of Q_e gives a mean value of the ion production rate over the whole globe. Equation (12) is evaluated by approximating the ionization cross section over the spectral interval and also by taking an average value of the solar radiation $\mathfrak{F}$ over the relevant spectral regions. The values used are shown in the Table 2.

The ionization sections and the corresponding wavelengths for He, H_2, and H are given in Table 2. Although there is a significant overlapping in the relevant spectral regions for the ionization of the individual gases, it may, however, be noted that H_2 is the principal absorber of the far ultraviolet radiation, even when He is the principal constituent, due to the following reasons: (a) The density scale height is large compared to He by a factor of 2, and (b) at altitudes of ~180 km and above, H_2 is the principal constituent. (At much higher altitudes where H is the major constituent, it is optically too thin to be the principal absorber.)

TABLE 2.—*Mean Cross Sections and Fluxes*

$\bar{\sigma}(H_2)$	($\lambda < 504$)	1.7×10^{-18} cm²
$\bar{\sigma}(H_2)$	($804 > \lambda > 504$)	6.1×10^{-18} cm²
$\bar{\sigma}$(He)	($\lambda < 504$)	3.3×10^{-18} cm²
$\bar{\sigma}$(H)	($912 > \lambda > 804$)	5.0×10^{-18} cm²
$\bar{\sigma}$(H)	($804 > \lambda > 504$)	3.0×10^{-18} cm²
$\bar{\sigma}$(H)	($\lambda < 504$)	6.0×10^{-19} cm²
$\bar{\mathfrak{F}}\infty$	($\lambda < 504$)	6.7×10^{8} ph/cm²/sec[a]
$\bar{\mathfrak{F}}\infty$	($804 > \lambda > 504$)	4.0×10^{9} ph/cm²/sec[a]

[a] Hinterreger, 1961.

In Table 2 the values of $\bar{\sigma}$ have been calculated for the relevant spectral interval for the various overlapping bands. $\bar{\mathfrak{F}}\infty$, the total incident solar flux in a wavelength band, is calculated for the distance of Jupiter from the values obtained recently by Hinterreger (1961) at the distance of the Earth.

The ionization cross sections of atomic hydrogen are theoretical and have been obtained from Bates (1962). References for $\sigma(H_2)$ and σ(He) are given in Table 1. From the numerical values listed in Table 2, we calculate the production rates of the H, He, and H_2 ions from Eq. (12), using a mean approximation over the band, and the results are shown in Figs. 4 and 5.

It may be noted that the rate of production of H^+ is 10 times less than the rate of production of H_2^+ in both our model atmospheres. As the recombination rate of H^+ is much slower than that

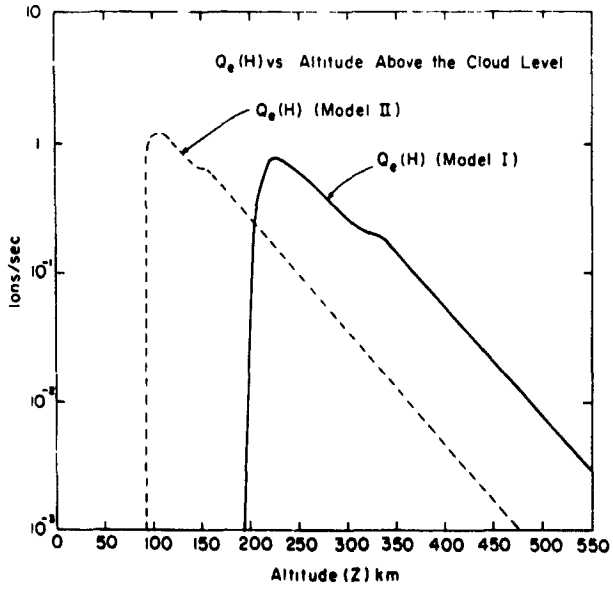

FIGURE 4.—Rate of production of H^+ in the upper atmosphere of Jupiter

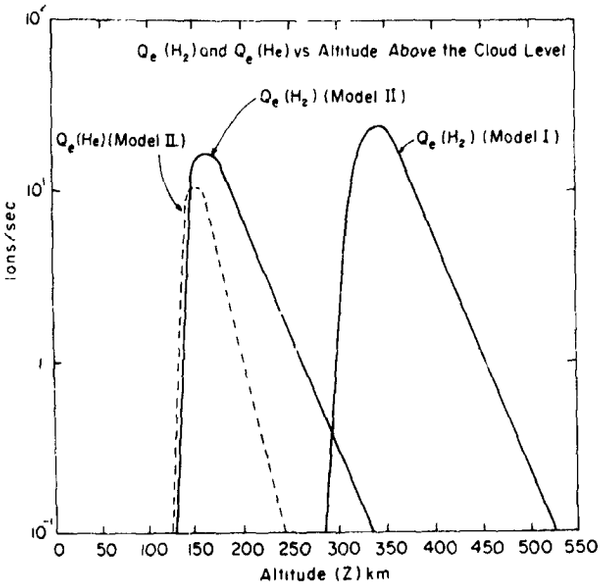

FIGURE 5.—Rate of production of H_2^+ and He^+ for Model I and Model II atmospheres.

of H_2^+ [which is via H_3^+ or HeH^+, or dissociatively via reaction (9), Table 1], it is expected that the atomic hydrogen will be a significant contributor to the total electron density. In the case where He makes up 97 percent of the total atmosphere, Fig. 4 shows that even then the rate of production of He ions is less than H_2^+, though the amount of hydrogen in the atmosphere has been assumed to be only 3 percent. This circumstance is due to the screening of the radiation less than 504 Å by the H_2 above.

Using these computed values of $Q_e(H_2)$, $Q_e(He)$, and $Q_e(H)$, we can now calculate the total electron densities as a function of altitude from Eq. (11). The results are shown in Fig. 6, which is a plot of n_e vs altitude for both models.

When H/He=20, the peak electron density is 7×10^5 cm^{-3} and occurs at ~200 km above the cloud level, with a secondary maximum of about 3×10^5 at ~350 km altitude. In the Model II atmosphere, the maximum electron density occurs at 110 km with a peak value of about 10^6 cm^{-3}. The extent of the ionosphere in the two cases is of the order of ~ 500 km.

The major constituent of the ionosphere for both models is H^+, contributing more than 99 percent of the ions. The maximum concentration of H_3^+ and HeH^+, for the two cases, is ~10^3 to 10^4 cm^{-3}. H_2^+ and He^+ ions have a peak concentration even less, ~10^2 cm^{-3}.

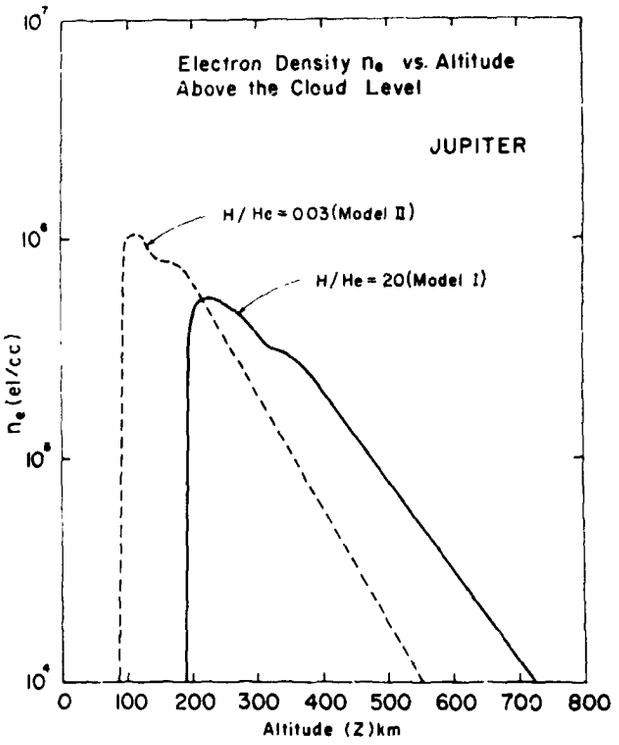

FIGURE 6.—Distribution of total equilibrium electron density as a function of altitude in the upper atmosphere of Jupiter.

RESULTS

The following are some of the important results of the preceding calculations regarding the atmosphere of Jupiter:

(1) If the cloudtop temperature of Jupiter is 153° K and the amounts of NH_3 and CH_4 above the clouds are 700 and 15 000 cm-atm, then the total average optical thickness of the atmosphere in the infrared is 0.66.

(2) Assuming the atmosphere to be in radiative equilibrium, the approximate temperature profile calculated by a simplified version of the equation of radiative transfer for a gray atmosphere indicates that the temperature near the cloudtop decreases with altitude slowly to reach an asymptotic value of 128° K at approximately 35 km for Model II and at approximately 70 km for Model I (Fig. 2). These temperature profiles are consistent with the recently measured temperatures of the planets in the far infrared and in the mm region of the planetary spectrum.

(3) The temperature of the upper atmosphere of Jupiter has been calculated, assuming that 50

percent of the ultraviolet energy deposited in the thermosphere is converted to heat and the energy is conducted downwards to the mesopause to be radiated away by CH_4 and NH_3. The mesopause levels for Model I and II are at 187 km and 106 km, respectively, and the corresponding exospheric temperatures are found to be 140° and 135° K. The results are summarized in Fig. 2.

(4) Calculations of the equilibrium electron density for Model I (H/He=20) result in an ionospheric layer with a maximum density of $\sim 7\times10^5$ electrons cm^{-3} at an altitude of 200 km above the cloud level. A slightly higher electron density (1.0×10^6 cm^{-3}) is achieved in the second case when H/He=0.03, the peak being at 120 km above the clouds.

(5) The major constituent of the ionosphere in both cases in H^+.

DISCUSSION

Results on the electron density distribution in the upper atmosphere of Jupiter may be compared with the earlier studies of the Jovian ionosphere.

The most comprehensive study to date of the possible structure of the ionosphere of Jupiter has been made by Zabriskie (1960). His main conclusion is that a Jovian ionosphere of peak electron density greater than 10^5 cm^{-3} is highly unlikely. The disagreement of our results with those of Zabriskie is probably due to the following differences in our basic assumptions and approach to the problem:

(1) The exospheric temperatures assumed arbitrarily by Zabriskie were, for his two cases, 600° K and an isothermal atmosphere at 100° K.

(2) Only hydrogen was assumed to be the ionizable constituent of the Jovian atmosphere.

(3) Zabriskie underestimates the ionization of atomic hydrogen by neglecting the ionizing radiation band of 804–912 Å, for which he assumes an ionization cross section of 10^{-20} cm^2. According to Bates (1962), however, it may be $\sim 5.0\times10^{-18}$ cm^2. This enhances the contribution of H^+ to the total electron density.

(4) The solar flux values for the far ultra-violet adopted by Zabriskie are a factor of 2 less than those recently given by Hinterreger (1961) and used in this study.

(5) Zabriskie neglected the reaction $H_2^+ + H_2 \rightarrow H_3^+ + H$ which contributes significantly in the formation of H.

Rishbeth (1959) has made a very rough study of the ionosphere of Jupiter with the main result that an ionosphere mainly composed of H^+ is formed with a maximum density of 10^6 electrons cm^{-3}. This result is very similar to ours, but it is based on the erroneous assumption that the major fraction of H_2 is directly photodissociated into atomic hydrogen which then ionizes to H^+. From the results of Rishbeth, it is not clear at precisely what altitude this maximum occurs.

The photodissociation of H_2 is a very inefficient process (Bates and Nicolet, 1950) and although we are in agreement with Rishbeth for the maximum electron density, our process of formation of atomic hydrogen is through the dissociative recombination of H_3^+ and H_2^+.

Zhelezniakov (1958) has also briefly discussed the formation of a Jovian ionosphere and quotes a maximum electron density value of 10^7 cm^{-3}. This estimate is based on the assumption that the "effective recombination coefficient in the hydrogen layer" is 4×10^{-14} cm^{-3} sec^{-1}, which is incompatible with the values given in Table 1.

It may be mentioned that in our calculations we have neglected the possible dissociation and ionization of methane and ammonia, which may be quite important at the level of the mesopause and may give rise to a secondary ionization peak at that altitude.

The results of this study may have an important bearing on the validity of those hypotheses which invoke the ionosphere of Jupiter as a direct participant in the generation of the decameter radiation. For example, a mechanism has recently been proposed which required electron densities of the order of 10^8 cm^{-3} in the Jovian ionosphere (Chang, 1963).

ACKNOWLEDGMENTS

It is our pleasure to thank Dr. Alex Dalgarno of Queens College, Belfast, Ireland, and Dr. A. G. W. Cameron of the Goddard Institute for Space Studies for numerous valuable discussions and suggestions during this work. We would also like to thank Professor Edwin Salpeter of Cornell University and Dr. Siegfried Bauer of the Goddard Space Flight Center for critically reading the

manuscript. We are grateful to Allan Liebman who helped us with the computations.

REFERENCES

BATES, D. R. (1951). The temperature of the upper atmosphere. *Proc. Phys. Soc. (London)* **B64**, 805–821.

BATES, D. R. (1962). "Atomic and Molecular Processes." Academic Press, New York.

BATES, D. R., and NICOLET, M. (1950). The photochemistry of atmospheric water vapor. *J. Geophys. Res.* **55**, 301–327.

BAUM, W. A., and CODE, A. D. (1953). A photometric observation of the occultation of σ Arietis by Jupiter. *Astron. J.* **58**, 108.

CHAMBERLAIN, J. W. (1962). The upper atmosphere of the planets. *Astrophys. J.* **136**, 582.

CHANG, D. B. (1963). Amplified whistlers as the source of Jupiter's sporadic decameter radiation. *Astrophys. J.* **138**, 1231.

CHAPMAN, S., and COWLING, T. G. (1939). "The Mathemathical Theory of Non-Uniform Gases." Cambridge Univ. Press, London.

FOLTZ, J. V., and RANK, D. H. (1963). Intensity of the quadrupole band of molecular hydrogen. *Astrophys. J.* **138**, 1319.

GALLET, R. (1962). Private communication.

GILLE, J. (1964). Dissertation, Harvard University, Cambridge, Massachusetts.

HINTERREGER, H. E. (1961). Preliminary data on solar extreme ultraviolet radiation in the upper atmosphere. *J. Geophys. Res.* **66**, 2367.

KIESS, C. C., CORLISS, C. H., and KIESS, H. K. (1960). High dispersion spectra of Jupiter. *Astrophys. J.* **132**, 221.

KUIPER, G. P. (1952). Planetary atmospheres and their origin. *In* "Atmospheres of the Earth and Planets." Univ. of Chicago Press, Chicago, Illinois.

LEE, Po, and WEISSLER, G. L. (1952). Absolute absorption of the H_2 continuum. *Astrophys. J.* **115**, 570.

MENZEL, D. H., COBLENTZ, W. W., and LAMPLAND, C. O. (1926). Planetary temperature derived from water-cell transmissions. *Astrophys. J.* **63**, 177.

MURRAY, B. C., and WILDEY, R. L. (1963). Stellar and planetary observations at 10 microns. *Astrophys. J.* **137**, 692.

NICOLET, M. (1959). La Thermosphère. *Ann. Géophys.* **15**, 1.

ÖPIK, E. J. (1962). Jupiter: chemical composition, structure and origin of a giant planet. *Icarus* **1**, 200.

RISHBETH, H. (1959). The ionosphere of Jupiter. *Australian J. Phys.* **12**, 466.

SPINRAD, H., and TRAFTON, L. M. (1963). High dispersion spectra of the outer planets. I. Jupiter in the visual and red. *Icarus* **2**, 19.

THORNTON, D. D., and WELCH, W. J. (1963). 8.35 mm radio emission from Jupiter. *Icarus* **2**, 228.

UREY, H. C. (1959). The atmospheres of the planets. *In* "Handbuch der Physik," Vol. 52, p. 363. Springer-Verlag, Berlin.

ZABRISKIE, F. R. (1960). Dissertation, Princeton University, Princeton, New Jersey.

ZHELEZNIAKOV, V. V. (1958). On the theory of sporadic radio emission from Jupiter. *Soviet Astron.–A.J. (Engl. transl.)* **2**, 2, 230.

THE INFRARED INTERFEROMETER SPECTROMETER EXPERIMENT (IRIS)*

R. A. HANEL AND L. CHANEY†

ACKNOWLEDGMENTS

In addition to the experimenters, the following people made substantial contributions to the effort presented here:

Frank Bartko, Goddard Space Flight Center

Fred Bartman, University of Michigan

Lawrence Byrne, Goddard Space Flight Center

Grady Nichols, Goddard Space Flight Center

Dr. David Wark, United States Weather Bureau

1. SCOPE

The purpose of this report is

to show how significant information on the atmosphere and surface of Mars can be extracted from the thermal-emission spectrum of the planet

to describe the design of an infrared interferometer capable of measuring the thermal-emission spectrum

to document requirements and constraints of the infrared interferometer experiment on a planetary fly-by spacecraft

2. SCIENTIFIC OBJECTIVES

The objective of the infrared interferometer spectrometer (IRIS)‡ experiment is to obtain information on the composition and structure of the atmosphere and surface of the planet Mars. This information will be extracted from the thermal-emission spectrum within the interval of 2000 cm^{-1} (5 microns) to 500 cm^{-1} (20 microns) and possibly to 300 cm^{-1} (33 microns) with a spectral resolution of 5 cm^{-1}. The IRIS experiment is deliberately aimed at a wide spectral range to permit clear identification of many predictable spectral features and, even more important, to allow a search for unexpected phenomena. For a nominal fly-by distance of 5000 km, the resolved area will be a circle of 250-km diameter, approximately equivalent to the resolution now obtained by photographic techniques with ground-based telescopes.

The wide spectral range of the instrument, combined with the relatively high spectral resolution, makes a variety of scientific studies possible; these can be grouped into investigations concerning the atmosphere, and those concerning the planetary surface. In addition, many other inferences can be made from the results of the measurements. The following discussions indicate the wide scope of scientific investigations made possible by this experiment.

2.1 The Thermal-Emission Spectrum

The thermal-emission spectrum of a planetary atmosphere depends on many parameters, of which the most important are the temperature profile, the surface temperature and emissivity, the concentration of atmospheric constituents, and the surface pressure. Under the condition of radiative equilibrium, the temperature profile is completely defined by the parameters mentioned above as well as the solar zenith angle. In theory, if a greater number of measurements of the specific intensity are obtained than the unknown parameters which exist, then all parameters influencing the thermal-emission spectrum can be determined; however, the measurements must be made in independent spectral regions or at different zenith angles. In practice, the extraction of individual parameters is more difficult, and within the limited accuracy of the instruments, different

*Published as *Goddard Space Flight Center Document X-650-64-204*, July 1964.

†University of Michigan.

‡IRIS is the Greek word for rainbow.

parameters can be determined only within certain limits.

To study the influences of the various parameters on the thermal-emission spectrum and to see how these parameters can be determined from the measurements, some preliminary calculations have been made (Figure 1, Table 1).

The radiative equilibrium temperature distribution for a simulated Martian atmosphere has been calculated, using technique described in Reference 1. Some cases are shown in which the temperature distributions require modification due to convective energy transport. Five individual cases were studied:

Case 1 corresponds to the estimated maximum conditions which could possibly occur near the subsolar point. The surface temperature was assumed to be 320°K, slightly above the maximum measured from the earth in the atmospheric window. The calculated temperature profile is shown in Figure 1.

Case 2 corresponds to the expected nominal condition in the late afternoon local Martian time and $\pm 45°$ latitude.

Cases 3 and 4 have been calculated for higher surface pressures.

Case 5 is representative of the coldest conditions expected during the Martian night.

All calculations were carried out for an N_2–CO_2 atmosphere with trace amounts of H_2O. Other gaseous constituents that may be detected (by techniques described later) may influence the equilibrium temperatures, and will have to be considered in addition to the CO_2 and the small amount of water vapor. Furthermore, these calculations assume only pressure broadening of the spectral lines. In the low-pressure conditions to be expected on Mars, Doppler broadening will be an important factor and must be considered in a more refined treatment.

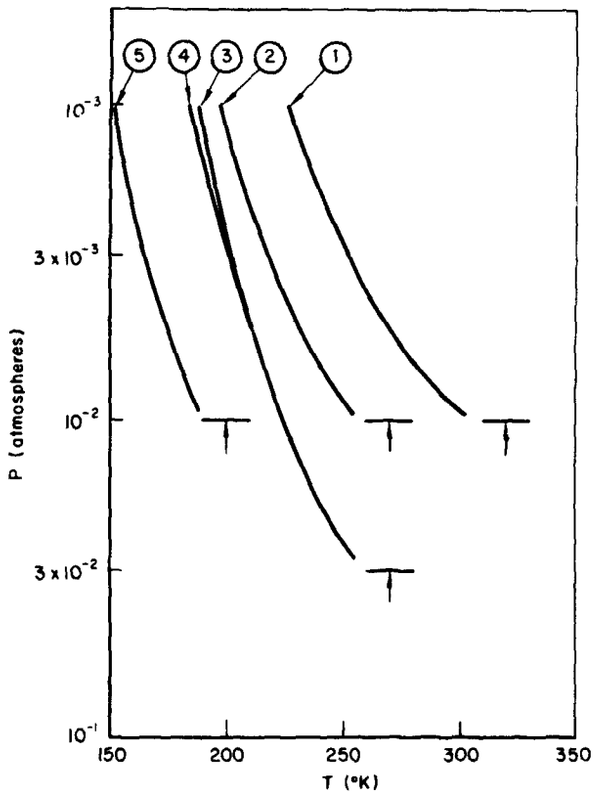

FIGURE 1.—Radiative equilibrium temperatures in a simulated N_2–CO_2 atmosphere with trace amounts of water.

TABLE 1.—*Summary of Assumptions Made in the Calculations of Temperatures for the Five Cases Shown in Figure 1.*

Case	1	2	3	4	5
Solar zenith angle	0°	60°	60°	60°	night
Surface temperature (degrees Kelvin)	320°	270°	270°	270°	200°
Surface pressure (atmospheres)	.01	.01	.03	.03	.01
CO_2 concentration	.25	.25	.10	.25	.25
H_2O concentration	$.4 \cdot 10^{-4}$	$.4 \cdot 10^{-4}$	$.4 \cdot 10^{-4}$	$.4 \cdot 10^{-4}$	$.4 \cdot 10^{-4}$
Surface emissivity	1	1	1	1	1
Surface reflection for near-infrared	.25	.25	.25	.25	.25

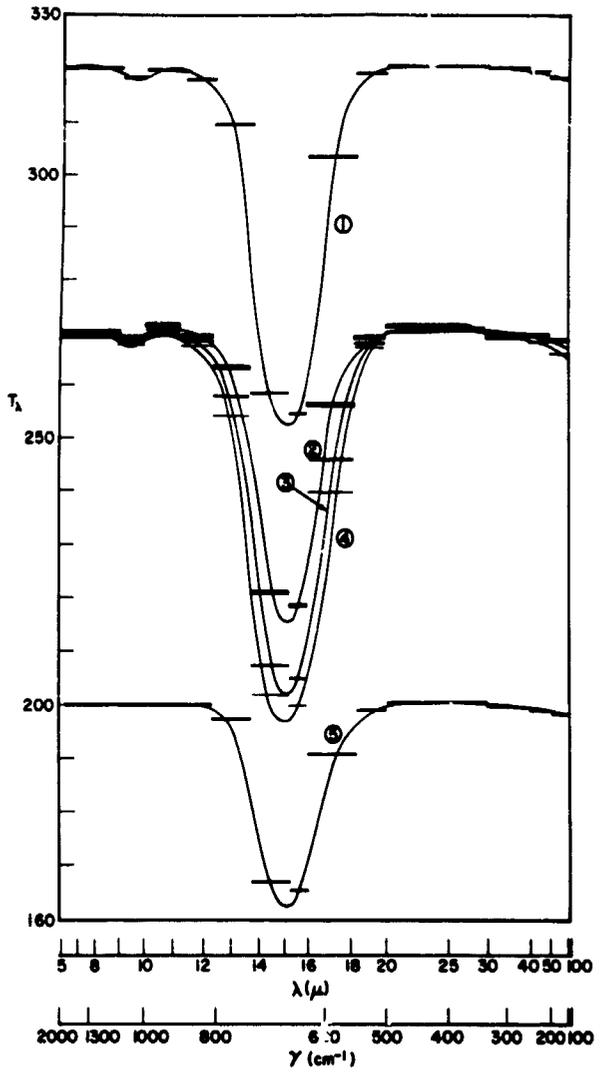

FIGURE 2.—Low-resolution thermal spectra calculated for temperature profiles shown in Figure 1.

Figure 2 shows the corresponding thermal spectra. The spectral resolution of the diagram is very low, varying between approximately 50 and 100 wavenumbers in the most interesting portions. The abscissa is proportional to the fraction of the energy available from a blackbody at 270°K. The wavenumber and the wavelength scales are nonlinear. The strong 15-micron CO_2 band dominates the central part in all spectra. Although the temperature profiles of Cases 3 and 4 are almost the same, the higher abundance of CO_2 in Case 4 causes lower temperatures in the 15-micron band. A comparision between Cases 2 and 4 clearly show the strong influence of the surface pressure, evidence that the surface pressure may be extracted from the emission spectrum.

2.2 Atmospheric Composition

Identification of gases known to be present in the Martian atmosphere (CO_2, H_2O) and estimates of their abundances are among the objectives of the IRIS experiment. But an even more important objective is the possible detection; as well as the establishment of better upper limits, of yet unidentified but suspected constituents (N_2O, NO, NO_2, CH_4, C_2H_4, C_2H_6, NH_3, O_3).

The identification of gases is based on the characteristic absorption spectrum of each gas. Gases in the atmosphere absorb thermal radiation from the surface and, according to Kirchhoff's law, re-emit blackbody radiation as determined by their own temperature. As most atmospheric temperatures will be somewhat lower than surface temperatures, the atmospheric spectra will appear as absorption spectra. However, this is not necessarily true under all conditions; for example, under the condition of a strong temperature inversion in the atmosphere, or in spectral regions where the surface emissivity is low, a reversal may take place and the spectrum of a gas may appear in emission. These complications do not exist in the interpretation of spectra in the visible or near-infrared (say below 2 microns) where thermal emission is negligible compared to reflected solar radiation.

The long-wave infrared spectra may be more difficult to interpret, and the theory of radiative transfer must be used extensively in a proper treatment of the long-wave spectra; but the thermal-emission spectra yield additional information, such as the temperature profile, which will be discussed later. Furthermore, many atmospheric constituents which might be of biological interest, such as CH_4, are relatively complex molecules which show strong vibrational and rotational bands in the middle and far infrared but very little detectable absorption phenomena in the visible part of the spectrum. For these reasons, the analysis of atmospheric contituents in the far infrared is extremely interesting in spite of the difficulties associated with their interpretation.

Figure 3 shows the spectra of constituents which may be expected in the atmosphere of Mars. The spectra are drawn schematically only, without the many details which can be recognized with a resolution of 5 wavenumbers. The abundance of the gases was taken according to the

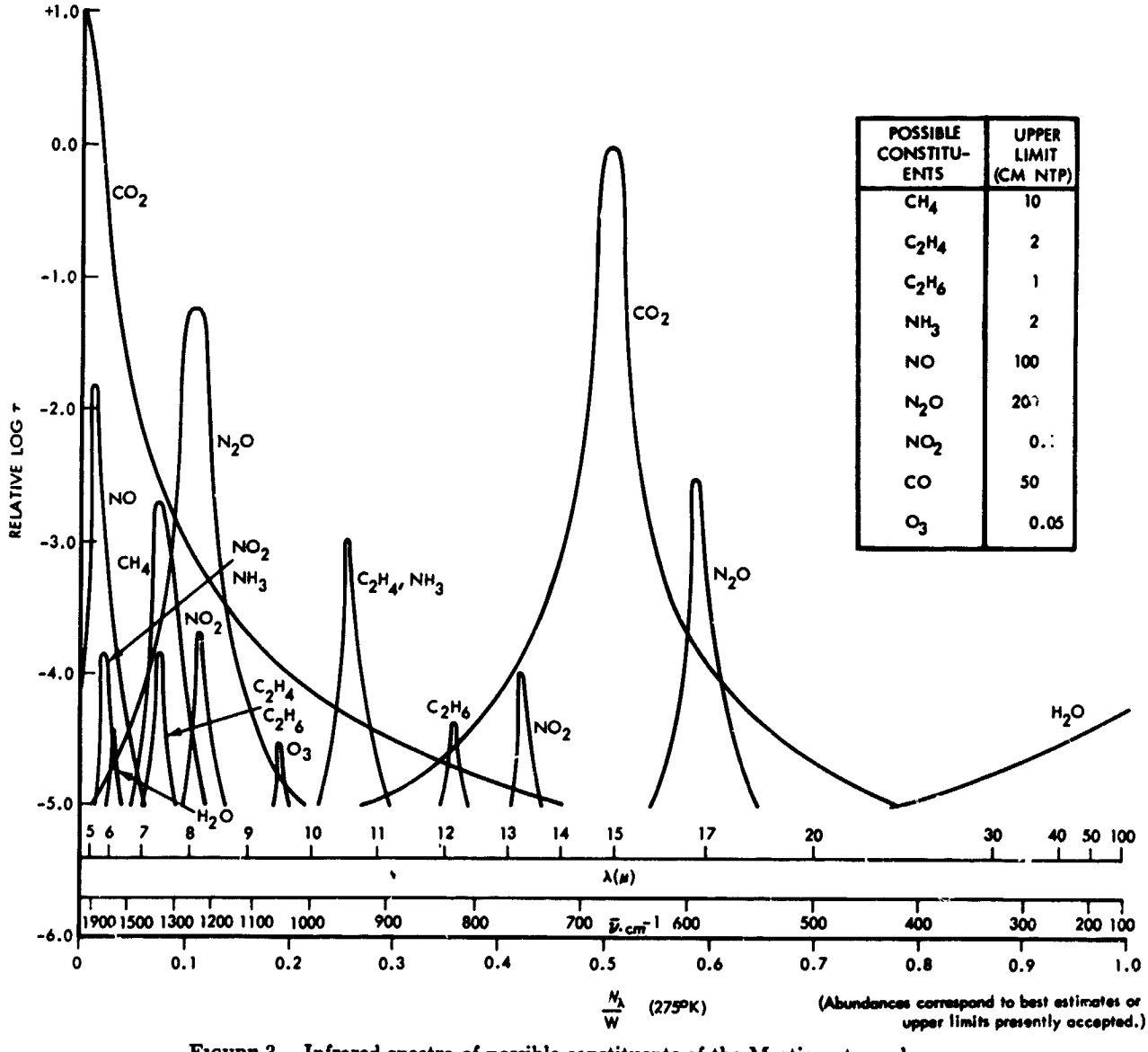

FIGURE 3.—Infrared spectra of possible constituents of the Martian atmosphere.

upper limits presently accepted (Kuiper, 1952; Sinton, 1961)*. The optical depth is shown on a relative scale.

The broad wings of the bands shown in Figure 3 correspond to the absorption continuum arising from the sum of the wings of all individual lines in the band. The situation for the Lorentz line shape is shown. This must be considered an upper limit for a number of reasons: First, as Benedict has shown, the Lorentz shape does not strictly apply far away from the line centers; second, and more important, Doppler broadening will be an important factor which causes a much faster decay of the line shape away from the line center and consequently gives rise to a much weaker continuum than that indicated. The 15-micron CO_2 band and the N_2O band near 8 microns, using the above upper limits and measured band intensities, are strong enough to be totally opaque. Methane (CH_4) and other hydrocarbons (C_2H_4) may also be detected. Water vapor, ozone, and others are more difficult to extract from the spectra But, because water vapor is extremely important both from an atmospheric-physics and from a biological viewpoint, a technique for the possible identification of this as well as other less abundant constituents will be described here.

*References 2 and 3.

Water vapor has strong vibration-rotation bands near 6.3 microns and the rotational band beyond 20 microns. If the spectral response of the instrument is restricted to 20 microns, then only the first bands are available for analysis. Figure 4 shows the transmission of a synthetic atmosphere consisting of the expected amount of CO_2 and water vapor, in the full detail to which the spectra can be generated by the interferometer. In addition, the figure shows spectral transmission of CH_4 and N_2O, both present in a quantity corresponding ot the presently accepted upper limit, and under the expected average atmospheric conditions. As can be seen, the atmosphere is nearly opaque between 600 and 750 wavenumbers (15-micron CO_2 band) and near 1300 (N_2O). Water vapor shows absorption phenomena between about 1300 and 2000 wavenumbers. Even in the strongest parts, the maximum absorption does not exceed a few percent. Consequently, it will be difficult to recognize the presence of water vapor in this band, and even more difficult to determine the abundance quantitatively. Fortunately, however, the water-vapor band spreads over almost 700 wavenumbers and shows considerable structure. This feature allows the use of statistical methods to obtain information about water vapor from almost 140 individual spectral data points derived from a single interferogram. The cross-correlation function of the received spectrum and the known spectrum of water vapor is obtained by

$$C_{(x)} = \int I_\nu W_{(\nu+x)} d\nu.$$

Even under conditions of severe noise, the cross-correlation function shows a maximum for $x = 0$. The correlation technique is a powerful tool for recognizing and estimating the amount of particular constituents in a complicated and possibly noisy spectrum. Figure 5 shows a sample of a cross-correlation function of the water-vapor spectrum with a combination of random noise and water vapor (signal-to-noise ratio equal to one). The same technique may also be employed to assess the amounts or upper limits for other atmospheric constituents.

2.3 Atmospheric Structure

Use of satellite-measured radiation values to determine the atmospheric temperature distribution of the earth's atmosphere has been discussed by Kaplan (1960), Wark (1961), Yamamoto (1961), King (1963), and Fleming, et al. (1964).*

Temperature distribution in the atmosphere is related to the absorption characteristics and the upward radiance through the radiative transfer equation expressed, for example, in terms of the pressure. In the spectral region of strongest

*References 4, 5, 6, 7, and 8.

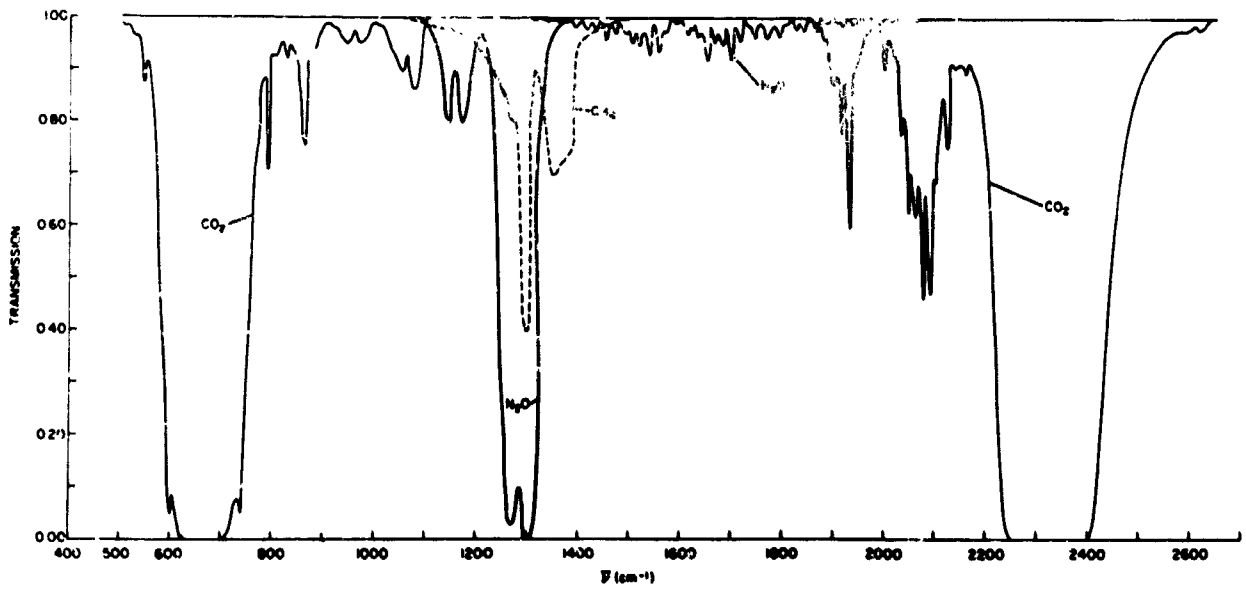

FIGURE 4.—Transmission of a synthetic atmosphere of the expected amount of CO_2 (55m atm) and water vapor (14 precipitable microns) and the upper limits of N_2O and CH_4.

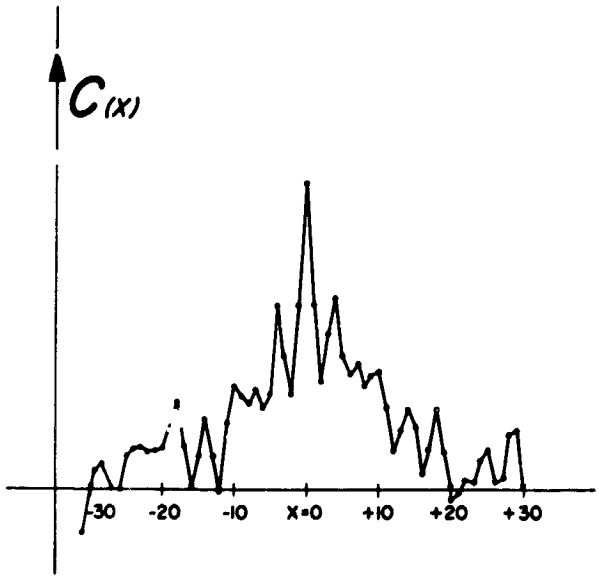

FIGURE 5.—Cross-correlation function of the spectrum of water vapor and a combination of water vapor plus random noise with a signal-to-noise ratio of unity.

absorption, the atmospheric emission arises from the upper portion of the atmosphere. Radiation in spectral regions of weaker absorption originates from lower layers in the atmosphere. Similar considerations can be applied to the extraction of the temperature distribution of the Martian atmosphere.

To illustrate, Figure 6 shows the transmission in selected spectral intervals within the 15μ carbon dioxide band. The transmission data were provided by Wark and Yamamoto. The transmission curves are based upon unpublished laboratory measurements (Yamamoto, Sasamori, Wark and Moore abstract in Publication IAMAP No. 13 on the XIIIth General Assembly of the IUGG, 1963) which assumed that the total amount of CO_2 was 5500 cm atmospheres, and the surface pressure 10 mb (Kuiper, 1964)* which corresponds approximately to the expected conditions on Mars.

Temperature corrections were made in the same manner as in the Meteorological Satellite Laboratory (USWB) reports #10 and #21, using a Mars model atmosphere to calculate effective temperatures T_e (surface temperature 270°K, adiabatic lapse rate to 6.5 mb, radiative equilibrium to 1 mb, extrapolation above.)

Figure 7 shows the atmospheric zones contributing to the outgoing radiance which can be

*Reference 9.

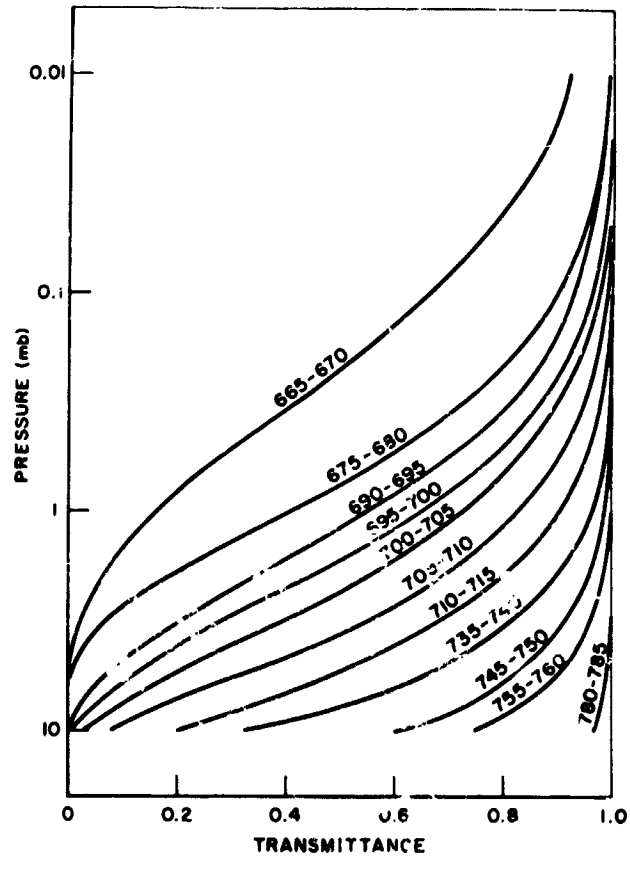

FIGURE 6.—Transmission function of CO_2 in selected spectral intervals in the 15μ band.

detected by the probe. Lorentz broadening only was taken into account; this approach is inaccurate, especially at the lower atmospheric pressures. In general, a somewhat greater absorption will be found than that shown, but the differences will be very small in all but the intervals of greatest absorption. Figure 7 demonstrates that the radiance values recovered by the interferometer allow a determination of the temperature profile. As the interferometer resolution is 5 cm^{-1} over the whole band, redundant measurements are available which increase the accuracy of the temperature determination.

2.4 Surface Studies

After the atmospheric constituents are identified, the effect of atmospheric absorption can be removed from the spectrum in those spectral ranges where the atmosphere is not opaque. The specific intensity emitted by the surface in the non-opaque regions is then obtained,

$$I_\nu(\text{surface}) = \epsilon_\nu B_\nu(T_{surface}).$$

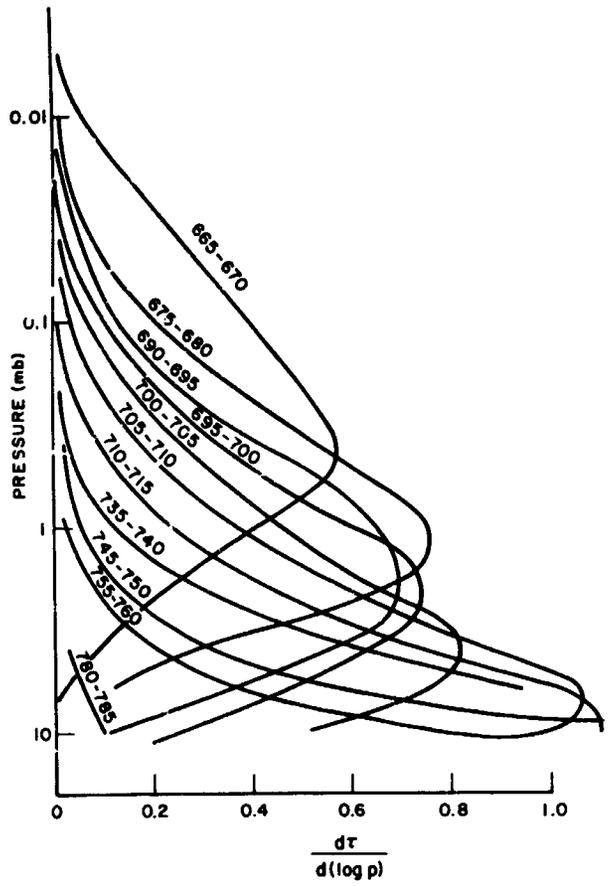

FIGURE 7.—Weighting functions indicating the pressure range from which thermal emission originates.

In the far infrared, most natural surfaces known on earth (rocks, gravel, plants, snow, etc.) have a high emissivity over large spectral ranges. However, the crystalline structure of minerals and the structure of complex molecules create stretching and bending resonances. For example, quartz exhibits strong stretching bands between 800 and 1100 cm^{-1} caused by the Si-O bond; other stretching groups (Si-Si) appear between 600 and 800 cm^{-1}. The same mineral has a bending mode (Si-O-Si) at 430 to 460 cm^{-1}. These resonances give a pronounced rise in the infrared reflectivity which can best be observed on polished samples. The increase in reflectivity is necessarily associated with a reduction in emissivity over the same spectral range.

The sharp rise in reflectivity has been well known since the early days of infrared studies. Rubens used the selective reflectivity of quartz plates to isolate narrow spectral bands in the far infrared. The reststrahlen phenomenon depends somewhat on the temperature of the sample and to a much higher degree on the surface roughness. Lyon (1963)* has studied the emission and reflection spectra of many minerals in great detail. The emissivity of several rocks in solid but unpolished form can be judged from Figure 8.

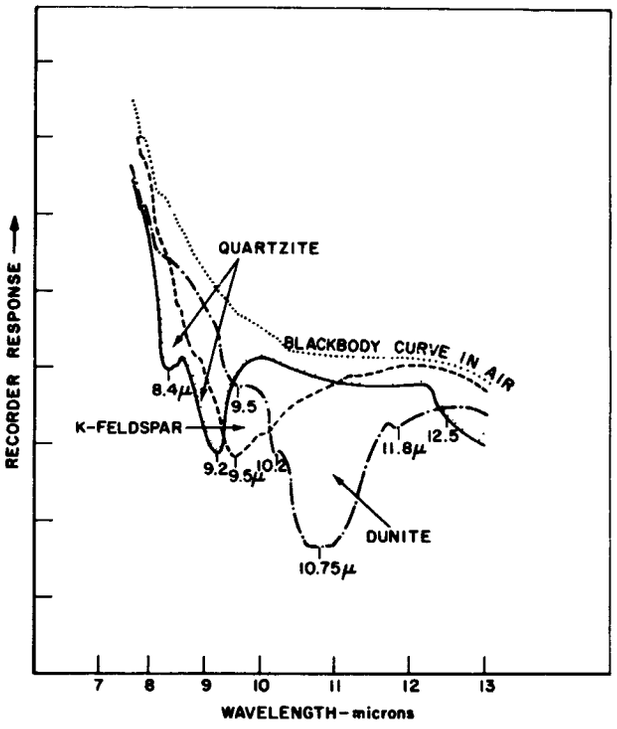

FIGURE 8.—Emissivity in the infrared of rock samples.

Polished samples show an even stronger reststrahlen effect. Grooves on a rough surface act as small cavities and increase the emissivity considerably. Similar phenomena can be recognized in the sandy or powdered form, as shown in Figure 9. Fine dust of a particle size below 1 micron loses the reststrahlen effect almost completely, and the surface emits almost with the characteristics of a graybody or possibly even a blackbody. Scattering effects also become important for these particle sizes. For a grain the size of fine sand, approximately 25 to 50 microns, the reststrahlen phenomenon is weak, but the identification of the material may still be possible, as has been demonstrated also by Bell and Eisner (1956).† Identification of the mineralogical com-

*Reference 10.
†Reference 11.

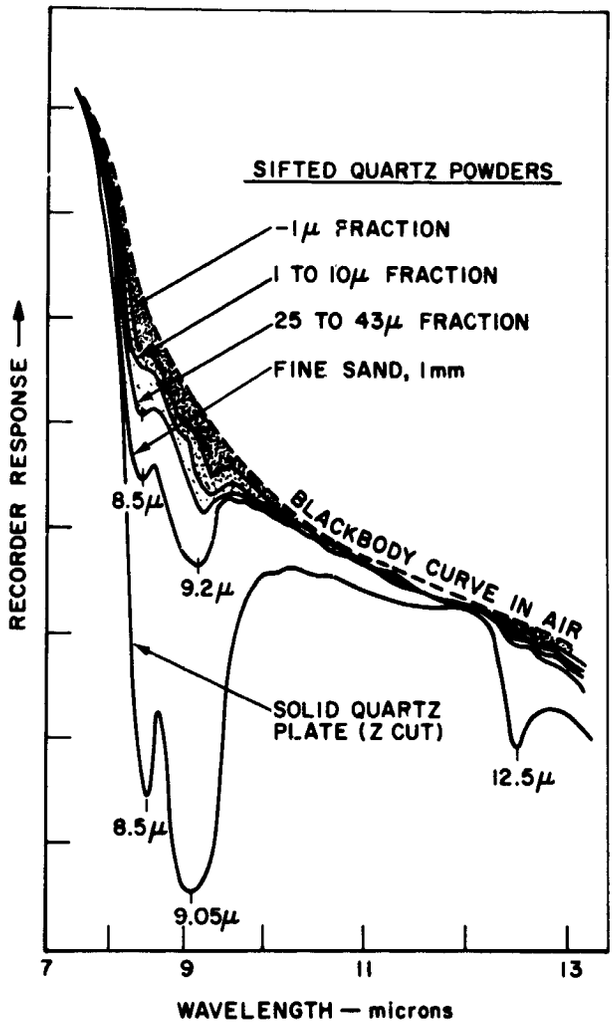

FIGURE 9.—Emissivity in the infrared of quartz and quartz sand of different grain size.

position of the Martian surface by the thermal-emission spectrum is, therefore, very promising, except for areas where fine dust may cover a large portion of the surface. Such areas may exist on Mars, but other areas may expose more solid rocks or gravel or coarse sand. Winds may sweep highlands clear of the finer particles and dust may accumulate in the valleys. The appearance of a pronounced reststrahlen effect would not only allow identification of a particular mineral, but would also be indicative of a coarse surface structure.

The surface emission spectrum may also yield important information on the existence of other chemical substances of inorganic, or possibly even organic, nature if they occur in a sufficiently high concentration. The Sinton bands near 3.5μ, although outside the spectral range of this experiment, are a typical example of unexpected (and so far unexplained) spectral features. The search for reflection or absorption phenomena is especially interesting if the spatial resolution allows measurements in predominantly bright and predominantly dark areas.

A broad program of laboratory and field measurements on earth is an indispensable requirement for proper interpretation of planetary emission spectra. The engineering model of the interferometer under construction will be used for experimental studies in this area.

2.5 Additional Investigations

In addition to the generally well defined tasks already mentioned, a number of inferences may be derived directly or indirectly from the spectra:

Chemistry of the Atmosphere and Surface

Chemical equilibrium between identified gases and others can be used to estimate the abundance of unidentified but suspected constituents; the photochemical equilibrium between CO_2, CO, O_2, and O_3 is one example. Furthermore, the atmospheric gases must be in chemical equilibrium with the surface materials.

Ultraviolet Radiation

Knowledge of the composition of the atmosphere, especially the CO_2 content and upper limits for O_3, allows calculations of the upper limits of the solar ultraviolet spectrum at the surface of the planet. The ultraviolet radiation at the surface is of biological significance.

Relative Humidity in the Atmosphere

The relative humidity near the surface is again of great biological interest. Low temperatures near the morning terminator may allow water vapor to condense in the form of dew or frost; condensation of this nature may be the only source of water available to vegetation if it is present. High temperatures near the subsolar point would cause the water to boil there. At 10 mb, water boils at +7°C. The relative humidity in the atmosphere also governs the condensation of clouds. Atmospheric regions where water or

ice clouds are possible, or likely, can therefore be determined. All these considerations will be greatly aided by theoretical studies of radiative and convective equilibrium conditions in the Martian atmosphere.

Meteorology

The temperature distribution in the atmosphere and the mode of energy transport are intimately connected. The measured temperature profile will give an indication of atmospheric stability. Lapse rates close to the adiabatic one may indicate a convective layer in the atmosphere (troposphere). Theories on the general circulation, or more concisely the Martian meteorology, are intimately related to the temperature profile.

The temperature-versus-pressure data will also be important in investigating the existence and occasional sudden disappearance of the blue haze. If this phenomenon is associated with condensing or sublimating material, the phase diagram of suggested materials must be consistent with the temperature structure derived by the experiment.

The planning of missions designed to land probes on the surface of Mars will benefit also from a better knowledge of the temperature profile, the atmospheric composition, and the surface pressure.

Spectral Emissivity and Surface Temperature

Determination of the spectral emissivity allows a more accurate determination of the true surface temperature. Most materials which show residual ray phenomena in certain parts of the spectrum radiate as nearly blackbodies elsewhere. Therefore, the maximum equivalent blackbody temperature determined over a wide spectral range will be closer to the true temperature of the surface than measurements obtained by radiometers covering a wide or narrow spectral interval. A better interpretation will be possible of radiometric data obtained in the atmospheric window from the earth, or of radiometric measurements performed from fly-by spacecraft. However, special care must be taken in interpreting surface temperatures if the surface is covered with very fine powdery material; this situation will require application of the scattering theory of small particles densely packed, which is quite complicated and not well understood today.

Thermal Inertia of Surface Material

The surface temperature as a function of solar zenith angle, especially near the morning terminator, provides data about the thermal inertia of the surface material. Calculations similar to those performed for the lunar surface can be applied. The great difference in thermal inertias of loose sand and solid rock provides a tool for distinguishing among various surface conditions.

3. THE INTERFEROMETER SPECTROMETER

The instrument, basically a Twyman-Green modification of the Michelson interferometer (Figure 10), departs from the classical laboratory designs in several areas:

The drive mirror is suspended by a parallel leaf-spring system.

The mirror assembly is driven by a moving coil in a strong magnetic field; nearly critical damping is provided by electronic means.

The mirror motion is monitored by an auxiliary interferometer to assure proper sampling times and uniformity in the mirror speed by closed-loop feedback control.

The compensating plate is moved to a position adjacent to the beam-splitter.

The particular configuration of the interferometer (Figure 11) was chosen because of its inherent compactness, large light-gathering power, and design simplicity.

Radiation arriving within the field of view is divided by the beam-splitter into two components which recombine and interfere after reflections on the fixed and moving mirrors respectively. The recombined beam, focused on the detector, is modulated by the motion of the scan mirror proportional to the speed of the mirror and the wavenumber of the incident radiation. The output signal from the detector, called the interferogram, is the Fourier transformation of the spectrum of the incident radiation. The signal is amplified, digitized, and transmitted over the spacecraft telemetering system. On the ground, the spectrum is reconstructed by applying the inverse transformation. The original spectrum can be precisely reconstructed only within certain limits of accuracy of spectral range and of spectral resolution.

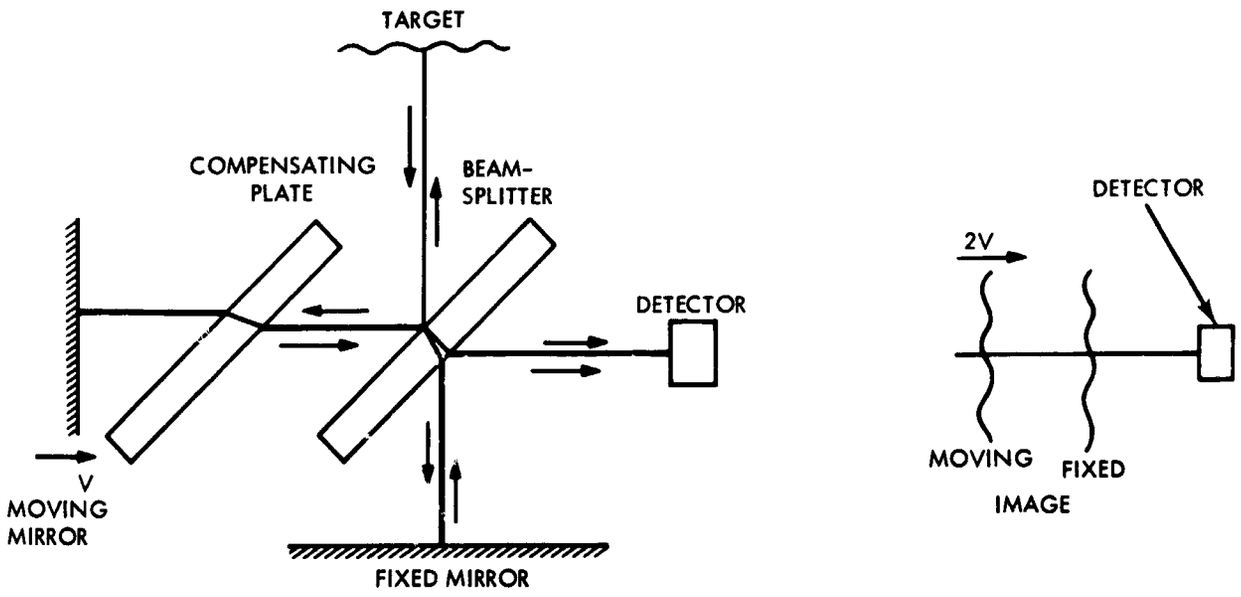

FIGURE 10.—Schematic operation of Michelson interferometer.

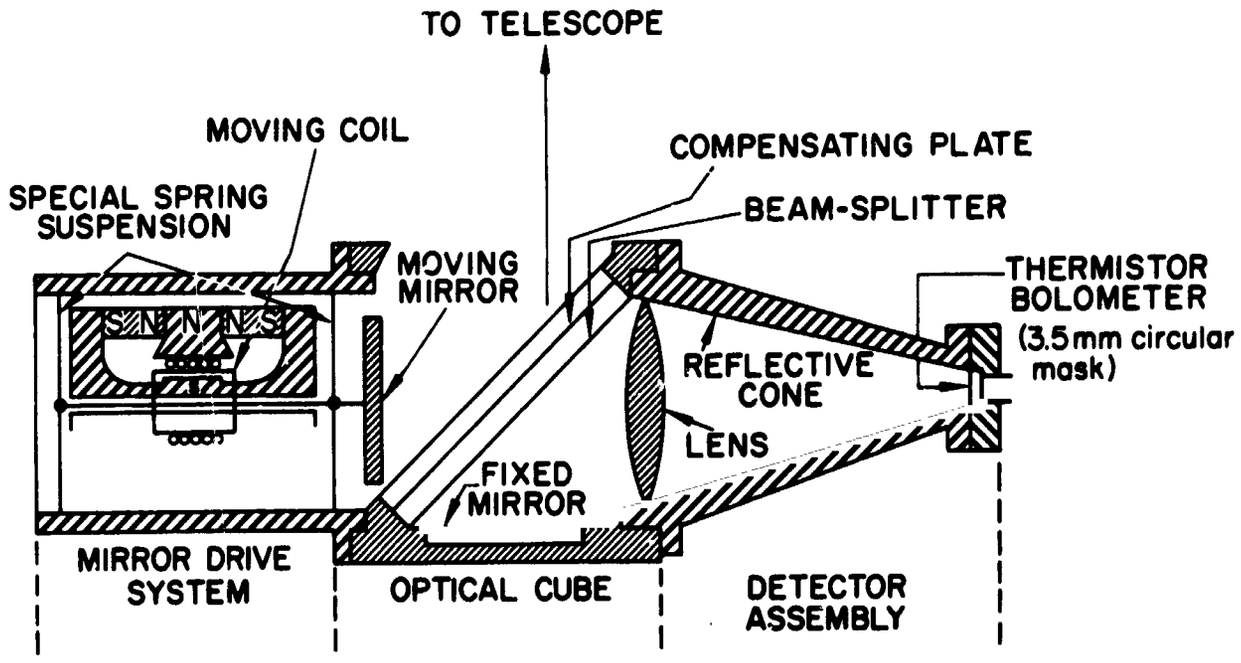

FIGURE 11.—Schematic diagram of interferometer cube, mirror drive system, and detector assembly.

3.1 Theory of Fournier Spectroscopy

Interference spectroscopy, first suggested by Michelson after the development of his original interferometer, was not pursued because of extreme computational difficulties, and further development was forced to wait upon the advent of electronics and high-speed digital computers. In the last decade, interference spectroscopy has made great advances; work has been reported by Fellgett (1958), Gebbie (1959), Mertz 1956), Connes (1961), Strong and Vanesse (1958–59), Loewenstein (1963),* and many others. Excellent summaries may be found in articles by Jacquinot (1960) and by Connes (1961).†

*References 12, 13, 14, 15, 16, 17, and 18.
†References 19 and 20.

The interferometer is shown schematically in Figure 10; the source of radiation will be an extended source which completely fills the field-of-view with radiation passing through the instrument without collimation. The output fringe pattern of the interferometer is focused on the detector, which is masked to eliminate all but the central fringe. The output of the detector is amplified and recorded as a function of path difference, d, between the fixed and movable mirror.

The relationship between the effective path difference, the order of interference, and the radiation wavelength is

$$m\lambda = 2d \cos \theta$$

where

d is the path difference between the two interferometer paths (cm)

m is the order of interference

λ is the wavelength (cm)

θ is the angle of an oblique ray through the interferometer.

This expression shows that, for a given monochromatic signal of wavelength λ, the circular fringe corresponding to a given order m expands away from the center of the pattern as the separation of the mirrors is increased. The detector is mounted behind the mask so that only the central fringe is detected; each spectral element is thereby modulated sinusoidally at a rate inversely proportional to its wavelength. As the source has an appreciable range of spectral elements, the signal detected will be the superposition of many modulated intensities multiplied by a parameter which is the "responsivity" of the system; i.e.,

$$\phi_x = \frac{1}{2}\int_0^\infty K_\nu N_\nu d\nu + \frac{1}{2}\int_0^\infty K_\nu N_\nu \cos 2\pi\nu x \, d\nu$$

where N_ν is the spectral radiance of the source (assumed to be the same at all parts of the field-of-view)

ν is the wavenumber, $\text{cm}^{-1}\left(\nu = \frac{1}{\lambda}\right)$

x is the instantaneous value of the effective path difference of the two beams of the interferometer (cm)

K_ν is a parameter which expresses the effective spectral responsivity of the interferometer, including the characteristics of the optics, the detector, and the electronic amplifiers

The interferogram is then taken to be

$$I_x = 2\left[\Phi_x - \frac{1}{2}\Phi(0)\right]$$

$$= \int_0^\infty K_\nu N_\nu \cos 2\pi\nu x \, d\nu,$$

which is the Fourier cosine transform of $K_\nu \cdot N_\nu$. The product $K_\nu \cdot N_\nu$ can be obtained uniquely from the measured interferogram, taking the inverse transform by digital computation. The relationship between N_ν and the product $K_\nu \cdot N_\nu$ will be established by laboratory calibrations; the validity of the laboratory calibrations is established by in-flight calibrations.

The true spectral distribution $K_\nu \cdot N_\nu$ is found only when the interferogram is recorded for an infinite range of x. For a finite range of x, each spectral component is spread out into a shape known as the instrumental profile. This profile also depends on the obliquity of rays through the interferometer, and thus on the solid angle of the field-of-view. The instrument profile may be modified as desired during computation of the transform; this process, called apodization, usually is done to remove secondary maxima at the expense of resolution. Including all these effects, the expression for the interferogram becomes

$$I_x = \int_0^\infty N\nu \cdot s(\nu, x) \cdot \cos\left[2\pi\nu x + \phi(\nu, x)\right] d\nu,$$

where

$$S(\nu, x) = s(\nu, x) \exp\left[i\phi(\nu, x)\right]$$

is the Fourier transform of the instrument profile (including the parameter K_ν mentioned previously).

The spectral distribution is again obtained by computing the Fourier transform of $I_{(x)}$. Reconstruction of the spectral distribution of the source

N_ν is obviously an approximation of the actual spectral distribution. This approximate solution (i.e., the transform of the interferogram) is the convolution of the actual spectral distribution with the instrument profile; therefore, it is mandatory to determine the form of the instrument profile. This can be done experimentally, because the instrument profile is the apparent spectral distribution given by a monochromatic source. This determination of the instrument profile is an important part of the laboratory calibrations.

Two factors which influence the instrument profile and reduce the quality of the data are the limitation arising from the finite path of the movable mirror, and the effect of oblique rays through the interferometer. The resolution limit imposed by the finite-path limitation is

$$R = \nu L \text{ or } \Delta\nu = \frac{1}{L},$$

(assuming linear apodization to remove secondary maxima in the instrument function). The resolution limit imposed by oblique-ray effects is

$$R\Omega = 2\pi, \text{ or } \Delta\nu = \frac{\nu\Omega}{2\pi}.$$

In the above, R is the resolution $\nu/\Delta\nu$, L is the maximum path difference on either side of zero path difference, and Ω is the solid-angle field-of-view of the interferometer.

Advantages of the Interferometer

An analysis by Jacquinot indicates that, where a source whose spectrum is defined by a radiance N_ν, having M spectral elements of interest, is to be analyzed with a resolution R in a time T with an optical system which is detector-noise-limited (as presently in the infrared), then the signal-to-noise ratio is increased by maximizing the time t of observation of each spectral element, the admissible solid angle Ω, and the transmission factor ϵ_ν (the optical efficiency).

An interferometer fulfills these requirements to a high degree. The time of observation is $t = T(m/M)$, where m is the number of spectral elements studied simultaneously. For an interferometer, m equals M, and m/M has the maximum value 1. The luminous energy received by the detector is $N_\nu \cdot A \cdot \Omega$. The quantities A and Ω can both be made large for an interferometer, as long as the resolution limitation $R\Omega = 2\pi$ is not exceeded (for comparison, the same resolution limit for a grating spectrometer is $R\Omega < 0.1$). The transmission factor ϵ is the only area where the superiority of the interferometer, may be questioned for a given application. The reflectivity and transmissivity of the beam-splitter is of primary importance and it may be difficult to obtain high efficiency from mechanically suitable materials in certain portions of the infrared spectrum.

3.2 Mechanical and Electromechanical Design

The instrument for the IRIS experiment consists of:

- interferometer (cube, detector, mirror drive system, preamplifiers)
- two auxiliary detectors, one for reflected solar radiation, the other for total thermal radiation
- telescope with calibration target (blackbody)
- electronics compartment, containing all electronic circuits except for the preamplifiers in the cube
- mechanical structure to receive the interferometer, the auxiliary detectors, the telescope, and the calibration target, and to provide mechanical strength and thermal protection

The electronics compartment, located separately, is connected to the interferometer and to the auxiliary detectors by a cable.

The mechanical design of the interferometer is modular. The drive unit, the fixed mirror assembly, the detector assembly, and the monochromatic reference source-detector combination are integral components attached to the optical cube, which houses the beam-splitter and provides mechanical strength and thermal conduction to all components.

The scan mirror is one of the most critical items in the design because it must be moved through a distance of 2 mm with a total angular rotation of less than 2 seconds of arc.

The use of parallel leaf springs to support the mirror was chosen in preference to slides on ways, or pivot-point mounts, since it avoids

frictional surfaces undesirable in space applications. The driving force is generated by an electrical current in a moving coil in a strong magnetic field. As Figure 11 shows, the magnetic gap is inside the dual-magnet design, thus minimizing residual magnetic fields on the outside.

Lack of uniformity in drive-mirror speed normally produces catastrophic effects on the wavenumber calibration of interferometers. A resolving power of 400 would require a drive-speed constancy of better than 1 part in 400. Two methods used to eliminate virtually all errors and uncertainties in the mirror motion, and in the subsequent wavelength calibration, are both based on the use of an auxiliary interferometer:

- A monochromatic source (0.5852 micron) feeds the interferometer and generates a sine wave at an auxiliary detector. The frequency of the sine wave is directly proportional to the speed of the mirror. An error signal, derived by a digital comparison of this frequency to a reference frequency generated by a clock, provides fine adjustment of the mirror-drive system. The speed of the drive mirror is therefore feedback-controlled.
- Sampling times of the interferogram are also derived from the reference frequency.

Actually, either of the aforementioned methods would suffice.

3.3 Optical Design

The optical design of the interferometer is conventional. The flat mirrors and the detector determine the limiting apertures. The condition of optimum solid angle $R\Omega = 2\pi$ is fulfilled at the highest wavenumber to be analyzed (2000 cm^{-1}, 5μ). The optimum angle is then 8 degrees (± 4 degrees) for a resolving power of 400 (5 cm^{-1} at 2000 cm^{-1}).

The fixed mirror and the scan mirror are made of gold-coated quartz polished to a flatness better than 0.1μ. Gold was selected because of its stability and its high reflectivity in the infrared. The two-axis mirror mount is machined from a single piece of metal. A differential screw which produces the fine adjustment required also anchors each adjustment plane at three points.

The condensing optic consists of a KRS–5 lens, combined with a gold-coated reflective cone which increases the effective detector area. Dimensions are chosen to provide the 8-degree optimum acceptable angle. This particular optic has sensitivity to almost 40μ, which will be important for the future development of the instrument in extending the long wavelength limit. The f-number of this system will approach the ideal limit of 0.5.

The bolometer in this design is essentially an integral part of the condensing optic. The detector is a 3.5-mm square masked to a circle of 3.5-mm diameter, having a time constant of 1 millisecond.

The beam-splitter is the most critical item in the optical train. All the rays make two passes through the beam-splitter; hence, all the losses arising in this unit are doubled. Although metallic beam-splitters are preferable from the standpoint of uniformity with wavelength, they have the serious disadvantage that an absorption loss from 25 to 35 percent occurs, depending on the metal used. Dielectric beam-splitters cannot be made uniform with wavelength, but over the wavelength span of interest the efficiency will be at least equal to that of a metallic splitter. The dielectric material selected is germanium, which has the additional advantage of being highly reflective for wavelengths shorter than 2μ so that most of the reflected visible radiation will not be collected.

The substrate material selected for the beam-splitter and the compensating plate is IRTRAN–4, basically a glass, which can be optically worked in the same fashion as any optical glass. This is a great advantage, because the beam-splitter must be flat to 1/10 wavelength of the shortest wavelength of interest. The principal disadvantage of IRTRAN–4 is its long wavelength cutoff at 20μ.

Other materials investigated for their suitability as beam-splitters (including KBr, KRS–5, CsI, and plastic pellicles) have higher transmission to long wavelengths, but are less suitable in other respects. Further investigations are in process.

The radiation source for the monochromatic reference signal will be the 0.5852μ neon line, which is quite strong; in conjunction with a suitable interference filter, the signal is suitably monochromatic. Neon was selected because lamps are available in small sizes and very little power is required. The focusing and condensing

optics are all glass of conventional and straightforward design. A silicon photovoltaic cell serves as a detector.

The telescope is designed to accept a beam of parallel radiation with an angular aperture of 2.8 degrees and to fill completely the 8-degree field-of-view of the interferometer. The primary and secondary mirror are electroformed for lightweight construction and then gold-coated.

3.4 Electronic Design

The electronic circuitry for the interferometer package is designed to operate as independently of the spacecraft as possible. The spacecraft supplies the power and command signals necessary to operate the experiment; the electronics subsystem of the experiment processes the interferometer data and presents them to the spacecraft in a digital format. The spacecraft supplies a single command at the beginning of each interferometer frame, but the necessary sequence of events to complete the data frame is generated by means of the interferometer system.

Functions of the interferometer electronics (Figure 12) are:

- To convert the 2400-cps 100v *p-p* spacecraft power into the voltages required to operate the interferometer instrument
- To provide the necessary power and control to drive the mirror
- To amplify the thermistor bolometer output signal
- To sample the bolometer signal, and to present it in digital form to the spacecraft

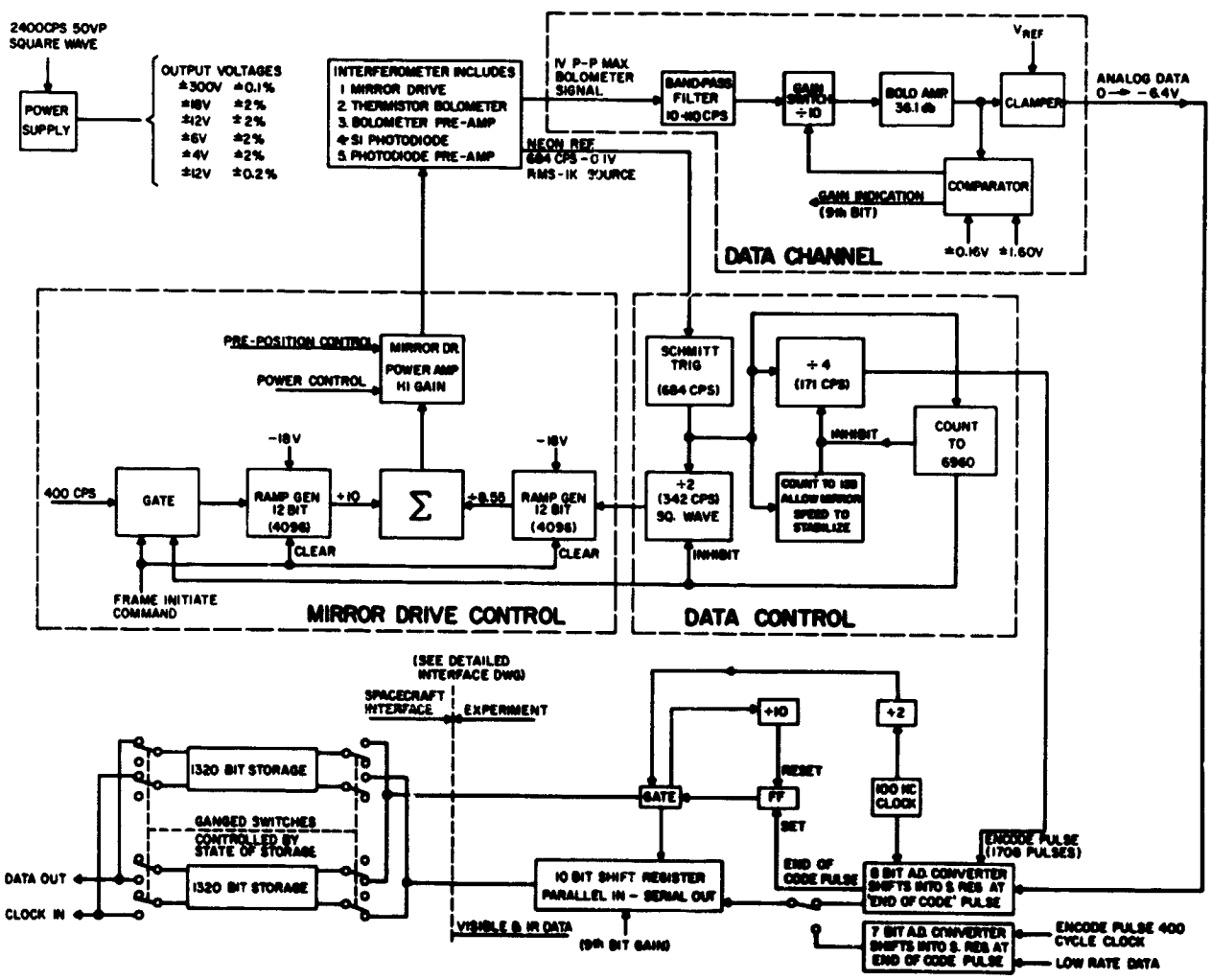

FIGURE 12.—Interferometer electronics, block diagram.

The power supply converts the 2400-cps 100v *p-p* spacecraft power to the voltage levels necessary for operating the interferometer. The power supply includes the necessary regulation (±5 percent) to maintain the voltage to the required accuracy. Three telemetry points are included to monitor:

- Spacecraft input voltage
- 300v ±0.1 percent bolometer bias supply
- 12v ±0.2 percent reference for mirror drive

The power supply is regulated to 1 percent by feedback to the primary of the power transformer; the 300-volt supply has an additional control that maintains 0.1 percent regulation.

The data channel receives the signal from the thermistor bolometer preamplifier. The signal is band-limited between 10 cps and 110 cps in an electrical filter network. This band-limited signal is then coupled to a switched attenuator and amplified.

The attenuator has two positions, controlled by the level of the preamplifier output voltage: 0–db attenuation and 20–db attenuation. The preamplifier output fed into a comparator generates an output to switch in the 20–db attenuator when the preamplifier output exceeds ±3.2 volts, and to switch out the attenuator when the signal falls below ±0.32 volts. The gain change is necessary to accommodate the extremely large dynamic range (2000:1) of the input signal from the bolometer preamplifier. The output of the bolometer preamplifier is maintained between 0 and 6.4 volts, a value which is compatible with the analog-to-digital converter.

The function of the data control channel is to:

- Provide the necessary encode pulses to the analog-to-digital converter at proper mirror positions
- Ensure that data points are not transmitted until the mirror velocity has stabilized
- Allow precisely 1708 data points for each data frame

The count-to-128 inhibits the encode pulse for a sufficient time to allow the mirror velocity to stabilize at 0.2 mm/sec. After 128 counts, the 171-cps squarewave is coupled to the analog-to-digital converter as encode pulses. The count-to-1708 circuit counts the number of encode pulses that have been applied to the analog-to-digital converter. After 1708 samples, the mirror drive circuit is de-energized and reset to zero, preparing the experiment for the next frame-initiate command from the spacecraft.

The analog-to-digital converter generates an 8-bit binary word from the bolometer amplifier output. The encode pulse from the data-control channel initiates the digital-to-analog voltage ramp that is compared with the analog voltage from the data channel. When the reference analog voltage matches the data voltage, the digital-to-analog circuit is stopped and the digital word transferred in parallel into the 10-bit shift register as the 8 least significant bits. The ninth bit is generated by comparator in the data channel designating the amplifier gain; the tenth bit is word synchronization.

At the end-of-code pulse, a gate is opened that allows the 50-kc clock to shift the 10-bit word serially into the spacecraft buffer storage. After 10 counts, the gate between the 50-kc clock and the 10-bit shift register is closed. The tenth bit in the shift register is used for synchronizing the data words in the ground stations.

An additional 7-bit analog-to-digital converter and a set of analog gates are included to sample the low data-rate channels. The analog-to-digital converters are sequentially switched into the spacecraft buffer storage system. The frame-initiate command switches the high data-rate channel into the spacecraft storage, and the end-of-frame pulse switches in the low data-rate channel.

The 400-cps spacecraft clock is coupled to the low data-rate commutator and the 7-bit analog-to-digital converter to serve as switching pulses and encode pulses.

The low data-rate channel contains the housekeeping telemetry and auxiliary measurements of the integrated visible and thermal radiation from the planet; these measurements are transmitted in real time as well as in the low data rate.

The function of the mirror-drive servo-loop is to maintain the mirror velocity constant at 0.2 mm/sec for the 10-second duration of the interferometer data frame. The control system consists of two digital-to-analog voltage ramp generators fed into a summing circuit that drives the mirror drive-power amplifier. The first ramp is a positive-going voltage generated from the 400-cps

spacecraft clock; the second ramp is a negative-going voltage generated from the 342-cps neon signal from the interferometer. The output voltages from the two digital-to-analog circuits are weighted so that no signal is applied to the mirror power amplifier when the mirror velocity is constant at 0.2 mm/sec. The loop characteristics of the servo stabilize the mirror velocity at 0.2 mm/sec ±1 percent within a fraction of a second after the frame-initiate pulse is received from the spacecraft. After the 1708 data points have been sampled, a pulse from the data-control circuit closes the gate between the 400-cps clock and the digital-to-analog circuits, and resets the counters in the digital-to-analog circuits to zero.

The electronics for the IRIS instrument are designed to perform the functions necessary to control the interferometer and process the data presentation to the spacecraft. The design consists primarily of digital electronics, because of the inherent reliability of digital systems. The digital circuits are constructed of Texas Instrument modules. This subsystem is a self-contained instrument requiring a minimum of external control for the operation of the experiment. A reliability survey will be conducted as one of the system evaluation parameters.

3.5 Signal-to-Noise Ratio

The peak signal falling on the detector (for zero path difference) is

$$P=\frac{1}{2}N\cdot A\cdot\Omega\cdot\epsilon,$$

where

P = radiant power (watts)

N = target radiance (watt cm^{-2} ster^{-1})

A = effective aperture (cm^2)

Ω = solid angle (ster)

ϵ = average optical efficiency

The factor ½ accounts for the 50-percent reflection losses inherent in this type of interferometer. The noise at the detector is given by the noise equivalent power (NEP) of a thermistor bolometer, which is approximately

$$NEP=1.6\cdot10^{-10}\sqrt{a}\sqrt{\frac{\Delta f}{\tau}},$$

where

a = area of detector (cm^2)

Δf = noise bandwidth (cps)

τ = detector time constant (sec)

Additional noise will be contributed by the compensating thermistor ($\sqrt{2}$), noise in the bias supply ($\sqrt{2}$), and preamplifier noise ($\sqrt{2}$). For operation at 260 or 270°K, the NEP is lower; however, this improvement will not be considered here.

The peak signal-to-noise ratio in the interferogram, for zero path displacement, is then

$$\frac{S}{N}=\frac{P}{NEP}\approx10^9NA\,\Omega\epsilon\sqrt{\frac{\tau}{2a\Delta f}}.$$

The signal power in the spectral interval $\Delta\nu$ will be approximately equal to the peak power P times the ratio $N_\nu\Delta\nu\epsilon_\nu/N\epsilon$. In addition, a signal-to-noise improvement factor proportional to $\sqrt{n/2}$ (n = number of samples per interferogram) is obtained; therefore,

$$\left(\frac{S}{N}\right)_{\Delta\nu}\approx10^9N_\nu\Delta\nu\epsilon_\nu A\cdot\Omega\sqrt{\frac{\tau n}{2a\Delta f}}.$$

Assuming reasonable numerical values for some parameters,

effective aperture $A=10$ cm^2

solid angle $\Omega=1.57\cdot10^{-2}(8°)$

optical efficiency $\epsilon\approx\epsilon_\nu=0.2$

detector time const. $\tau=1$ ms

detector area $a=.1225$ cm^2

number of samples $n=1708$

spectral element $\Delta\nu=5$ cm^{-1}

noise equivalent bandwidth $\Delta f\approx136$ cps

the peak signal-to-noise ratio becomes

$$\frac{S}{N}=2.5\cdot10^5N_\nu,$$

and for a spectral interval

$$\left(\frac{S}{N}\right)_{\Delta\nu}=3.6\cdot10^7N_\nu.$$

The instrument temperature (270°K) was chosen to give approximately equal signals for the maximum blackbody temperature to be measured (320°K), and for outer space (0°K), which is used as a check of calibration. The maximum radiance between 500 and 200 cm^{-1} is about $8 \cdot 10^{-3}$ watt cm^{-2} $ster^{-1}$ (320°K); therefore, the maximum signal-to-noise ratio is about 2000.

Within the spectral intervals, the signal-to-noise ratios depend largely on spectral radiance. A plot of the N_ν for various blackbody temperatures is shown in Figures 13 and 14; in both cases, the instrument is at 270°K. However, before the final signal-to-noise ratio can be discussed realistically, errors in the coding process must be taken into account.

The most efficient way to encode is to set one coding step equal to the rms value of the noise in the interferogram. Higher coding accuracy yields

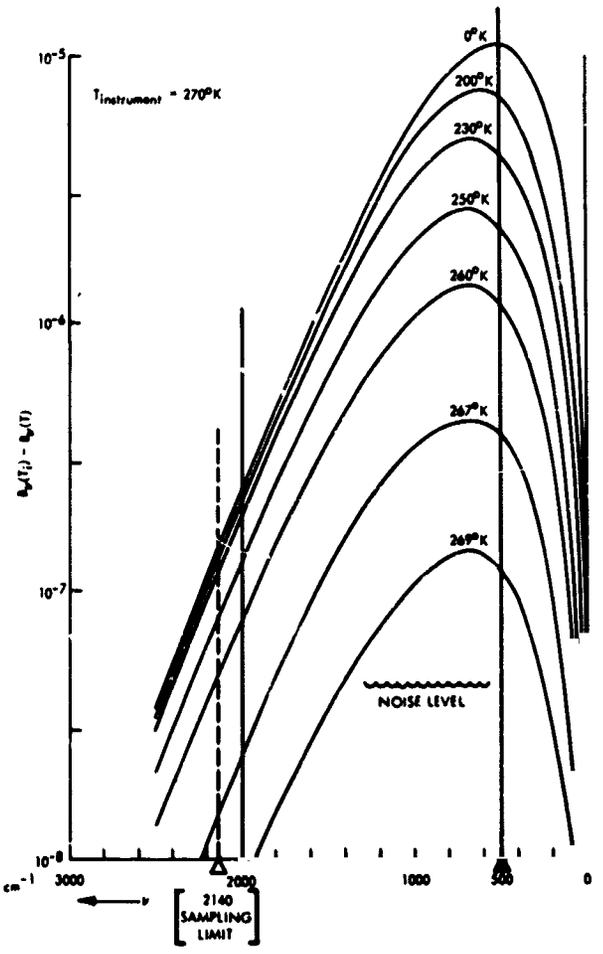

FIGURE 13. — Difference in spectral radiance of a target colder than the interferometer.

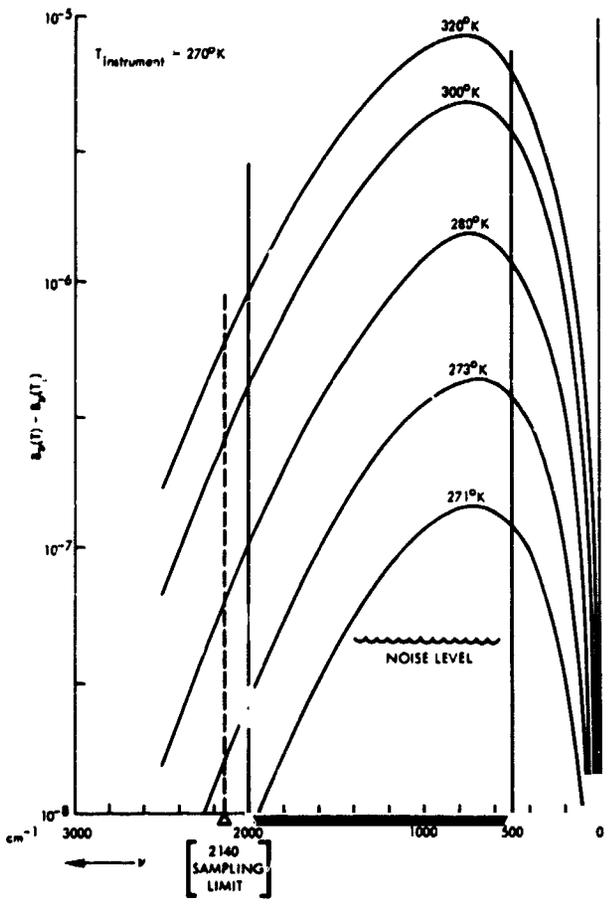

FIGURE 14. — Difference in spectral radiance of a target warmer than the interferometer.

insignificant improvement; lower coding accuracy is undesirable. If encoding is performed to 1 part in 2000 of the maximum possible amplitude in the interferogram, the uncertainties introduced by the coding process will equal errors caused by detector noise. The final signal-to-noise value, including the coding error, becomes

$$\frac{S}{N} = 1.7 \cdot 10^{3} N \text{ and } \left(\frac{S}{N}\right)_{\Delta\nu} = 2.5 \cdot 10^{7} N_\nu.$$

A $(S/N)_{\Delta\nu}$ equal to unity is obtained for $N_\nu = 4 \cdot 10^{-8}$. This value is indicated in Figures 13 and 14. A temperature difference of 1°K should therefore be detectable below 1400 cm^{-1} (above 7 microns); at 1800 cm^{-1} (5.5 microns), 3°K corresponds to the noise, and at 2000 (5 microns) only about 6°K.

These numbers were derived for 5 cm^{-1} resolution. Clearly, numerical smoothing techniques

can be applied and resolving power can be traded against accuracy. This operation is done on the ground after the interferogram has been received, so that considerations of this nature do not influence the design of the instrument.

It remains to be shown how a signal-to-noise ratio of 2000 can be obtained in the coding process. The large central peak in the middle of most interferograms is very pronounced; in most cases, the amplitudes in the rest of the interferogram are considerably smaller. An 8-bit word is used to encode on a scale of plus and minus 128 levels, or a total of 256. One level is equal to the rms value of the noise. Larger amplitudes are divided by 10 electronically and then encoded. The position of the divide-by-10 circuit is indicated by a ninth bit. This effective dynamic compression maintains full accuracy for most points in the interferogram, but only one-tenth of the full accuracy for all points exceeding a tenth of the maximum possible amplitude. However, the one-tenth value in amplitude is exceeded for only a very small number of data points, compared to the total of 1708 points. The slightly reduced accuracy of a few data points can be shown to have negligible influence on the reproducibility of the spectra.

3.6 Auxiliary Measurements

A number of auxiliary measurements will be performed to facilitate better interpretation of the interferograms and to validate the operation of the instrument.

Reflected Solar Radiation

Reflected solar radiation between 0.5 micron and about 1 micron will be measured by a small radiometer, bore-sighted with the optical axis of the interferometer and having the same field-of-view as the interferometer. The purpose of this measurement is to allow correlation of dark and bright areas on the planet with the interferograms. This instrument will use a silicon cell as a detector, with a time constant of about 10 seconds. A 2-percent relative accuracy and a 10-percent absolute accuracy are sufficient for this measurement.

Thermal Radiation

Also bore-sighted with the interferometer will be a thermopile having the same spectral response and the same field of view as the interferometer. The purpose of this instrument is to furnish additional calibration of the interferometer during planetary encounter. The time constant of this instrument will also be 10 seconds. A 2-percent relative accuracy are likewise sufficient for this measurement.

Temperature Sensors

Various temperatures will be measured in the optical cube (the temperature of the bolometer mounting, the drive mirror, the beam-splitter mounting, and a point near the entrance aperture) with an accuracy of 0.5°C. These temperature measurements will aid in the proper interpretation of the interferograms. In addition, the temperature of the primary and secondary mirror will be monitored (±5.0°C). The blackbody used for calibration purposes before and after planetary encounter will be monitored by two lead thermistors to provide redundancy in this measurement. Twelve temperature sensors are provided, including the two temperature sensors in the auxiliary radiometers and the two sensors located in the electronics compartment.

Voltage Measurements

A number of important voltages and execution commands will be monitored to certify proper operation of the instrument. The measured voltages include the bolometer bias voltage, the main power in the optical cube (−12 and −18 volts), and other strategically important voltages in the electronics compartment. A total of 25 auxiliary measurements will be performed.

4. DATA REDUCTION

Computational efforts concerned with the IRIS experiment fall into two major categories: computer simulation of the interferogram, and subsequent analysis to retrieve the optimum amount of information from the received data. The artificially synthesized interferograms will serve as aids for signal-to-noise requirements and in verifying the encoding and digitizing techniques to be applied, as well as in furnishing the basis for the early development of the data analysis techniques to be used. The synthesis of the interferograms has been divided into two phases and the analysis of the data into three phases.

4.1 Synthesis

The purpose of this portion of the study is to simulate the interferogram in order to study the effects of various levels of detector noise, to analyze the possible methods of digital encoding, and to determine the total effect on the ability to recover the underlying frequencies of interest.

The objective of the first phase of the study is a computer program which generates (for specified wavenumbers, instrument and target temperatures, time duration, and sampling rates) the amplitudes of a Fourier series (interferogram) according to the basic instrument characteristics. All computer outputs are formatted, if desired, for plotting offline on an x-y plotter. This part of the program has been completed, and artificial interferograms which were constructed have played an important role in the initial design of the digitization scheme for the instrument.

The first step of the second phase of the interferogram synthesis program is to include the instrument function. The second step is to generate and apply any desired level of detector noise to the signal. The third step is to apply several scaling techniques to find the best one, which will then be used for the actual instrument. Finally, the digitized version of the interferogram will be formatted to become identical to the output of the physical instrument. The result—the final, simulated interferogram—is again formatted for offline plotting.

4.2 Analysis

The analysis program is being developed concurrently with the synthesis program, because it is essential that the actual interferogram provide the best possible analysis of the data, and of the information extracted. In order to accomplish this, the synthesis and analysis process must be a "closed-loop" learning and improvement system. The resulting analysis program should, therefore, be one which is best fitted to analyze the data from the actual instrument.

The purpose of the first phase of the analysis program is to apply the inverse of the "second-order" effects of the synthesis program; that is, given an interferogram in digital form, the inverse operations of scaling digitizing must be applied, and an apodization function applied, before the frequency analysis is begun.

The second phase of the analysis consists of performing a general Fourier analysis to determine the individual frequency components contributing to the overall composite signal. The Fourier analysis is carried out using both cosine and sine terms.

As a third phase, refinements in the analysis are comtemplated. A spectral analysis typically consists of resolving ambiguities and questions that usually cannot be answered by a single analytical technique. The third phase is devoted to the study and development of techniques to be used instead of (or in addition to) the classical, generalized Fourier analysis mentioned above. Techniques to be investigated include auto-regressive analysis—to be used in conjunction with stepwise Fourier analysis—and digital bandpass filters, based on the Laplace transform.

5. INSTRUMENT CALIBRATION

To verify the proper operation of the instrument and to assure accuracy in the received data, an in-flight calibration technique will be used. Following is a summary of the final calibrations to be performed on earth, prelaunch check-of-calibration procedures, and in-flight calibration requirements.

5.1 Primary Calibration

The primary calibration and check of performance of the instrument will be carried out in a vacuum chamber with cryogenic walls at liquid N_2 temperature. The thermostat of the instrument will maintain the proper operating temperature of about 270°K in the optical cube. A blackbody will be placed in the field-of-view whose temperature can be adjusted between +80°K and +320°K. Interferograms will be taken at 10°K increments. Adjustments of gains, thresholds, etc., will be set at this time. Calibration with the instrument's own reference blackbody will also be checked at this time.

Spectral calibration and resolution will be checked by two methods: First, a polyethylene sheet will be inserted in front of the blackbody in vacuum. Polyethylene has numerous absorption bands of precisely known wavelengths. Second, while in air (or in a chamber with walls and instrument at room temperature), a blackbody at a distance of about 10m (1 m in the CO_2 chamber) will be kept 10 to 20 degrees above the instrument

temperature. The strong Q branch of the 15μ CO_2 band, which should be clearly observable in absorption, serves as a wavelength standard. As the mirror speed is derived from the 0.5852-micron neon reference line, this test will verify only proper scan speed. Adjustments will not be necessary.

The field-of-view of the instrument with respect to the mounting interface will be measured on an optical bench. The interferometer will not be operated in the conventional sense for this measurement; the output of the thermistor bolometer will be monitored while a chopped, high-intensity source is moved at a fixed distance. The response will be mapped as a function of the angular position of the source.

5.2 Calibration Checks During Environmental Tests

Before and after vibration, during vacuum thermal tests, etc., check of calibration are performed by exposure to blackbodies. In air, blackbodies above room temperature are used; in vacuum tests, blackbodies above and below operating temperatures (+80°K to 320°K). Also, exposure to the electrically-heated reference blackbody which is part of the instrument is performed regularly.

The spectral response is checked by placement of filters (polyethylene or mylar) in front of a blackbody.

The field-of-view is checked in air only, by exposure to a small hot source placed in front of a room temperature background. Readout takes place in the normal operation mode of the interferometer.

5.3 Check of Calibration in the Launch Area and on Launch Pad

Exposure to the electrically heated, thermostatically controlled reference blackbody will serve as the check of calibration.

5.4 Check of Calibration During Interplanetary Flight

Two complete interferometer frames will be required for each check of calibration. During the first frame, the reference blackbody will be placed within the field-of-view; this is the normal position of the reference blackbody during flight. The second calibration frame will be taken without the blackbody, with the interferometer viewing outer space. After this, the blackbody will be returned into its normal stowed position. In-flight calibration is required at regular intervals of 15 or 30 days, except during the first week, when one calibration every other day is required.

5.5 Calibration at Planetary Encounter

Shortly before and shortly after planetary encounter, a sequence of two calibration frames is required. The pre-encounter calibration should be as close as possible before encounter but definitely not earlier than 1 hour before. Both pre-encounter calibration frames and post-encounter frames should be stored and transmitted together with the data frames. After encounter, the sequence of the calibration frames will be reversed: first, the sky background will be measured as the planet moves out of the field-of-view of the instrument; then the reference blackbody will be brought in, and the final calibration frame will be taken. Thereafter no further data will be required from the interferometer.

6. MISSION PROFILE

6.1 Planetary Transfer

If possible, the instrument will be launched and stowed in the "power on" position. All circuits will be energized and the scan mirror placed in the midrange neutral position. The calibration target (blackbody) will be in front of the telescope so that it seals the instrument thermally; in this position, the blackbody will protect the optical elements during launch and will minimize the heater power necessary to maintain the proper operating temperatures of the instrument (270°K) and the blackbody (285°K). Total electrical power required during this time will not exceed the power required during the data-gathering period (approximately 7 watts). Check of calibration is performed at regular intervals as discussed in 5.4.

The following command and readout sequence constitutes the in-flight calibration:

- Frame-initiate command to obtain one interferogram of the reference target
- Command to move the blackbody out of the field-of-view of the telescope

- Frame command to obtain an interferogram of outer space
- Command to return the blackbody to the normal position in front of the telescope

6.2 Planetary Encounter Mode

The planetary encounter mode consists of calibration before and after encounter, as discussed in 5.5, with an intervening data-gathering period. The following sequence of commands and events constitutes the encounter mode:

- Frame-initiate command to obtain one interferogram of the reference target
- Command to move the blackbody to a position which will clear the field-of-view of the telescope
- Frame command to obtain an interferogram of outer space
- Frame command at least every 30 seconds (or, if possible, every 15 seconds) during planetary encounter
- Frame command after the planet has left the field-of-view
- Command to return the blackbody to the normal position in front of the telescope
- Frame-initiate command to obtain interferogram of reference target

After the encounter mode, the data-gathering part of the experiment will be completed and electrical power may be removed from the instrument.

6.3 Other Experiment Considerations

- Trajectory—No special requirements
- Fly-by distances—A fly-by distance of 2000 km (closest approach to surface) would be most desirable; at this distance, the interferometer can be used without a telescope. Presently the telescope is designed to cover the range between 5000 and 10,000 km. An approach distance between 10,000 and 20,000 km would also be acceptable, but would require a new (larger) design of the telescope.
- Fly-by velocity—Low fly-by relative velocity is desirable primarily to minimize the spatial smear during the 10-second time required for each interferogram.
- Aiming point—The aiming point should be chosen to fulfill the following conditions, listed in sequence of importance:
  (1) Equal chance to observe "dark" and "bright" areas of Mars
  (2) View of the subsolar point and equatorial regions
  (3) Scan across the terminator (morning terminator preferred)
  (4) Observe primarily the illuminated portion of Mars, but to have a chance to see part of the dark side also
- Magnetic cleanliness—No special requirements
- Electrical noise—Only the output circuit of the bolometer and the input to the preamplifier would be sensitive to stray electrical fields. Care will be taken to have proper shielding. The rest of the circuit, which is digital, should be insensitive to stray electrical fields. The noise level which can be tolerated at the electrical interface will be small, but numerical values cannot be specified at this time.
- Acoustical and structural noise—During the 10-second periods of data collection or calibration, the platform should not be exercised. The normal motion of adjustment (hunting) of the spacecraft's control system should not provide problems. The effect of structural noise is not fully known at this time, and specifications of the vibrational environment to which the instrument will be exposed on the spacecraft are urgently needed.
- Interaction and coordination with other experiments—It is strongly suggested that all radiometric experiments be bore-sighted to allow cross-correlation among the data obtained. Simultaneous ground-based observations should be encouraged.
- Spacecraft engineering measurements—No engineering measurements are required from the spacecraft. All auxiliary measurements are part of the interferometer experiment.

7. EXPERIMENT-SPACECRAFT INTERFACE

The interface between the experiment and the spacecraft (Figure 15) consists of power input, commands, clock pulses and data signals.

The frame-initiate commands supplied by the spacecraft consist of pulses occurring every 30 or 15 seconds after planet acquisition. The pulse should be about 2 milliseconds in duration and +2 volts in amplitude, with a risetime of about 10 microseconds from a source impedance of about 100 ohms.

The end-of-frame command supplied by the experiment and coupled into the spacecraft is a pulse with an amplitude of 2.5 volts, and a risetime of less than 5 microseconds from a source impedance of about 5K ohms.

The 400-cps clock consists of pulses of a 4-volt amplitude with a 0.3-microsecond risetime and a source impedance of about 100 ohms.

The 50-kc clock coupled from the experiment to the spacecraft will have a source impedance of about 100 ohms and an amplitude of 2.5 volts. The risetime will be on the order of 1 microsecond.

Data output from the experiment will consist of a series of 10-bit digital words, a "one" corresponding to +2.5 volts and a "zero" corresponding to 0 volts. The source impedance in the data channel is 5K ohms.

The real-time data from the thermal and visible channel will consist of a pulse-width about 10 microseconds in duration, with an amplitude of +2.5 volts and a 1-ms risetime.

Design Parameters for Infrared Interferometer

Spectral range	2000–500 cm^{-1} (5–20μ) (possible extension to 300 cm^{-1} (33μ)
Spectral resolution	5 cm^{-1} over total range
Travel of drive mirror	0.2 cm
Diameter of effective aperture	3.6 cm
Dectector	Thermistor bolometer in conical light pipe
Detector time constant	1–2 ms
Duration of interferogram	10 sec
Electrical frequencies at detector	20–80 cps
Sampling	Every fourth fringe of monochromatic source 5852.5 Å
Sampling rate	171 samples sec^{-1}
Samples per interferogram	1708

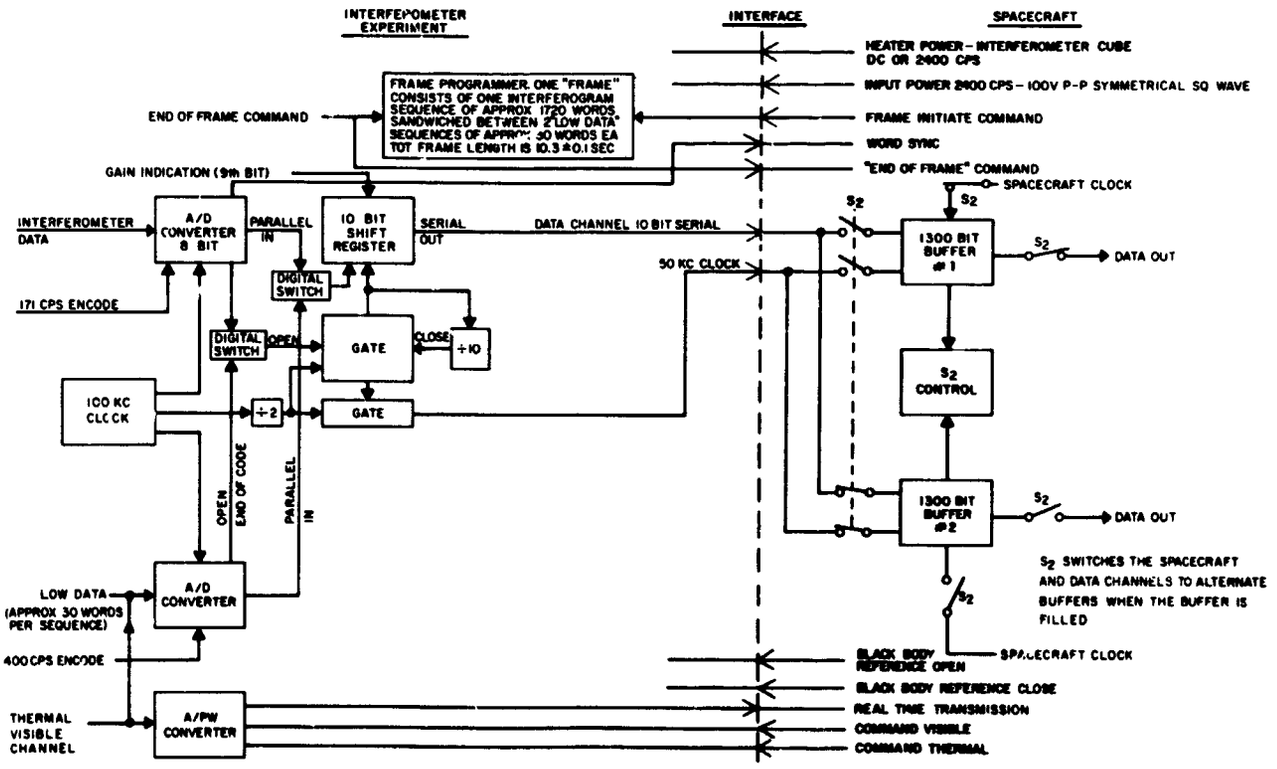

FIGURE 15.—Spacecraft-experiment interface.

Housekeeping information	25 samples per interferogram
Samples per frame	1733 samples
Frame synchronization	3 words
Words per frame	1736
Bits per word	10
Bits per frame	17360
Calibration frames in vincinity of planet	4
Minimum number of data frames for minimum fly-by speed	40 (every 30 sec) 80 (every 15 sec)
Total number of frames	44 (for 30-sec interval) 84 (for 15-sec interval)
Total number of bits to be stored	$.765\times10^6$ (for 30-sec interval) 1.46×10^6 (for 15-sec interval)
Field-of-view of interferometer	1.57×10^{-2} ster ($\sim8°$)
Field-of-view with telescope	2×10^{-3} ($\sim2.8°$) (approx. circle of 250 km diameter at 5000 km)
Calibration during interplanetary flight before and after planetary encounter	
a. space	
n. blackbody	
Monochromatic source	Neon lamp plus interference filter
Monochromatic wavelength	5852.5 Å
Detector for monochromatic light	Silicon junction
Frequency of reference signal	684 cps

REFERENCES

1. Hanel, R. A., and Bartko, F., Radiative Equilibrium in Planetary Atmospheres, NASA TN-G569 (1964).
2. Kuiper, G. P., ed., "The Atmospheres of the Earth and Planets," University of Chicago Press (1952).
3. Sinton, W. M., An Upper Limit to the Concentration of NO_2 and N_2O_4 in the Martian Atmosphere. *Publ. Astron. Soc. Pacific.*, Vol. 73, p. 125 (1961).
4. Kaplan, L. D., "The Spectroscope as a Tool for Atmospheric Sounding by Satellites," *Inst. Soc. of Amer. Conf.* (Sept. 1960).
5. Wark, D. Q., "On Indirect Soundings of the Stratosphere from Satellites," *J. Geophys. Res.*, Vol. 66, p. 77 (1961).
6. Yamamoto, G., "Numerical Methods for Estimating the Stratospheric Temperature Distribution from Satellite Measurements in the CO_2 Band," *J. of Meterol.*, Vol. 18, p. 581 (1961).
7. King, J. I. F., "Meterological Inferences from Satellite Radiometry, I," *J. Atmos. Sci.*, Vol. 20, p. 245 (1963).
8. Fleming, H., Twomey, S., and Wark, D. Q., "The Inference of the Vertical Distribution of Atmospheric Parameters from Spectral Measurements," paper presented at the 25th national meeting of the Amer. Meteorol. Soc., Los Angeles (Jan. 1964).
9. Kuiper, G. P., paper presented at 45h American Geophysical Union meeting, Washington, D. C. (April 1964).
10. Lyon, R. J. P., Evaluation of Infrared Spectrophotometry for Compositional Analysis of Lunar and Planetary Soils. NASA Contract (NASA-49/04) Quarterly Status Report No. 4, Stanford Research Institute (June 1963).
11. Bell, E. E., and Eisner, I. L., Infrared Radiation from the White Sands at White Sands National Monument, New Mexico. *Jour. Opt. Soc. of Amer.*, Vol. 46, p. 303 (1956).
12. Fellgett, P., Spectrometric Interferential Multiples Power Measures Infra-Rouges sur les Etoiles. *J. d'Physique et la Rad.*, Vol. 19, p. 237 (1958).
13. Gebbie, H. A., *J. Phys. Radium*, Vol. 19, p. 230 (1959).
14. Mertz, L., *J. Opt. Soc. Amer.*, Vol. 46, p. 548 (1956).
15. Connes, J., *Rev. d'Opt.*, Vol. 40, p. 45, 101, 151, 213 (1961).
16. Strong, J., *Concepts of Classical Optics*, W. H. Freeman and Co., San Francisco (1958).
17. Strong, J., and Vanesse, G. A., Interferometric Spectroscopy in the Far Infrared. *J. Opt. Soc. Amer.* Vol. 49, p. 844 (1959).
18. Loewenstein, E. V., On the Correction of Phase Errors in Interferograms. *App. Optics*, Vol. 2, p. 491 (1963).
19. Jacquinot, P., *Reports on Progress in Physics*, Vol. 23, p. 263 (1960).
20. Connes, J., Recherches sur la Spectroscopie par Transformation de Fourier. *Rev. d'Opt.*, Vol. 40, pp. 45, 101, 157, 213 (1961).

See also:

Öptik, E. J., The Atmosphere and Haze of Mars, *J. Geophys. Res.*, Vol. 65, p. 3057 (1960).

Rea, D. G., and Welch, W. J., The Reflection and Emission of Electromagnetic Radiation by Planetary Surfaces, *Space Science Review*, Vol. 2, p. 558 (1963).

Steel, W. H., Interferometers Without Collimation for Fourier Spectroscopy. *J. Opt. Soc. Amer.* Vol. 54, p. 151 (1964).

De Vaucouleurs, G., Physics of the Planet Mars, Faber and Faber, London (1954).

Kiselev, B. A. and Parshin, P. F., Some Distortion in Fourier Spectroscopy. *Opt. i. Spektr.*, Vol. 12, p. 311 (1961).

Meissner, K. W., Interference Spectroscopy. *J. Opt. Soc. Amer.*, Vol. 31, p. 405 (1941).

Strong, J., Interferometry for the Far Infrared. *J. Opt. Soc. Amer.*, Vol. 47, p. 354 (1957).

Kuiper, G. P., "Planets and Satellites," Vol. 3 of The Solar System (Kuiper, G. P. and Middlehurst, B. M., ed.), Chicago: Univ. of Chicago Press (1961).

Urey, H. C. "The Atmosphere of the Planets" in Handbuch der Physik (S. Fluegge, ed.), V. 52:363–418, Berlin: Springer-Verlag (1959).

Sagan, C., and Kellogg, W. W., "The Terrestrial Planets," *Ann. Rev., Astron. Astrophys.*, 1:235–266 (1963).

RADIATIVE EQUILIBRIUM IN PLANETARY ATMOSPHERES. I. APPLICATION OF THE STRONG LINE ABSORPTION LAW TO THE ATMOSPHERE OF VENUS*

RUDOLF A. HANEL AND FRANK BARTKO

The interpretation of the data obtained for Venus in the $8-12\mu$ atmospheric window clearly requires some knowledge of the temperature distribution in the planet's upper atmosphere. For this purpose temperatures, net fluxes, and specific intensities were calculated for a CO_2-N_2 atmosphere in radiative equilibrium. The wavelength, temperature, and pressure dependence of the CO_2 absorption, including the excited bands, was considered. Solar radiation absorbed in the clear atmosphere influences the temperature profile distinctly. The effects of various CO_2 concentrations, cloud top pressure levels, and cloud reflectivities on the equilibrium temperatures are also discussed.

LIST OF SYMBOLS

$\bar{A}_i$	Fractional absorptance in the wavelength interval i.
$B_\nu(T)$	Planck function at temperature T (watts cm^{-2} $ster^{-1}$ wave $number^{-1}$).
c	Subscript denoting cloud surface.
$E_n(\tau)$	Exponential integral of order n.
$\pi F_\nu(\tau_\nu)$	Spectral total flux at τ_ν (watts cm^{-2} wave $number^{-1}$).
H	Pressure scale height (H_0=value at 273°K).
i	Index denoting wave number interval.
$I_\nu(\mu, \tau_\nu)$	Specific intensity (watts cm^{-2} $ster^{-1}$ wave $number^{-1}$).
j	Index denoting vertical coordinate.
$J_\nu(\tau_\nu)$	Spectral mean intensity at optical depth τ_ν (watts cm^{-2} wave $number^{-1}$ $ster^{-1}$).
l_ν	Generalized absorption coefficient, $l=m^n$ (cm^{-1} NTP).
m	Parameter defined in Equation 19.
n	Exponent defined in Equations 2 and 19.
P	Pressure (P_0=1 atm).
q	CO_2 volume concentration.
r_{ic}	Cloud reflectivity in wave number interval i.
s	Geometric path length (cm).
S_ν	Solar constant in wave number interval 18 (watts cm^{-2}).
t	Integration variable.
T	Atmospheric temperature (T_0=273°K).
u	Path length of active gas at NTP (cm).
u*	Modified pressure- and temperature-reduced path length (cm). See Equation 16.
X	Parameter proportional to the product of the spectral line intensity and the ratio of path length to line half width.
α	Flux convergence criterion (Equation 40).
β	Parameter proportional to the ratio of the spectral line half-width to the average line spacing.

*Published as *NASA Technical Note* D-2397, August 1964; also presented at the Conference on Atmospheric Radiation, Eppley Laboratories, Newport, R. I.

γ Exponent describing the temperature dependence of excited bands (Equation 13).

$\epsilon_{\nu 0}$ Spectral emissivity of cloud surface.

ζ Cosine of the solar zenith angle.

μ Direction cosine ($\mu = \cos\theta$).

ν Wave number (cm^{-1}).

ρ Atmospheric density.

$\tau_{\mu\nu}$ Optical thickness in direction μ at wave number ν.

ω Solid angle (ster).

INTRODUCTION

The structure of a planet's atmosphere is governed primarily by convective and radiative energy transport. On the earth, convective processes preponderate in the troposhpere and radiative processes in the stratosphere. Similarly, the atmospheres of Mars and Venus should exhibit zones of convective and radiative transfer. Convection probably characterizes the Venus atmosphere below the cloud level, especially if the clouds consist of dust particles, whereas the region above the cloud layer is probably dominated by radiative transfer. The interpretation of infrared measurements of the atmospheres of the terrestrial planets must, therefore, be based on the theory of radiative transfer and appropriately modified for convection where necessary. The objectives of the program discussed in this paper were to establish an analytical tool for the study of planetary atmospheres based on the radiative transfer theory. An initial version of this program has been applied to the atmosphere of Venus. This application must be used with relatively inaccurate estimates of physical parameters which influence the solution of the transfer equation. However, the program permits a parametric study where the number of possible solutions is ultimately restricted by observational constraints.

The equilibrium temperature distribution of an N_2–CO_2 atmosphere was calculated for several volume concentrations of CO_2. The wavelength, temperature, and pressure dependence of the absorption coefficients was taken into account. The effect of direct and diffusely reflected solar radiation absorbed by the atmosphere was also included. An effective surface emissivity was introduced as an additional parameter and permitted a deviation from the usual assumption that the surface radiates like a blackbody in the infrared. In addition to the radiative equilibrium temperatures, the specific intensities were calculated. Net fluxes were obtained by angular integration, taking into account fully the dependence of the intensity on direction. The simplifying procedure of converting parallel beam radiation to an equivalent diffuse radiation field was avoided (References 1–3).

The net flux of a planet can be determined independently from the heat budget by considering the observed albedo and the appropriate value of the solar constant. This restricts the number of theoretically possible solutions, since only those which yield total flux values consistent with the albedo can be admitted. The number of solutions can be restricted further by a comparison of calculated and measured values of the specific intensity at several wavelength intervals and zenith angles.

In the discussion below, the assumptions and limitations of the calculations are stated and the mathematical formulation is presented. An illustration of the effects of the various parameters on the temperature profiles follows, but further conclusions will be discussed elsewhere.

SOLUTION OF THE RADIATIVE TRANSFER EQUATION

In order to calculate the equilibrium temperatures in a finite, nongrey, optically thick atmosphere, the equation of radiative transfer must be solved, subject to appropriate boundary conditions (Reference 4, for example). The assumption of radiative equilibrium holds as long as the atmosphere is stable against convection (Reference 5, for example). Stability, in turn, is maintained as long as the temperature gradient is everywhere less than the adiabatic gradiet.

For the particular application considered here, the surface is taken to be the cloud tops and is assumed to be the demarcation between regions of energy transport dominated by radiation and convection. It is realized that the assumption of a solid surface for the clouds is a severe simplification. A more rigorous treatment would apply

the theory of radiative transfer for a scattering medium (Reference 6, for example).

For an atmosphere in local thermodynamic equilibrium the equation of transfer is

$$\frac{dI_\nu(\mu, \tau_{\mu\nu})}{d\tau_{\mu\nu}} = I_\nu(\mu, \tau_{\mu\nu}) - B_\nu(T) \quad (1)$$

where $B_\nu(T)$ is the Planck function and $I_\nu(\mu, \tau_{\mu\nu})$ the specific intensity of the radiation field. For radiative transfer calculations dealing with strong molecular band absorption, the optical thickness $\tau_{\mu\nu}$ can be expressed

$$\tau_{\mu\nu}(l_\nu, u^*, \mu) = l_\nu \left(\frac{u^*}{\mu}\right)^n = \frac{\tau_\nu(l_\nu, u^*)}{\mu^n} \quad (2)$$

where l_ν is a generalized absorption coefficient and u^*/μ a pressure- and temperature-reduced path length. It is convenient to use the optical path in the vertical direction, τ_ν, and the direction cosine μ, instead of the optical path, $\tau_{\mu\nu}$, in an arbitrary direction. The appearance of μ under the exponent n has a significant influence on the transfer problem. The value of n is unity for weak line or grey absorption and one-half or less for the square root or strong line absorption law (Reference 7). In contrast to weak line or grey absorption, the strong line absorption law reduces the thermal coupling between adjacent atmospheric layers and permits a more effective exchange of radiative energy over greater optical distances.

Very general boundary conditions have been selected. At some optical depth, $\tau_{\nu c}$, the atmosphere is assumed to be bounded by a perfectly diffuse reflector of effective emissivity $\epsilon_{\nu c}$, related to the surface reflectivity by

$$\epsilon_{\nu c} = 1 - r_{\nu c} \quad (3)$$

For positive values of μ this assumption requires the solution of Equation 1 at the boundary $\tau_{\nu c}$ to be

$$I_\nu^+(\tau_\nu = \tau_{\nu c}) = \epsilon_{\nu c} B_\nu(T_c) + r_{\nu c} F_\nu^-(\tau_{\nu c}) + \frac{S_\nu}{\pi} \zeta r_{\nu c} e^{-\frac{\tau_{\nu c}}{\zeta^n}} \quad (4)$$

The first term on the right represents the thermal emission by the surface of temperature T_c. The second term arises from the nonblack characteristic of the surface; the downward flux incident on the surface is partially reflected back into the atmosphere. The third term describes the reflected solar component.

At the top of the atmosphere where $\tau_\nu > 0$ only solar radiation is assumed incident. For thermal radiation outer space is considered a perfect sink. Hence the upper boundary condition is

$$I_\nu^-(\zeta, \tau_\nu = 0) = \frac{S_\nu}{\pi} \zeta \quad (5)$$

The solution of the transfer equation subject to the boundary conditions and the absorption law for τ_ν may be verified to be

$$I_\nu^+(\mu, \tau_\nu) = \epsilon_{\nu c} B_\nu(T_c) e^{-\frac{\tau_{\nu c} - \tau_\nu}{\mu^n}} + \int_{\tau_\nu}^{\tau_{\nu c}} B_\nu(t) e^{-\frac{t - \tau_\nu}{\mu^n}} \frac{dt}{\mu^n}$$

$$+ r_{\nu c} e^{-\frac{\tau_{\nu c} - \tau_\nu}{\mu^n}} \frac{2}{n} \int_0^{\tau_{\nu c}} B_\nu(t) E_{\frac{2}{n}}(\tau_{\nu c} - t) dt + \frac{S_\nu}{\pi} r_{\nu c} \zeta e^{-\frac{\tau_{\nu c}}{\zeta^n}} e^{-\frac{\tau_{\nu c} - \tau_\nu}{\mu^n}} \quad (6)$$

and

$$I_\nu^-(\mu, \tau_\nu) = \int_0^{\tau_\nu} B_\nu(t) e^{-\frac{\tau_\nu - t}{\mu^n}} \frac{dt}{\mu^n} + \frac{S_\nu}{\pi} \zeta e^{-\frac{\tau_\nu}{\zeta^n}} \quad (7)$$

In Equation 6 $I_\nu^+(\mu, \tau_\nu)$ is the upward intensity whose respective components arise from the surface emission, the atmospheric emission by all layers at optical depths greater than τ_ν, and the downward fluxes diffusely reflected upwards. $I_\nu^-(\mu, \tau_\nu)$ is the downward intensity consisting of the atmospheric emission arising from all layers with optical depths less than τ_ν and the incident solar radiation.

The temperature distribution is obtained from a solution of the equation of radiative equilibrium which equates the total emitted and absorbed radiation for each volume element. For a stratified atmosphere each layer must satisfy the energy balance condition

$$\int_\nu \int_\omega \int_V l_\nu \, e^{-\frac{\Delta\tau}{\mu^n}} B_\nu \, dV \, d\omega \, d\nu = \int_\nu \int_\omega \int_V l_\nu \, e^{-\frac{\Delta\tau}{\mu^n}} I_\nu \, dV \, d\omega \, d\nu \, . \qquad (8)$$

The exponential term represents the attenuation losses due to self-absorption in the layer of finite optical thickness. Integration over all directions is required since I_ν as well as $e^{-\Delta\tau/\mu^n}$ is a function of μ. Furthermore, since absorption and emission may occur in different parts of the spectrum the equality holds only if the integration is taken over all frequencies. This general form of the condition of radiative equilibrium applies to any volume element as well as to different forms of absorption laws. If $\Delta\tau$ is very small in all directions, the familiar form (References 8 and 9) of the radiative equilibrium equation results:

$$\int_\nu l_\nu \, B_\nu \, d\nu = \int_\nu l_\nu \, J_\nu \, d\nu \, . \qquad (9)$$

Substitution of the intensities obtained (Equations 6 and 7) into the equation of radiative equilibrium leads to a Milne-type integral equation in $B_\nu(\tau)$, whose solution is required in obtaining the temperature distribution. The solution is obtained by iteration beginning from an assumed temperature distribution. The net flux is computed after each iteration. When the distribution of the net flux is constant within specified limits, radiative equilibrium is achieved and the calculation proceeds to the final step, the computation of limb darkening.

The components of the upward and downward intensities, the net flux, and the condition of radiative equilibrium will be examined in more detail in the manner required for computer solution. Hence a brief description of the coordinate system and the calculation of τ_ν follows.

COORDINATE SYSTEM

A plane parallel atmosphere is assumed and the computations are carried out in a 33 layer coordinate system (Figure 1). The interface between

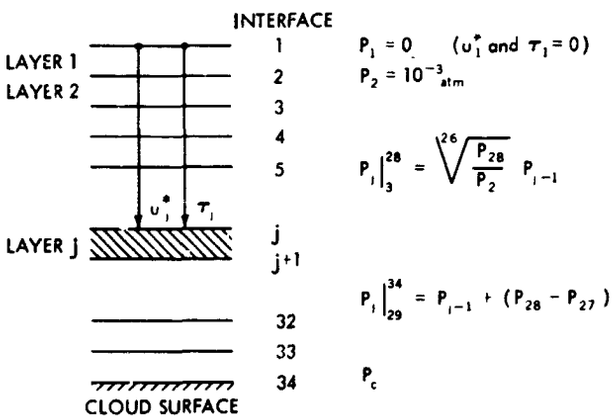

FIGURE 1.—Coordinate system.

layer j–1 and j is called interface j and the quantities u_j^* and τ_j are computed from the top of the atmosphere (interface one, zero pressure) to interface j and the corresponding pressure P_j. In all computations the pressure at interface j=2 was taken equal to 10^{-3} atm. Layer one above this level is included for the sake of completeness. The computed temperature is only an average value and it should not be interpreted that layer one is isothermal. For this region of the atmosphere, local thermodynamic equilibrium may not exist (Reference 10, for eaxmple) and the absorption lay adopted may not strictly apply (Reference 11). In addition, photochemical and other atmospheric processes will have a strong effect on

the temperature in this region. For layers between j = 2 and 28, pressures are calculated according to the recursion formula

$$P_j = \sqrt[26]{\frac{P_{28}}{P_2}}\, P_{j-1} \quad . \tag{10}$$

This mode of pressure slicing yields layers of approximately the same geometrical height but of increasing optical thickness. To avoid a very thick layer adjacent to the cloud boundary, a linear pressure slicing was applied between j = 28 and the surface (j = 34).

ABSORPTION COEFFICIENTS

The calculation of the optical thickness requires a value of the absorption coefficient, which varies with pressure and temperature, and a value for the mass of the absorbing gas. For pressures greater than 10^{-3} atm the individual line shape is determined primarily by collision broadening. The effect of this factor on atmospheric structure has been studied by several authors (Reference 12, for example). For band absorption the concept of optical thickness defined for a single frequency is still very useful, but τ becomes, in general, a complicated function of u*. For all cases studied in this paper, an analytical expression can be derived for this function, based on the so-called strong line absorption law (Reference 7). This approximation applies to CO_2 within the pressure ranges of interest, namely from 10^{-3} to 1 atm for CO_2 concentrations exceeding 0.01 part per volume.

The mass of active gas is usually expressed in terms of a path length. An element of the path length is defined by the product of the geometric path length ds and the normalized density of the active gas

$$du = q\frac{\rho}{\rho_0}\, ds \quad . \tag{11}$$

Since $\rho = MP/RT$,

$$du = q\,\frac{P}{P_0}\,\frac{T_0}{T}\, ds \quad . \tag{12}$$

In the domain of collision broadening, the pressure and temperature dependences of the half-width of absorption lines are usually considered by defining a reduced path length equal to the product of du, the pressure, and the inverse square root of the temperature. The temperature dependence of the excited bands may be included by an exponential term which represents the increase of the population of the lower vibrational energy state with temperature (References 13, for example). An additional temperature dependence of the rotational levels, within each vibrational state, has the effect of altering the band shape. However, this effect is much smaller than that due to changes in the population of the vibrational state. The reduced path length, with these effects, is then

$$du^* = q\left(\frac{P}{P_0}\right)^2 \left(\frac{T_0}{T}\right)^{3/2} e^{\gamma\left(\sqrt{250} - \sqrt{T}\right)}\, ds \quad . \tag{13}$$

The numerical value of γ was computed from Reference 14 for each spectral region, and the adopted values are listed in Table 1. The value

Table 1

Values used in the Computation of CO_2 Absorption for Various Spectral Intervals.

i	ν (cm^{-1})	m	n	γ
1	0-200	0	0.50	0
2	200-300	0	0.50	0
3	300-400	0	0.50	0
4	400-495	0	0.50	0
5	495-550	7.8×10^{-5}	0.60	0
6	550-625	4.6×10^{-3}	0.42	0
7	625-660	9.0×10^{-1}	0.38	0
8	660-720	4.9×10^{-1}	0.42	0
9	720-810	9.5×10^{-4}	0.40	0
10	810-880	6.5×10^{-5}	0.55	2200
11	880-920	8.6×10^{-6}	0.56	2760
12	920-1000	4.9×10^{-6}	0.54	2330
13	1000-1100	4.4×10^{-5}	0.52	2290
14	1100-1400	0	0.50	0
15	1400-2000	0	0.50	0
16	2000-2600	6.6	0.50	0
17	2600-8000	1.1×10^{-3}	0.50	0
18	1700-8000 (solar)	4.9×10^{-7}	0.27	0

μds equals the vertical path element dh. Thus, by using the hydrostatic equation

$$\frac{dh}{H} = -\frac{dP}{P} \quad . \tag{14}$$

the reduced path length in a direction μ can be expressed by

$$du^*(\mu) = -\frac{1}{\mu} qH_0 \left(\frac{T_0}{T}\right)^{1/2} e^{\gamma\left(\frac{1}{250} - \frac{1}{T}\right)} \frac{P\,dP}{P_0^2} \quad (15)$$

For the remainder of this paper, only the reduced path length in the vertical direction, $u^*(\mu=1)$, is used. The reduced path length from a level P to outer space is a function of the wavelength as well as the temperature profile,

$$u_\nu^* = qH_0 \int_0^P \left[\frac{T_0}{T(P)}\right]^{1/2} e^{\gamma_\nu \left(\frac{1}{250} - \frac{1}{T(P)}\right)} \frac{P\,dP}{P_0^2} \quad (16)$$

For the numerical computations Equation 16 was reformulated in terms of the adopted coordinate system,

$$u_{i,j}^* = u_{i,j-1}^* + qH_0 \left(\frac{T_0}{T_{j-1}}\right)^{1/2} e^{\gamma_i \left(\frac{1}{250} - \frac{1}{T_{j-1}}\right) \frac{P_j^2 - P_{j-1}^2}{2P_0^2}} \quad (17)$$

A constant temperature within each layer is assumed. The scale height H_0 for standard temperature is a function of the molecular weight and, therefore, of the fractional concentration of each gas; adopted values are given in Table 2.

Table 2

Pressure Scale Height in the Atmosphere of Venus as a Function of the CO_2 Concentration.

q(CO_2 per volume)	H_0 (cm)	q H_0 (cm)
1.0	5.901×10^5	5.901×10^5
0.75	6.491×10^5	4.865×10^5
0.5	7.212×10^5	3.606×10^5
0.25	8.114×10^5	2.029×10^5
0.1	8.771×10^5	8.771×10^4
0.05	9.015×10^5	4.508×10^4
0.01	9.210×10^5	9.210×10^3

Since CO_2 is the primary absorbing constituent, an accurate representation of its absorption spectrum as a function of pressure, temperature, and path length is required. The absorption spectrum of CO_2 can be separated into three important regions. The near infrared region from 1 to about 6μ is most important in regard to the absorption of solar radiation but less significant in regard to the thermal emission spectrum of the clouds (Reference 15). The 9.4 and 10.4μ excited bands of CO_2 are within the second region considered in this calculation. They lie in a spectral region for which planetary observations exist (References 16–18), although they play only a minor role in the determination of the atmospheric structure. Any realistic interpretation of the data from References 16–18 must necessarily represent this part of the spectrum adequately. The strong bands near 15μ determine the atmospheric structure in the radiative regime; the interval of 12–20μ is the third region considered.

The spectrum should be divided into many intervals for accurate representation, but the number of intervals must be limited to avoid unreasonably long computing times. As a compromise, the 18 intervals listed in Table 1 were selected.

For the pressure and temperature ranges considered, the individual line shapes are controlled primarily by collision broadening. For high concentrations of CO_2 ($q \geq 0.01$) the distribution of the lines and their spacings in the major bands indicates appreciable overlapping. The square root law would overestimate the absorption in such intervals; but the strong line approximation is a generalization of this law which is valid even when overlapping occurs. This approximation is expressed in terms of a single variable u^* and is well suited to extrapolation of the absorption to large path lengths and low pressures (Reference 7).

For each spectral interval, the fractional absorption was computed from the expression

$$\bar{A}_i = 1 - e^{-\tau_i} \quad (18)$$

where

$$\tau_i = (m_i u_i^*)^{n_i} \quad (19)$$

The m_i are similar to the generalized absorption coefficients and the n_i are constants determined by the degree of overlapping of the individual lines and the slope of the curve of growth.

Wherever possible, the spectral intervals were chosen to coincide with the intervals used by Burch et al (Reference 13). The coefficients m_i and n_i were determined graphically by a fit of the strong line curve with applicable data points taken from this source. Where experimental data were not available the calculated tables of CO_2 absorption compiled by Stull et al. (Reference 14) were used. A sample is shown in Figure 2 and the various values of m and n are listed in Table 1.

The application of the strong line approximation is valid whenever the central regions of the various lines become opaque. For each spectral interval a check of the validity of the strong line approximation for the conditions considered was carried out. A relatively weak absorbing region (720–810 cm^{-1}) of the 15μ CO_2 band may serve as an illustration. If the approximation holds for this spectral interval, then it will be valid for stronger absorbing regions. According to Plass (Reference 7) the strong line approximation applies for all values of β to an accuracy of 10 percent, if $X > 1.63$. For this interval

$$\left.\begin{aligned} \beta &= 0.023\ P\ , \\ X &= 0.01\ \frac{u}{P}\ . \end{aligned}\right\} \qquad (20)$$

According to Equations 12 and 14, u/P equals qH and defines the CO_2 concentration (see Table 2). As can be seen, the strong line approximation is valid within an accuracy of 10 percent for CO_2 concentrations in excess of 10^{-3} and more accurate for concentrations in excess of 10^{-2}, which is the range of interest for Venus.

SPECIFIC INTENSITY

The formulas derived in the section concerned with the solution of the radiative transfer equation must be expressed in terms of the adopted coordinate system. The specific intensity is a function of ν, τ, and μ and is conveniently expressed by

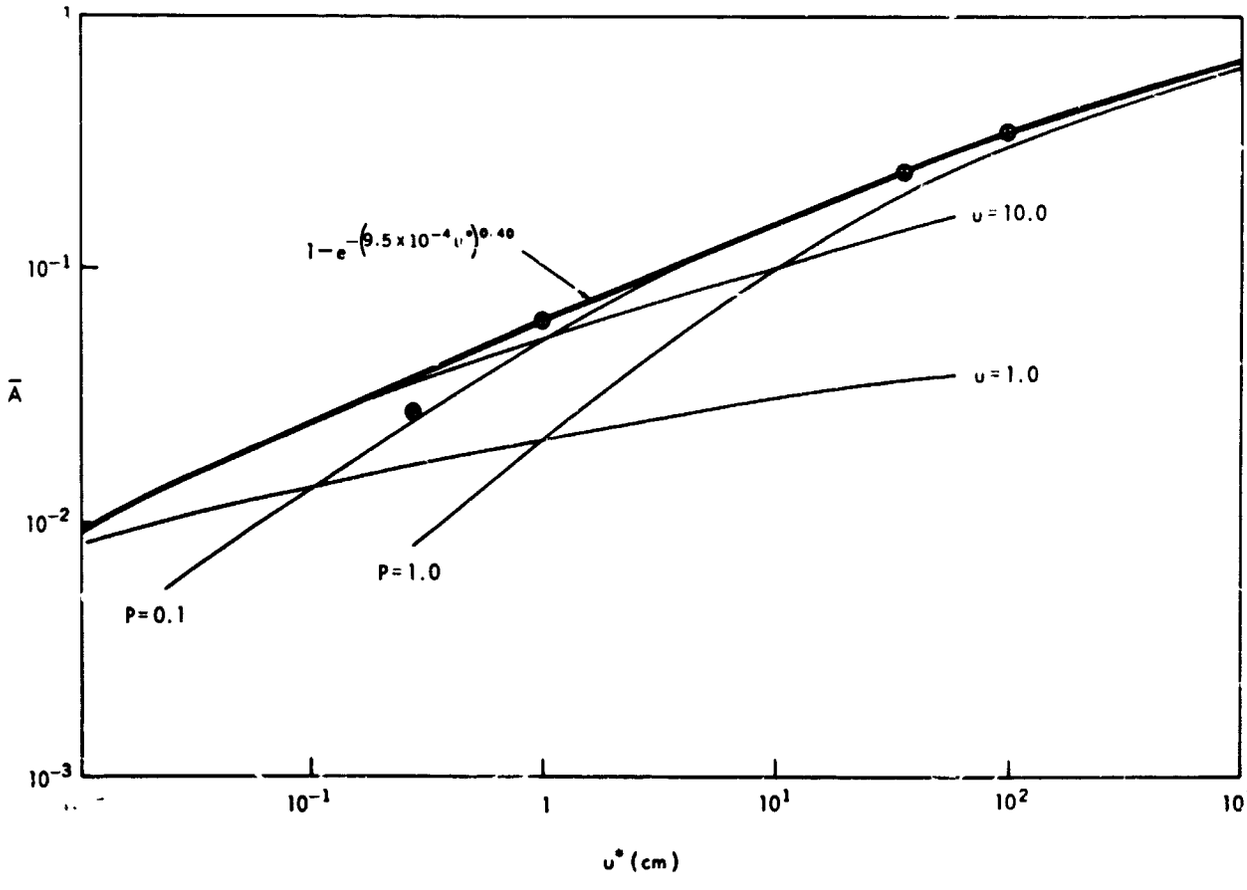

FIGURE 2.—Illustration of strong line approximation fit for the spectral interval 720–810 cm^{-1}, as derived from Stull et al. (Reference 14). Data points taken from Burch et al. (Reference 13) and slightly modified are included for comparison.

upward and downward vectors. As mentioned before, the solution of the transfer equation appropriate here requires four components for the upward intensity:

1. Thermal emission from the cloud surface
2. Direct thermal emission from the atmosphere below interface j
3. Downward thermal emission from the whole atmosphere, reflected upward by the clouds
4. Downward solar radiation reflected upward by the clouds.

The downward intensity includes values for:

5. Direct emission from the atmosphere above interface j
6. Direct solar radiation.

These six components are shown in Figure 3 and discussed below.

Surface Emission

For a frequency interval i and an interface j, the thermal radiation emitted, which is attenuated between the sufrace and the interface j, is given by

$$I_{ij} = \epsilon_{ic} B_{ic} e^{-\frac{\tau_{ic} - \tau_{ij}}{\mu^n}} . \qquad (21)$$

The designation of emissivity applies directly for a solid or liquid surface, but some qualifications regarding the interpretation of ϵ_{ic} are necessary for a scattering medium such as a cloud surface. At this level the gas and cloud particles have a

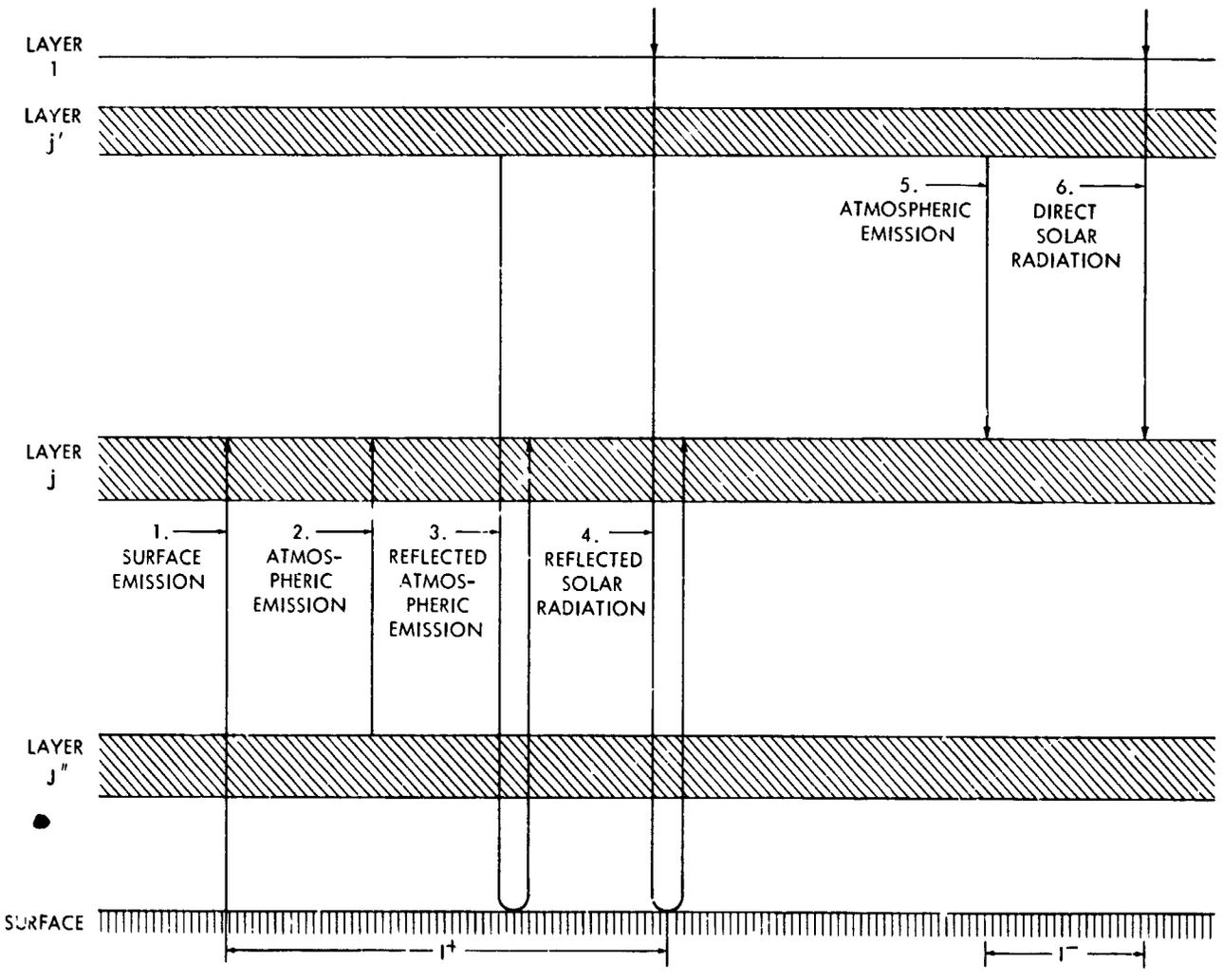

FIGURE 3.—Schematic diagram of the radiation components considered.

temperature T_c. For those spectral intervals where the atmospheric gas is opaque, the optical properties of the cloud particles are not important. In regions of the spectrum where the gas between particles is transparent the optical properties of the particles and their concentration become very important. For these intervals ϵ_c is defined as a boundary value, which indicates how much smaller the emerging radiation is compared with a blackbody at temperature T_c. The cloud emissivity was taken as unity in the strong absorption bands and set equal to a constant value in the transparent regions. In general, ϵ_{ic} may be a complicated function of wavelength and μ but this dependence is ignored.

Emission from the Atmosphere below Interface j

The contribution from each layer is proportional to the Planck function, an attentuation factor, and the optical thickness,

$$I_{ij} = \sum_{j'=j}^{33} B_{ij'} \, e^{-\frac{\tau_{ij'} - \tau_{ij}}{\mu^n}} \, \frac{\Delta\tau_{ij'}}{\mu^n} \quad . \tag{22}$$

Emission from the Atmosphere Reflected by the Clouds

This component is the product of the downward flux at the cloud surface, the reflectivity, and the attenuation factor of the atmosphere between the surface and τ_j. Since constant temperature is assumed within a layer, the flux integral (see below) can be integrated for each layer by using the recursion formula for exponential integrals,

$$E_n(\tau) \, d\tau = dE_{n+1}(\tau) \quad . \tag{23}$$

The reflected intensity becomes

$$I_{ij} = r_{ic} \, e^{-\frac{\tau_{ic} - \tau_{ij}}{\mu^n}} \, \frac{2}{n} \sum_{j'=1}^{33} B_{ij'} \left[E_{\frac{2}{n}+1}\left(\tau_{ic} - \tau_{i,\,j'+1}\right) - E_{\frac{2}{n}+1}\left(\tau_{ic} - \tau_{ij'}\right) \right] \quad . \tag{24}$$

Reflected Solar Radiation

Similarly, the reflected solar intensity is calculated from

$$I_{18,\,j} = \frac{S}{\pi} \, \zeta \, r_{18,\,c} \, e^{-\left(\frac{\tau_c}{\zeta^n} + \frac{\tau_c - \tau_j}{\mu^n}\right)} \quad . \tag{25}$$

Within the spectral range of 1.25 to 5.9μ the reflectivity of the clouds for solar radiation was taken equal to 0.6 which is consistent with recent observations (Reference 19). Again clouds were considered to be perfect diffusers.

Direct Emission from Atmospheric Layers above Interface j

This contribution is analogous to the emission from lower layers:

$$I_{ij} = \sum_{j'=1}^{j-1} B_{ij'} \, e^{-\frac{\tau_{ij} - \tau_{ij'}}{\mu^n}} \, \frac{\Delta\tau_{ij'}}{\mu^n} \quad . \tag{26}$$

Direct Solar Radiation

The direct solar radiation is given by the solar constant for 1.25 to 5.9μ appropriate for the distance of Venus (0.047 watt cm^{-2}):

$$I_{18,\,j} = \frac{S}{\pi} \, \zeta \, e^{-\frac{\tau_j}{\zeta^n}} \quad . \tag{27}$$

FLUX

The flux is derived conventionally by integration of the components of specific intensity over μ (Reference 9, for example):

$$\pi F = \int I \, \mu \, d\omega = 2\pi \int I \, \mu \, d\mu \quad . \tag{28}$$

Integration leads to exponential integrals of the form of

$$\int_0^1 e^{-\frac{\tau}{\mu^n}} \, \mu \, d\mu = \frac{1}{n} \, E_{\frac{2}{n}+1}(\tau) \quad , \tag{29}$$

$$\int_0^1 e^{-\frac{\tau}{\mu^n}} \, \frac{d\mu}{\mu^{n-1}} = \frac{1}{n} \, E_{\frac{2}{n}}(\tau) \quad . \tag{30}$$

The results are expressed by exponential integrals tabulated for integral order numbers (Reference 20). For all wavelength intervals concerned with thermal radiation (i = 1 to 17) n is close to 1/2; for integration, n was taken equal to 1/2, which leads to exponential integrals of the fifth and fourth orders respectively. For the interval concerned with solar radiation (i = 18) the exponent n is 0.27; for integration, n was taken equal to 1/4, which leads in this case to exponential integrals of the ninth and eighth orders respectively.

Analogous to the intensity, the upward flux consists of four components, and the downward flux consists of two.

The individual components of the upward flux F_{ij}^{+} are

$$1. \quad 4\epsilon_{ic} B_{ic} E_5(\tau_{ic} - \tau_{ij}) \quad , \tag{31}$$

$$2. \quad 4 \sum_{j'=j}^{33} B_{ij'} \left[E_5(\tau_{ij'} - \tau_{ij}) - E_5(\tau_{i,j'+1} - \tau_{ij}) \right] \quad , \tag{32}$$

$$3. \quad 16 r_{ic} E_5(\tau_{ic} - \tau_{ij}) \sum_{j'=1}^{33} B_{ij'} \left[E_5(\tau_{ic} - \tau_{i,j'+1}) - E_5(\tau_{ic} - \tau_{ij'}) \right] \quad , \tag{33}$$

$$4. \quad 8 \frac{S}{\pi} r_{18,c} \zeta e^{-\frac{\tau_c}{\zeta^n}} E_9(\tau_c - \tau_j) \quad . \tag{34}$$

The components for the downward flux F_{ij}^{-} are

$$5. \quad 4 \sum_{j'=1}^{j-1} B_{ij'} \left[E_5(\tau_{ij} - \tau_{i,j'+1}) - E_5(\tau_{ij} - \tau_{ij'}) \right] \quad , \tag{35}$$

$$6. \quad \frac{S}{\pi} \zeta e^{-\frac{\tau_j}{\zeta^n}} \quad . \tag{36}$$

The net flux ($\pi F_\nu = \pi F_\nu^{+} - \pi F_\nu^{-}$) is calculated for each layer j, for each wavelength interval i, and for the sum over all spectral intervals.

CONDITION OF RADIATIVE EQUILIBRIUM

The general condition of radiative equilibrium (Equation 8) will now be applied to an atmosphere consisting of many layers of finite optical thickness. For an element of area dA in a layer of optical thickness $\Delta\tau_\nu$, the element of reduced volume is

$$dV = \mu \, dA \left(\frac{\Delta u^*}{\mu} \right)^n \quad . \tag{37}$$

In this expression μdA represents the projection of the element of area in a direction μ, and $(\Delta u^*/\mu)$ is the effective element of the radiating gas. For convenience and consistency with the equation for τ (Equation 2), l_ν in Equation 8 may be included with Δu^*. Upon inserting Equation 37 into Equation 8, the factor $(m\Delta u^*/\mu)^n e^{-\Delta\tau/\mu^n}$ becomes just the increment of absorptance of the layer. Upon integration from 0 to $\Delta\tau$ the radiative equilibrium condition becomes

$$\int_\nu \int_\mu I_\nu(\mu) \left(1 - e^{-\frac{\Delta\tau}{\mu^n}} \right) \mu \, d\mu \, d\nu = \int_\nu B_\nu \int_\mu \left(1 - e^{-\frac{\Delta\tau}{\mu^n}} \right) \mu \, d\mu \, d\nu \quad . \tag{38}$$

The computed intensities were inserted into Equation 38 and integration over μ was carried out analytically. In terms of the adopted coordinate system, the radiative equilibrium condition is

$$
\begin{aligned}
&4\sum_{i=1}^{17}\epsilon_{ic}B_{ic}\left[E_5(\tau_{ic}-\tau_{i,j+1})-E_5(\tau_{ic}-\tau_{ij})\right]\\
&+4\sum_{i=1}^{17}\sum_{\substack{j'=1\\ j'\neq j}}^{33}B_{ij'}\left[E_5\left(|\tau_{ij}-\tau_{i,j'+1}|\right)-E_5\left(|\tau_{i,j+1}-\tau_{i,j'+1}|\right)+E_5\left(|\tau_{i,j+1}-\tau_{ij'}|\right)-E_5\left(|\tau_{ij}-\tau_{ij'}|\right)\right]\\
&+16\sum_{i=1}^{17}r_{ic}\left[E_5(\tau_{ic}-\tau_{i,j+1})-E_5(\tau_{ic}-\tau_{ij})\right]\sum_{j'=1}^{33}B_{ij'}\left[E_5(\tau_{ic}-\tau_{i,j'+1})-E_5(\tau_{ic}-\tau_{ij'})\right]\\
&+\frac{S}{\pi}\zeta\left\{e^{-\frac{\tau_{18,j}}{\zeta^{1/4}}}\left(1-e^{-\frac{\Delta\tau_{18,j}}{\zeta^{1/4}}}\right)+8e^{-\frac{\tau_{18,c}}{\zeta^{1/4}}}r_{18,c}\left[E_9(\tau_{18,c}-\tau_{18,j+1})-E_9(\tau_{18,c}-\tau_{18,j})\right]\right\}\\
&=2\sum_{i=1}^{17}B_{ij}\left[1-4E_5(\Delta\tau_{ij})\right]\quad .
\end{aligned}
\tag{39}
$$

The terms on the left side are arranged in the adopted sequence; the contribution from the surface, then the contribution from the atmosphere (direct and reflected), and finally solar radiation, (direct and reflected).

Radiation from the atmospheric layers above and below layer j is combined into one expression by the use of absolute value signs in the arguments of the exponential integrals. The right side represents the emission from layer j and the left side represents radiation absorbed by layer j.

The numerical solution of Equation 39 was carried out on an IBM 7094 computer. For each layer j and temperature T (between 100 and 350°K) the i wave number intervals of the right side of Equation 39 were summed by using the appropriate value of $\Delta\tau_{ij}$. A functional relationship between the total thermal emission E_j from a layer at temperature T_j was tabulated. The thermal emission from a layer depends on the Planck function and the optical thickness; both are functions of the temperature. The optical thickness depends on temperature through u^* (Equation 16). With this set of E vs. T tables for each layer, the calculation of the temperature profile continued as follows.

First the energy absorbed by a layer j (left side of Equation 39) was computed from an estimate of the temperature profile. After the absorbed energy was obtained, the computer searched the previously computed table for a temperature for layer j which balanced Equation 39. In other words, it determined the temperature at which layer j could reradiate the absorbed energy. This was repeated for each layer and the resulting temperature distribution was checked for constancy of the net flux. If the flux criterion was not satisfied, the computed temperature distribution was re-inserted and the iteration procedure continued.

The convergence criterion used in terminating the calculation was

$$
\left|\frac{F_{(\text{layer }10)}-F_{(\text{layer }j)}}{F_{(\text{layer }10)}}\right|\leq\alpha\quad,
\tag{40}
$$

where α was chosen according to the desired accuracy. In general α was taken equal to 0.005. Obviously, higher accuracy would require more iterations. Once the convergence criterion was satisfied, the limb function was calculated in the final step,

$$\frac{I_i^{\uparrow}(j = 1, \mu)}{I_i^{\uparrow}(j = 1, \mu = 1)} \quad . \tag{41}$$

The limb function was computed for each spectral interval i and for a range of specified μ, by using the computed equilibrium temperature distribution. This expression (41) includes all upward components of the specific intensity.

The iteration process converges rapidly for low surface pressures, where, for a praticular layer, radiation from the surface dominates radiation from other atmospheric layers. For optically dense atmospheres the convergence process takes much longer. These effects are demonstrated in Figures 4 and 5 where samples of the iteration process for low and high surface pressures and for low and high initial temperature estimates are shown. More general studies of the convergence of iterative processes are available (Reference 21, for example).

RESULTS

As stated earlier, a portion of the atmosphere of Venus was selected for analysis with the formulated program. Several sets of good observational material presently exist which can serve as a basis for comparison with the computed results.

The atmosphere of Venus above the clouds is more amenable to analysis and consequently is better understood than the region between the surface and the upper cloud layer (References 22–27). However, starting from essentially the same set of observational data, various students of Venus have reached different conclusions. Estimates of the cloud top pressure range from 0.007 to 1 atm (References 23 and 28–30). Large discrepancies exist in estimates of the water vapor content (References 31–33), and the abundance of

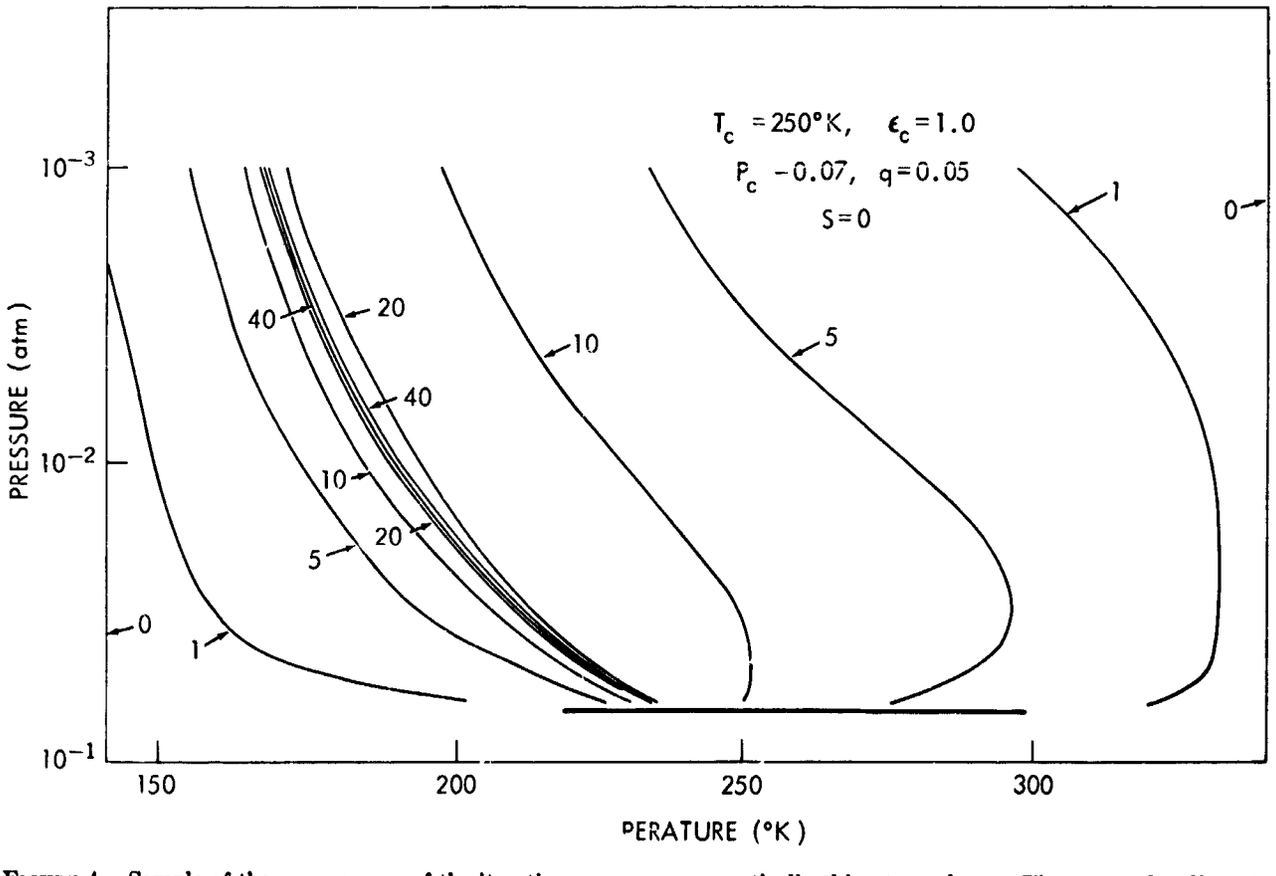

FIGURE 4.—Sample of the convergence of the iteration pr r an optically thin atmosphere. The numerals adjacent to each curve in the figure indicate the iteration numbe corresponding to each temperature distribution sl n.

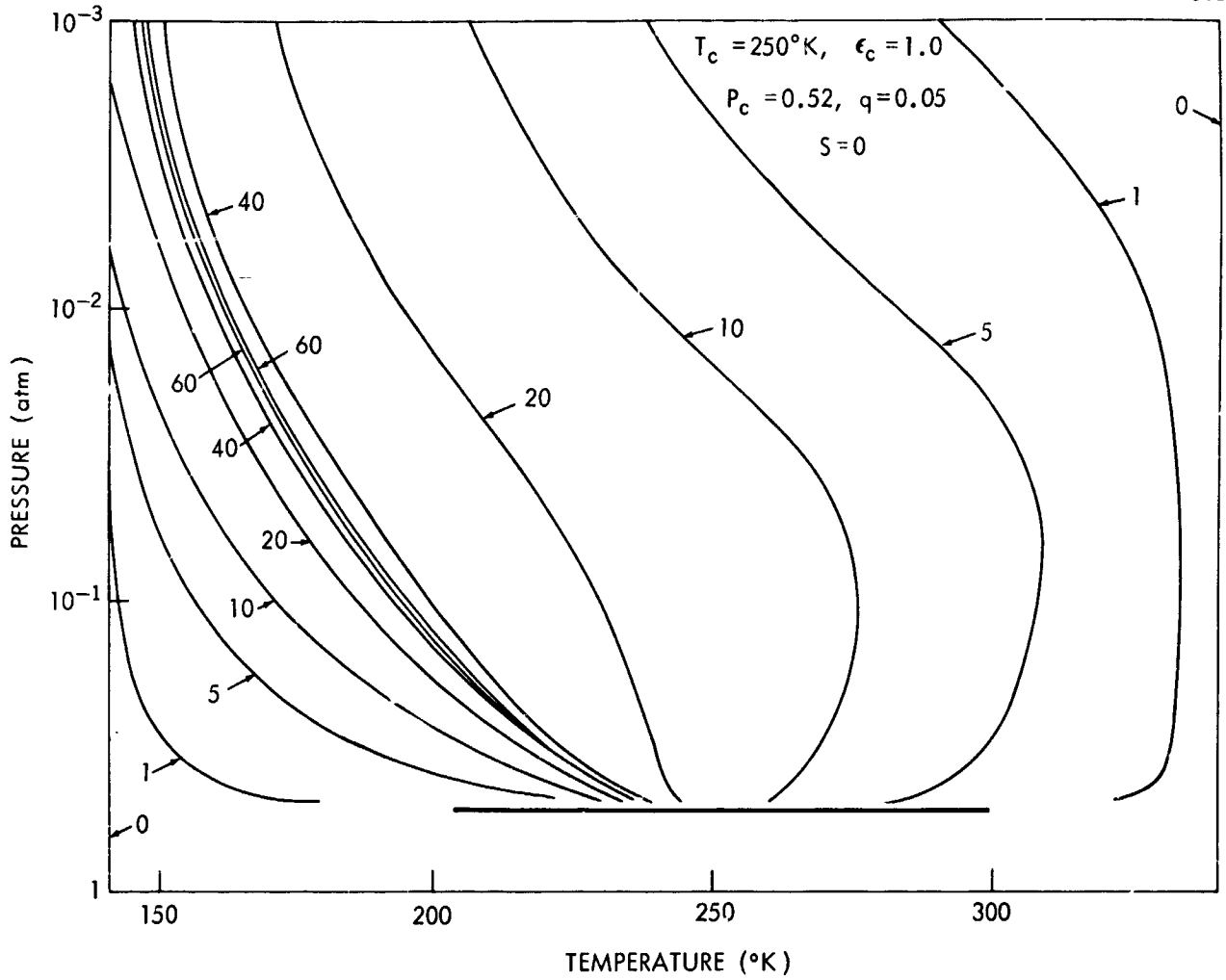

FIGURE 5.—Sample of the convergence of the iteration process for a more optically dense atmosphere than that considered in Figure 4. The numerals adjacent to each curve in the figure indicate the iteration number corresponding to each temperature distribution shown.

CO_2 (References 34–36) is still subject to discussion. The reasons for the discrepancies are manyfold, but the solution to the problem will depend on better observations and more refined interpretation of existing data.

The interpretation of the intensities measured within the atmospheric window by Sinton and Strong (Reference 16), Murray, Wildey and Westphal (Reference 17), and by Chase, Kaplan, and Neugebauer (Reference 18) clearly requires some knowledge of the temperature profile in the upper atmosphere of Venus. So far, only the black-transparent model used by Mintz (Reference 37) and the grey model used by Rasool (Reference 38) and Ostriker (Reference 39) have been applied. None of these calculations consider the strong temperature dependence of the 9.4 and 10.4μ CO_2 excited bands or the solar heating in the clear atmosphere.

It is instructive to note that early application of the grey atmospheric model to the earth's atmosphere by Humphreys (Reference 40), Gold (Reference 41), and Emden (Reference 42) yielded only crude agreement between calculations and reality. Subsequent treatments (References 5 and 43–47, for example) which included the wavelength dependence of the H_2O, CO_2, and O^3 absorption were necessary for satisfactory temperature profiles. Similarly, a more exact and detailed study of the atmosphere of Venus should give better results.

Highly developed nongrey atmospheric models (Reference 48, for example) used to describe the earth's stratosphere exist but have not been

applied to Venus. However, recent work by Arking (Reference 49) and Ohring (Reference 46) with nongrey models have been applied to the atmosphere of Mars. For Venus, the discrepancies in estimates of composition, cloud top pressure, and other parameters necessary for accurate calculations have probably discouraged the application of these models. Furthermore, CO_2 absorption coefficients for relatively large concentrations have become available only recently (References 13, 14, and 50). However, it is felt that a parametric study with a variety of values for cloud top pressure and temperature and for CO_2 concentration should improve our understanding of the physical conditions in the atmosphere of Venus. Results of the calculations can be compared with existing and forthcoming measurements, and the range of values for importar parameters then, hopefully, can be narrowed.

The effect of solar heating, carbon dioxide concentration, and assumed cloud top pressure, temperature, and emissivity, on the atmospheric temperature above the clouds can now be discussed. A number of conclusions can be drawn from this parametric study. However, the attempt to match, in detail, the calculated intensities, fluxes, and limb functions with the observations is still underway.

The pronounced effect of solar heating in the clear atmosphere is apparent in Figure 6. A realistic interpretation of planetary observations of a partially illuminated disk requires further averaging over zenith angles. The temperature maximum disappears for larger zenith angles and the temperature distribution approaches the

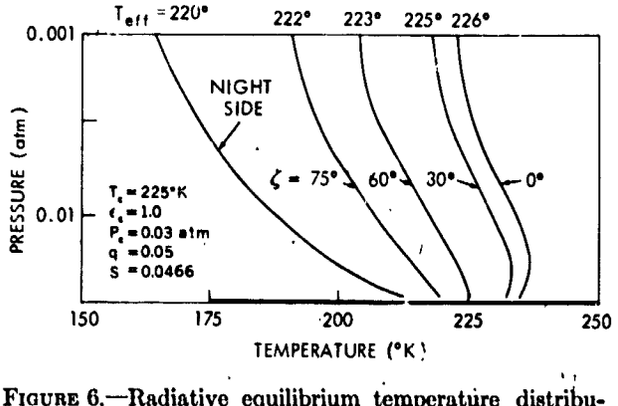

FIGURE 6.—Radiative equilibrium temperature distribution in the Venus atmosphere, illustrating the effects of solar heating for various solar zenith angles.

equilibrium condition on the dark side. Three factors make the large amount of solar heating understandable. Relative to the earth, the solar constant is nearly double; secondly, the high reflectivity of the clouds gives rise to strong reflected radiation and consequently to an additional heat source; and finally, the CO_2 concentration is much higher. The high CO_2 concentration increases the ability of the layers to cool very effectively, but at long wavelengths many spectral regions are already saturated. This atmospheric greenhouse effect is very pronounced. The near infrared absorption region considered in this discussion, spectral interval number 18 (1.25–5.9μ), would saturate at much higher pressures (between 3 and 10 atmospheres). Observations at the 8–12μ window and at 3.75μ (Reference 51) indicate essentially the same brightness temperatures in the sunlit and dark hemispheres. This is not in contradiction to the calculated large temperature differences in the clear atmosphere since the observations exist only for relatively transparent spectral regions. Larger differences are expected in moderately strong absorption regions, but unfortunately data are not available there.

The equilibrium temperatures with and without solar heating for various cloud top pressures are illustrated in Figure 7. For low cloud top pressures and consequently low optical thicknesses, the surface can be observed more readily and hence the effective temperature approaches the cloud top temperature. The discontinuity in the temperature profile near the lower boundary is characteristic of radiative equilibrium considerations in a bounded, finite atmosphere and has been discussed by several authors (References 5 and 52, for example). A more realistic representation of the cloud top which does not assume a "solid surface" will remove the discontinuity and limit the gradient to an adiabatic one. If necessary, allowance for convective as well as radiative transport of energy must be made. It can also be seen from Figure 7 that some of the calculated gradients approach and even exceed the adiabatic one near the cloud top surface. Convection would be induced and an upward transport of cloud particles would occur.

A curve which indicates saturation temperatures for CO_2 is included in Figure 7. For the conditions considered, condensation and possible

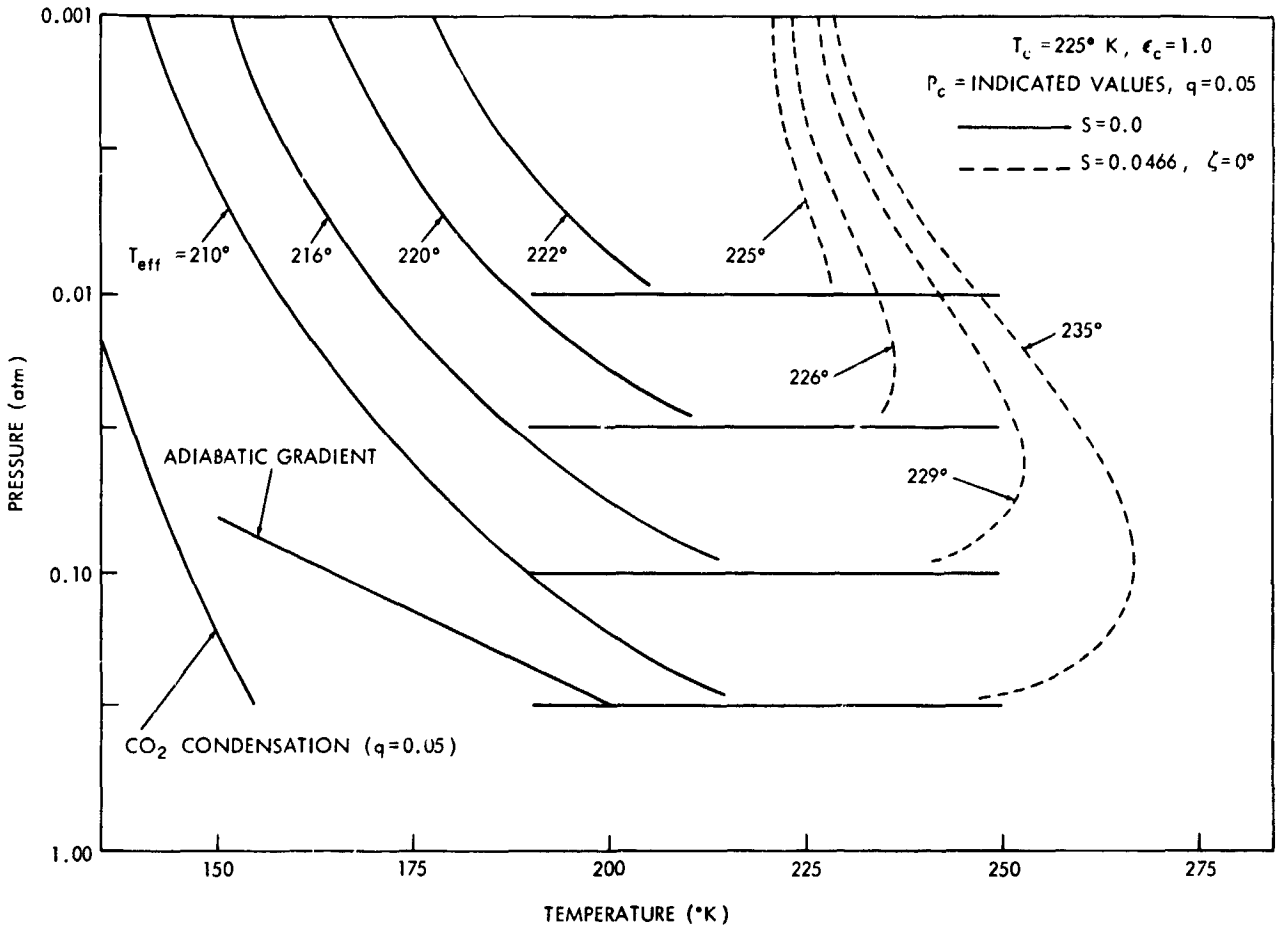

FIGURE 7.—Radiative equilibrium temperature distributions as a function of cloud top pressure level, for the dark and sunlit hemispheres.

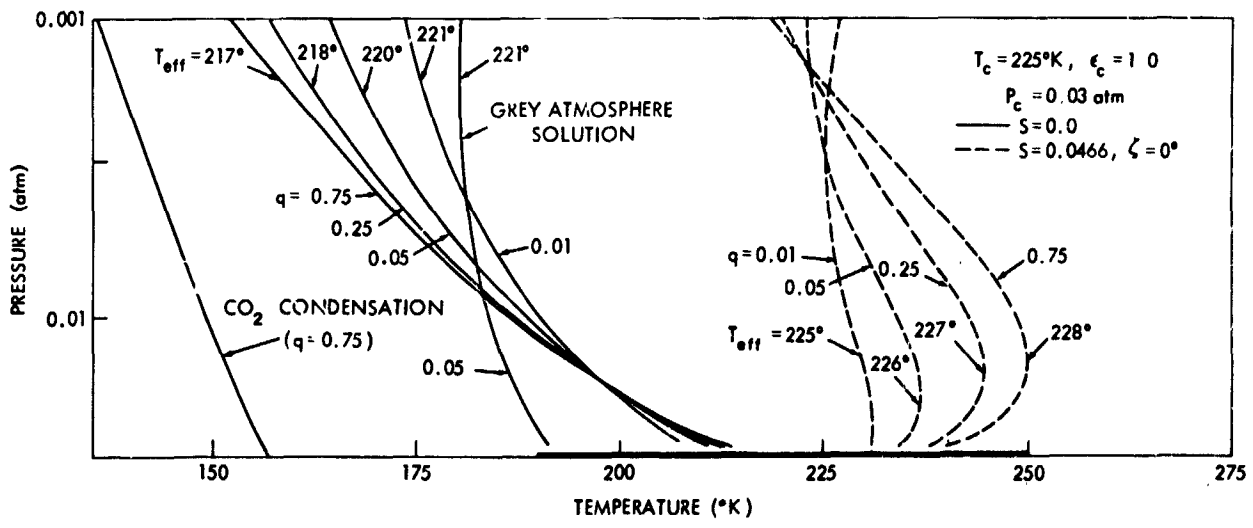

FIGURE 8.—Radiative equilibrium temperature distributions showing the effects of various CO_2 concentrations, for the dark and sunlit hemispheres.

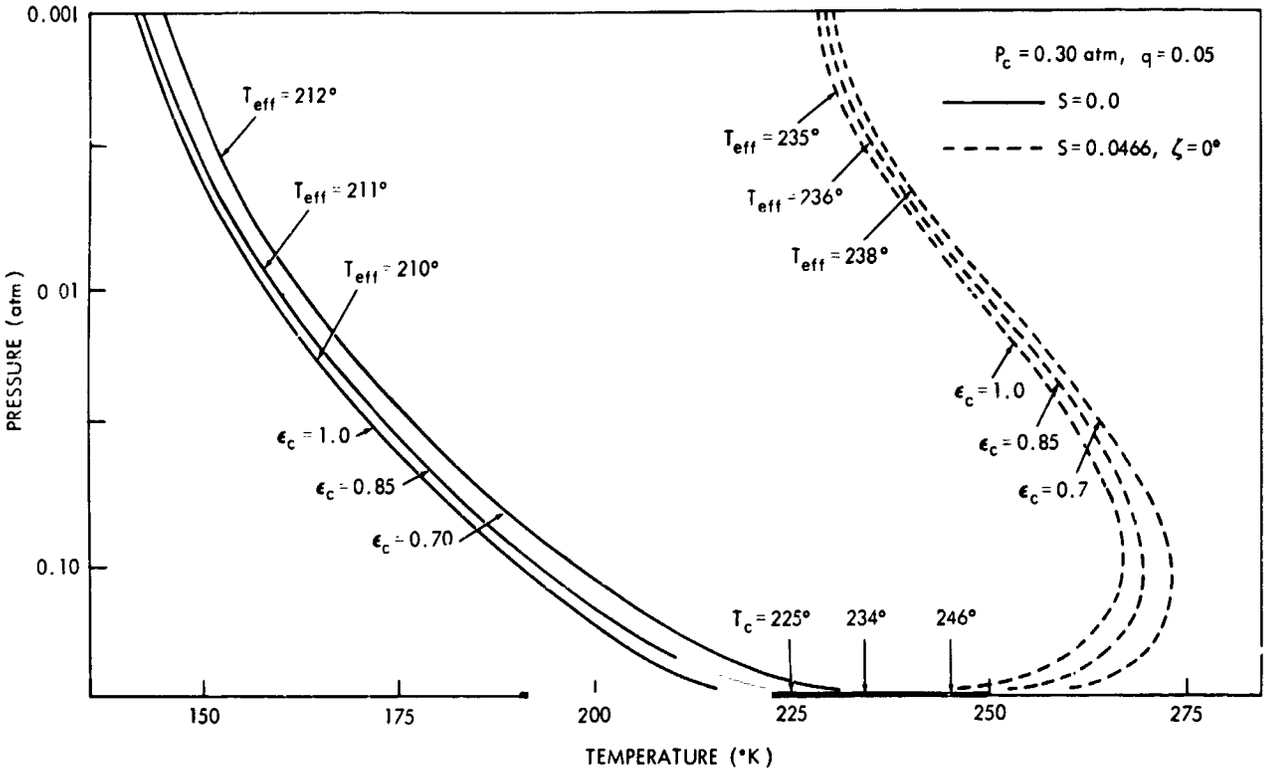

FIGURE 9.—Radiative equilibrium temperature distributions illustrating the effect of cloud top emissivity and temperature, for an almost constant net flux, for the dark and sunlit hemispheres.

formation of CO_2 clouds is unlikely. The wide spread and the slope of temperature profiles shown in Figure 7 make it difficult to extrapolate the temperatures, in detail, to much lower pressures. Caution must be exercised, especially in extrapolations to the low pressures for the occultation measurements $\approx 2.6 \times 10^{-6}$ atm (Reference 53).

The effects of CO_2 concentration on the temperature distribution (Figure 8) are different for the dark and sunlit hemispheres of the planet. On the dark side, the temperatures depend very little on the CO_2 concentration, with the exception of very high layers which can cool more effectively for the higher concentrations. The effects of solar heating have already been discussed.

The temperature distribution of a grey atmospheric model is included for comparison and clearly illustrates the difference between the isothermal character of the grey model and the larger gradients obtained by applying nongrey absorption.

The final illustration (Figure 9) demonstrates the effect of nonblackness for the cloud top surface. The total net flux is kept approximately the same for all cases by adjusting the surface temperature upwards as the emissivity is lowered. As discussed before, the value of ϵ was set equal to unity for the intervals i = 7, 8 and 16, where CO_2 absorption is strongest. In all other intervals ϵ was set equal to the value designated in the figure. The effect on the resulting temperature distribution is small.

In summary then, radiative transfer calculations, which include pressure, temperature, and wavelength dependence of molecular absorption, are a strong analytical tool for the exploration of planetary atmospheres. The full capability of this tool has by far not been exhausted. Further analysis of the spectral and angular dependence of the emitted energy is required for more specific conclusions.

ACKNOWLEDGMENTS

The authors would like to express their gratitude to the following people for their contributions to the effort presented here: Mr. A. F. Simmons, for an expertly written computer program, Mr. T. Mahuron and Miss L. Coury for numerous calculations, and Mr. W. R. Bandeen and Dr. F. Möller for helpful criticism and discussion.

REFERENCES

1. ELSASSER, W. M., and CULBERTSON, M.F., "Atmospheric Radiation Tables," *Meteorol. Monographs* 4(23):1–43, August 1960.
2. KAPLAN, L. D., "On the Calculation of Atmospheric Transmission Functions for the Infrared," *J. Meteorol.* 9(2):139–144, April 1952.
3. PLASS, G. N., "Parallel-Beam and Diffuse Radiation in the Atmosphere," *J Meteorol.* 9(6):429–436, December 1952.
4. KOURGANOFF, V., "Basic Methods in Transfer Problems; Radiative Equilibrium and Neutron Diffusion," Oxford: Clarendon Press, 1952.
5. GOODY, R. M., "The Thermal Equilibrium at the Tropopause and the Temperature of the Lower Stratosphere," *Roy. Soc. Proc.* Ser. A, 197(1051): 487–505, July 7, 1949.
6. CHAMBERLAIN, J. W., and KUIPER, G. P., "Rotational Temperature and Phase Variation of the Carbon Dioxide Bands of Venus," *Astrophys. J.* 124(2):399–450, September 1956.
7. PLASS, G. N., "Useful Representations for Measurements of Spectral Band Absorption," *J. Opt. Soc. Amer.* 50(9):868–875, September 1960.
8. MILNE, E. A., "Thermodynamics of the Stars," *Handbuch der Astrophysik* 3(1):65–255, 1930.
9. CHANDRASEKHAR, S., "Radiative Transfer," Oxford: Clarendon Press, 1950.
10. GOODY, R. M., "Physics of the Stratosphere," Cambridge Univ. Press, 1958.
11. PLASS, G. N., and FIVEL, D. I., "Influence of Doppler Effect and Damping on Line-Absorption Coefficient and Atmospheric Radiation Transfer," *Astrophys. J.* 117(1):225–234, January 1953.
12. STRONG, J., and PLASS, G. N., "The Effect of Pressure Broadening of Spectral Lines on Atmospheric Temperature," *Astrophys. J.* 112:365–379, November 1950.
13. BURCH, D. E., GRYVNAK, D., and WILLIAMS, D., "Infrared Absorption by Carbon Dioxide," Ohio State University Research Foundation, Columbus, report SR-2, January 1961.
14. STULL, V. R., WYATT, P. J., and PLASS, G. N., "The Infrared Absorption of Carbon Dioxide," Air Force Systems Command, Los Angeles, California, report SSD-TDR-62-127, V. III, January 1963.
15. YAMAMOTO, G., "Direct Absorption of Solar Radiation by Atmospheric Water Vapor, Carbon Dioxide and Molecular Oxygen," *J. Atmos. Sci.* 19(2):182–188, March 1962.
16. SINTON, W. M., and STRONG, J., "Radiometric Observations of Venus," *Astrophys. J.* 131(2):470–490, March 1960.
17. MURRAY, B. C., WILDEY, R. L., and WESTPHAL, J. A., "Infrared Photometric Mapping of Venus through the 8–14 Micron Atmosphere Window," *J. Geophys. Res.* 68(16):4813–4818, August 1963.
18. CHASE, S. C., KAPLAN, L. D., and NEUGEBAUER, G., "The Mariner 2 Infrared Radiometer Experiment," *J. Geophys. Res.* 68(22):6157–6170, November 1963.
19. MOROZ, V. I., "The Infrared Spectrum of Venus (1–2.5μ)," *Sov. Astronom. AJ* 7(1):109–115, July–August 1963.
20. PAGUROVA, V. I., "Tables of the Exponential Integral," London: Pergamon Press, 1961.
21. STONE, P. H., "Approximate Integral Equations for the Temperature in Non-Gray Model Atmospheres," *Astrophys. J.* 137(2):628–640, February 1963.
22. UREY, H. C., "The Atmospheres of the Planets," *in: Handbuck der Physik* (S. Elügge, ed.), V. 52:363–418, Berlin: Springer-Verlag, 1959.
23. OPIK, E. J., "The Aelosphere and Atmosphere of Venus," *J. Geophys. Res.* 66(9):2807–2819, September 1961.
24. KUIPER, G. P., "Planets and Satellites, V. 3, The Solar System," (Kuiper, G. P., and Middlehurst, B. M., ed.) Chicago: Univ. of Chicago Press, 1961.
25. REA, D. G., "Molecular Spectroscopy of Planetary Atmospheres," *Space Sci. Rev.* 1(2):159–196, October 1962.
26. SAGAN, C., and KELLOGG, W. W., "The Terrestrial Planets," *Ann. Rev. Astron. Astrophys.* 1:235–266, 1963.
27. ROZENBERG, G. V., "Investigations of the Atmosphere of the Planet Venus by Optical Methods," *Sov. Phys. Doklady*, 8(1):1–2, July 1963.
28. KAPLAN, L. D., "A Preliminary Model of the Venus Atmosphere," Jet Propulsion Laboratory, California Institute of Technology, Pasadena, report JPL TR-32-379, December 12, 1962.
29. SAGAN, C., "The Radiation Balance of Venus," California Institute of Technology, Pasadena, report JPL TR-32-34, September 15, 1960.
30. ANDERSON, C. E., and EVANS, D. C., "The Nature of the Venus Cloud System," Institute of Aerospace Science paper, National Summer Meeting, Los Angeles, California, June 18–22, 1962.
31. STRONG, J., Ross, M. D., and MOORE, C. B., "Some Observations on the Atmosphere of Venus and the Earth during the Strato Lab IV Balloon Flight," *J. Geophys. Res.* 65(8):2526, August 1960.
32. SPINRAD, H., "A Search for Water Vapor and Trace Constituents in the Venus Atmosphere," *Icarus* 1(3):266–270, October 1962.
33. DOLLFUS, A., "Observations of Water Vapor on the Planet Venus," *C. R. Acad. Sci.* 256(15):3250–3253, April 8, 1963 (In French).
34. DUNHAM, T., JR., "Spectroscopic Observations of the Planets at Mount Wilson," in: "The Atmospheres of the Earth and Planets," (G. P. Kuiper, ed.) 288–305, Chicago: Univ. of Chicago Press, 1952, pp 288–305.
35. KAPLAN, L. D., "A New Interpretation of the Structure and CO_2 Content of the Venus Atmosphere," *Planet. Space Sci.* 8(1):23–29, October 1961.
36. SPINRAD, H., "Spectroscopic Temperature and Pressure Measurements in the Venus Atmosphere," *Astron. Soc. Pacific Publ.* 74:187–201, June 1962.

37. MINTZ, Y., "Temperature and Circulation of the Venus Atmosphere," *Planet. Space Sci.* 5(2):141–152, June 1961.

38. RASOOL, S. I., "Structure of Planetary Atmospheres," *AIAA J.* 1(1):6–19, January 1963.

39. OSTRIKER, J. P., "Radiative Transfer in a Finite Atmosphere," *Astrophys. J.* 138(1):281–290, July 1963.

40. HUMPHREYS, W. J., "Vertical Temperature-Gradients of the Atmosphere, Especially in the Region of the Upper Inversion," *Astrophys. J.* 29:14–32, January 1909.

41. GOLD, E., "The Isothermal Layer of the Atmosphere and Atmospheric Radiation," *Roy. Soc. Proc.* Ser. A, 82(551):43–70, February 1909.

42. EMDEN, R., "Über Strahlungsgleichgewicht und Atmosphärische Strahlung. Ein Beitrag zur Theorie der Oberen Inversion," *Sitzungsberichte der mathematisch–physikalischen Klasse*, Akademie der Wissenschaften, Munchen, Part I: 55–142, January–March 1913.

43. SIMPSON, G. C., "Studies in Terrestrial Radiation," *Roy. Meteorol. Soc. Mem.* 2(16):69–95, March 1928.

44. KING, J. I. F., "Line Absorption and Radiative Equilibrium," *J. Meteorol.* 9(5):311–321, October 1952.

45. YAMAMOTO, G., "Radiative Equilibrium of the Earth's Atmosphere, I. The Grey Case," *Science Reports of the Tohoku University, 5th Series, Geophysics* 5(2):45–57, October 1953.

46. OHRING, G., "A Theoretical Estimate of the Average Vertical Distribution of Temperature in the Martian Atmosphere," *Icarus*, 1(4):328–333, January 1963.

47. KONDRATI'EV, K., "Teplovoi Rezhim Verkhnikh Sloev Atmosfery," ("Thermal Conditions of Upper Strata of the Atmosphere"). Leningrad: Gidrometeoizdat, 1960.

48. MANABE, S., and MÖLLER, F., "On the Radiative Equilibrium and Heat Balance of the Atmosphere," *Monthly Weather Rev.* 89(12):503–532, December 1961.

49. ARKING, A., "Non-Grey Convective Planetary Atmospheres," Eleventh International Astrophysical Symposium, Liege, July 9–12, 1962, 7:180–189, 1963.

50. HOWARD, J. N., BURCH, D. E. and WILLIAMS, D. E., "Near-infrared Transmission Through Synthetic Atmospheres," Ohio State University Research Foundation, Columbus, report SR-1, December 1954.

51. SIMPSON, W. M., *Proc. Eleventh Internat. Astrophys. Sym.*, Liege, July 9–12, 1962.

52. MÖLLER, F., "Über das Strahlungsgleichgewicht in der Nähe der Erdoberfläche," *Meteorol Rundsch.* 13(5): 134–139, September–October 1960.

53. MENZEL, D. H., and DE VAUCOULEURS, G., "Final Report on the Occultation of Regulus by Venus, July 7, 1959," Harvard College Observatory, Cambridge, report SR-1, January 10, 1961.

MIDDLE ULTRAVIOLET DAY RADIANCE OF THE ATMOSPHERE*

J. P. HENNES, W. B. FOWLER AND L. DUNKELMAN

The day radiance of the atmosphere has been measured, photoelectrically, at two middle ultraviolet wavelengths by rocket-borne photometers. Filters and collimators provided an effective field of view of 1.4×10^{-2} steradians, and bandpasses of approximately 100A at 2600A and 230A and 2200A. At a height of 146 km, nadir radiance values of about 0.5 ergs/sec cm² ster 100A were obtained at both wavelengths. There is good agreement between the radiance values measured and those which have been calculated on the basis of single Rayleigh scattering in the presence of ozone. From the radiance data an atmospheric diffuse reflectivity of about 8×10^{-4} at 2600A has been calculated. This may be contrasted with 1957 rocket observations of Mars and Jupiter which yielded albedos at 2700A of 0.94 and 0.26 respectively.

I. INTRODUCTION

If the earth's sunlit side is viewed from space it exhibits a bright appearance in the visible portion of the spectrum. In contrast, the appearance of the sunlit earth in the ultraviolet wavelength region below about 3100A may be expected to be rather dim and relatively uniform. In the visible region the upward flux out of the atmosphere is made up of Rayleigh scattered sunlight, sunlight reflected directly from clouds or from the earth's surface, light scattered from atmospheric dust, and a relatively small amount of resonant and fluorescent scattered sunlight or day airglow. In the middle ultraviolet region from 2100–3000A, however, because of the totally absorbing ozone region located from approximately 10 to 40 km, the day radiance will be produced only by Rayleigh scattering of sunlight in the thin upper atmosphere above the ozone region and by fluorescent scattered sunlight or ultraviolet dayglow. The combination of a thin atmosphere and strong ozone absorption produces a correspondingly low albedo. The absence of contributions from reflections by clouds and surface features and the strong wavelength dependence of Rayleigh scattering will produce a relatively uniform appearance.

The spherical albedo of a planet is the ratio of the total flux emitted in all directions by the planet to the total flux incident on the planet from the sun. Both quantities are being measured over the same wavelength interval. The earth's visual, spherical albedo has been experimentally determined, by studies of earth light on the moon, to range from 0.29–0.56 depending on the season and on which side of the earth is facing the moon. The average value of these visual albedos is given as 0.39–0.40 (Danjon, 1954; Dzhasybekova, Kazachevskii, and Kharitonov, 1960). The major part of the earth's visual albedo comes from contributions by reflection from clouds. If atmospheric scattering is considered separately, assuming no clouds, calculations (Kano, 1958) show the spectral albedos due to Rayleigh scattering to be: infrared region—.0075; visible region—0.096; and near ultraviolet region—0.23. The weighted sum of these various spectral albedos for a Rayleigh atmosphere is given as 0.066 by Kano (1958) for the entire spectral region $\lambda>2900$A, and has been independently calculated by Coulson (1959) to be p. 069. The contribution in these spectral regions from airglow is negligible except over narrow wavelength intervals near the more pronounced dayglow emission lines. The uses and difficulties of dayglow measurements have been summarized recently by Chamberlain (1963).

*Published as *Goddard Space Flight Center Document* X-613-64-70, April 1964; also published in the *Journal of Geophysical Research*, 69(13):2835–2840, July 1, 1964.

The calculations which have been made for scattered solar radiation in the near ultraviolet have included multiple scatterings, ozone distributions, and upward and downward fluxes (Sekera and Dave, 1961a, and Larsen, 1959).

In the middle ultraviolet region calculations have assumed single Rayleigh scattering with ozone absorption (Ban, 1962; Hubbard, 1963; Green, 1964; and Hrasky and McKee, 1964). Multiple scattering or fluorescence has not been included. The middle ultraviolet day radiance must originate in scattering above the ozone region. This insures a relatively small flux since even the high altitude ozone distribution is strongly absorbing in this spectral region. Dalgarno (1962, 1963) and Chamberlain and Sobouti (1962) have derived equations to show the effect of non-Rayleigh resonant and fluorescent scattering near atomic and molecular resonance lines, and point out that this effect could be significant in the ultraviolet where small Rayleigh scattered fluxes are expected.

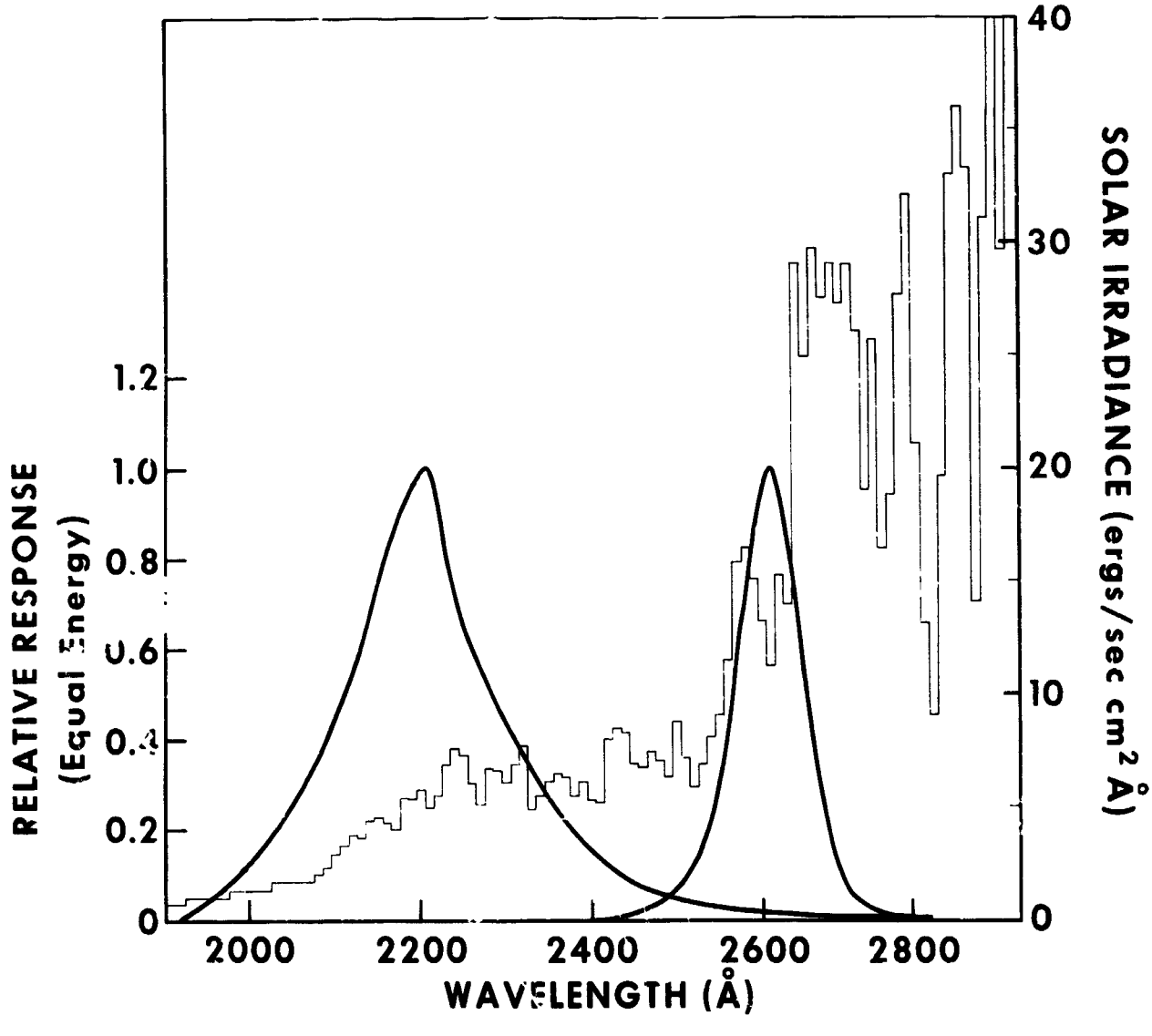

FIGURE 1.—Photometer response curves. Relative response of both photometers is shown on an equal energy basis. The solar spectrum, averaged over 10A intervals, is also shown. (Wilson et al., 1954; Malitson et al., 1960). The 2200A photometer response is provided by a combination of an interference filter and 4 mm $NiSO_4(H_2O)_6$, crystal. The 2600A photometer combines an interference filter, Corning 7-54, 4 mm $NiSO_4(H_2)_6$, Cation-X, and 2 mm Pb doped KCl:KBr crystal (Childs. 1961).

II. THE EXPERIMENT

At 1155 EST (1655 UT) on 8 August 1962 two middle ultraviolet photometers were included in an Aerobee rocket (NASA 4.60) launched from Wallops Island, Virginia. Measurements of the ultraviolet day radiance were taken continuously as the rocket climbed to a peak altitude of 150 km. Each photometer consisted of a mechanical collimator, a filter, and a photomultiplier sensitive only to ultraviolet radiation. The collimator produced an effective field of 1.4×10^{-2} ster (about a 7 degree square field). The filters were of the type described by Childs (1961). The phototubes were type EMR 541F–05 photomultipliers with sapphire windows and cesium-tellurium cathodes (Dunkelman, Fowler, and Hennes, 1962).

The relative spectral response of these photometers is given in Figure 1 on an equal energy basis (amps/watt). Also included in Figure 1 is the solar spectrum, averaged over 10A intervals, taken from data reported by Wilson, et al., (1954) and Malitson, et al., (1960). The effective wavelengths of the photometers were at 2217A and 2610A with effective bandwidths of 230A and 100A respectively. The contribution from the long wavelength region beyond 2800A has been examined and found to be much less than the magnitudes of the radiance measurements made.

During the flight the rocket pitched through a wide range of zenith angles. Its motion, however, was confined by an attitude control system to a single plane having an azimuth of 175° passing through the zenith and the sun. The sun was at a zenith angle of 22°. The photometers, which were pointed out the side of the rocket approximately in the pitch plane and at an angle of 122° with the rocket axis, swept from the nadir up to a zenith angle of about 80° in both the north and south sky at various times.

III. RESULTS

The data are shown in Figure 2 which give (curve a) the zenith angle of the photometers as a function of both flight time and altitude. The aspect data was obtained from solar sensing aspect cells, magnetometers, and the attitude control system error signals and pitch-rate signals. During the flight the rocket's attitude control system malfunctioned to the extent that, although controlled in two axis, the vehicle pitched through much larger angles than those for which the aspect instruments had been designed. Pitch rate signals were integrated to find approximate zenith angles outside of the region of aspect sensor operation. These calculations could be checked by fitting with the aspect signals as the rocket periodically moved back throu the sensor region. The photometer data, reduced from the original telemetry record at one second intervals, are shown in curves (b) and (c). Relative intensity is plotted, with the data normalized to unity for nadir (180°) values. The scatter in the relative intensity values is produced by photometer noise introduced because the signal level was near the bottom of a three-decade logarithmic scale. The photometer sensitivity in this exploratory measurement had been set low to avoid the possibility of saturation due to either unexpectedly large reflectivities or unusually intense dayglow or auroral emissions. Lines have been added to clarify the peaks beyond 260 seconds.

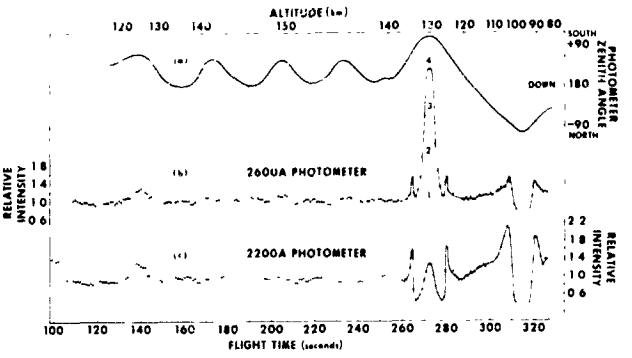

FIGURE 2.—Rocket flight data. Curve (a) is the zenith angle of the photometer direction as a function of time. Curves (b) and (c) are a sampling of the reduced telemetry data plotted in terms of the relative intensity received by the photometer. The points show scatter produced by photometer noise and a small amount of structure as a function of zenith angle. The peaks after 260 seconds correspond to the horizon limb brightening. The large peak at 273 seconds, which is extraneous, is produced by sunlight reflected off the photometer entrance with the photometers pointed above the horizon in the south. Without this sunlight effect the record would appear as it does at 310–320 seconds with the photometers pointed above the horizon in the north.

In Figure 3 the data are replotted as a function of zenith angle. Data are shown only for 10 degree intervals of zenith angle. Part of the spread in the points is due to photometer noise,

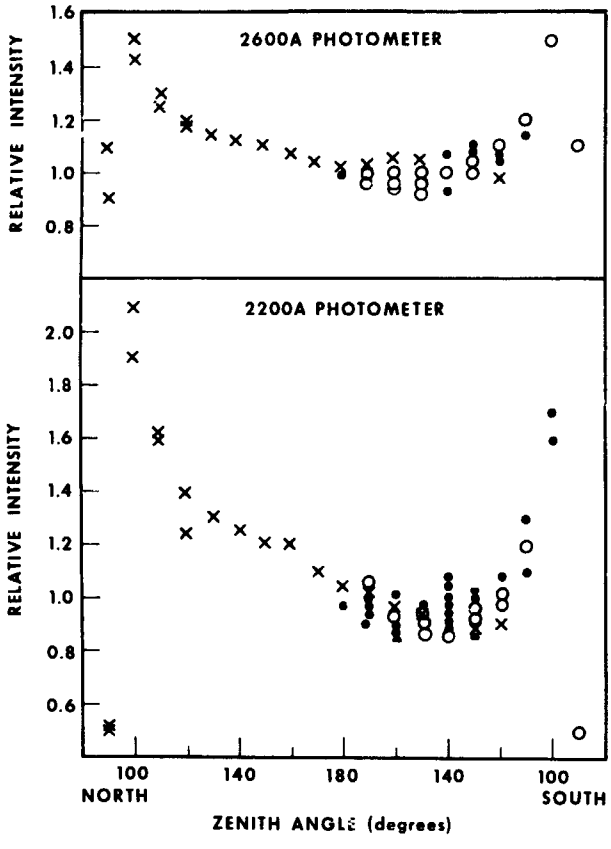

FIGURE 3.—Ultraviolet day radiance as a function of zenith angle. The data in Figure 2 are replotted here as a sampling of telemetry data taken at 10 degree intervals. The crosses indicate data taken at altitudes less than 120 km. Circles indicate data taken at altitudes above 120 km. Solid circles are single points, open circles represent several data points (2–5) occupying the same position. The limb brightening is evident.

part is due to combining data taken at the same zenith angles but from different altitudes.

The values of day radiance measured during this flight are notable for the lack of features seen over a large range of zenith angles. Even the horizon brightening is only a factor of two times the nadir radiance. The photometer field of 1.4 $\times 10^{-2}$ steradians would, of course, diminish the effect of any increased radiance that extended over only a relatively narrow field.

The peaks at about 272 seconds in Figures 2 represent direct sunlight reflected off the photometer entrance. The photometer was pointed up in the southern sky at that point at a zenith angle of about 70 degrees. The magnitude of the reflected solar signal under those conditions was determined by laboratory measurements to be about 10^{-5} that of direct sunlight. Note that this scattered light signal is still larger than the earth radiance signal. The problem of making measurements in the presence of direct sunlight is emphasized by this result.

The magnitude of the radiances detected by the photometers is expressed in Table 1. The nominal effective wavelength and the effective band width are given. The third column gives the earth's radiance, at the nadir, with the sun at 22° zenith angle, assuming a uniform and equal distribution across the wavelength region described by the effective bandwidth. The equivalent photon emission rate in kilo-rayleighs per 100A is also given. The day radiance values determined by these measurements have uncertainties of about 10–15 percent arising from noise in the photometer signal and uncertainties in ultraviolet radiometric standards.

The last column gives the diffuse spectral reflectivity of the earth's sunlit atmosphere averaged over each of the wavelength intervals. This number is arrived at by assuming the scattered sunlight has the same spectral distribution as the incident sunlight throughout each bandwidth (see Figure 1). The values of solar irradiance are taken from the sources cited. The uncertainties in the calculated reflectivities are greater than

TABLE 1.—*Ultraviolet Day Radiance Measurements of the Earth Taken 8 August 1962, at 146 km, with Photometers Pointed at the Nadir; Solar Zenith Angle 22°.*

Nominal Wavelength (A)	Effective Bandwidth (A)	Radiance (ergs/sec cm² ster 100A)	Emission (kilorayleigh/100A) Rate	Diffuse Reflectivity
2600	100	0.5	8×10^{2}	8×10^{-4}
2200	230	0.5	7×10^{2}	3×10^{-3}

those for our observed radiance values by the amount of uncertainty in published absolute spectral solar intensities. If we make the further assumption that the entire earth is a diffuse Lambert reflector, then the diffuse reflectivity of about 8×10^{-4} at 2600A becomes the earth's spherical albedo. This number can be contrasted with the earth's total observable spherical albedo of 0.39–0.40, and with the calculated Rayleigh scattered albedo contribution in the near ultraviolet of 0.23 as given in the introduction.

Of interest also is a comparison of the earth's low middle ultraviolet effective albedo with measurements of the relatively high effective albedos of Mars and Jupiter made in 1957 with a photometer of about 300A bandwidth centered at 2700A (Boggess and Dunkelman, 1959). They obtained values of about 0.24 for Mars and 0.26 for Jupiter.

One other known experimental observation has been made of the middle ultraviolet day radiance. Friedman, Rawcliffe, and Meloy (1963) have reported a satellite borne photometer measurement of the day radiance with a spectral pass band of 140A centered at 2550A. Their result, with the sun at a zenith angle of 49° and the detector pointed at the nadir with a field of 1.2×10^{-4} steradian, showed an atmospheric radiance of 2.0 ± 0.3 ergs/sec cm^2 ster 100A.

Table 2 gives the various measured and calculated middle ultraviolet day radiance values. The calculated values tend to support our results rather well. It should be borne in mind that the data were all taken or calculated using different parameters of altitude, solar zenith angle, ozone distribution, season, etc. so that the results cannot be compared too directly. The relatively large factor of four between the experimental results of Friedman, Rawcliffe and Meloy and ourselves is possibly explained by either a large change in the high altitude ozone distribution between the time of the two measurements or the difficulties in maintaining calibration during the preparations for and launching of a satellite. The similarity of the various calculations and our measurements indicate that the simple approach to ultraviolet atmospheric radiance calculations, involving use of ozone distributions and single scattering with plane atmospheres (Ban, 1962; Hubbard, 1963; and Green, 1964) or spherical atmospheres (Hrasky and McKee, 1964) is adequate for broadband measurements. If higher spectral resolution were to be considered the agreement might be strongly affected by resonant or fluorescent scattering.

The calculated results depend very strongly on ozone distribution, especially in the region around

TABLE 2.—*Comparison of Measured and Calculated Nadir Ultraviolet Day Radiance Values. Radiance in ergs/sec cm² ster 100A.*

Source	2600A Region		2200A Region		Solar Zenith Angle
	Average Radiance Over Interval[a]	Wavelengths (A)	Average Radiance Over Interval[a]	Wavelengths (A)	
This work[b]	0.5	2560–2660	0.5	2100–2330	22°
Friedman, et al. (1963)[b]	2.0	2480–2620			49°
Ban (1962)[c]	0.5	2550–2650			0°
Hubbard (1963)[c]	0.4[d]	2550–2650			0°
Green (1964)[c]	0.5[e]	2550–2650	0.7	2100–2330	0°
Hrasky & McKee[c] (1964)	0.4	2550–2700	0.5	2000–2100	22°

(a) Values estimated or rounded off from data published by the referenced authors.
(b) Measured values.
(c) Calculated values.
(d) A range of 0.05—0.8 is estimated depending on the ozone distribution chosen. The radiance listed is taken from Figure 14 representing a "standard" ozone curve.
(e) A range of 0.15—0.6 is estimated depending on the ozone distribution chosen. The radiance listed is taken from Figure 6 representing an analytical fit to the same "standard" ozone curve as used by Hubbard.

the peak of the ozone absorption curve at 2600A where the very high altitude ozone has a dominant role. The ozone distribution at higher altitudes is relatively unknown, however, so that appreciable uncertainties may be introduced into the calculated values. At the shorter wavelength region around 2200A and at longer wavelengths beyond 2800A the ozone is much less absorbing and incident solar radiation will penetrate more deeply into the atmosphere, thus permitting more scattering and producing higher albedos. By use of satellite-borne photometers with narrow spectral bandpasses, well removed from strong dayglow emission lines, and situated at various middle ultraviolet wavelengths from 2100 and 3000A, a profile of high altitude ozone distribution should be obtainable. Such an idea was proposed in 1957 by Singer and Wentworth (1957), who considered only wavelengths at 2800 and 3000A. Twomey (1961) carried out further calculations in this same wavelength region. The calculations in the near ultraviolet above 3000A have been considered in detail by Sekera and Dave (1961b). The altitudes above 50 km would require, however, use of wavelengths below 2800A where analysis should be much easier. The seasonal and latitudinal variations in upper atmosphere ozone, so important to atmospheric heating processes, would thus be available.

ACKNOWLEDGEMENT

We wish to express our appreciation to William Russell, Jr. of this Center who graciously provided support and the space for this experiment on one of the rockets under his supervision.

REFERENCES

BAN, G. R., "Scattered Radiance in the Middle Ultraviolet Region," in *Symposium on Military Applications of Ultraviolet Radiations*, Report LAS-TR-199-37, University Chicago, Laboratory for Applied Science, 1962.

BOGGESS III, A., and L. DUNKELMAN, "Ultraviolet Reflectivities of Mars and Jupiter," Astrophys. J., **129**, 236, 237, 1959.

CHAMBERLAIN, J. W., "Airglow and the Physics of Upper Atmospheres," Science, **142**, 921–924, 1963.

CHAMBERLAIN, J. W. and Y. SOBOUTI, "Fluorescent Scattering in Planetary Atmospheres. I. Basic Planetary Considerations," Astrophys. J., **135**, 925–937, 1962.

CHILDS, C. B., "Broad Band Ultraviolet Filters," J. Opt. Soc. Amer., **51**, 895–897, 1961.

COULSON, K. L., "Characteristics of the Radiation Emerging from the Top of a Rayleigh Atomsphere. II. Total Upward Flux and Albedo," Plant Space Sci., **1**, 277–284, 1959.

DALGARNO, A., "Spectral Reflectivity of the Earth's Atmosphere, III: The Scattering of Light by Atomic Systems," Geophysics Corp. of America Report 62–28–A, 1962.

DALGARNO, A., "Rayleigh Scattering Near an Absorption Line," J. Opt. Soc. Amer., **53**, 1222, 1963.

DANJON, A., "Albedo, Color, and Polarization of the Earth," in *The Earth as a Planet*, edited by G. P. Kuiper, pp. 726–738, Univ. of Chicago Press, Chicago, 1954.

DUNKELMAN, L., W. B. FOWLER, and J. P. HENNES, "Spectrally Selective Photodetectors for the Middle and Vacuum Ultraviolet," Appl. Optics, **1**, 695–700, 1962.

DZHASYBEKOVA, E. K., V. M. KAZACHEVSKII, and A. V. KHARITONOV, "Determination of the Earth's Albedo," Astron. Zh., **37**, 131–134, 1960; translated in Soviet Astronomy–AJ, **4**, 125–128, 1960.

FRIEDMAN, R. M., D. RAWCLIFFE, and G. E. MELOY, "Radiance of the Upper Atmosphere in the Middle Ultraviolet," J. Geophys. Res., **68**, 6419–6423, 1963.

GREEN, A. E. S., "Attenuation by Ozone and the Earth's Albedo in the Middle Ultraviolet," Appl. Optics, **3**, 203–208, 1964.

HRASKY, W. C., and T. B. McKEE, Langley Research Center, NASA, Hampton, Virginia, private communication, 1964.

HUBBARD, E. L., "Calculation of the Intensity of Light Scattered in the Atmosphere in the Wavelength Region 2300A to 3100A with Absorption by Oxygen and Ozone Considered," Report Sciences, Sept. 1963.

KANO, M., "The Albedo of the Earth's Atmosphere," Papers in Meteorology and Geophysics, Tokyo, **9** (2), 113–122, 1958.

LARSEN, S. H. H., "On the Scattering of the Ultraviolet Solar Radiation in the Atmosphere with the Ozone Absorption Considered," Geofys. Publ., **21** (4), 1959.

MALITSON, H. H., J. D. PURCELL, R. Tousey, and C. E. MOORE, "The Solar Spectrum from 2635 to 2085A," Astrophys. J., 132, 746–766, 1960.

SEKERA, Z. and J. V. DAVE, "Diffuse Transmission of Solar Ultraviolet Radiation in the Presence of Ozone," Astrophys. J., **133**, 210–227, 1961a.

SEKERA, Z. and J. V. DAVE, "Determination of the Vertical Distribution of Ozone from the Measurement of Diffusely Reflected Ultraviolet Solar Radiation," Planet. Space Sci., **5**, 122–136, 1961b.

SINGER, S. F., and R. C. WENTWORTH, "A Method for the Determination of the Vertical Ozone Distribution from a Satellite," J. Geophys. Res., **62**, 299–308, 1957.

TWOMEY, S., "On the Deduction of the Vertical Distribution of Ozone by Ultraviolet Spectral Measurements from a Satellite," J. Geophys. Res., **66**, 2153–2162, 1961.

WILSON, N. L., R. TOUSEY, J. D. PURCELL, and F. S. Johnson, "A Revised Analysis of the Solar Spectrum from 2990–2635A," Astrophy. J., **119**, 590–612, 1954.

LYMAN-α RESONANT SCATTERING USING RANDOM STOKES VECTORS*

S. O. KASTNER

The case of relatively few scatterings of Lyman-α resonance radiation in a uniform hydrogen gas is treated by using Stokes vectors as random variables in a Monte Carlo type of calculation. Doppler redistribution of frequencies and the doublet nature of the line are taken into account.

INTRODUCTION

In radiative transfer problems in which the number of scatterings is low, the nature of the individual scattering process becomes important, i.e. whether isotropic or anisotropic. Lyman-α resonance scattering is an example in which one line component scatters isotropically, the other anisotropically.

We describe here a use of random Stokes vectors in a Monte Carlo type of calculation, to obtain the fluxes of Lyman-α radiation at various levels in a uniform (density and temperature) atmosphere of hydrogen atoms. The method incorporates Doppler redistribution of frequencies, and takes account accordingly of the fact that a photon may be scattered by either of the components of the Lyman-α doublet in the course of its flight. The polarization at each level could also be obtained from the same calculation, if required, by adding up the Stokes vectors. A non-uniform atmosphere was initially attempted, but pointed up a problem in that the mean free path of a photon becomes anisotropic and the anisotropy varies with level.

The interest in this approach stemmed from the possibility of its application to upper atmosphere night glow and similar phenomena in which the intensities, frequencies and polarization of the radiation may be sampled directly by rocket instruments as a function of altitude.

DESCRIPTION OF GENERAL APPROACH

A convenient way to characterize a beam of photons is by the Stokes vector, whose four components describe its intensity and state of polarization completely. The scattering of a photon may then be described by a scattering matrix operating on its Stokes vector to produce a new Stokes vector. If the photon suffers a subsequent scattering, the process is repeated on the new stokes vector, after first taking account of the fact that the coordinate system has changed. McMaster[1] gives an example of this in double Compton scattering.

The scattering matrix for resonant scattering is given in a general form by Chandrasekhar.[2] This is specialized to the Lyman-α case by putting in the appropriate atomic constants. There are two scattering matrices involved in Lyman-α scattering, because two transitions are involved, one isotropic and the other anisotropic.

Successive scatterings of this kind are set up in the present calculation. An incident photon (specified Stokes vector) is injected into the plane parallel atmosphere of H atoms. Its frequency is randomly picked within an assumed Doppler profile, and its direction of incidence may be either randomly picked from an isotropic distribution or chosen at a fixed angle.

The photon encounters an H atom every mean free path λ, where

$$\lambda = \frac{1}{N\sigma},$$

N being hydrogen number density, σ the cross-section for resonant scattering. However, it is not actually scattered if its frequency relative to the H atom is not the same as either one of the two Lyman-α components. It continues on until it does encounter an H atom such that its relative

*Published as *Goddard Space Flight Center Document X-614-64-165.*

frequency lies within the natural width of either of the two Lyman-α components; its Stokes vector is then multiplied by the corresponding scattering matrix. The direction of the scattered photon is decided on the basis of the intensity distribution given by the first two components of the Stokes vector.

(The atom absorbing a photon at any frequency within the natural width is made to re-emit the photon at only the center frequency. This corresponds to an arbitrary kind of redistribution. Actually, when a given atom is illuminated by a line broader than its natural width, its scattering redistributes the radiation over the natural width Heitler.[3] The natural width is negligible compared to the line width here, however.)

This process is repeated for the scattered photon so that successive scatterings are undergone, and the photon describes a random walk in the medium. The medium is divided into 100 zones, and a count of positive and negative flux is kept for each zone.

When the photon escapes from the prescribed region, either forward or backward, a new photon is injected.

DETAILS OF CALCULATION

[a] Photon Path

The medium is taken to extend from $z=0$ to $z=1$ and is infinite in the x, y directions. Photons are injected at $z=0$. The i-$^{\text{th}}$ collision-free path of a given photon has the direction cosines (l_i, m_i, n_i). The first scattering results in a scattering direction (l_2, m_2, n_2) which makes an angle θ with the incident direction (l_1, m_1, n_1) and has azimuthal angle φ (Cashwell and Everitt,[4] Ch. VII): θ and φ are chosen as in section (c) below. In subsequent scatterings the scattering angle θ is obtained by the procedure of section (d).

[b] The Lyman-α Scattering Matrix

The general resonant scattering matrix is given by Chandrasekhar[2] as:

$$T=\begin{vmatrix} (\frac{3}{4}E_1\cos^2\theta+\frac{1}{2}E_2) & \frac{1}{2}E_2 & 0 & 0 \\ \frac{1}{2}E_2 & (\frac{3}{4}E_1+\frac{1}{2}E_2) & 0 & 0 \\ 0 & 0 & \frac{3}{2}E_1\cos\theta & 0 \\ 0 & 0 & 0 & \frac{3}{2}E_3\cos\theta \end{vmatrix}$$

in which θ is the scattering angle and the constants E_1, E_2, E_3 depend on the particular energy levels involved.

In the case of Lyman-α, the transitions involved in resonant scattering are $(1s^2S\frac{1}{2}-2P^2P\frac{1}{2})$ and $(1s^2S\frac{1}{2}-2p^2P\frac{3}{2})$. For the first, $j=0$, initial $j=\frac{1}{2}$, and for the second $j=+1$, initial $j=\frac{1}{2}$. The constants E_1, E_2, E_3 are therefore respectively (0, 1, $\frac{2}{3}$) and ($\frac{1}{2}$, $\frac{1}{2}$, $\frac{5}{6}$).

[c] The First Scattering

The incident Stokes vector, which is multiplied by the scattering matrix T, is:

$$S_0=\begin{vmatrix} I_l^0 \\ I_r^0 \\ U^0 \\ V^0 \end{vmatrix}$$

(The relation between this set of components and the alternative set used by McMaster is discussed by Van de Hulst.[5] The component V does not mix with the others in the scattering process so that we can work with the first three components only throughout the calculation. It will be seen that U does get mixed with I_l and I_r in successive scatterings, however.

The scattered photon has its Stokes vector given then by

$$S_1=TS_0$$

If S_0 is the Stokes vector for natural (unpolarized) light,

$$S_0=\begin{vmatrix} \frac{1}{2} \\ \frac{1}{2} \\ 0 \end{vmatrix}$$

the first scattering gives a Stokes vector S_1 which is a function only of the scattering angle θ:

$$S_1=\begin{vmatrix} \frac{3}{4}E_1\cos^2\theta+\frac{1}{2}E_2 \\ \frac{3}{4}E_1+\frac{1}{2}E_2 \\ 0 \end{vmatrix} \equiv \begin{vmatrix} I_l' \\ I_r' \\ U' \end{vmatrix}$$

The probability of the photon actually being scattered at an angle θ_1 is taken to be proportional to the intensity sum $I_l'+I_r'$; θ_i is chosen randomly within this probability distribution by the Von Neumann device described by Cashwell and

Everitt.[4] The azimuth angle φ of the scattered photon is chosen at random within the interval $(0-2\pi)$.

[d] Subsequent Scatterings

Because the plane of the second scattering is rotated in general by an angle χ about the direction of incident propagation with respect to the plane of the first scattering, the Stokes vector S_1 is transformed by a matrix $M(\chi)$, where

$$M(\chi)=\begin{vmatrix} \cos^2\chi & \sin^2\chi & \frac{1}{2}\sin 2\chi \\ \sin^2\chi & \cos^2\chi & -\frac{1}{2}\sin 2\chi \\ -\sin 2\chi & \sin 2\chi & \cos 2\chi \end{vmatrix}$$

into a vector:

$$S_1'=\begin{vmatrix} \cos^2\chi(\frac{3}{4}E_1\cos^2\theta+\frac{1}{2}E_2)+\sin^2\chi(\frac{3}{4}E_1+\frac{1}{2}E_2) \\ \sin^2\chi(\frac{3}{4}E_1\cos^2\theta+\frac{1}{2}E_2)+\cos^2\chi(\frac{3}{4}E_1+\frac{1}{2}E_2) \\ -\sin 2\chi(\frac{3}{4}E_1\cos^2\theta+\frac{1}{2}E_2)+\sin 2\chi(\frac{3}{4}E_1+\frac{1}{2}E_2) \end{vmatrix} \equiv \begin{vmatrix} S_1'(1) \\ S_1'(2) \\ S_1'(3) \end{vmatrix}$$

multiplying this by T gives the resultant scattered Stokes vector S_2:

$$S_2=\begin{vmatrix} (\frac{3}{2}E_1\cos^2\theta+\frac{1}{2}E_2)S_1'(1)+(\frac{1}{2}E_2)S_1'(2) \\ \frac{1}{2}E_2\,S_1'(1)+(\frac{3}{2}E_1+\frac{1}{2}E_2)S_1'(2) \\ (\frac{3}{2}E_1\cos\theta)S_1'(3) \end{vmatrix} \equiv \begin{vmatrix} S_2(1) \\ S_2(2) \\ S_2(3) \end{vmatrix}$$

photons. Fig. 1 is a simplified flow chart of the program.

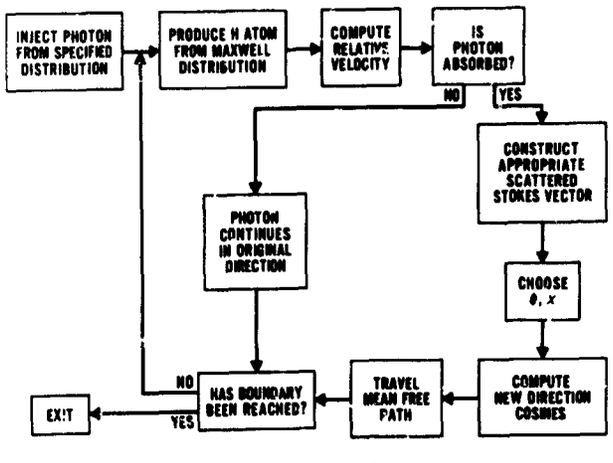

FIGURE 1.—Simplified flow chart.

To find an actual angle θ_2 resulting from the second scattering, the Von Neumann device is again used on the probability distribution

$$p^\theta=S_2(1)+S_2(2)$$

after first randomly choosing χ in the interval $(0-2\pi)$. (The assumption is thereby made that the plane of the second scattering is randomly related to that of the first).

[e] Computer Program

A computer program was written by C. Wade to carry out the calculation. It includes provision for injecting either a unidirectional beam at any specified angle, or isotropically incident

RESULTS AND DISCUSSION

A uniform plane-parallel atmosphere of hydrogen atoms at temperature 500°K, and of 500 km thickness, was taken as the medium on which to run the calculation. Two densities were successively assumed, 1.0×10^5/cc and 2.0×10^5/cc, and with each density two different isotropically incident radiation profiles were used, corresponding to Doppler temperatures T_D of 500°K and 5000°K. The curves of Fig. 2 were obtained for the four cases, each representing results for about 5000 photons. (A computer run for 5000 photons was about one half hour long). The ordinate represents the relative number of photons passing forward through a given plane in the atmosphere specified by the abscissa. Since all photons crossing a given plane are counted, the number corre-

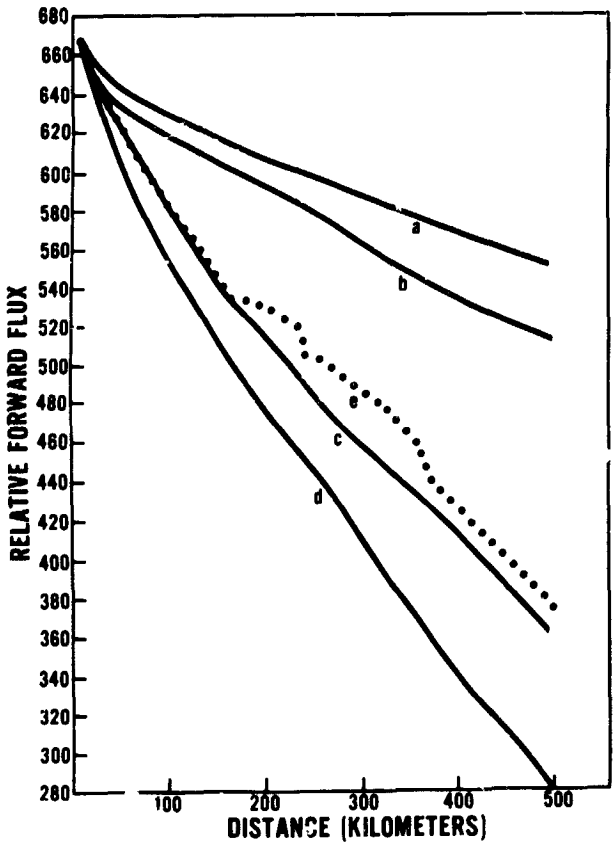

FIGURE 2.—Relative flux distributions.

sponds to the hemispheric flux πF of transfer theory, or to photometric radiancy.

The dotted curve represents the results of case (*c*) for a smaller sample of 1000 photons. The curve (*c*) for 5000 photons departs somewhat from the dotted curve, showing that "statistical equilibrium" has not yet been completely reached. Further runs were not made, however, because the models considered here are not of interest in themselves.

The average number of scatterings per photon in each case was: (*a*) 0.67, (*b*) 1.28, (*c*) 1.96, (*d*) 3.43. The reflection coefficients or albedos were: (*a*) 0.18, (*b*) 0.23, (*c*) 0.46, (*d*) 0.58. Broadening of the incident frequency profile gives greater transparency of the atmosphere to the radiation, as expected, while the two-fold increase in atmospheric density gives greater opacity.

An analytic treatment of the problem would involve the solution of a system of transport equations,[6] with a kernel which incorporates both the resonant scattering matrix and the Doppler redistribution in frequency.[7] The difficulty of this analysis precludes a complete check of the results, but at the same time is an argument for the convenience of the present method.

It may be that the use of a simpler scattering process, i.e. scattering by a single $1s-2p$ transition, would give essentially the same results.

SUMMARY

The use of Stokes vectors as random variables appears to be an effective way of handling some radiative transfer problems. We have applied the method here to Lyman-α scattering in a uniform gas of hydrogen atoms, of density low enough that few scatterings occur. It may be possible, with further work, to extend it to the case of a non-uniform atmosphere.

The same calculation can also, if required, give the frequency, profile and the polarization of the radiation at any level if the frequencies and Stokes vectors are recorded.

REFERENCES

1. W. H. McMASTER, Am. Jour. of Phys. *22*, 351 (1954).
2. S. CHANDRASEKHAR, Radiative Transfer, p. 51. Dover Publications: New York (1960).
3. W. HEITLER, The Quantum Theory of Radiation, 3rd ed., p. 201. Oxford Univ. Press, Oxford (1954).
4. CASHWELL and EVERETT, The Monte Carlo Method, Pergamon Press (1959).
5. H. C. VAN DE HULST, Light Scattering by Small Particles, p. 41. John Wiley and Sons, Inc., New York (1962).
6. U. FANO, L. V. SPENCER and M. J. BERGER, in Handbuch der Physik *38/2*, p. 684. Springer-Verlag, Berlin (1959).
7. L. G. HENYEY, Proc. Nat. Acad. Sci. *26*, 50 (1940).

NG4-23372

INFRASONIC WAVES FROM THE AURORAL ZONE*

KAICHI MAEDA AND TOMIYA WATANABE†

Pulsating aurorae are proposed as a source of the infrasonic waves associated with geomagnetic activity reported by Chrzanowski et al. One of the most plausible generation mechanisms of these long period pressure waves is the periodic heating of the air around 100 km, corresponding to the auroral coruscation reported by Campbell and Rees. In order to show the energetic relationship between source input and pressure change at sea level, some theoretical calculations are performed by using a simple model of auroral distribution in the isothermal atmosphere.

INTRODUCTION

The purpose of this paper is to interpret the origin of the strange traveling atmospheric waves observed at the ground during intervals of high geomagnetic activity (Reference 1). In particular, discussion centers on possible modes of atmospheric oscillations caused by the periodic bombardment of auroral particles in the polar mesosphere.

Trains of the waves are detected by a system of four microphones placed on each corner of a quadrant roughly 8 km square, located north of Washington, D. C. The presence of a traveling wave is established when the same wave forms can be found on all four records with certain time shifts between them. These time displacements are used to determine the direction of wave propagation and the horizontal phase velocity of the waves. The periods of these infrasonic waves are usually 20 to 80 sec, but occasionally 100 to 300 sec waves are recorded. The pressure amplitude ranges from about 1 to 10 dynes/cm^2.

One of the peculiar features of these waves is the change of arrival direction with time of day. The general trend is from the northeast in the evening, from the north about midnight, and from the northwest in the morning. The shift back to northeast is somewhat discontinuous. These waves occur less frequently in the daytime.

Since auroral activity predominates at about midnight local time, the time dependence of the appearance of infrasonic waves during intervals of high geomagnetic activity can be explained by assuming that the source of this kind of wave is located somewhere in the auroral region, as can be seen from Figure 1. The left side of this figure shows the diurnal variation of the arrival of sound waves during magnetic storms, reported by Chrzanowski et al. (Reference 1). This assumption is consistent with the finding that the enhancement of the wave intensity at Washington, D. C. is generally delayed several hours after the increase of geomagnetic activity, except in the case of very severe magnetic storms. During these storms the delay is less than 30 minutes, indicating southward spread of the source of these waves near Washington, D. C.

In attempting to understand these peculiar pressure waves, it is proposed that they originate from a certain domain of the ionospheric region in the auroral zone which is heated periodically by a severe bombardment of auroral particles. It is thought that this periodic precipitation of auroral particles occurs simultaneously with geomagnetic pulsations.

INTERRELATIONS BETWEEN GEOMAGNETIC FLUCTUATIONS, PULSATING AURORAE, AND INFRASONIC WAVES

The auroral luminosity often fluctuates with incoming auroral particles. The fluctuations of these particles, mostly electrons, can be explained by either a periodic change in the acceleration mechanism of incident particles or by the change of mirror heights of trapped particles in the earth's atmosphere, following the variations of the field intensity of the earth's magnetosphere. The variations of geomagnetic field intensity and of auroral brightness are therefore closely related. A clear example of the correspondence between

*Published as *NASA Technical Note* D-2138, June 1964.
†University of British Columbia.

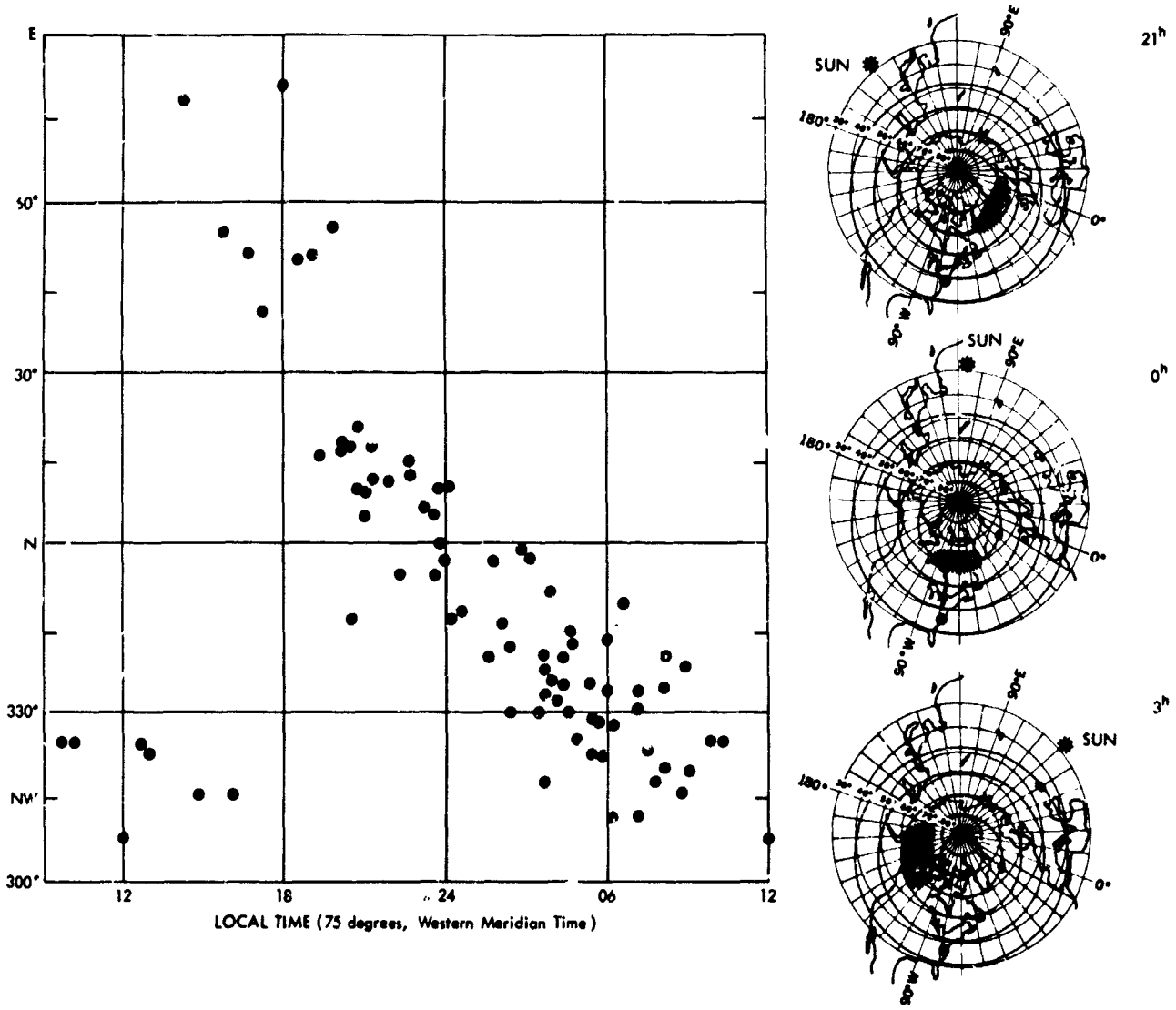

FIGURE 1.—Diurnal variation of the arrival direction of infrasonic waves during magnetic storms observed at the National Bureau of Standards, Washington, D.C. The three figures on the right indicate the shifts of the source of the pressure waves, corresponding to the movement of auroral activity.

the pulsating aurorae and the rapid variation of geomagnetic intensity observed at the ground has been given by Campbell (Reference 2).

According to the analysis of the space probe data given by Sonnet et al. (Reference 3), and that of Explorer X (1961 κ1) given by Heppner et al. (References 4 and 5), the region near the geomagnetic equator beyond about 10 earth radii is occasionally greatly disturbed. Such disturbances may be propagated along the magnetic lines of force as hydromagnetic waves, and are transformed into electromagnetic waves when they reach the conducting ionosphere (References 6–8). After penetrating the ionospheric region as electromagnetic waves, they are almost perfectly reflected at the earth's surface (Reference 9). This produces standing hydromagnetic waves along magnetic lines of force. The simplest mode of such standing waves is the fundamental mode, whose unique node is on the geomagnetic equatorial plane, with two loops of oscillation on the ends of the line of force on the earth, one in each hemisphere. This mode of oscillation has been investigated theoretically by Dungey (Reference 10), who called it the normal mode of torsional oscillations of the magnetic field in the earth's cavity. The eigen period of these oscillations increases rapidly with the latitude of the magnetic

line of force intersecting the earth's surface, varying from several tens of seconds in the subauroral region to about 10 minutes in the polar region (References 11–13).

In addition to the above mode, there is another mode of oscillation responsible for geomagnetic pulsations of shorter periods. As noted by Dessler (Reference 11), the velocity of Alfvèn waves decreases very rapidly with decreasing height in the exospheric region below around 2,000 km. Therefore, because of the continuity of energy flow Alfvèn waves of certain periods coming from the outer exosphere can be expected to be intensified. In this mode of oscillation, the layer of maximum Alfvèn velocity, approximately between 1500 and 3000 km, becomes the node of oscillation, and the loop of oscillation is near the earth's surface. This mode of hydromagnetic oscillation corresponds to the geomagnetic pulsations with periods from about 1 to several seconds, which appear more frequently in nighttime than in daytime (Reference 15).

In considering the above facts, it might be speculated that a possible mechanism for the production of infrasonic waves during auroral activity would be the penetration of Alfvèn waves, including modified Alfvèn waves and retarded sound waves (Reference 13), through the ionosphere. However, as will be shown later, these contributions are very small compared with the pressure disturbances produced by the periodic heating of the lower ionosphere caused by auroral bombardments.

As shown by Heppner (Reference 16) auroral activity predominates around midnight local time and the active region extends towards lower latitudes with increasing activity; pulsating aurorae appear at this phase of auroral activity. In other words, among several types of auroral displays pulsating aurorae appear with the largest disturbance in energy and they occur in fairly low latitudes.

According to Campbell and Ress (Reference 17) the peak of pulsating aurorae is around 100 km, the bottom is at 90 km, the effective thickness is of the order of 20 km, and the most frequent period is from 6 to 10 sec. From the direct measurement of auroral particles by means of rocket borne detectors, the energy flux of auroral particles, mostly electrons, is of the order of several tens of ergs/cm²–sec at weak aurora and increases by more than a factor of 50 at bright aurora (Reference 18). Thus, the energy flux in a strong pulsating aurora can be estimated to be of the order of 10^3 ergs/cm²–sec or more. This figure is consistent with the estimate given by Chamberlain (Reference 19), based on measurements of auroral luminosity.

On the other hand, the energy flux of hydromagnetic waves deduced from the magnetic pulsation data is less than 10 ergs/cm²–sec below 200 km. The energy flux of hydromagnetic waves increases with height. However, the contribution to pressure waves in the lower atmosphere decreases with the increasing height of the source, as will be shown later.

Another evidence for the present idea is the very good correspondence between the appearance of pulsating aurorae and that of infrasonic waves (Figure 2). The occurrence of pulsating aurorae shown on the right of Figure 2 is taken from the visoplot of auroral activity, reported by IGY

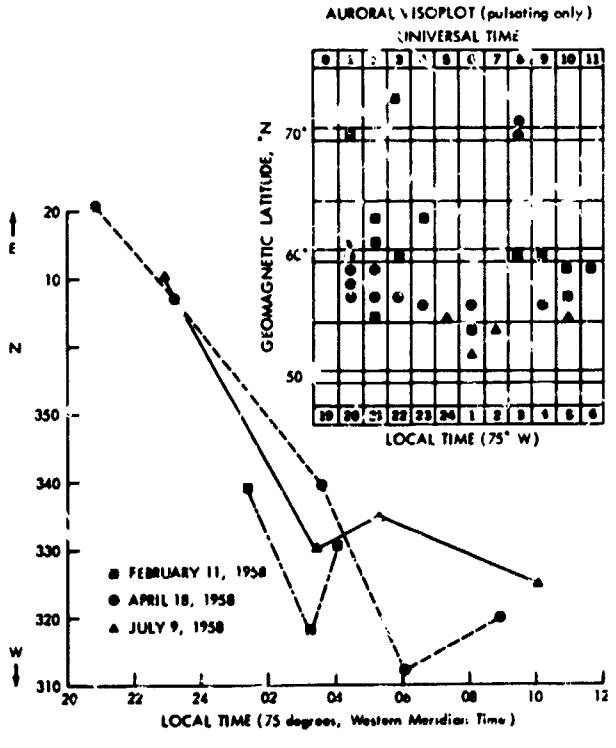

FIGURE 2.—Diurnal variation of the arrival direction of infrasonic waves during specific magnetic storms detected at the National Bureau of Standards, Washington, D. C. (Chrzanowski et al., 1960), and corresponding auroral activities observed in the northern hemisphere.

World Data Center A, on days which correspond to the events, reported by Chrzanowski et al. (Reference 1), shown on the left of this figure. Two occurrences of infrasonic waves in 1957 were reported, but since no visoplots of auroral activity are available before the IGY, they are omitted from this figure. The arrival direction of these waves might deviate from their true direction because of strong wind systems in high altitudes. Therefore, the appearances of pressure waves do not necessarily match the pulsating auroral events in detail. However, it is quite clear that there is a close correspondence between infrasonic waves and pulsating aurorae.

MATHEMATICAL TREATMENT

It is obvious that ray theory is not applicable in this problem, because the wavelength is of the order of an atmospheric depth or more for the infrasonic waves observed.

The excitation and propagation of long period pressure waves in the atmosphere have been investigated by several workers, mainly in two fields of geophysics, i.e., meteorology and ionospheric physics. The former consists of the study of atmospheric oscillations (References 20–24), and the study of micro-barometric disturbances (References 25–36). The latter is mostly concerned with the investigation of ionospheric disturbances and has been discussed by Martyn (Reference 37), Sen and White (Reference 38), White (References 39 and 40) and Hines (References 41 and 42).

Although the subjects considered in the noted references are quite different, the mathematical treatments are essentially the same. They are based on a differential equation of velocity divergence, which is derived from three fundamental equations, i.e., the equations of motion, continuity, and of first law of thermodynamics. The theoretical aspects of the problems in geophysics, including oceanography, are reviewed in References 43–46. Mathematical technique has been developed to solve these problems, introducing the so-called field variables instead of simple hydrodynamical variables.

In the present calculations, however, the classical method based on the equations of velocity divergence will be used, because of the convenience in comparing the results with observed data.

Notations and Fundamental Equations

Preliminary notation will now be given:

- c velocity of sound in the atmosphere in cm/sec, $c^2=\gamma gH$ where $H=RT/g$ is the scale height of the isothermal atmosphere,
- D/Dt Eulerian derivative, $\partial/\partial t+U\nabla$,
- $\mathbf{f}$ resultant of external forces except gravity, dynes/gm,
- $\mathbf{g}(0, -g)$ acceleration of gravity, $g=980$ cm/sec^2,
- k horizontal wave number corresponding to λ, in cm^{-1}, i.e., $2\pi/\lambda$,
- ℓ vertical wavelength of a pressure wave in cm,
- p, ρ, T small departures from static values of pressure, density, and temperature, functions of x, z, and t, in dynes/cm^2, gm/cm^3, and °K,
- p_0, ρ_0, T_0 static values of pressure, density, and temperature, functions of z only,
- p_s, ρ_s, T_s static values of pressure, density, and temperature of air at seal level.
- p_T, ρ_T, T_T total pressure, density, and temperature, i.e., p_0+p, $\rho_0+\rho$, and T_0+T,
- $q'(x, z)$ rate of net accession of heat, erg/gm–sec; $s(x, z)=(\gamma-1)q$ where $q=\rho_T q'$ in ergs/cm^3–sec,
- R gas constant of air, $B/M=2.87\times10^6$ ergs/gm–°C, where B is the universal gas constant, 8.314×10^7 ergs/mol–°K, and M is the molecular weight of air, approximately 28.97,
- $\mathbf{U}(u, w)$ velocity vector, where u is the horizontal (southward) and w is the upward component of air flow in cm/sec,
- x, z horizontal (southward) and vertical (upward) coordinates,
- γ ratio of the specific heats of air, $C_p/C_v\approx1.4$, where C_p and C_v are the specific heat of air at constant pressure and constant volume, respectively,
- η entropy of air in ergs/gm–°K,
- λ horizontal wavelength of a pressure wave in cm,
- σ frequency of the pressure wave corresponding to τ, i.e., $2\pi/\tau$,

τ period of pressure wave in sec,
$\chi(x, z)$ the divergence of velocity in sec^{-1}, i.e., $\chi = \partial u/\partial x + \partial w/\partial z$,
Ω Coriolis vector in rad/sec.

In Eulerian notation, the equation of motion is

$$\frac{DU}{Dt} + \frac{1}{\rho}\nabla p + g + \Omega \times U = f \quad . \tag{1}$$

and the equation of continuity is

$$\frac{D}{Dt}\left(\frac{1}{\rho}\right) - \frac{1}{\rho}\nabla U = 0 \tag{2}$$

The variations of pressure due to thermal excitations can be derived from the first law of thermodynamics, which gives the change of entropy (References 43–45),

$$\frac{D\eta}{Dt} = \frac{q'}{T} \quad . \tag{3}$$

By making use of the perfect gas function for entropy (Reference 46) it can be shown that Equation 3 is equivalent to

$$\frac{Dp}{Dt} - c^2 \frac{D\rho}{Dt} = s(x, z, t) \quad . \tag{4}$$

where

$$s(x, z, t) = (\gamma - 1)\rho q'(x, z, t) = (\gamma - 1) q(x, z, t) \quad .$$

Since, in the present problem, the period of oscillation is less than a few minutes, the Coriolis force due to the earth's rotation is negligible, and all other external forces can be assumed to be zero. The equation of motion for the present problem is then simply

$$\frac{DU}{Dt} + \frac{1}{\rho_0}\nabla p = g \quad . \tag{6}$$

One-Dimensional Model

For the one-dimensional case atmospheric motion has only the z component of velocity, w; therefore, in its linear approximation form, the equation of motion (Equation 6) is

$$\rho_0 \frac{\partial w}{\partial z} = \frac{-\partial p}{\partial z} - \rho g \quad . \tag{7}$$

The equation of continuity in its linear approximation form is

$$\frac{\partial \rho}{\partial t} + \rho_0 \frac{\partial w}{\partial z} - \frac{\rho_0}{H} w = 0 \quad . \tag{8}$$

And the linear approximation form of the entropy equation (Equation 4) is:

$$\frac{\partial p}{\partial t} = -\rho_0 c^2 \frac{\partial w}{\partial z} + \rho_0 g w + (\gamma - 1) q \quad , \tag{9}$$

where $q = q(z, t)$ is the periodically changing heat source, which can be assumed to be

$$q(z, t) = \begin{cases} q(z)\, e^{i\sigma t} & \text{for } z \geq 0 \quad , \\ 0 & \text{for } -z_0 \leq z < 0 \quad , \end{cases} \tag{10}$$

where

$$q(z) = \frac{q_0 e^{-z/h}}{h} \quad ; \tag{11}$$

h is a constant and q_0 is the maximum rate of heat generation in an atmospheric column with unit cross section, in ergs/cm²-sec; $z = 0$ is taken as the height of the base of heating; and the value at the earth's surface is given by $z = -z_0$.

By eliminating p and ρ from the above equations, the following differential equation is obtained:

$$\frac{\partial^2 w}{\partial z^2} - \frac{1}{H}\frac{\partial w}{\partial z} - \frac{1}{c^2}\frac{\partial^2 w}{\partial t^2} = \frac{\gamma - 1}{\rho_0 c^2}\frac{\partial q}{\partial z} \quad . \tag{12}$$

In the region $z \geq 0$, where the heat source exists,

$$w = \frac{i}{k_2 - k_1} e^{ik_1^2} \left[\int_0^z e^{-ik_1\xi} Q(\xi)\, d\xi + C\right] + \frac{i}{k_1 - k_2} e^{ik_2^2} \left[\int_0^z e^{-ik_2\xi} Q(\xi)\, d\xi + D\right] \quad , \tag{13}$$

where k_1 and k_2 are given by

$$\left.\begin{aligned} k_1 &= \sqrt{\frac{1}{l^2} - \frac{1}{4H^2}} - i\,\frac{1}{2H} \\ k_2 &= -\sqrt{\frac{1}{l^2} - \frac{1}{4H^2}} - i\,\frac{1}{2H} \end{aligned}\right\} \quad (14)$$

and

$$\frac{1}{l} = \frac{\sigma}{c} ,$$

$$Q(\xi) = \frac{\gamma - 1}{\rho_0 c^2}\frac{dq(\xi)}{d\xi} . \quad (15)$$

C and D are integration constants, to be determined by the boundary conditions. The t[illegible] dependent factor, $e^{i\sigma t}$, is dropped in Equation 13 and will be always dropped hereafter.

For the region $-z_0 \leq z < 0$, where no heat source exists,

$$w = \frac{i}{k_2 - k_1} e^{ik_1 z} A + \frac{i}{k_1 - k_2} e^{ik_2 z} B ; \quad (16)$$

where A and B are constants. The condition that $w = 0$ at the earth's surface gives

$$B = e^{i(k_2 - k_1)z_0} A . \quad (17)$$

The vertical velocity w should be continuous at $z = 0$, and therefore

$$A - B = C - D . \quad (18)$$

The pressure p also should be continuous at $z = 0$, so that the following condition is to be satisfied:

$$\rho_c c^2 \left(\frac{dw}{dz}\right)_{z=0+\epsilon} - (\gamma - 1)\,q(0) = \rho_c c^2 \left(\frac{dw}{dz}\right)_{z=0-\epsilon} , \quad (19)$$

where $\epsilon \to 0$ and

$$\rho_c = (\rho_0)_{z=0} , \quad (20)$$

the atmospheric density at $z = 0$.

The above equations give

$$k_1 C - k_2 D - k_1 A + k_2 B = \frac{k_1 - k_2}{\rho_c c^2}(\gamma - 1)\,q(0) . \quad (21)$$

For $z \to \infty$, there should be no wave downward, thus from Equation 13

$$C = -\int_0^\infty e^{-ik_1 \xi} Q(\xi)\, d\xi . \quad (22)$$

From Equations 18 and 19,

$$A = C - \frac{\gamma - 1}{\rho_c c^2} q(0) . \quad (23)$$

To find the pressure variation at the earth's surface, we must obtain $(dw/dz)_{z=-z_0}$, which is given by using Equations 16 and 17;

$$\left(\frac{dw}{dz}\right)_{z=-z_0} = e^{-ik_1 z_0} A . \quad (24)$$

Then Equation 9 gives the pressure variation at the earth's surface,

$$p_{z=-z_0} = \frac{i}{\omega} \rho_s c^2 e^{-ik_1 z_0} A . \quad (25)$$

where ρ_s is the atmospheric density at the earth's surface. By substituting Equation 22 into Equation 23,

$$|A| = \frac{(\gamma - 1)\, q_0}{\rho_c\, c^2} \frac{1}{l} \left(1 - \frac{h}{H} + \frac{h^2}{l^2}\right)^{-1/2} , \quad (26)$$

provided that the angular wave frequency σ is larger than a critical frequency σ_A,

$$\sigma_A = \frac{\gamma g}{2c} . \quad (27)$$

By using Equations 14

$$\left|e^{-ik_1 z_0}\right| = e^{-z_0/2H} . \quad (28)$$

Thus the final expression of the amplitude of pressure variations at the ground, caused by the periodic disturbance in the upper atmosphere q(z, t), is

$$p_s = \frac{\gamma - 1}{c} q_0 \left(\frac{\rho_s}{\rho_c}\right)^{1/2} \left(1 - \frac{h}{H} + \frac{h^2}{l^2}\right)^{1/2} . \quad (29)$$

The values for p_s/q_0 which may be derived from this equation are plotted vs. h in Figure 3 for several values of angular frequency, σ. The full lines and dashed lines stand for the scale heights of 8 km and 6.8 km, respectively, for an isothermal atmosphere. The latter gives the proper ratio of $(\rho_c/\rho_s)^{1/2}$ as compared with the observed atmospheric densities. From this figure, it can be seen that periodic heating corresponding to a flux of the order of 100 ergs/cm²–sec produces pressure waves with amplitudes of the order of 1 dyne/cm² at the ground.

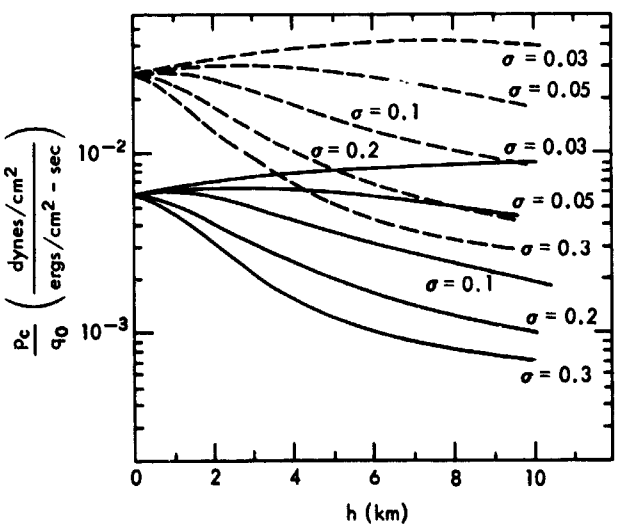

FIGURE 3.—Relative intensity of pressure waves on the ground, produced by periodic auroral heating, vs. the scale height of the heat source, for the one-dimensional model with an isothermal atmosphere.

Two-Dimensional Model

Equation of Velocity Divergence

From Equation 6 the equation of motion for the two-dimensional case is

$$\rho_0 \frac{\partial u}{\partial t} = -\frac{\partial p}{\partial x} , \quad (30)$$

$$\rho_0 \frac{\partial w}{\partial t} = -\frac{\partial p}{\partial z} - g\rho . \quad (31)$$

The equation of continuity (Equation 2) can be written in a first order approximation as

$$\frac{\partial p}{\partial t} + w \frac{\partial \rho_0}{\partial z} = -\rho_0 \chi , \quad (32)$$

where $\chi = \chi(x, z, t)$ is the velocity divergence. By using Equation 32, Equation 4 can be written as

$$\frac{\partial p}{\partial t} = \rho_0 gw - \rho_0 c^2 \chi + s . \quad (33)$$

Under the assumption that the time variations of u, w, p, ρ, and s are proportional to a factor $e^{i\sigma t}$, the following relations between u, w, and p are obtained from Equations 30–33:

$$-\sigma^2 u = \frac{\partial}{\partial x}\left(c^2 \chi - gw\right) - \frac{1}{\rho_0}\frac{\partial s}{\partial x} , \quad (34)$$

$$-\sigma^2 w = c^2 \frac{\partial \chi}{\partial z} - \gamma g \chi + g \frac{\partial u}{\partial x} - \frac{1}{\rho_0}\frac{\partial s}{\partial x} , \quad (35)$$

$$i\sigma p = \rho_0 gw - c^2 \rho_0 \chi + s . \quad (36)$$

By eliminating u, w, and p from these equations, the following differential equation for the velocity

divergence $\chi(x, z)$ is obtained:

$$\nabla^2 \chi + \frac{1}{c^2}\left(\frac{dc^2}{dz} - \gamma g\right)\frac{\partial \chi}{\partial z} - \frac{g}{c^2\sigma^2}\left[\frac{dc^2}{dz} + (\gamma - 1)g\right]\frac{\partial^2 \chi}{\partial x^2} + \frac{\sigma^2}{c^2}\chi$$

$$= -\frac{1}{c^2\sigma^2}\left[\frac{g}{\rho_0(z)c^2}\left(\frac{dc^2}{dz} + \gamma g\right)\frac{\partial^2 s}{\partial x^2} - \frac{\sigma^2}{\rho_0 c^2}\left(\frac{dc^2}{dz} + \gamma g\right)\frac{\partial s}{\partial z} - \frac{\sigma^2}{\rho_0}\nabla^2 s\right] \quad . \quad (37)$$

The derivation of this equation is given in Appendix A.

The Diagnostic Diagram

If there is no thermal excitation, the right side of Equation 37 is zero, and the solution of this homogenous differential equation corresponds to the free oscillation of the atmosphere on the nonrotating earth.

We will now consider pressure waves traveling horizontally in this flat atmosphere. If u, w, p, and ρ are proportional to a factor $e^{i(\sigma t - kx)}$, the following is the equation for the vertical change of $\chi(\sigma, z)$:

$$\frac{d^2\chi}{dz^2} + \frac{1}{c^2}\left(\frac{dc^2}{dz} - \gamma g\right)\frac{d\chi}{dz} + \left[\frac{\sigma^2}{c^2} - k^2 + \frac{gk^2}{\sigma^2 c^2}\left(\frac{dc^2}{dz} + \gamma g - g\right)\right]\chi = 0 \quad .$$

Since $c^2 = \gamma g H(z)$, this may be written

$$\frac{d^2\chi}{dz^2} + \frac{1}{H}(H' - 1)\frac{d\chi}{dz} + \left[\frac{\sigma^2}{\gamma g H} - k^2 + \frac{k^2 g}{\sigma^2 H}\left(H' + \frac{\gamma - 1}{\gamma}\right)\right]\chi = 0 \quad ,$$

where $H' = dH/dz$.

For simplicity, consider the case of an isothermal atmosphere, where $H' = 0$. Equation 39 becomes

$$\frac{d^2\chi}{dz^2} - 2N\frac{d\chi}{dz} + M^2\chi = 0 \quad , \quad (40)$$

where the constant $N = 1/2H$ and

$$M^2 = \frac{\sigma^2}{c^2} - k^2 + \frac{k^2 g^2}{c^2\sigma^2}(\gamma - 1) \quad . \quad (41)$$

This differential equation has the solution:

$$\chi(\sigma, z) = e^{Nz}\left(Ae^{-\mu z} + Be^{+\mu z}\right) \quad , \quad (42)$$

where A and B are constants,

$$\mu^2 = N^2 - M^2 \geq 0 \quad , \quad (43)$$

for the noncellular solution, and

$$\mu = i\eta \quad , \qquad \eta^2 = M^2 - N^2 > 0 \quad , \quad (44)$$

for the cellular solution. As was shown by Pekeris (Reference 27) for the noncellular solution in an isothermal atmosphere (Equation 42) the term with $e^{\mu z}$ must vanish, i.e, $B = 0$. Otherwise the kinetic energy of noncellular waves, which is proportional to $\rho_0(z)\chi^2$, would diverge. Furthermore, because of the condition that the vertical component of velocity must vanish at the ground, we get only two possible types of free oscillation, specified by the following characteristic relations:

Type I: $$k = \frac{\sigma}{c} \quad , \qquad V = U = c \quad , \quad \text{and} \quad \mu = \frac{g(2 - \gamma)}{2c^2} \quad , \quad (45)$$

Type II: $$k = \frac{\sigma^2}{g} \quad , \qquad V = \frac{g}{\sigma} \quad , \quad U = \frac{1}{2}V \quad , \quad \text{and} \quad \mu = \frac{\sigma^2}{g} - \frac{\gamma g}{2c^2} \quad . \quad (46)$$

where $V=\sigma/k$ and $U=d\sigma/dk$, the phase velocity and group velocity of noncellular horizontal waves. Type I corresponds to Lamb's wave (Reference 20), which exists at all frequencies; the waves of type II can be propagated only above a critical value σ_c,

$$\sigma_c = \frac{g}{c}\sqrt{\frac{\gamma}{2}} \qquad (47)$$

(the corresponding period is about 250 sec), and the wave is dispersive.

It should be noted that, because of the decrease of atmospheric density, the amplitude of the Lamb wave (pressure variation) decreases with altitude by a factor $\exp(-gz/c^2)$, preventing the propagation of waves in any except horizontal directions (Reference 46). On the other hand, for the cellular solution η stands for the wave number in the vertical direction and Equation 44 is equivalent to

$$\eta^2 c^2 = \frac{(\sigma^2-\sigma_A^2) + k^2c^2(\sigma_B^2-\sigma^2)}{\sigma^2} \qquad (48)$$

where

$$\sigma_A = \frac{g\gamma}{2c}$$

$$\sigma_B = \frac{g(\gamma-1)^{1/2}}{c} \qquad (49)$$

Brunt's frequency, σ_B, is the frequency of the vertical oscillation of a free air parcel in the atmosphere, changing adiabatically. This expression was also derived by Väisälä as a stability parameter of the atmosphere (Reference 46). The frequency σ_A can be called the atmospheric resonance sound frequency (Reference 47).

The curve for $\eta^2=0$ shown in Figure 4 (a plot of σ vs. k) consists of two branches, A and B. The curve A starts from the σ-axis at $\sigma=\sigma_A$ and is asymptotic to the line C, which corresponds to the solution of the noncellular Lamb wave, $\sigma=kc$. The other curve B passes through the origin and is asymptotic to the horizontal line $\sigma=\sigma_B$. Every point in the two regions where

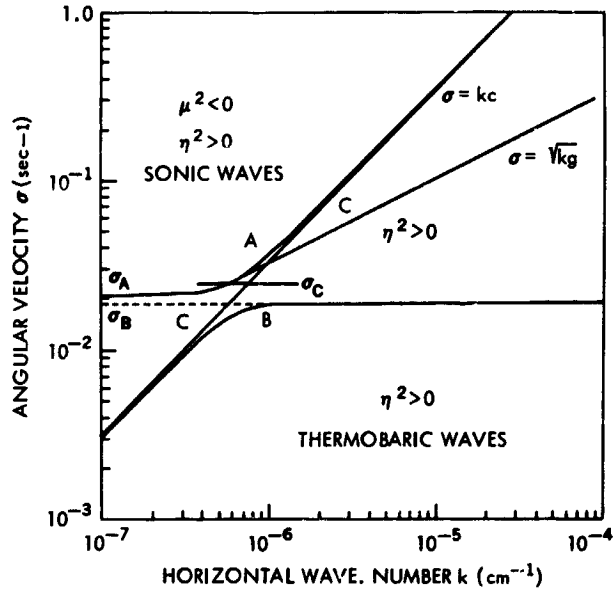

FIGURE 4.—Diagnostic diagram for an isothermal atmosphere with scale height H = 8 Km (T_0 = 273°K).

$\eta^2>0$, one surrounded by curve A and the other surrounded by curve B, leads to an eigen solution of Equation 39. In the third region (between the other two), where $\eta^2<0$, only the points on the line $\sigma=$ kc and $\sigma=\sqrt{kg}(\sigma>\sigma_c)$ lead to eigen solutions. Figure 4 is called the diagnostic diagram of the isothermal atmosphere, and the waves corresponding to the two domains in which $\eta^2>0$ are named Sonic (mode A) and Thermobaric (mode B), respectively (Reference 46). Sonic and thermobaric waves are called acoustic and internal gravity waves, respectively, by Hines (Reference 42).

Intensity of Pressure Waves at the Ground

Since the source of excitation s(x, z) is limited to a certain area inside the auroral zone, the right side of Equation 37 is not uniform with respect to x. Therefore, this differential equation is not in general separable with respect to the variables x and z, and the following assupmtions are made in solving the equation:

1. The atmosphere is isothermal, with scale height H, in km.
2. The distribution of the heat source is uniform along the y direction (this is assumed at the beginning to reduce the problem to two dimensions), but it is limited horizontally in the x direction within $\pm\lambda_0$ (i.e., $-\lambda_0 \le x < \lambda_0$) and is

extended vertically above a certain height z (i.e., $z \geq z_0$).

3. The time variation of the heat source is periodic with an angular frequency σ, and the same phase within the domain indicated in item 2 above.

The first assumption reduces Equation 37 to the following form:

$$\left(1 - \frac{\sigma_B^2}{\sigma^2}\right)\frac{\partial^2 \chi}{\partial x^2} + \frac{\partial^2 \chi}{\partial z^2} - \frac{1}{H}\frac{\partial \chi}{\partial z} + \frac{\sigma^2}{c^2}\chi = \frac{1}{\rho_0(z)c^2}\left[\left(1 - \frac{g}{\sigma^2 H}\right)\frac{\partial^2 s}{\partial x^2} + \frac{\partial^2 s}{\partial z^2} + \frac{1}{H}\frac{\partial s}{\partial z}\right] . \quad (50)$$

Assumptions 2 and 3 can be written as

$$s(x, z, t) = s(z)\, e^{i\sigma t}\, \theta(z - z_0)\left[\theta(x + \lambda_0) - \theta(x - \lambda_0)\right] , \quad (51)$$

where

$$s(z) = \frac{s_0}{h} e^{-(z - z_0)/h} = \frac{(\gamma - 1) q_0}{h} \exp\left[\frac{-(z - z_0)}{h}\right] , \quad (52)$$

and $\theta(\xi)$ is a unit step function of ξ,

$$\theta(\xi) = \begin{cases} 1 & \text{for } \xi \geq 0 , \\ 0 & \text{for } \xi < 0 . \end{cases} \quad (53)$$

It should be noted that q_0 is the maximum rate of heat release in the atmosphere in an air column of unit cross-section (in ergs/cm²-sec).

Since the atmosphere is assumed to be isothermal, the density of air in equilibrium at height z is

$$\rho_0(z) = \rho_s e^{-z/H} , \quad (54)$$

where ρ_s is the atmosphere density at the earth's surface and H is the scale height.

In order to solve Equation 50 under the conditions listed, the following Fourier transforms are applied with respect to x,

$$X(k, z) = \frac{1}{\sqrt{2\pi}} \int_{-\infty}^{\infty} e^{ikx}\, \chi(x, z)\, dx , \quad (55)$$

$$S(k, z) = \frac{1}{\sqrt{2\pi}} \int_{-\infty}^{\infty} e^{ikx}\, s(x, z)\, dx . \quad (56)$$

Since the heat source s(x, z) vanishes outside of the auroral zone, both s(x, z) and $\chi(x, z)$ must vanish at $x = \pm\infty$. Thus

$$\frac{1}{\sqrt{2\pi}} \int_{-\infty}^{\infty} \frac{\partial^2 \chi}{\partial x^2} e^{ikx}\, dx = -k^2 X(k, z) , \quad (57)$$

$$\frac{1}{\sqrt{2\pi}} \int_{-\infty}^{\infty} \frac{\partial^2 s}{\partial x^2} e^{ikx}\, dx = -k^2 S(k, z) . \quad (58)$$

With these transforms, Equation 50 is written

$$\frac{d^2 X}{dz^2} - 2N\frac{dX}{dz} + M^2 X = F(z, k) , \quad (59)$$

where

$$F(z, k) = \frac{1}{c^2 \rho_0(z)}\left[\frac{d^2 S}{dz^2} + \frac{1}{H}\frac{dS}{dz} - k^2\left(1 - \frac{g}{\sigma^2 H}\right)S\right] . \quad (60)$$

and N and M^2 are the same as in Equations 40 and 41. The solution of Equation 59 can be written:

$$X(k, z) = e^{n_1 z}\left[C_1 - \frac{1}{2\mu}\int_0^z F(z', k)\, e^{-n_1 z'}\, dz'\right] + e^{n_2 z}\left[C_2 + \frac{1}{2\mu}\int_0^z F(z', k)\, e^{-n_2 z'}\, dz'\right] , \quad (61)$$

where $F(z', k)$ is given by Equation 60 and n_1 and n_2 are the roots of the characteristic equation

$$n^2 - 2Nn + M^2 = 0 . \quad (62)$$

We assume

$$n_1 = N - \mu , \quad (63)$$

$$n_2 = N + \mu , \quad (64)$$

where

$$\left.\begin{aligned} \mu &= \sqrt{N^2 - M^2} \geq 0 \qquad \text{for } N^2 \geq M^2 , \\ \mu &= i\eta, \quad \eta^2 = M^2 - N^2 > 0 \qquad \text{for } N^2 < M^2 \end{aligned}\right\} . \quad (65)$$

The integration constants C_1 and C_2 are determined by the following two boundary conditions:

1. The vertical component of velocity vanishes at the ground,

$$w(x, z = 0) = 0 . \quad (66)$$

2. The kinetic energy of the waves at $z = \infty$ is either zero or remains finite. In the latter case, the vertical component of the disturbance should never be propagated downward at $z = \infty$.

The pressure change at the ground can be obtained from $\chi(x, z=0)$, which is given by the inverse Fourier transform of $X(k, z=0)$, i.e.,

$$\chi(x, 0) = \frac{1}{\sqrt{2\pi}}\int_{-\infty}^{\infty} e^{-ikx}\, X(k, 0)\, dk . \quad (67)$$

where $X(k, 0)$ is the solution of Equation 59 at $z=0$ satisfying the above conditions. It is given by Equation B15 in Appendix B.

Since $w(x, 0)=0$, then $s(x, 0)=0$ and Equation 36 reduces to

$$p(x, 0) = -\frac{c^2 \rho_s}{i\sigma}\chi(x, 0) . \quad (68)$$

where $\chi(x, 0)$ is given by the inverse Fourier transform of $X(k, 0)$. The evaluations of $p(x, 0)$ are given in Appendix C and the results are shown in Figures 5–10. Various values are given in Tables 1 and 2. The symbols p_r and p_i signify the real and imaginary parts of the cellular mode, respectively.

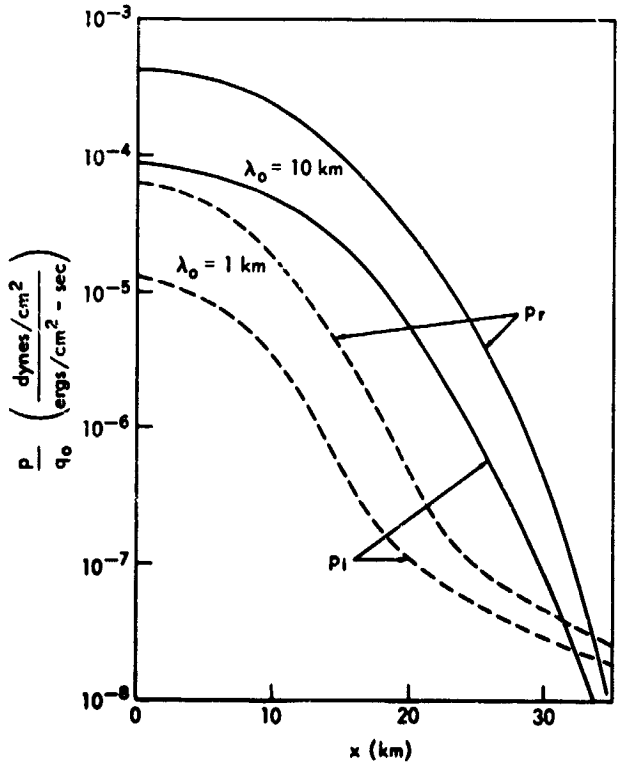

FIGURE 5.—A plot of the intensity of the cellular waves p_r and p_i on the ground, as a function of the input energy flux q_0 for $\tau = 30$ sec and $h = H$, vs. x, the horizontal distance from the center of the source. Full lines and dashed lines correspond to $\lambda_0 = 10$ km and $\lambda_0 = 1$ km, respectively.

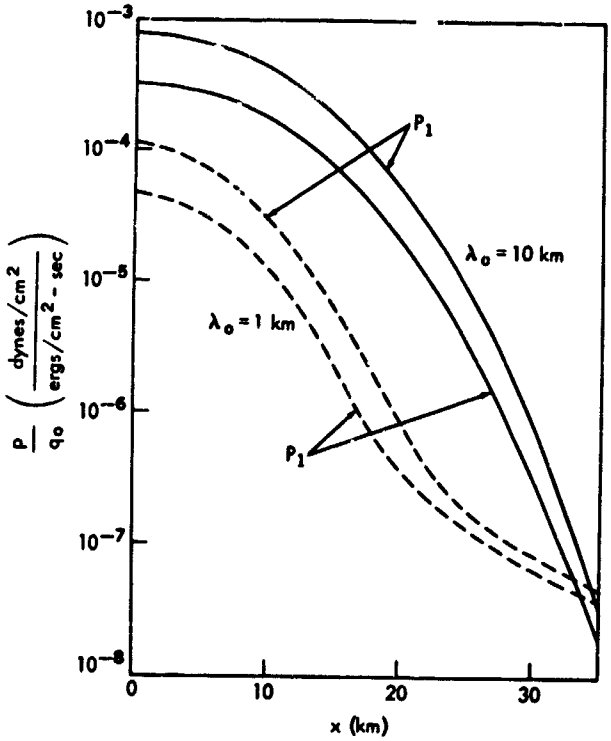

FIGURE 6.—The same plot as Figure 5 except that $h = \frac{1}{2}H$ instead of $h = H$.

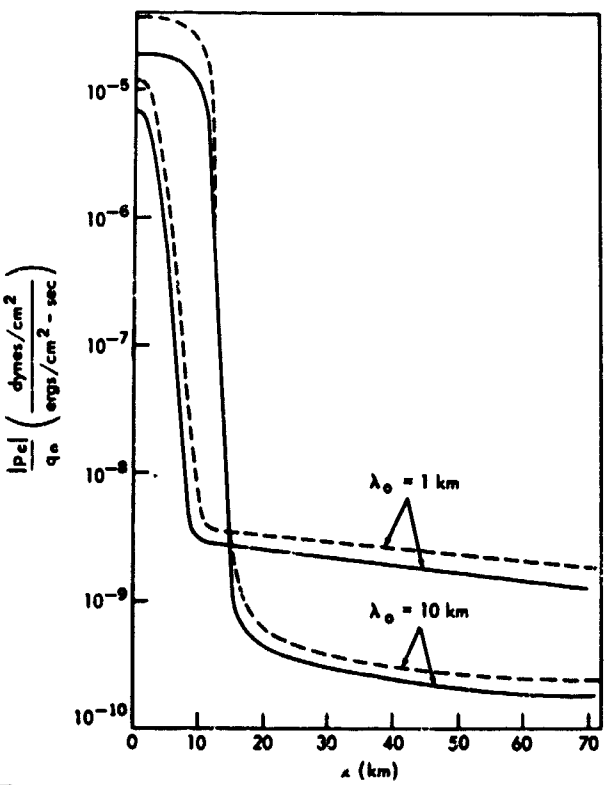

FIGURE 7.—A plot of the intensity of cellular waves produced by periodic auroral heating $|p_e| = \sqrt{p_r^2 + p_t^2}$, vs the horisontal distance from the center of the source for $\tau = 10$ sec. Full lines and dashed lines stand for $h = H$ and $h = \frac{1}{2}H$, respectively.

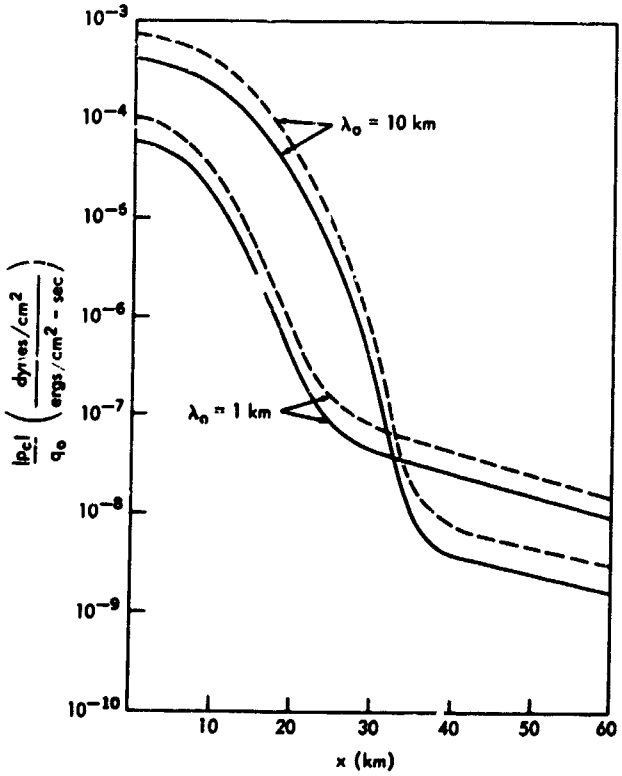

FIGURE 8.—The same plot as Figure 7 except that $\tau = 30$ sec.

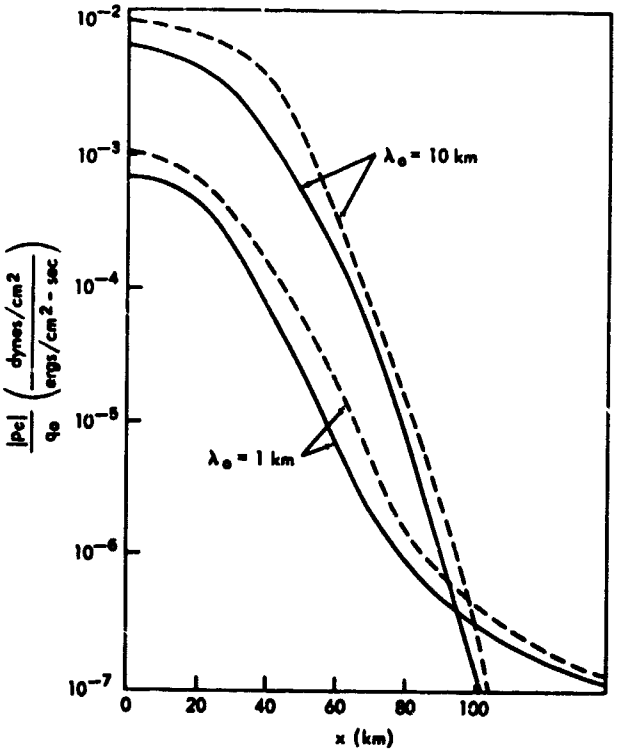

FIGURE 9.—The same plot as Figure 7 except that $\tau = 100$ sec.

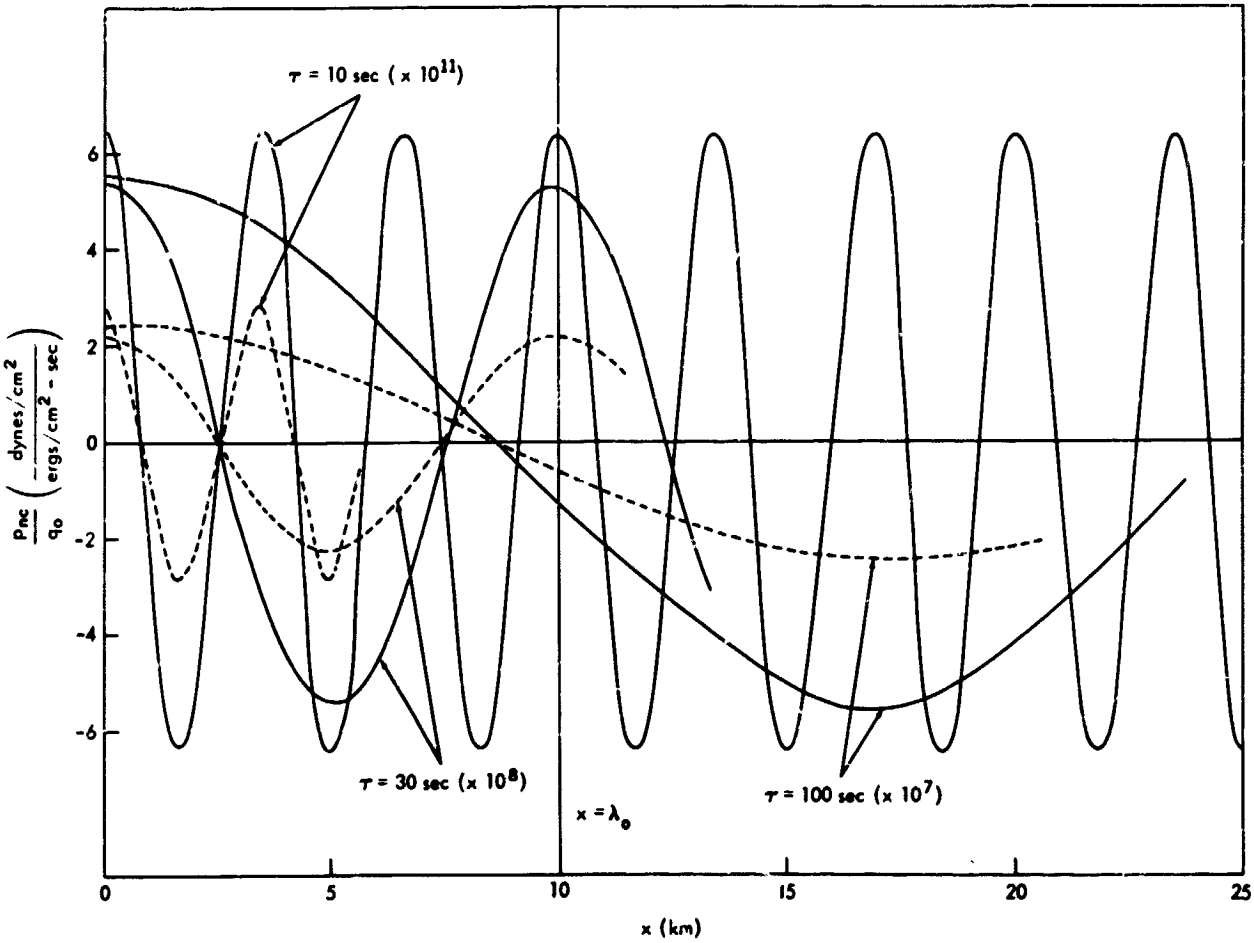

FIGURE 10.—Intensity distribution of noncellular waves on the ground, p_{nc}, in the units of q_0, vs. horizontal distance x from the center of the source of width $\lambda_0 = 10$ km. Notice that the vertical scales are magnified by a factor attached to each curve. Full lines and dashed lines stand for $h = H$ and $h = \frac{1}{2}H$, respectively.

Table 1

Intensity of the Cellular Mode of Infrasonic Waves on the Ground Below the Center of the Source in Units of q_0.

h = H	p_r	p_i	$\lvert p_c \rvert$	h = 1/2H	p_r	p_i	$\lvert p_c \rvert$
λ_0 = 1 km				λ_0 = 1 km			
τ = 10 sec.	6.74×10^{-6}	4.40×10^{-7}	6.75×10^{-6}	τ = 10 sec.	1.33×10^{-5}	1.79×10^{-6}	1.34×10^{-5}
30 sec.	6.15×10^{-5}	1.21×10^{-5}	6.28×10^{-5}	30 sec.	1.10×10^{-4}	4.79×10^{-5}	1.23×10^{-4}
100 sec.	5.46×10^{-4}	4.26×10^{-4}	6.92×10^{-4}	100 sec.	2.77×10^{-4}	1.02×10^{-3}	1.06×10^{-3}
λ_0 = 10 km				λ_0 = 10 km			
τ = 10 sec.	1.82×10^{-5}	1.20×10^{-6}	1.83×10^{-5}	τ = 10 sec.	3.62×10^{-5}	4.80×10^{-6}	3.65×10^{-5}
30 sec.	4.29×10^{-4}	8.57×10^{-5}	4.38×10^{-4}	30 sec.	7.91×10^{-4}	3.32×10^{-4}	8.58×10^{-4}
100 sec.	5.25×10^{-3}	4.11×10^{-3}	6.67×10^{-3}	100 sec.	2.68×10^{-3}	9.85×10^{-3}	1.02×10^{-2}
λ_0 = 100 km				λ_0 = 100 km			
τ = 10 sec.	1.82×10^{-5}	1.20×10^{-6}	1.83×10^{-5}	τ = 10 sec.	3.62×10^{-5}	4.80×10^{-6}	3.65×10^{-5}
30 sec.	4.84×10^{-4}	1.01×10^{-4}	4.94×10^{-4}	30 sec.	8.92×10^{-4}	3.73×10^{-4}	9.68×10^{-4}
100 sec.	1.43×10^{-2}	1.14×10^{-2}	1.83×10^{-2}	100 sec.	7.62×10^{-3}	2.72×10^{-2}	2.83×10^{-2}

Table 2

Values for p_{nc} · $p_{nc}/|p_c|$, and x_0, the Horizontal Distance of the first Nodal Lines from the Center of the Source (horizontal width assumed to be λ_0 = 10 km).

h = H	p_{nc}	$p_{nc}/\|p_c\|$	x_0 (km)	h = 1/2H	p_{nc}	$p_{nc}/\|p_c\|$	x_0 (km)
τ = 10 sec	1.28×10^{-9}	7.0×10^{-5}	0.85	τ = 10 sec	1.11×10^{-9}	3.03×10^{-5}	0.85
30 sec	3.24×10^{-8}	7.4×10^{-5}	2.56	30 sec	2.73×10^{-8}	3.18×10^{-5}	2.56
100 sec	1.10×10^{-5}	1.66×10^{-3}	8.31	100 sec	1.02×10^{-5}	9.8×10^{-4}	8.30

ATTENUATION

Because of the viscosity and thermal conductivity of air, acoustic waves in the atmosphere attenuate. The attenuation coefficient $\alpha(\tau)$, in cm^{-1}, for a wave of period τ is given approximately by (Reference 48)

$$\alpha(\tau) = \frac{4\pi^2}{\tau^2}\frac{1}{c^3}\left(\frac{4}{3}\nu + \frac{\gamma-1}{\gamma}a^2\right), \quad (69)$$

where the coefficient of kinematic viscosity ν is approximately

$$\nu = \frac{1.7 \times 10^{-4}}{\rho(z)} \quad (70)$$

in cm^2/sec, and the coefficient of thermal conductivity a^2 is

$$a^2 = \frac{2.1 \times 10^{-5}}{\rho(z)}, \quad (71)$$

in cm^2/sec.

Since the air density ρ decreases exponentially with height, a^2 and ν increase exponentially with altitude. The so-called attenuation factor,

$$f_a(\tau, z) = \exp\left[-\int_0^z \alpha(\tau, z')\,dz'\right], \quad (72)$$

is shown in Figure 11 as a function of height, for $\tau = 10$ sec, 30 sec, and 100 sec.

It should be noted that the relative amplitude of the pressure wave grows as it propagates upward by a factor $e^{z/2H}$, where H is the scale height, whereas the absolute amplitude decreases by a factor $e^{-z/2H}$, because of the exponential decrease of air density (Reference 49). Therefore, if the amount of excitation energy is the same, the absolute intensity of the pressure wave at the ground increases with the base of the

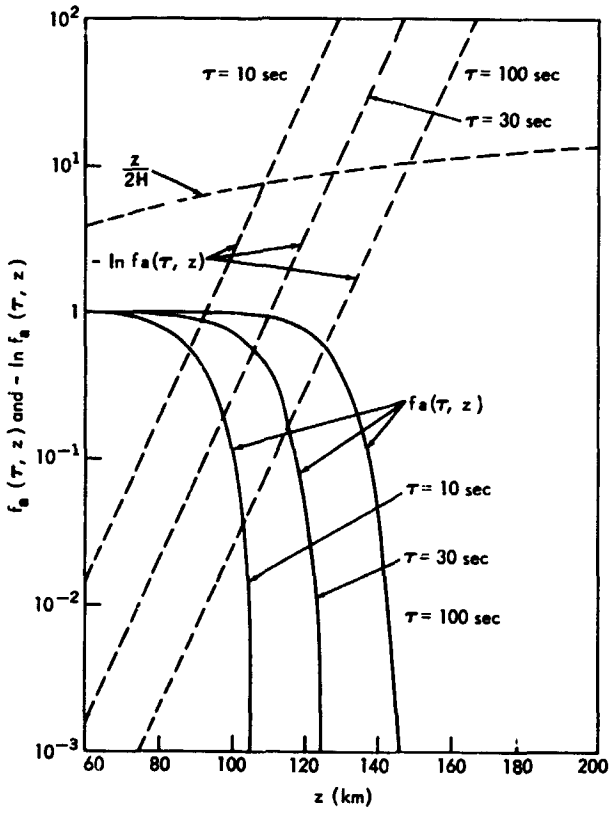

FIGURE 11.—Attenuation factor $f_a(\tau, z)$ vs. altitude of the source z in km and $-\ln f_a(\tau, z)$ vs. z:

$$-\ln f_a(\tau, z) = \int_0^z \alpha(\tau, z')\,dz',$$

a dashed line is also used to indicate the exponential amplification factor $\ln (\rho_z \rho_0)^{\frac{1}{2}} \approx z/2H$, where the scale height H is assumed to be 8 km.

excitation level. This is shown by Equation 29 and Equations C9 and C10 with a factor $e^{z_0/2H}$ for p_s, p_c ($z=0$), and $p_{nc}(z=0)$, and by a curved dash line in Figure 11.

However, because of the steep increase of the kinematic viscosity of air with altitude, the yield of pressure wave excitation drops sharply above a certain altitude for a given period (or frequency)

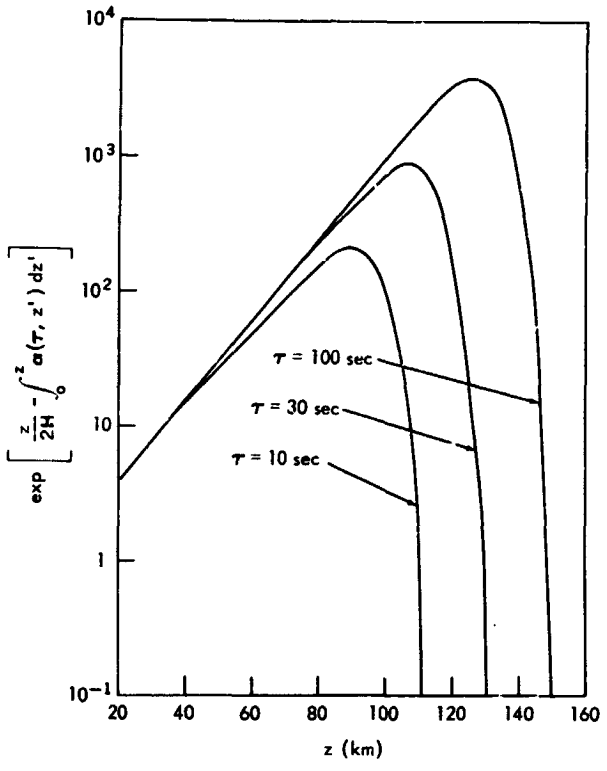

FIGURE 12. —Relative yield of the source to the infrasonic waves in the isothermal atmosphere

$$\sqrt{\frac{\rho(z)}{\rho_0}}\, f_a(\tau, z) \approx \exp\left[\frac{z}{2H} - \int_0^z \alpha(\tau, z')\,dz'\right]$$

vs. the altitude of the source z, where the scale height H is assumed to be 8 km.

of the wave. This is shown in Figure 12 for wave periods of $\tau = 10$, 30, and 100 sec. It can be seen that there is an effective height of excitation of atmospheric acoustic waves for a given period and that this height increases with the period.

As mentioned in the introduction, the excitation of pressure waves by hydromagnetic waves is only effective above the height of auroral activities. Figure 12 shows that waves produced at such a height are greatly attenuated before they reach the ground. Therefore, the contribution of hydromagnetic waves to the excitation of internal atmospheric waves is practically negligible. A more quantitative discussion will be given in the next section.

CONDITIONS FOR WAVE FORMATION

According to previous calculations, a pressure variation at the ground of the order of 1 dyne/cm² can be expected if the maximum rate of heat generation is of the order of 100 ergs/cm²-sec and the layer of periodic heating is around 100 km altitude, with a thickness less than 10 km. Electrons with an energy of the order of 100 kev will lose most of their energy within a layer of the order of 10 km thickness around the height of 100 km (Reference 19, p. 290). According to Chamberlain, the rate of heat generation is the order of 60 ergs/cm²-sec in a bright aurora. Therefore, if the rate of heat generation changes periodically with this order of amplitude, barometric oscillations of the order of 1 dyne/cm² at sea level can be expected from the sources in the upper atmosphere.

However, several other conditions must be satisfied in order that the energy brought into the upper air by auroral electrons can be converted efficiently to pressure waves in the atmosphere. At first, the time τ_1, in which an electron arrives at auroral height from outer space, should be smaller than the period, τ, of the waves concerned. If $\tau_1 \gg \tau$, the phase of the time variation of the source differs from place to place, and the resultant pressure wave originating from those different sources is weakened by superposition.

Since the auroral electrons, whose velocity is of the order of 10^9 cm/sec, lose their energy within a layer of 10 km thickness, $\tau_1 <$ approx. 10^{-4} sec. This is much smaller than the period of the acoustic waves considered here.

As discussed by Hanson and Johnson (Reference 50), electrons impinging into the upper atmosphere lose their energy mostly by inelastic collisions with neutral air particles until ≈ 2 ev, which is the lowest excitation energy of atomic oxygen (^{1}D state). The time τ_2 for ^{1}D excitation collisions with oxygen atoms is of the order of 10^{-3} sec at 100 km and of the order of 1 sec at 400 km.

Below 2 ev, the electrons lose energy in the upper atmosphere mainly by elastic collisions with ambient electrons. The time for those low energy electrons to equilibrate with ambient electrons, τ_3, is obtained from the expression for the rate of energy loss of a fast electron immersed in a thermalized plasma (Reference 50),

$$\tau_3 \approx \frac{5.7 \times 10^3\, E^{3/2}}{N_e}, \qquad (73)$$

where E is the electron energy, i.e., $E \approx 2$ ev, and

N_e is the electron concentration in cm^{-3}. The equilibration time, τ_3, given by this expression is about 10^{-1} sec at 100 km and of the order of 10^{-2} sec above 350 km. Thus $\tau_2+\tau^3$ is much smaller than the periods of the acoustic waves under discussion

It should be noted that elastic collisions with neutral particles dominate over those with ambient electrons below the F2 maximum (around 300 km). The time constant τ_4 for these elastic collisions consists of τ (O) and $\tau(N_2)$, the time constants for the loss of excess electron energy to atomic oxygen and to molecular nitrogen, respectively (Reference 50), and is given by

$$\tau_4 = \frac{2.08 \times 10^{11} E^{-1/2}}{n(O) + 2.36 n(N_2)} , \qquad (74)$$

where n(O) and $n(N_2)$ are the concentration per cm^3 of atomic oxygen and of molecular nitrogen, respectively. For E=2 ev, τ_4 is of the order of 0.1 sec at 100 km and increases with height. It is of the order of 100 sec at 350 km.

As shown in the previous section, the excitation of atmospheric pressure waves above 200 km is not important; the time constant τ_4 does not destroy the condition of wave formation. In other words, below 200 km $\tau_1+\tau_2+\tau_3+\tau_4 <$ approx. τ.

Another condition necessary for wave formation is that the time constant for cooling in a certain domain of auroral activity must be much longer than the period of oscillation. If the initial temperature T_0 is assumed to be horizontally uniform within the domain of the source, $-\lambda_0 \leq x \leq \lambda_0$, then the temperature at the center after t(sec) is

$$T(t) = (T_0 - T_a)\, \Phi\left(\frac{\lambda_0}{2\sqrt{a^2 t}}\right), \qquad (75)$$

where

$$\Phi(y) = \frac{2}{\sqrt{\pi}} \int_0^y e^{-x^2}\, dx , \qquad (76)$$

and a^2 is the thermal diffusivity (coefficient of thermal conduction) of air. T_a is the temperature outside the source.

The time, t_a, necessary to reduce the initial temperature difference between the inside and outside of the source region can be estimated from

$$\left.\begin{aligned} \Phi\left(\frac{\lambda_0}{2\sqrt{a^2 t_a}}\right) &= \frac{1}{2} , \\ t_a &\approx \frac{\lambda_0^2}{a^2} . \end{aligned}\right\} \qquad (77)$$

Since the thermal diffusivity of air a^2 at a height of 100 km is of the order of 10^6 cm^2/sec (see Equation 71), the minimum source width necessary to satisfy the condition for thermal oscillation is of the order of 30m for a period of 10 sec, and of the order of 100m for a period of 100 sec. The source width considered in the present calculation is significantly larger than these widths. In other words, the time constant for source cooling is sufficiently long for pressure wave production.

OTHER POSSIBLE MECHANISMS

Now the possibility of other suitable mechanisms for the generation of microbarometric oscillations during magnetic disturbances will be considered.

Periodic Heating Due to the Absorption of Hydromagnetic Waves

As stated in the introduction, hydromagnetic waves from the magnetosphere lose part of their energy in the lower exosphere and in the ionosphere. The remaining energy, which leaks through the ionosphere, is observed as fluctuations of the geomagnetic field intensity or geomagnetic pulsations.

The rate of energy dissipation of hydromagnetic waves in the ionosphere increases with increasing frequency (References 6, 51, and 52). According to Watanabe, the dissipation of the hydromagnetic wave energy in the ionosphere is negligible for waves with periods longer than 20 sec. In the auroral region, the amplitude of geomagnetic pulsations sometimes exceeds several tens of gammas (i.e., giant pulsations) and the periods are sometimes longer than several tens of seconds. The intensity of the incident wave is usually smaller for higher frequencies (Reference 15). As shown by the power density of the small scale fluctuations of magnetic field intensity observed

in the earth's magnetosphere between 5 and 15 earth radii (Reference 3), the frequency spectrum of hydromagnetic waves, which are regarded as the origins of geomagnetic pulsations observed at the earth's surface, is a decreasing function of frequency above the ionosphere. In any case, the upper limit of the incident wave amplitude may be taken as 100γ. The energy flux associated with these hydromagnetic waves is then of the order of several ergs/cm^2-sec^1, under the assumption that the Alfvèn wave velocity above the ionosphere is of the order of 10^8 cm/sec. The rate of heat generation by absorption of these hydromagnetic waves in the upper ionosphere has been estimated by several authors and their results are shown in Table 3.

The rate of heat generation is generally less than 1 erg/cm^2-sec, except when the period is 1 sec. Therefore the amount of heat generated by hydromagnetic waves penetrating the ionospheer is smaller than that due to the auroral particles. Table 3 also contains estimates of the thickness of the layer of heat generation. In every case the thickness is much larger for hydromagnetic waves than for auroral particles.

As shown in Figure 12, the effective height of pressure wave generation by periodic heating of the upper air is limited, and it is lower for the shorter period. Therefore, generation of acoustic waves by the attenuation of hydromagnetic waves is less efficient than generation by the periodic heating due to auroral particles, even if the energy flux of the incident wave is increased to be the same as the latter.

Pressure Waves Due to the Impacts of Auroral Particles

A particle coming into the atmosphere loses its energy by transferring its downward momentum to the air particles. A pressure wave can be generated if the flux of the particle changes periodically with time.

The upper limit of the pressure intensity, from this process, can be estimated by assuming that all the incoming particles would stop in a very short time within a very thin layer. By assuming the average energy of incident electrons is 6 kev and the maximum flux is of the order of 10^{10}cm^{-2}-sec^{-1}, the maximum pressure exerted upon the thin layer of virtual shock absorber is estimated to be of the order of 4.10^{-8} dynes/cm^2. The corresponding intensity at the earth's surface is of the order of 10^{-5} dyne/cm^2, if all electrons stop at an altitude of 100 km.

Penetration of Hydromagnetic Waves Through the Ionosphere

As mentioned above, most geomagnetic pulsations are due to hydromagnetic oscillations in the exosphere. These oscillations are related to electromagnetic oscillations in the space between the earth's surface and the lower boundary of the ionosphere. Any oscillation mode in which the compression of atmospheric matter is involved gives rise to a variation in the density, and consequently a pressure variation. Therefore, it may be possible that geomagnetic pulsations and microbarometric oscillations have the same origin,

Table 3

Rate of Heat Generation Due to Attenuation of Hydromagnetic Waves with a 100γ Incident Amplitude.

Source	Period of HM waves (sec)	Rate of Heat Generation in an Air Column of unit cross section (erg/cm^2-sec)	Thickness of Heating Layer (km)	Altitude of the Center of the Heat Generating Layer (km)
Dessler (Reference 53)	1	1.3	100	170
Francis and Karplus (Reference 51)	6.3 0.3	0.7 1.6	50 100	125 180
Akasofu (Reference 52)	1 10 100	9.7 0.17 0.028	100 200 300	225 240 250

i.e., hydromagnetic oscillations of the earth's exosphere.

A simple situation can be found at the geomagnetic equator, where geomagnetic pulsations appear sometimes in the N–S component of the geomagnetic field, with amplitudes of the order of several tens of gammas and periods of several minutes (Reference 54). The origins of this kind of pulsation presumably exist in the outer boundary of earth's magnetosphere near the geomagnetic equatorial plane, and it may be propagated as a modified Alfvèn wave. A modified Alfvèn wave is a transverse wave with respect to changes in the electric and magnetic fields. On the other hand, it is a longitudinal wave when viewed as fluid motion (Reference 55). An electromagnetic wave as well as a pressure wave should be in the space between the earth's surface and the lower boundary of the ionosphere. The energy flux associated with an incident modified Alfvèn wave is roughly $(B^2/8\pi)\ V_A$, where V_A is the group velocity of the modified Alfvèn waves and can be taken as the Alfvèn wave velocity at a higher portion of the ionosphere. B is the amplitude of the wave, i.e., the intensity of magnetic fluctuation above the ionosphere.

By assuming conservation of energy flux, the upper limit of the amplitude of the pressure wave at the earth's surface, p_e, can be estimated as follows:

$$\frac{1}{2}\frac{p_e^2}{c_s \rho_s} = \frac{B^2}{8\pi} V_A ,$$

where c_s is the sound wave velocity at the earth's surface, and ρ_s is the air density at the earth's surface. By taking $V_A = 3.10^7$ cm/sec (corresponding to daytime at the sunspot maximum activity) $B = 30\gamma$, $c_s = 3.10^4$ cm/sec, and $\rho_s = 1.25 \times 10^{-3}$ gm/cm^3, we find $p_e \approx 3$ dynes/cm^2. In this estimate the conversion factor between the energy of incident Alfvèn waves and that of secondary pressure waves is assumed to be unity. This factor must actually be very small because of reflections and energy dissipations of incident waves at the upper part of the ionosphere. If it is not small, infrasonic waves could appear in the equatorial region during strong magnetic disturbances. Since the occurrence of aurorae in these regions is negligible, this might provide a method of direct detection of modified Alfvèn waves coming into the earth's atmosphere from the magnetosphere.

CONCLUSIONS

We have shown that one of the most plausible mechanisms for pressure wave generation during geomagnetic disturbances is the periodic heating of the polar ionosphere by auroral particles, observed as pulsating aurorae. As emphasized by Campbell (Reference 56) the main energy source for this type of auroral activity is not necessarily incident auroral particles, but a flow of secondary electrons called the electro-jet. In this respect periodic heating by these intermittent electric currents is essentially the same as the so-called Joule heating discussed by Cole (References 57 and 58).

The following conclusions can be drawn from the present calculation:

1. From Figures 3, 5–9, and 13 it can be seen than an incident energy flux of more than 100 ergs/cm^2-sec will produce acoustic waves observable at the ground, provided the periods are longer than about 10 seconds.
2. The relative intensity of the pressure wave at the ground is higher when the heating is concentrated within a thin layer than when it is distributed over a wide range of altitudes (Figures 3, 5, and 6).
3. The intensity ratio between the inside of the source region and the outside is smaller for long periods than for short periods, as expected.
4. The gradient of intensity around the boundary of the source is steeper when the width of the source is wide.
5. Inside the source the ratio of noncellular to cellular wave intensity is of the order of 10^{-5} for $\tau = 10$ sec and 10^{-3} for $\tau = 100$ sec. Although the noncellular intensity exceeds the cellular at large distances from the source, the contribution of the noncellular wave to the observed intensity is negligible, because both waves attenuate in long distance propagation.
6. According to the present calculations, which are based on an isothermal atmosphere, the intensity of acoustic waves more than several hundred km from the region of

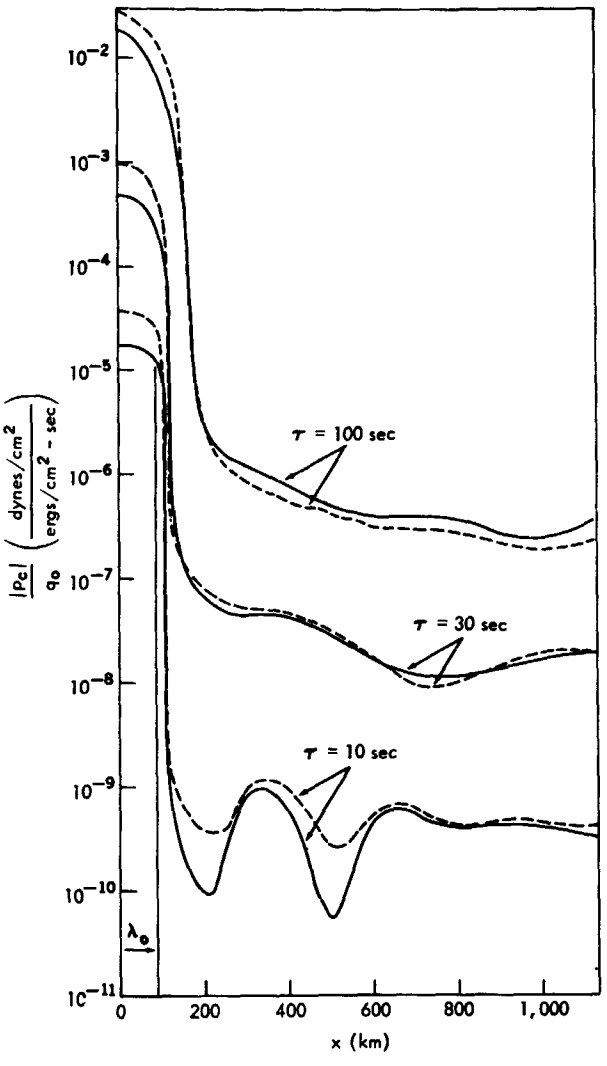

FIGURE 13.—Intensities of cellular waves on the ground in the units of q_0 vs. the horizontal distance x from the center of the source, of which the width λ_0 is 100 km, for τ=10 sec, 30 sec and 100 sec. Full lines and dashed lines stand for h=H and h=½H, respectively.

auroral activity is negligible. For the real atmosphere, therefore, the horizontal propagation of acoustic waves through the ducts around the mesopause and the stratopause is rather important in explaining the diurnal variation of the arrival direction of these waves during the period of high geomagnetic activity, as shown in Figure 1.

7. It should be noted that auroral activities are not necessarily within the auroral zone but, rather, extend toward lower latitudes (nearly to 50°N), when these sonic waves are observed during the periods of magnetic disturbances (as can be seen from the auroral visoplot shown in Figure 2).

To show the position and structure of sonic ducts as well as attenuation of the waves requires the actual atmospheric temperature distributions. This is discussed elsewhere (Reference 59).

Finally, it should be noted that the energy flux of acoustic waves at the ground S in ergs/cm²-sec is

$$S = Ec \quad , \tag{78}$$

where

$$E = \frac{p_s^2}{2\rho_s c^2} \quad ; \tag{79}$$

p_s and ρ_s are the maximum aplitude of pressure change in dynes/cm² and the static density of air atat sea level, and c is the sound velocity in cm/sec.

Since ρ_s is of the order of 1.25×10^{-3} gm/cm³, the energy flux corresponding to $p_s=1$ dyne/cm² is approximately 1.4×10^{-2} erg/cm²-sec. To show the energy relation between the input power and the observed output intensity, as given in Figures 3, 5–10, and 13, the above relation must be used.

ACKNOWLEDGMENTS

The authors wish to express their appreciation to Dr. J. M. Young and his co-workers at the National Bureau of Standards in Washington, D. C., who gave detailed information on their observations of infrasonic waves during magnetic disturbances. Thanks are also due to Dr. G. D. Mead for his comments, and Mr. E. Monasterski for his help on the computer calculations.

REFERENCES

1. CHRZANOWSKI, P., GREEN, G., LEMMON, K. T., and YOUNG, J. M., "Traveling Pressure Waves Associated with Geomagnetic Activity," *J. Geophys. Res.* 66(11):3727–3733, November 1961.
2. CAMPBELL, W. H., "Natural Electromagnetic Energy Below the ELF Range," *Nat. Bur. Stand. J. Res.* 64D(4):409–411, July–August 1960.
3. SONETT, C. P., JUDGE, D. L., SIMS, A. R., and KELSO, J. M., "A Radial Rocket Survey of the Distant Geomagnetic Field," *K. Geophys. Res.* 65(1):55–68, January 1960.
4. HEPPNER, J. P., NESS, N. F., SCEARCE, C. S., and SKILLMAN, T. L., "Explorer 10 Magnetic Field Measurements," *J. Geophys. Res.* 68(1): 1–46, January 1, 1963.

5. HEPPNER, J. P., NESS, N. F., SKILLMAN, T. L., and SCEARCE, C. S., "Magnetic Field Measurements with the Explorer X Satellite," in: *Goddard Space Flight Center Contributions to the 1961 Kyoto Conf. on Cosmic Rays and the Earth Storm*, ed. by F. B. McDonald, NASA Technical Note D-1061, June 1962, pp. 1-20.
6. WATANABE, T., "Electrodynamical Behaviour and Screening Effect of the Ionosphere," *Sci. Rept. Tohoku Univ.* Ser. 5, 9:81-98, 1957.
7. WATANABE, T., "Law of Electric Conduction for Waves in the Ionosphere, *J. Atmos. Terres. Phys.* 24:117-125, February 1962.
8. PIDDINGTON, J. H., "The Transmission of Geomagnetic Disturbances Through the Atmosphere and Interplanetary Space," *Geophys. J.* 2(3):173-189, September 1959.
9. SCHOLTE, J. G., and VELDKAP, J., "Geomagnetic and Geoelectric Variations," *J. Atmos. Terres. Phys.* 6(1):33-45, January 1955.
10. DUNGEY, J. W., "The Propagation of Alfven Waves Through the Ionosphere," Penn. State Univ. Sci. Rept. 57, 1954.
11. KATO, Y., and WATANABE, T., "Further Study on the Cause of Giant Pulsations," *Sci. Rept. Tohoku Univ.* Ser. 5, 8:1-10, 1956.
12. OBAYASHI, T., and JACOBS, J. A., "Geomagnetic Pulsations and the Earth's Outer Atmosphere," *Geophys. J.* 1(1):53-63, March 1958.
13. OBAYASHI, T., "Geomagnetic Storms and the Earth's Outer Atmosphere," *Rept. Ionosphere Res. Japan* 12(3):301-335, September 1958.
14. DESSLER, A. J., "The Propagation Velocity of World-Wide Sudden Commencements of Magnetic Storms," *J. Geophys. Res.* 63(2):405-408, June 1958.
15. JACOBS, J. A., and WATANABE, T., "Propagation of Hydromagnetic Waves in the Lower Exosphere and the Origin of Short Period Geomagnetic Pulsations," *J. Atmos. Terres. Phys.* 24:413-434, June 1962.
16. HEPPNER, J. P., "A Study of Relationships Between the Aurora Borealis and the Geomagnetic Disturbances Caused By Electric Currents in the Ionosphere," Canad. Defense Res. Board Rept. DR-135, 1958.
17. CAMPBELL, W. H., and REES, M. H., "A Study of Auroral Coruscations," *J. Geophys. Res.* 66(1):41-55, January 1961.
18. MCILWAIN, C. E., "Direct Measurement of Particles Producing Visible Auroras," *J. Geophys. Res.* 65(9): 2727-2747, September 1960.
19. CHAMBERLAIN, J. W., "Physics of the Aurora and Airglow," New York: Academic Press, 1961.
20. LAMB, H. "Hydrodynamics," 6th ed., Cambridge, England: The University Press, 1932.
21. BJERKNES, V. F. K., BJERKNES, J., SOLBERG, H., and BERGERON, T., "Physikalische Hydrodynamik," Berlin: J. Springer, 1933.
22. WILKES, M. V., "Oscillations of the Earth's Atmosphere," Cambridge, England: The University Press, 1949.
23. WILKES, M. V., "The Thermal Excitation of Atmospheric Oscillations," *Roy. Soc. Proc.* A207:358-370, July 6, 1951.
24. SAWADA, R., "On the Role of Thermal Excitation in the Atmospheric Tides," *Geophys. Mag.* 26(4):267-281, August 1955.
25. TAYLOR, G. I., "Waves and Tides in the Atmosphere," *Roy. Soc. Proc.* A126:169-183, December 2, 1929.
26. PEKERIS, C. L., "The Propagation of a Pulse in the Atmosphere," *Roy. Soc. Proc.* A171:434-449, July 7, 1939.
27. PEKERIS, C. L., "The Propagation of a Pulse in the Atmosphere. II," *Phys. Rev.* 73:145-154, January 15, 1948.
28. [illegible]ORER, R. S., "The Dispersion of a Pressure Pulse in the Atmosphere," *Roy. Soc. Proc.* A201:175-186, March 22, 1950.
29. GOSSARD, E. E., and MUNK, W., "On Gravity Waves in the Atmosphere," *J. Met.* 11:259-269, 1954.
30. GOSSARD, E. E., "Vertical Flux of Energy into the Lower Ionosphere from Internal Gravity Waves Generated in the Troposphere," *J. Geophys. Res.* 67(2):745-757, February 1962.
31. YAMAMOTO, R., "Study of the Microbarographic Waves (I), Theory of the Microbarographic Waves (I)," *Met. Soc. Japan J.* 34:235-243, December 1956.
32. YAMAMOTO, R., "A Study of Microbarographic Waves (II), Theory of the Microbarographic Waves (II) (continued), *Met. Soc. Japan J.* 35:321-326, 1957.
33. PRESS, F., and HARKRIDER, D., "Propagation of Acoustic-Gravity Waves in the Atmosphere," *J. Geophys. Res.* 67(10):3889-3908, September 1962.
34. WESTON, V. H., "The Pressure Pulse Produced by a Large Explosion in the Atmosphere," *Canad. J. Phys.* 39(7):993-1009, July 1961.
35. WESTON, V. H., "The Pressure Pulse Produced by a Large Explosion in the Atmosphere. II," *Canad. J. Phys.* 40(4):431-445, April 1962.
36. WESTON, V. H., "Gravity and Acoustical Waves," *Canad. J. Phys.* 40(4):446-453, April 1962.
37. MARTYN, D. F., "Cellular Atmospheric Waves in the Ionosphere and Troposphere," *Roy. Soc. Proc.* A201:216-234, March 22, 1950.
38. SEN, H. K., and WHITE, M. L., "Thermal and Gravitational Excitation of Atmospheric Oscillations," *J. Geophys. Res.* 60(4):483-495, December 1955.
39. WHITE, M. L., "Gravitational and Thermal Oscillations in the Earth's Upper Atmosphere," *J. Geophys. Res.* 61(3):489-499, September 1956.
40. WHITE, M. L., "Thermal and Gravitational Atmospheric Oscillations—Ionospheric Dynamo Effects Included," *J. Atmos. Terres. Phys.* 17(3):220-245, February 1960.
41. HINES, C. O., "Hydromagnetic Resonance in Ionospheric Waves," *J. Atmos. Terres. Phys.* 7(1-2): 14-30, August 1955.
42. HINES, C. O., "Internal Atmospheric Gravity Waves at Ionospheric Heights," *Canad. J. Phys.* 38(11): 1441-1481, November 1960.

43. ECKART, C., "The Thermodynamics of Irreversible Processes. I. The Simple Fluid," *Phys. Rev.* 58(3): 267–269, August 1, 1940.
44. ECKART, C., "The Thermodynamics of Irreversible Processes. II. Fluid Mixtures," *Phys. Rev.* 58(3): 269–275, August 1, 1940.
45. ECKART, C., and FERRIS, H. G., "Equations of Motion of the Ocean and Atmosphere," *Rev. Mod. Phys.* 28(1):48–52, January 1956.
46. ECKART, C., "Hydrodynamics of Oceans and Atmospheres," New York: Pergamon Press, 1960.
47. TOLSTOY, I., "The Theory of Waves in Stratified Fluids Including the Effects of Gravity and Rotation," *Rev. Mod. Phys.* 35(1):207–230, January 1963.
48. RAYLEIGH, J. W. S., "The Theory of Sound, Vol. II, Cambridge Trans," 1929, p. 315.
49. SCHRÖDINGER, E., "Zur Akustik der Atmosphäre," *Phys. Zeits.* 18:445–483, October 1, 1917.
50. HANSON, W. B., and JOHNSON, F. S., "Electron Temperature in the Ionosphere," *Mem. Roy. Soc. Sci. Liege* 4:390–423, 1960.
51. FRANCIS, W. E., and KARPLUS, R., "Hydromagnetic Waves in the Ionospher," *J. Geophys. Res.* 65(11): 3593–3600, November 1960.
52. AKASOFU, S., "On the Ionospheric Heating by Hydromagnetic Waves Connected with Geomagnetic Micropulsations," *J. Atmos. Terres. Phys.* 18(2–3): 160–173, June 1960.
53. DESSLER, A. J., "Ionospheric Heating by Hydromagnetic Waves," *J. Geophys, Res.* 64(4):397–401, April 1959.
54. MATSUURA, N., and NAGATA, T., "Turbulence in the Upper Atmosphere," *Rept. Ionosphere Res. Japan,* 12:147–149, 1958.
55. VAN DE HULST, H. C., "Interstellar Polarization and Magneto-Hydrodynamic Waves," in: *Problems of Cosmical Aerodynamics, Proceedings of the Symposium on the Motion of Gaseous Masses of Cosmical Dimensions,* Paris: August 16–18, 1949, Dayton, Ohio: Central Air Documents Office, 1951, pp. 45–56.
56. CAMPBELL, W. H., "Theory of Geomagnetic Micropulsations," AGU annual meeting at Washington, D. C., April 28, 1962.
57. COLE, K. D., "A Source of Energy for the Ionosphere," *Nature* 194:75, April 7, 1962.
58. COLE, K. D., "Atmospheric Blow-Up at the Auroral Zone," *Nature* 194:761, May 26, 1962.
59. MAEDA, K., "Acoustic Heating of the Polar Night Mesosphere," NASA Technical Note D-1912, November 1963.

Appendix A

DERIVATION OF DIFFERENTIAL EQUATION 37

By differentiating Equations 30 and 31 with respect to t and using Equation 33

$$\frac{\partial^2 u}{\partial t^2} = \frac{\partial}{\partial x}\left(c^2 \chi - gw\right) - \frac{1}{\rho_0}\frac{\partial s}{\partial x} \quad . \tag{A1}$$

$$\frac{\partial^2 w}{\partial t^2} = \frac{\partial}{\partial z}\left(c^2 \chi - gw\right) - \left[(\gamma - 1)\, g + \frac{dc^2}{dz}\right]\chi - \frac{1}{\rho_0}\frac{\partial s}{\partial z} \quad . \tag{A2}$$

When the time dependences of u, w, p, ρ, and s are proportional to a common factor $e^{i\delta t}$, a straightforward calculation leads to Equations 34, 35, and 36 from Equations A1, A2, and 33, respectively.

Differentiating Equations A1 and A2 with respect to x and z, respectively, and adding them gives

$$\frac{\partial^2 \chi}{\partial t^2} = c^2 \nabla^2 \chi - g\frac{\partial \zeta}{\partial x} + \left(\frac{dc^2}{dz} - \gamma g\right)\frac{\partial \chi}{\partial z} - \left(\frac{dc^2}{dz} + \gamma g\right)\frac{1}{\rho_0 c^2}\frac{\partial s}{\partial x} - \frac{1}{\rho_0}\nabla^2 s \quad . \tag{A3}$$

where

$$\zeta = \frac{\partial w}{\partial x} - \frac{\partial u}{\partial z} \quad . \tag{A4}$$

Similarly, by differentiating Equations A1 and A2 with respect to z and x, respectively, and subtracting the former from the latter,

$$\frac{\partial^2 \zeta}{\partial t^2} = -\left[\frac{dc^2}{dz} + (\gamma - 1)\, g\right]\frac{\partial \chi}{\partial x} + \frac{1}{\rho_0 c^2}\left(\frac{dc^2}{dz} + \gamma g\right)\frac{\partial s}{\partial x} \quad . \tag{A5}$$

The elimination of ζ from Equations A3 and A5 results in

$$\frac{\partial^4 \chi}{\partial t^4} = c^2 \nabla^2 \frac{\partial^2 \chi}{\partial t^2} + g\left(\frac{dc^2}{dz} + (\gamma - 1)\, g\right)\frac{\partial^2 \chi}{\partial x^2} - g\frac{\partial}{\partial x}\left[\frac{1}{\rho_0 c^2}\left(\frac{dc^2}{dz} + \gamma g\right)\frac{\partial s}{\partial x}\right]$$

$$+ \left(\frac{dc^2}{dz} - \gamma g\right)\frac{\partial}{\partial z}\left(\frac{\partial^2 \chi}{\partial t^2}\right) - \left(\frac{dc^2}{dz} + \gamma g\right)\frac{1}{\rho_0 c^2}\frac{\partial}{\partial z}\left(\frac{\partial^2 s}{\partial t^2}\right) - \frac{1}{\rho_0}\nabla^2\left(\frac{\partial^2 s}{\partial t^2}\right) \quad . \tag{A6}$$

Since it is assumed that u, w, p, ρ, and s are proportional to $e^{i\delta t}$, the elimination of the time derivative from Equation A6 gives Equation 37.

Appendix B

SOLUTION OF EQUATION 59 AT z=0

Applying the Fourier transform to Equations 34 and 35 gives

$$-\sigma^2 U = ikc^2 X - ikgW - \frac{ik}{\rho_0} S \quad . \quad \text{(B1)}$$

$$-\sigma^2 W = c^2 \frac{dX}{dz} - \gamma g X + ikgU - \frac{ik}{\rho_0} \frac{dS}{dz} \quad . \quad \text{(B2)}$$

where U and W are the Fourier transforms of u and w. Solving these bilateral equations with respect to U and W yields

$$\left(\sigma^4 - k^2 g^2\right) U = -ikgc^2 \frac{dX}{dz} + ik\left(\gamma g^2 - \sigma^2 c^2\right) X + \frac{ik\sigma^2}{\rho_0(z)} S + \frac{kg}{\rho_0(z)} \frac{dS}{dz} \quad . \quad \text{(B3)}$$

$$\left(\sigma^4 - k^2 g^2\right) W = -c^2\sigma^2 \frac{dX}{dz} + g\left(\gamma\sigma^2 - k^2 c^2\right) X + \frac{k^2 g}{\rho_0(z)} S + \frac{\sigma^2}{\rho_0(z)} \frac{dS}{dz} \quad . \quad \text{(B4)}$$

Since $W(z=0)=0$ and $dS/dz|_{z=0}=S(z=0)=0$, from the above equations

$$\left.\frac{dX}{dz}\right|_{z=0} = m(\sigma) X(0) \quad , \quad \text{(B5)}$$

where

$$m(\sigma) = g\left(\frac{\gamma}{c^2} - \frac{k^2}{\sigma^2}\right) \quad . \quad \text{(B6)}$$

Similarly, the Fourier transform of Equation 33 is

$$i\sigma P(k, z) = g\rho_0(z) W - c^2 \rho_0(z) X(k, z) + S(k, z) \quad , \quad \text{(B7)}$$

where

$$P(k, z) = \frac{1}{\sqrt{2\pi}} \int_{-\infty}^{\infty} e^{ikx} p(x, z)\, dx \quad .$$

SOLUTION FOR X[z=0], DIRECT CALCULATION

From Equation 61

$$\frac{dX}{dz} = n_1 e^{n_1 z}\left[C_1 - \frac{1}{2\mu} \int_0^z F(z') e^{-n_1 z'} dz'\right] + n_2 e^{n_2 z}\left[C_2 + \frac{1}{2\mu} \int_0^z F(z') e^{-n_2 z'} dz'\right] \quad . \quad \text{(B8)}$$

Using Equation B5, from Equation B8 we get

$$C_1 = -\frac{n_2 - m(\sigma)}{n_1 - m(\sigma)} C_2 \quad . \quad \text{(B9)}$$

If we write

$$A_1 = C_1 - \frac{1}{2\mu} \int_0^z F(z') e^{-n_1 z'} dz'$$

and

$$A_2 = C_2 + \frac{1}{2\mu} \int_0^z F(z') e^{-n_2 z'} dz'$$

then from Equations B8 and B9, by assuming $h<2H$,

$$A_1 e^{-\mu z} = \begin{cases} C_1 e^{-\mu z} & \text{for } 0 \le z \le z_0 \\ \left[C_1 + Q_0 \frac{\sigma^4 - k^2 g^2}{2\mu c^2 \sigma^2} \frac{1}{n_1 + \beta} C^{-(n_1+\beta)z_0} \right] e^{-\mu z} + Q_0 \frac{\frac{\beta}{h} + \frac{k^2 g}{\sigma^2 H} - k^2}{2\mu\, n_1 + \beta} C^{-\left[(1/h)-(1/2H)\right]z} & \text{for } z_0 \le z < \infty \end{cases} \quad \text{(B10)}$$

and

$$A_2 e^{+\mu z} = \begin{cases} C_2 e^{\mu z} & \text{for } 0 \le z \le z_0 \\ \left[C_2 - Q_0 \frac{\sigma^4 - k^2 g^2}{2\mu c^2 \sigma^2} \frac{1}{n_2 + \beta} e^{-(n_2+\beta)z_0} \right] e^{\mu z} - Q_0 \frac{\frac{\beta}{h} + \frac{k^2 g}{\sigma^2 H} - k^2}{2\mu\, n_2 + \beta} e^{-\left[(1/h)-(1/2H)\right]z} & \text{for } z_0 \le z < \infty \end{cases} \quad \text{(B11)}$$

where

$$Q_0 = \sqrt{\frac{2}{\pi}} \frac{\sin \lambda_0 k}{k} \frac{(\gamma - 1) c_0}{\rho_s h c^2} e^{z_0/h} \quad \text{(B12)}$$

and

$$\beta = \frac{1}{h} - \frac{1}{H} \quad \text{(B13)}$$

The term including $e^{\mu z}$ represents the waves whose amplitudes increase with height. The corresponding kinetic energies diverge to infinity provided that $N^2 > M^2$. On the other hand, if $N^2 < M^2$ this term represents inward-going waves.

Because of the boundary conditions listed in the section "Mathematical Treatment," the terms including $e^{\mu z}$ must vanish. Therefore

$$C_2 = C_1 \frac{\sigma^4 - k^2 g^2}{2\mu c^2 \sigma^2} \frac{1}{n_2 + \beta} e^{-(n_2+\beta)z_0} \quad \text{(B14)}$$

Putting this constant into Equation 61, for $z=0$, gives

$$X(k, 0) = \sqrt{\frac{2}{\pi}} \frac{(\gamma - 1) q_0}{h \sigma^4 c^2 \rho_0} e^{(z_0/2H) - \mu z_0} \frac{\sin \lambda_0 k}{k} \frac{\sigma^4 - k^2 g^2}{(n_1 - m)(n_2 + \beta)} \quad \text{(B15)}$$

The continuity of $W(k, z)$ and $P(k, z)$ at $z = z_0$ is satisfied by the above choice of constants, i.e., it can be shown that

$$\lim_{\epsilon \to 0} W(z_0 - \epsilon) = \lim_{\epsilon' \to 0} W(z_0 + \epsilon')$$

$$\lim_{\epsilon \to 0} P(z_0 - \epsilon) = \lim_{\epsilon' \to 0} P(z_0 + \epsilon')$$

SOLUTION FOR X[k,0] BY MEANS OF THE LAPLACE TRANSFORM

By applying the Laplace transform with respect to z,

$$\tilde{X}(k, s) = \int_0^\infty e^{-sz} X(k, z)\, dz \tag{B16}$$

Equation 59 becomes

$$\left(s^2 - 2Ns + M^2\right) \tilde{X} - (s - 2N) X(0) - \left.\frac{dX}{dz}\right|_{z=0} = Q_0 \frac{e^{-(s+\beta)z_0}}{s+\beta} \left[s^2 - 2Ns - k^2\left(1 - \frac{g}{\sigma^2 H}\right)\right].$$

By making use of the relation shown by Equation B5, this is

$$\tilde{X}(k, s) = \frac{(s - 2N - m)}{(s - n_1)(s - n_2)} X(0) + \frac{Q_0 e^{-(s+\beta)z_0}}{\beta + s} \left[1 - \frac{\sigma^4 - k^2 g^2}{(s - n_1)(s - n_2) c^2 \sigma^2}\right] \tag{B17}$$

where n_1 and n_2 are given [illegible] and 64; $m = m(\sigma)$ and Q_0 are given by Equations B6 and B12.

By making use of the inverse [illegible] of Equation B16 the solution to Equation 59 is

$$X(k, z) = \left(\frac{2N - m - n_1}{2\mu} e^{n_1 z} - \frac{2N - m - n_2}{2\mu} e^{n_2 z}\right) X(0) + Q_0 e^{-\beta z} \theta(z - z_0)$$

$$- Q_0 \frac{\sigma^4 - k^2 g^2}{2\mu c^2 \sigma^2} e^{-\beta z_0} \left[\frac{e^{n_2(z - z_0)}}{\beta + n_2} - \frac{e^{n_1(z - z_0)}}{\beta + n_1} + \frac{e^{-\beta(z - z_0)}}{(\beta + n_1)(\beta + n_2)}\right] \theta(z - z_0) . \tag{B18}$$

Because of the boundary conditions at $z = \infty$, the term proportional to e^{nz} must vanish, i.e., from Equation B18

$$- \frac{2N - m - n_2}{2\mu} X(0) - Q_0 \frac{\sigma^4 - k^2 g^2}{c^2 \sigma^2} \frac{e^{-(\beta + n_2) z_0}}{2\mu(\beta + n_2)} = 0 . \tag{B19}$$

This gives the same solution as Equation B15. It should be noted that the above solution satisfies the conditions of continuity of w(x, z) and p(x, z) at $z = z_0$, although u(x, z) and s(x, z) are not continuous at $z = z_0$.

Appendix C

EVALUATION OF p[x, 0]

As can be seen from Equation B15 X(k, 0) is an even function of k. Therefore, the substitution of Equation B15 into Equation 67 gives

$$\chi(x, 0) = \frac{2}{\pi} \frac{(\gamma - 1) q_0 \sigma^2}{h k_g^2 \rho_s c^4} e^{z_0/2H} \int_0^\infty e^{-\mu z_c} \frac{\cos xk \sin \lambda_0 k}{k} \frac{k_g^2 - k^2}{(n_1 - m)(n_2 + \beta)} dk \quad \text{(C1)}$$

where

$$k_g = \frac{\sigma^2}{g} . \quad \text{(C2)}$$

Since μ is a real function of k for $k \geq k_c$ and complex for $0 \leq k < k_c$, where

$$k_c = \frac{\sigma}{c} \sqrt{\frac{\sigma^2 - \sigma_A^2}{\sigma^2 - \sigma_B^2}} . \quad \text{(C3)}$$

Equation C1 can be written

$$\chi(x, 0) = \chi_c(x, 0) + \chi_{nc}(x, 0) , \quad \text{(C4)}$$

where

$$\chi_c(x, 0) = \frac{2}{\pi} \frac{(\gamma - 1) q_0 \sigma^2}{h k_2^2 \rho_s c^4} e^{z_0/2H} \int_0^{k_c} e^{-i\eta z_0} \frac{\cos xk \sin \lambda_0 k}{k} \frac{k_g^2 - k^2}{(n_1 - m)(n_2 + \beta)} dk , \quad \text{(C5)}$$

and

$$\chi_{nc}(x, 0) = \frac{2}{\pi} \frac{(\gamma - 1) q_0 \sigma^2}{h k_2^2 \rho_s c^4} e^{z_0/2H} \int_{k_c}^\infty e^{-\mu z_0} \frac{\cos xk \sin \lambda_0 k}{k} \frac{k_g^2 - k^2}{(n_1 - m)(n_2 + \beta)} dk . \quad \text{(C6)}$$

The integrand of $\chi_{nc}(\chi, 0)$ has two singular points σ/c and σ^2/g, corresponding to the two types of free oscillations of the noncellular mode which were pointed out by Pekeris* and have been discussed earlier. Because of a steep exponential term $e^{-\mu z_0}$, however, contributions of these singularities to the integral is not as important as the contribution from the narrow band near $k \geq k_c$, where the exponential term is nearly unity.

The integrand of x_c has no singularities but oscillates by the term $e^{-i\eta z_0}$. The main contribution arises from a narrow domain near $k \leq$ approx. k_c. Equation 68 can be written

$$p(x, 0) = p_c(x, 0) + p_{nc}(x, 0) , \quad \text{(C7)}$$

where

$$p_c(x, 0) = p_r + ip_i , \quad \text{(C8)}$$

*Pekeris, C. L., "The Propagation of a Pulse in the Atmosphere. II," *Phys. Rev.* 73:145–154, January 15, 1948.

$$\left|p_c(x,0)\right| = \frac{2}{\pi}\frac{(\gamma-1)q_0\sigma}{hk_g^2c^2}e^{z_0/2H}\left|\int_0^{k_c} e^{-i\eta z_0}\frac{\cos xk\sin\lambda_0 k}{k}\frac{k_g^2-k^2}{(n_1-m)(n_2+\beta)}\,dk\right| = \sqrt{p_r^2+p_i^2}\,; \quad \text{(C9)}$$

and

$$p_{nc}(x,0) \approx \frac{2}{\pi}\frac{(\gamma-1)q_0\sigma}{hk_g^2c^2}e^{z_0/2H}\int_{k_c}^{k_g} e^{-\mu z_0}\frac{\cos xk\sin\lambda_0 k}{k}\frac{k_g^2-k^2}{(n_1-m)(n_2+\beta)}\,dk\,. \quad \text{(C10)}$$